# Description of Gallium Phosphide Epitaxy Growth by Computational Chemistry

**Andreas Stegmüller**
M.Phil, *14. September 1987 in Frankfurt am Main

Fachbereich Chemie

Philipps-Universität Marburg

Diese kumulative Dissertation wurde zur Erlangung des akademischen Grades

*Doctor rerum naturalium*

am 19. Juni 2015 vorgelegt.

Disputation am 17. Juli 2015 (UMR 1180)

Erstgutachter: Dr. Ralf Tonner
Zweitgutachter: Prof. Dr. Carsten von Hänisch

*Für Julie,*

*meine große Liebe.*

# Contents

# Chapter 1

# Introduction

## 1.1 Interdisciplinary Materials Science

The research presented in this dissertation originates in the interdisciplinary field of semiconductor materials science where novel functionality is to be explored and integrated into conventional silicon-based devices. One of the desired achievements is the development of optically active structures to be applied in efficient solar cells, laser optics or parallel-computing. The research challenges addressed concern material growth and encompass the comprehension of elementary processes on multiple time and length scales. Computational methods construed for specific regimes and questions deliver valuable insight where experimental evidence might be scarce. In the work presented, the smallest scales relevant for materials science are addressed by quantum-chemical calculations describing the atomic and electronic structure of molecules, extended surfaces and material films.

The system in focus is the growth of gallium phosphide on silicon substrates, however, many results obtained can be generalized to growth aspects of other III/V (groups 13 and 15)[A] compound materials. The materials are epitaxially grown from precursor compounds under specific, non-equilibrium thermodynamic conditions using metal-organic vapour phase epitxy (MOVPE). Growth parameters and materials compositions are under development and, thus, many aspects of growth are yet uncharacterized.

Elementary processes are investigated in this work as they determine the resulting material's properties and are often inaccessible for experimental analysis. Computational methods by means of density functional theory are applied. The investigations encompass chemical reactivity of triethylgallane (TEG, $Ga(C_2H_5)_3$),

---

[A] The elements from groups 13 and 15 in the periodic table are referred to as main groups III and V in materials science.

*tert*-butylphosphine (TBP, $P(C_4H_9)H_2$) and related precursors[B], surface processes like adsorption, diffusion or surface-assisted reactivity as well as interface properties of gallium phosphide thin films on silicon. New reaction mechanisms involved in precursor decomposition both in the gas phase and adsorbed on Si(001) are presented.

Material interface properties are studied profiting from a chemical rather than a solid state physics perspective which enabled the discussion on the origin of interface morphologies, local polarization and strain effects as well as atomic bonding situations based on chemical arguments.

Multi-scale approaches combine the kinetic data on elementary processes generated and provide comprehensible product distributions (or adsorbate configurations). A lattice-independent kinetic Monte Carlo algorithm for the simulation of precursor decompositions was developed, however, it is flexible enough to be applied for other e.g. surface- and growth-related systems.

## 1.2 Functional Materials for Electronic and Optoelectronic Devices

As to improve the performance of logical electronic devices according to Moore's law,[1] one pathway of development is to integrate novel materials on conventional silicon-based devices.[2] Thereby, two challenging research areas arise: (i) the optimization of the new materials' electronic properties and/or the introduction of new optoelectronic functionality and (ii) their integration into existing device structures.

The driving aspect of functionalization is to create compound materials from groups 13 and 15 which might have, in contrast to silicon, direct band gaps in the visible range. Recently, high-efficiency solar cells (44.7% quantum yield in GaInP/-GaAs//GaInAsP/GaInAs)[3] could be realized. On the other hand, the research field of *silicon photonics* develops light emitters (lasers, LEDs) from the same class of materials by exploiting the reverse electronic process.[4] Next to raising the efficiency of lighting sources, the substitution of wired inter-device communication by optical signals might revolutionize conventional (silicon-based) parallel computing.[5]

The conventional approach of raising performances of logical devices is given by increasing the transistor density[2] through miniaturization of existing and novel structures within devices. Note that this is only partly an engineering problem, however, as thin films reach the nanoscale, insight from fundamental research on the

---

[B] The term precursor refers to the molecular compound applied as material source in MOVPE rather than the pre-adsorbate state of a molecule in interaction with a surface.

growth mechanisms as well as size- and structure-dependent properties is inevitable.[6] The growth of most film-substrate combinations is constricted to limited thicknesses by mechanical strain and a multitude of growth-related effects.

Moreover, the concept of quantum well (QW) structures for optoelectronic devices relies on the integration of stacked thin films where electrons and holes (or electron-hole pairs in the active film) can move freely in two dimensions, however, are enclosed in a potential well along stacking direction. This effect can only be realized for film thicknesses within dimensions of the material's *de Broglie* wavelength $\lambda_{\text{deBroglie}}$. Figure 1.1 illustrates the concept of a (multi-) QW superstructure on a silicon substrate and structural buffer, with indicated barrier and active QW layers.

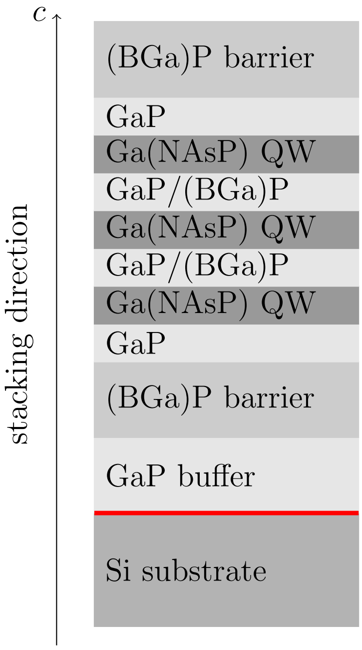

Figure 1.1: Schematic of a triple-quantum well structure with active Ga(NAsP) layers (QW), (BGa)P barrier layers as well as GaP structural buffers grown on a Si substrate.

There are, hence, several research questions to be adressed: **(1)** the development of suitable active and barrier (QW) materials, **(2)** the "engineering" of electronic properties including the effects of strain, confinement, and material composition for optical functionalization, and **(3)** the understanding of growth and structure-(interface-)determining processes.

**(1)**

Figure 1.2 provides an overview on the concept of band gap bowing used for exploring suitable active and barrier materials.

Retrace, for instance, the binary compositions of gallium/V materials, where the

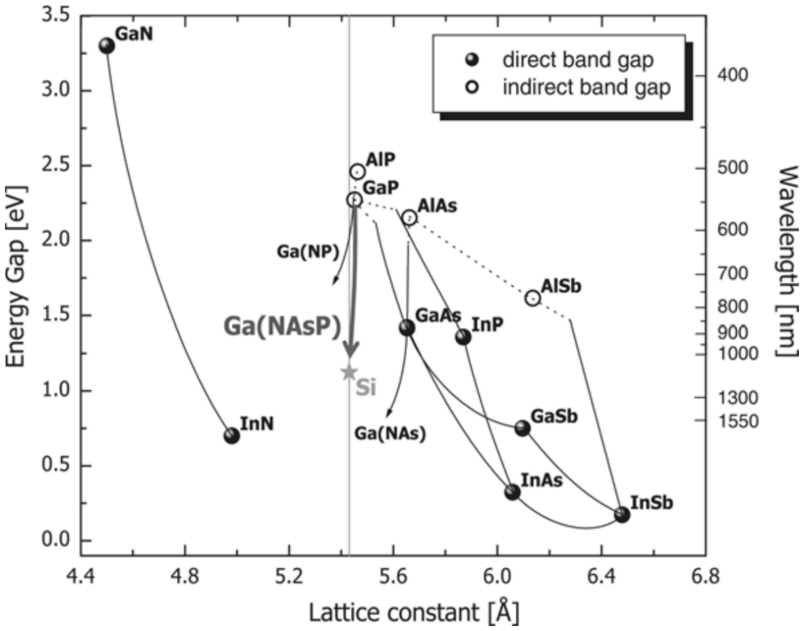

Figure 1.2: Energy band gap versus lattice constant of Si and illustrative III/V compound materials. Figure reprinted with permission from Kunert et al.[7]

band gap is not only (approximately linearly) reduced with increasing lattice constant (Végards rule) but also changes from *direct* (GaN) to *indirect* (GaP) and back to *direct* (GaAs, GaSb) gaps. On the other hand, a mixing of III/V elements towards ternary and quaternary compound materials changes the band gap in a non-linear, "bowed" fashion as can be retraced e.g. by the curves GaN-InN and GaP-GaAs.[7] The variability provides large space for modification as can be reenacted from following the development of band gaps of AlN (5.4 $eV$, indirect, zinc-blende structure, not shown),[8] GaN (3.3 eV) to InN (0.7 eV). The *direct*, quaternary semiconductor material Ga(NAsP) is compiled as almost lattice-matched to Si and GaP and delivers a photoluminescence maximum around 900 nm.[9] This is desired for the integration into laser devices operating in the near-IR range.

**(2)**

An illustration of a general *indirect* semiconductor band structure around the center of the Brillouin zone is provided in Figure 1.3 with the example of GaP. A terminology for conduction (CB) and valence bands (VB), *direct* (optical gap, $\Delta E_O$) and *indirect* (fundamental gap, $\Delta E_g$) electronic transitions, and the splitting of the valence bands into light hole (LH), heavy hole (HH) and spin-orbit(SO) split-off VB is provided.

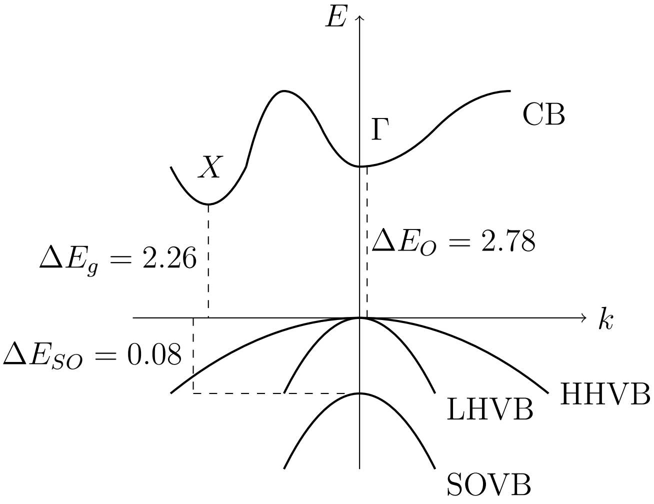

Figure 1.3: Schematic of GaP's band structure providing the optical energy gap $\Delta E_O$ at the $\Gamma$ point, the fundamental gap $\Delta E_g$ (conduction band minimum CBM at $X$)[10] and the spin-orbit split-off energy $\Delta E_{SO}$[11] in eV (at 300 K), respectively. The conduction band (CB), heavy hole (HH), light hole (LH) and spin-orbit valence bands (SOVB) are indicated.

The laser performance of QW structures depends on the alignment of the electronic band structure at the material interfaces. In order to raise the efficiency of III/V lasers, it is desired to increase the electronic barriers enclosing the active film in the QW heterostructure (see Figure 1.1). This can be achieved either by modifying the **composition and interface strain** of the film, or by utilizing the electronic **confinement** effect at the interface. Quantum confinement in the active QW heterostructure $Ga_{0.67}In_{0.33}As/Ga_{0.20}In_{0.80}As_{0.45}P_{0.55}/InP$ is illustrated in Figure 1.4.

At thermal equilibrium, energy offsets between VB and CB are represented by their bulk band edges, respectively, assuming abrupt material interfaces (Figure 1.4 (a)). Any holes present in the system will be confined in the VB, i.e. bound to discrete states. After an injection of carriers into the system (film excitation), an attractive electrostatic potential will bring holes (VB) and electrons in the CB close to each other and squeeze them into the well region (i.e. localization of excitons in 0...130 Å, Figure 1.4 (b)). If this region extends less than the electron-hole pair's $\lambda_{\text{deBroglie}}$, also the CB electrons are confined to discrete states in the CB well as shown.[13,14] The confinement effect in VB and CB wells can trap higher electron-hole ($e$-$h$ exciton) densities (keep $e$ and $h$ separated) and thus increase the amplification (gain) in lasers.

As mentioned above, mechanical strain is another important characteristic to affect the electronic barrier at a QW film interface.[15] Strain causes a splitting of the VB into LH and HH bands resulting in an opening of the gap by compression (lowering the VB maximum, VBM, HH) and a closing of the gap from tension (lifting VBM,

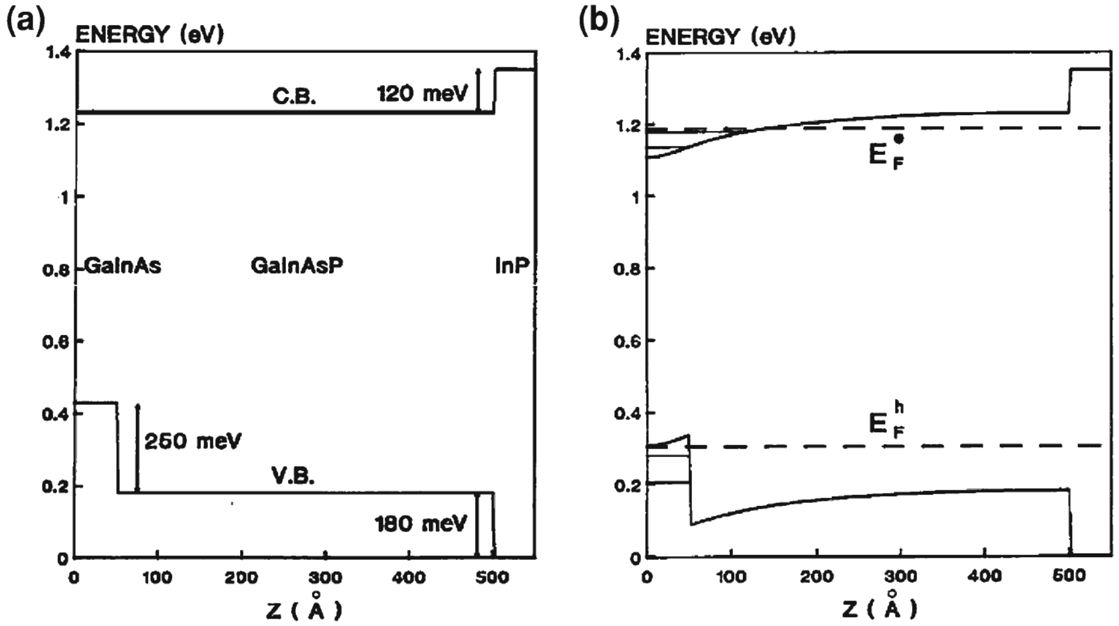

Figure 1.4: Electronic structure of a QW heterostructure (a) at thermal equilibrium and (b) after carrier injection to a density of $n_{inj} = 2 \times 10^{12}\ cm^{-2}$ leading to carrier self-confinement and bound states in the VB and CB. Figure reprinted with permission from Barrau et al.[12]

LH), in general.

The effect of strain and film thickness in a QW structure of InGaAs/GaAs with varied composition is presented in Figure 1.5. The largest gaps for the presented system (and hence smallest photoluminescence wavelengths) can be achieved by thin (6 nm) layers of compressively strained composition while mainly the VB is affected by mechanical strain (reduction of in-plane heavy-hole mass, opening of gap).[13] Typical QW structures from III/V compound materials are compressively strained with lattice-mismatches of ca. 1-2% (GaP-Si: 0.37%).Note that films must be grown below the film-substrate specific critical thickness to avoid the formation of crystal defects like misfit-dislocations.[16,17]

Alongside, strain also affects electron-hole recombination mechanisms as slightly strained layers might show reduced Auger (non-radiative) loss and intervalence band absorption.[18] For the Ga(NAsP)/GaP laser, however, defect-related recombination or carrier leakage were found to be dominant in contrast to temperature-independent loss mechanisms (Auger).[19–22] The performance strongly depends on the structural purity, composition and strain of the grown materials and clean crystal structures need to be realized. In general, defects or doping should be avoided in barrier films as it might significantly increase free carrier absorption, another possible loss mechanism in lasers.

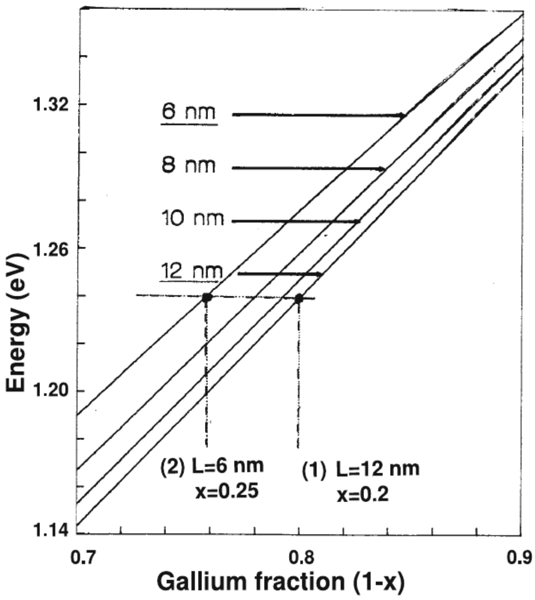

Figure 1.5: $In_xGa_{1-x}As/GaAs$ CBM-LHVB energy gap for different film thicknesses L and compositions for (1-x). Figure reprinted with permission from Carrére.[13]

**(3)**

All of these realization strategies for III/V-lasers require fundamental understanding of the underlying growth characteristics, elementary processes involved as well as film and interface stabilities.

The III/V material gallium phosphide (GaP), which is grown epitaxially on silicon substrates and typically serves as structural buffer layer, is in the focus of this dissertation. GaP and Si are almost lattice-matched materials and the integration has been investigated for electronic and optoelectronic application since the 1970s.[23] New electronic devices (transistors) with elevated charge carrier mobility based on GaP-Si buffer layers were realized.[24] Furthermore, with the QW structure Ga(NAsP)/GaP, a laser operating at room temperature was built.[9]

However, the optimum is not yet reached and control of the composition and structure formation is essential.[7] Jandieri et al.[25] showed how e.g. compositional disorder in the region between the barrier and QW films influences photoluminescence behaviour of a Ga(NAsP)/GaP diode laser. With an increasing concentration of nitrogen (less character of disorder), red-shifted photoluminescence was detected at low temperatures (increased effective mass in CB,[26] lowering of CB edge, gap closes).

In the following section, an overview of the characteristics and challenges present in III/V semiconductor epitaxial growth are presented. MOVPE is the state-of-the-art technique to construct multi-QW heterostructures of various compositions and substrate-layer combinations.

## 1.3 Metal-Organic Vapour Phase Epitaxy

Many compound materials cannot be grown in thermodynamic equilibrium conditions as either immensely high temperatures are required or the desired compositions cannot be reached at all. The fundamental concepts of equilibrium liquid-phase epitaxy (LPE) that used to be applied for the growth of some III/V compound materials are introduced further below. A comparison to the non-equlibrium MOVPE is provided.

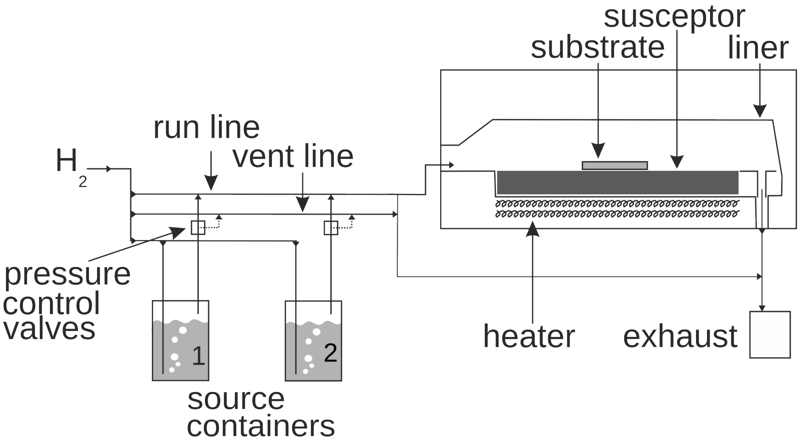

Figure 1.6: Set-up of a MOVPE reactor applying $H_2$ as carrier gas for the volatile sources (containers 1 and 2, e.g. TEGa and TBP). The susceptor chamber is supplied by two vapour lines and the substrate is heated indirectly by IR irradiation.

Figure 1.6 illustrates the typical set-up of a MOVPE reactor. The carrier gas ($H_2$) both ventilates (vent line) the susceptor chamber and also transports the vaporized precursors from the conditioned source containers into the reactor (run line) towards the substrate. The susceptor is heated by IR irradiation so that temperatures at the substrate and directly above (centimeter scale) are highest. An exhaust system filters, liquefies and stores the toxic waste.

The growth of novel compound materials is typically very sensitive towards several parameters and conditions.[27,28] The most striking requirements to the growth set up comprise the following list.

- produce stable & metastable III/V compound materials
  (including binary, ternary, quaternary etc. mixtures)
- grow to high crystalline perfection
- reach intended stoichiometric compositions (right element on each lattice site)
- deliver high purity deposition (impurity concentration in III/V sources and environment must be small, e.g. oxygen/water in $H_2$ or $N_2$ carrier gas: <100

ppt (10N), any (main group) dopants below 1-10 ppt (8-9N); no transition metals)

- grow thin films in nm-scale (typically 50 nm or less for device integration)[29]
- steer film thickness and deposition rate,
  intended: appr. 1 monolayer/s $\approx$ 1 $\mu$m/h
- achieve abrupt hetero interfaces (structural transitions between films)

In order to achieve these requirements for different material compositions, growth parameters are systematically refined. A fundamental understanding of the underlying chemical processes is desired to accelerate growth optimization and improve the resulting crystal quality.

### 1.3.1 Equilibrium Liquid-Phase vs. Non-equilibrium Vapour Phase Epitaxy

Thermodynamically stable compound materials like GaP ($T_{\mathrm{melt}}$(GaP) = 1470 °C) or GaAs ($T_{\mathrm{melt}}$(GaAs) = 1240 °C) can be grown in liquid-phase epitaxy (LPE) from e.g. elementary melts. Obviously, for many materials, high temperatures are necessary which is expensive and energy-intensive. The ternary compound material (GaIn)P can be grown from a solution of InP in a mixed In/Ga solvent ($T_{\mathrm{melt}}$(In/Ga,eutectic mixture) = 15.5 °C),[30] however, different phases and compositions are achieved depending strongly on the growth temperature applied.[31]

GaP is thermodynamically (very) stable in a stoichiometric composition (0.5:0.5), which can be grown from the liquid. As can be seen in Figure 1.7, for temperatures up to $T_{\mathrm{melt}}$ = 1470 °C the composition can only be varied in a small range separating the pure GaP(s) solid bulk phase from the mixed regimes of bulk GaP with liquid Ga (Ga-rich conditions, $T_{\mathrm{melt}}$(Ga) = 29.8 °C) or liquid P (P-rich conditions, $T_{\mathrm{melt}}$(P,white) = 44.2 °C). The realization of points close to GaP's solidus line (point data Figure 1.7) can be tailored by applying different doping conditions.[32]

However, for growth at such high temperatures, the entropy-driven formation of eigen-defects (intrinsic defects like vacancies or misfit dislocations) becomes a limitation. Furthermore, above a specific temperature $T_{\mathrm{inc}}$, incongruent evaporation of the elements occurs which destroys the crystal stoichiometry and introduces defects.[17]

On the other hand, microscopic strain caused by the lattice-mismatch $\Delta a/a$ is present in many ternary and higher order mixed compounds. This affects critically the stability (and meta-stability) of compound materials. Below a critical

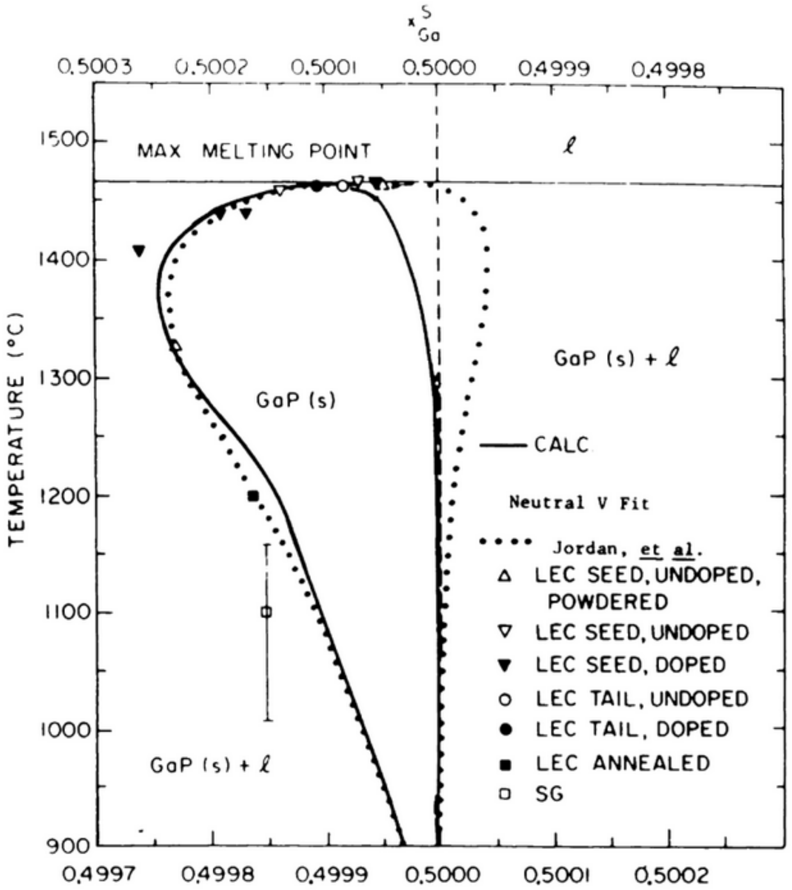

Figure 1.7: Phase diagram of GaP at varied composition (Ga mole fraction at top abscissa) around stoichiometric minimum from simulation (straight line) and experiment (dashed, data from Jordan et al.[33]). Figure reprinted with permission from Stringfellow.[32]

temperature $T_{\text{crit}}$ which is related to strain

$$E_{\text{strain}} \propto \Delta a/a, \tag{1.1}$$

stable phases might not be accessible and growth must be performed in the metastable regime. Table 1.1 shows how the critical temperature varies with composition (thus, strain). It becomes obvious that potentially interesting, strained compound materials cannot be achieved under equilibrium conditions.

Under non-equilibrium conditions, the partial pressures of the sources largely affect growth. In MOVPE growth temperatures are applied well above $T_{\text{crit}}$ and $T_{\text{inc}}$ so that the growth rate and material composition is thus determined by the partial pressures of the group III sources. The ratio

$$p_{\text{V}}^{\text{epi}}/p_{\text{III}}^{\text{epi}} = p^{\text{bep}} \tag{1.2}$$

Table 1.1: Estimated critical temperatures (in K) of several III/V compound semiconductor materials.

| III/V | (AlGa)As | Ga(AsP) | (InGa)N | Ga(NAs) |
|---|---|---|---|---|
| $T_{crit}$ | 65 | 270 | 1770[34] | 7500 |

is called beam equivalent pressure, typically $p^{\mathrm{bep}} \gg 1$.[35] Group V source(s) have high equilibrium partial pressures (as the elements are intrinsically stable inside the materials) and need to be provided in excess in order to avoid incongruent evaporation. Based on the phase diagram of most III/V materials,[32] the source with lower equilibrium pressure (group III) determines the overall growth rate. Total pressures are chosen in the range of 50-100 mbar aiming at total growth rates of 1 monolayer/s. Growth temperatures are chosen about half $T_{\mathrm{melt}}$ and well above $T_{\mathrm{crit}}$, if possible, avoiding equilibrium and eigen-defect formation.

There is a complex network of kinetically controlled, elementary processes underlying the results of an epitaxy growth experiment.[36–38] Most of these processes have not yet been described as their *in situ* observation during MOVPE growth is tedious. Often, only the total process rate, measured by film thickness grown per time interval at given growth conditions, is known and the individual rates and reaction pathways are not accessible.[39] Those processes can be studied by *ab initio* calculations which deliver sufficient accuracy on the microscopic scale.[40]

### 1.3.2 Description of Elementary Processes in MOVPE

The elementary processes involved in a MOVPE procedure are sketched illustratively in Figure 1.8. The growth was categorized into five phases following the chronology of events.

In the following, processes occurring within these five phases are shortly described including experimental analysis available as well as open research questions and challenges for successful semiconductor growth. Further, specific conditions applied in MOVPE growth of GaP on Si(001) (Materials Science Center WZMW, Marburg University) will be discussed.

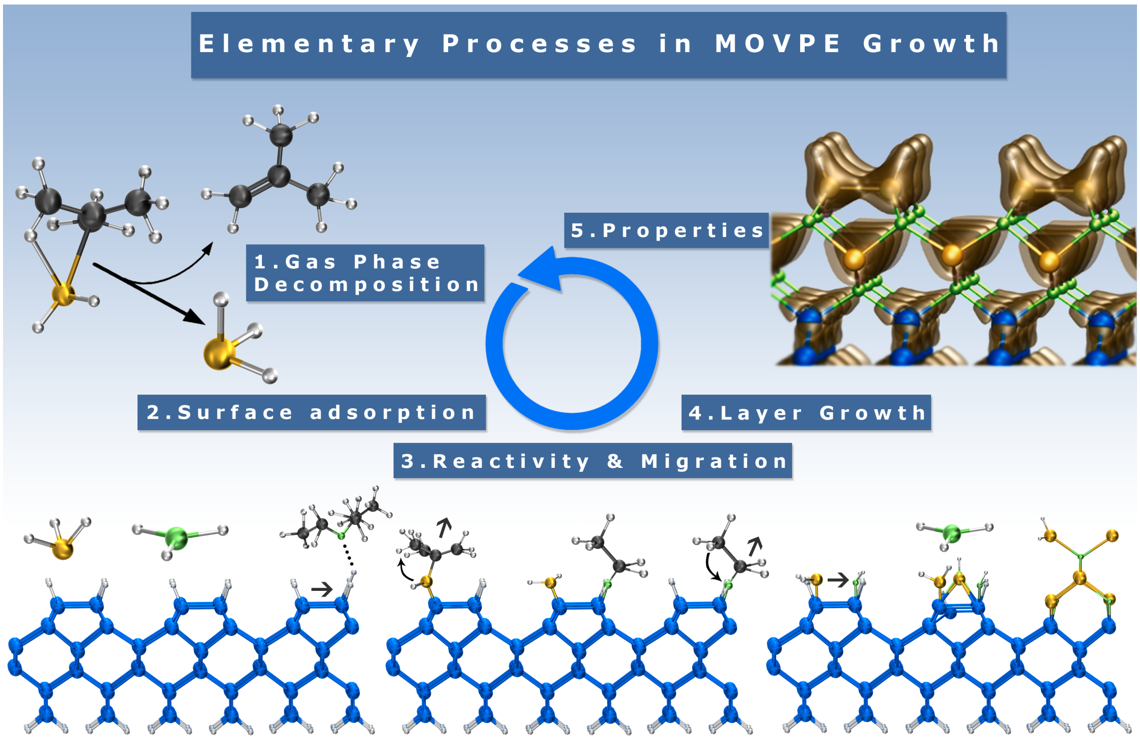

Figure 1.8: Elementary processes in MOVPE of III/V compound semiconductors on a passivated Si(001)-H substrate. Chemical events were categorized into five phases.

1. **Gas Phase Precursor Chemistry and Precursor Design**

   In MOVPE, instead of using elementary sources (molten metals or pnictogenes) the target elements are transported to the substrate as small precursor molecules diluted in an inert gas flux ($H_2$, $N_2$, Ar or similar). Among other requirements concerning handling and toxicity, the precursors need to be volatile in order to fulfill the above requirements for crystal growth (section 1.3).[41] The species need to decompose cleanly without leaving any side groups (carbon) in the material grown. Hence, chemical decomposition mechanisms are required which lead to volatile and stable side products leaving the reaction chamber with the carrier gas.[42] Designing those precursors is thus a multidisciplinary task involving conceptual and synthetic chemistry as well as materials science.[43–45]

   The gas phase reactivity can be studied by *ab initio* methods in the framework of quantum chemistry while direct tracking of individual processes is experimentally unfeasible. A variety of powerful analytical tools based on molecular wave functions and charge density is available offering the possibility to follow and comprehend chemical processes on the electronic scale.[46,47]

   For the growth of a GaP film on a Si substrate by MOVPE, *tert-*

butylphosphine (TBP, $P(C_4H_9)H_2$) and triethylgallane (TEGa, $Ga(C_2H_5)_3$) are applied.[27] In comparison to their predecessors, phosphine ($PH_3$) and trimethylgallane (TMG, $Ga(CH_3)_3$), they show much better decomposition performance measured by higher total growth rates with less carbon incorporation into the material deposited.[48–50] Some decomposition pathways were concluded from *in situ* mass spectrometry of the MOVPE gas phase environment identifying the important $\beta$-hydrogen elimination channel for TBP.[51]

2. **Surface Activation and Adsorption**

   Semiconductor surfaces are subject to structural reconstructions under thermal conditions. For the important Si(001) surface, for instance, the fundamental reconstructions (2x1), p(2x2) and c(4x2) stabilize the surface by reducing the number of unpaired electrons (unsaturated "dangling bonds") originating from a cleavage along the ideal lattice plane.[52,53] The periodicity of the surface reconstructions can be measured by electron diffraction experiments (RHEED, LEED) even during epitaxy growth.[54,55] The microscopic structure can be calculated from first principles, which is important as it affects, among others, the electronic structure (the band gap) of a thin film semiconductor.[56]

   The substrate surface structure is also relevant for materials growth as important elementary processes and chemical activity are affected.[48,57] Under MOVPE conditions, remaining dangling bonds are saturated by hydrogen atoms provided by the carrier gas or the decomposing group 15 source molecules. However, to adsorb precursor molecules, the Si−H bonds at the surface need to be broken in order to generate an active adsorption site. Furthermore, the adsorption/desorption kinetics of relevant precursor fragments are potentially growth-limiting and need to be investigated on the microscopic scale. The chemical aspects of coverage and adsorbate-assisted surface activation (e.g. vacancy stabilization) are not trivially accessible by experiments (such as Scanning Tunneling Microscopy, STM, or temperature-programmed desorption, TPD) but might be important for adsorption capabilities.

   Several mechanisms might participate in surface activation and adsorption. Simulation techniques from first principles can help to understand this interplay.[58,59] An important example is the desorption of $H_2$ from Si(001)(2x1) via recombination which has a barrier of 2.48 eV at 0.1 monolayer coverage as determined by optical second harmonic generation spectroscopy (SHG).[60] An *ab initio* study supported these findings quantitatively along with the conclusion that tunneling effects and molecular vibrations are negligible with respect to surface-phonon contributions.[61]

TEGa and group 13 homologues[62] adsorb on III/V surfaces via a physisorbed precursor state and decompose further via $\beta$-hydride eliminations there. In contrast to Si surfaces, the decomposition rates on GaAs decrease with higher temperatures as concluded from thermal desorption spectroscopy and mass spectrometry. Homolysis was observed on non-passivated surfaces.[63]

3. **Surface Decomposition and Surface Diffusion**

In MOVPE atmosphere containing $H_2$, hydrogen-substituted III/V elements (gallane, phosphine) are expected as decomposition intermediates,[64] however, it is essential that any remaining alkyl ligands can be eliminated. This is likely to be a surface-assisted mechanism, as the system's highest temperatures are available at the substrate surface. Moreover, the (activated) substrate surface and, potentially, co-adsorbates offer various decomposition pathways that are not available in the gas phase.[65–67] Phosphine, for example, decomposes on non-passivated Si(001) and GaP(001) surfaces via the intermediate adsorbates $PH_2$ and PH until, in competition with thermal desorption of $P_2$, atomic P is incorporated into the surface.[68–70] The decomposition of TBP is enhanced on GaP surfaces relative to Si(001), however, the mechanistic origin of this is yet non-proven.[71] For the above example on recombinative desorption of $H_2$,[72] the interaction of Si$-$H with an adsorbate or an activated surface site need to be investigated. Adsorbate chemical processes can be studied experimentally by electron energy loss spectroscopy (HREELS) or STM.[73,74]

However, it is generally assumed that growth is limited by surface transport. As to agglomerate adsorbed species to a layer or an island sufficiently sized for crystal nucleation, adsorbates need to be transported to and from preferred surface sites. Diffusion on Si(001) is anisotropic as large barriers exist across Si-Si dimer rows in contrast to hopping along the rows.[75] For the MOVPE growth of GaP on Si, different mobilities of Si, H, Ga and P species were calculated which determine the lateral transport characteristics. This is also linked to the microscopic growth mode of a crystal material (see below).

Due to the surface anisotropy calculated adatom diffusion barriers for H atoms range from 1.0 to 3.1 eV[76] while Si (0.6-1.0 eV)[77,78] and P (0.8-1.3 eV)[78,79] show slightly increased mobility.

Chemical processes are subject to huge configurational spaces, however, *ab initio* calculations can provide important insight into structure, thermodynamic stabilization and kinetics, given reasonable approximations are followed limiting the degrees of freedom.[66] A close cooperation with experimental analytics is thus inevitable.

Adsorbate chemistry has been calculated by non-periodic cluster models[80,81] although periodic surface systems are desirable for a more accurate description.[82,83] Again, kinetics of elementary processes will dominantly limit the decomposition in MOVPE.[29]

4. **Nucleation and Layer-by-layer Growth**

The nucleation of crystal growth is complex and not yet fully understood.[84,85] In a simplified model, multiple adsorbates potentially agglomerate given the (lateral) binding between them is strong against thermally driven diffusion.[86] Then, the quantification of lateral interactions as well as the chemistry between adsorbates has to be considered. Furthermore, as was shown for GaN semiconductor growth, diffusion might be affected by individual or periodically arranged co-adsorbates (In atoms, surfactants) leading to new diffusion properties (e.g. sub-surface or assisted diffusion).[87]

The observed growth mode in (binary) compound semiconductor MOVPE is layer-by-layer growth (Frank-van der Merwe mode). Typically, the flow-rate of III and V sources is modulated separating the precursors' gas phase decompositions and monolayer nucleations on the surface. However, two- and three-dimensional growth modes (e.g. Stranski-Krastanov or Vollmer-Weber) compete and are sensitive towards thermodynamic conditions and (desired) material composition. On a mesoscopic scale, mechanisms like step- or island formations and phase transitions occur while elementary chemical processes (adsorption, desorption, diffusion and surface transport, agglomeration) dominate the nano-scale.[40,88]

The microscopic processes determining the growth modes are not yet identified and can be subject to investigations from first principles. During modulated epitaxy growth of GaP-Si, atomic layers of Ga and P are subsequently deposited. It is yet unclear whether they are stabilized as plain, individual atomic layers on the surface or whether the characteristic layer-by-layer structure is the result of any subsequent thermal annihilation. Furthermore, under Ga-rich growth conditions, the formation of three-dimensional metal islands (droplets) is critical during nucleation.[89] As metallic Ga etches the Si substrate, the islands should be avoided as they might lead to a faceted instead of an abrupt GaP-Si interface morphology.[29]

5. **Interface and Material Properties**

   Finally, given completed films of the desired semiconductor compound materials, electronic and structural properties have to be investigated. As introduced in the above section, the atomic interface structure and film composition (strain) contribute to the electronic properties and are largely determined by the growth. Furthermore, those structural properties are critical for optoelectronic device performance. Experimentally, bulk-like structures can be analysed by transmission electron microscopy (TEM) and energy-dispersive X-ray spectroscopy (EDX), however, *ab initio* calculations are feasible for these periodic systems. Current computing capacities allow an accurate description even for large model systems. Leading research questions comprise the bulk material's electronic structure (band structure), electrostatic effects at film interfaces and local charges and dipoles in microscopic regions at the interfaces or surfaces during growth.[27,90]

   In contrast to the commonly assumed flat GaP-Si interface morphology, high-resolution STEM imaging displayed an intermixed region of eight atomic layers where facets form leaving the (001) growth orientation. The origin of this micro-structure was investigated by DFT calculations and bonding concepts were discussed in the context of the computed quantities.

The description of the various processes discussed above by *ab initio* methods is a valuable source of insight complementing experimental analytics.[58,91] Gas phase, surface and bulk properties next to chemical reactivity can be studied with sufficient accuracy.[57]

However, several intrinsic challenges remain that often require approximations to the system's complexity or limit the accuracy of calculated properties.

As becomes clear, a multitude of individual processes occurs during epitaxy growth. Often it is subject to the scientist's intuition whether the dominant processes were considered in a simulation. As MOVPE is a non-equlibrium procedure, elementary kinetics determine the material's quality which are tedious to compute.[38,48,91,92] In the presented screening of TEGa and TBP gas phase decompositions an extensive list of 70 elementary processes was addressed, however, another decomposition class relevant for lighter homologues of TEGa was discovered later.[93] The calculated catalogue provides a reliable synopsis on potential adsorbate species, unfortunately, there cannot be certainty whether pathways exist that have not been accounted for. Another fundamental challenge is the configurational diversity of structures and processes. Realistic surface and bulk material systems have large configurational spaces. Furthermore, the systems are often affected by vibrations, magnetic properties, external fields or other macroscopic effects. It is computationally impossible to explicitly incorporate all those variables in order to achieve a correction for entropic contributions.[94] It is thus necessary to find approximations that describe essential properties with sufficient accuracy.[91,95] For gas phase reactions, free energies and barriers were calculated including the vibrational partition sums into molecular entropic contributions.[64] For periodic systems, on the other hand, this was usually neglected due to high computational effort. Configurational entropy was estimated for GaP-Si interface structures in[96] concluding a minor contribution to the absolute formation energies calculated.

Finally, as the computations presented in this work are performed applying density functional theory (DFT), some intrinsic as well as technical shortcomings have to be mentioned. Most of the growth phenomena introduced above occur on longer time and length scales as accessible by the methods applied. One approach to include results from elementary processes in models covering larger scales is kinetic Monte Carlo. It was applied in the course of the projects presented. Transport characteristics of mass or heat on a macroscopic scale can be simulated by computational fluid dynamics, however, this is beyond the scope of this project.

Concerning the energy determined from electronic structure calculations, electron-electron correlation effects are only approximated in DFT as will be described in the following chapter. In principle, the complexity of the exchange-correlation functional can be raised systematically (LDA, GGA, meta-GGA, hybrid functionals), however, computational effort limits the applicability of high-rank methods to small systems often not sufficient to study diluted material compositions or microscopic structure. As was shown for the decomposition characteristics of TEGa and TBP, energies obtained on the generalized-gradient level of approximation (GGA) are sufficient to evaluate reaction thermodynamics and kinetics. This was evaluated against correlated wave function-based methods (MP2, CCSD(T)).[64]

# Chapter 2

# Theoretical Background & Methods Applied

## 2.1 *Ab initio* methods and Schrödinger equation

*Ab initio* methods describe physical properties without fitting parameters to experimental measurements. In practice, physical theories are applied if possible and approximations are introduced where necessary. Methods from *first principles*, in general, rely on theories, natural constants, postulates and approximations valid within the framework of quantum mechanics. In *quantum chemistry*, this means solving the time-independent Schrödinger equation within the Born-Oppenheimer approximation (BOA) neglecting the movement of the nuclei.

The Schrödinger equation characterizes any system represented by a wave function $\Psi$ that has the energy $E$.[97]

$$\hat{\mathrm{H}}\Psi = \mathrm{E}\Psi \tag{2.1}$$

$E$ is determined by the Hamilton operator $\hat{H}$ acting on $\Psi$, that takes into account the kinetic energy of the electrons $\hat{T}$ as well as Coulomb-like interactions of electrons with the nuclei $\hat{V}_{ne}$ and in between electrons $\hat{V}_{ee}$. The electrostatic repulsion between nuclei $V_{nn}$ is added as a constant within the BOA (atomic units apply).

$$\hat{H} = \hat{T} + \hat{V}_{ne} + \hat{V}_{ee} \tag{2.2}$$

$$= -\sum_i \frac{1}{2}\nabla_i^2 - \left(\sum_i \sum_A \frac{Z_A}{r_{iA}} - \sum_i \sum_{j>i} \frac{1}{r_{ij}}\right). \tag{2.3}$$

The lowest energy $E_0$ of a system can be solved as an eigenvalue problem by the Ritz-Rayleigh variational principle.[98]

The **Hartree-Fock method** (HF) uses a Slater determinant $\Psi_{SD}$ to represent $\Psi$ which is comprised of $N$ one-electron spinorbitals $\psi_i = \psi_i(r_i, \omega_i) = \psi_i(\tau_i)$ where $r_i$ and $\omega_i$ represent spatial and spin coordinates, respectively.

$$\Psi_{SD} = \frac{1}{\sqrt{N!}} \begin{vmatrix} \psi_1(\tau_1) & \psi_2(\tau_1) & \dots & \psi_N(\tau_1) \\ \vdots & \ddots & & \vdots \\ \vdots & & \ddots & \vdots \\ \psi_1(\tau_N) & \dots & \dots & \psi_N(\tau_N) \end{vmatrix} \tag{2.4}$$

The Slater determinant is normalized by $\frac{1}{\sqrt{N!}}$ and fulfills the antisymmetry principle (Pauli).[99]

The HF energy is evaluated by the one-electron operator

$$\hat{h}_i = -\frac{1}{2}\nabla_i^2 + \sum_A -\frac{Z_A}{r_{iA}} \tag{2.5}$$

and the two-electron operator

$$\hat{g}_{ij} = +\frac{1}{r_{ij}} \tag{2.6}$$

which result in the term

$$t_i = \langle \Psi_{SD} | \hat{h}_i | \Psi_{SD} \rangle , \tag{2.7}$$

and the two-electron Coulomb

$$J_{ij} = \langle \Psi_{SD} | \hat{g}_{ij} | \Psi_{SD} \rangle = \langle \psi_i(i)\psi_j(j) | \hat{g}_{ij} | \psi_i(i)\psi_j(j) \rangle \tag{2.8}$$

and exchange integrals

$$K_{ij} = \langle \Psi_{SD} | \hat{g}_{ij} | \hat{p}_{ij}\Psi_{SD} \rangle = \langle \psi_i(i)\psi_j(j) | \hat{g}_{ij} | \psi_j(i)\psi_i(j) \rangle \tag{2.9}$$

where $\hat{p}_{ij}$ is a permutation operator for electrons $i$ and $j$.

$\Psi_{SD}$ is to be optimized with respect to the energy $E$

$$E = \sum_i t_i + \sum_i \sum_{j>i} (J_{ij} - K_{ij}) + V_{nn} \tag{2.10}$$

by varying the spinorbitals $\psi_i$ under the orthonormality condition (Lagrangian multiplication).

This is performed by solving the one-electron HF equations

$$\hat{f}_i\psi_i = \sum_j \lambda_{ij}\psi_j \tag{2.11}$$

where $\hat{f}_i$ is an *effective* one-electron operator as the operators $\hat{J}_j$ and $\hat{K}_j$ are defined as acting on all other electrons implicitly (*mean-field approximation*, single determinant).

$$\hat{f}_i = \hat{h}_i + \sum_j (\hat{J}_j - \hat{K}_j) \tag{2.12}$$

After unitary transformation, the HF equations are represented as pseudo-eigenvalue problems

$$\hat{f}_i\psi'_i = \epsilon_i\psi'_i \tag{2.13}$$

that can be solved only iteratively. The canonical orbital energies $\epsilon_i$ are obtained.

### 2.1.1 Basis functions

In quantum chemistry, the one-electron molecular orbitals (MO) are represented as linear combinations of atomic orbitals (LCAO),

$$\psi_i = \sum_A \sum_{\mu\in A} c_{\mu i}\phi_\mu(r). \tag{2.14}$$

The functions $\phi_\mu(r)$ are usually provided by a pre-optimized basis set reasonably well describing the shape of one-electron atomic orbitals (AOs) according to the physical nature of a free hydrogen atom. Different classes of mathematical functions are used for this task.

For finite-sized systems, atom-centered basis functions are applied that resemble the shapes of hydrogen-like atomic orbitals according to the quantum numbers $n$, $m$, $l$. Generally, the functions are composed of a radial part $R_{n,l}$ and an angular part $Y_{l,m}$ (spherical harmonics) in polar coordinates ($r$,$\theta$,$\nu$).

$$\phi_\mu(r) = R_{n,l}(r)Y_{l,m}(\theta,\nu). \tag{2.15}$$

Gaussian-type orbitals are typically constructed from several contracted primitive *Gaussians* approximating a *cusp* at $r = 0$ (discontinuous first derivative) with the radial part

$$R_{n,l}(r) = r^{2n-2-l}\sum_c N(l,\alpha_c)c_c e^{-\alpha_c r^2}. \tag{2.16}$$

The coefficients $c_c$ and $\alpha_c$ are to be optimized. The more basis functions are included, the better is the resolution of the molecular wave function.
For periodic systems, in contrast, the basis sets typically chosen do not describe atomic orbitals but rather fill the system's volume with plane-wave functions. Those advantageously describe free electrons in delocalized (valence) states, however, the description of oscillating functions close to nuclei requires additional plane-waves of high energy and is therefore usually not well represented.

$$\psi_i(r,k) = e^{ikr} \sum_K c_i(k,K) e^{iKr} \tag{2.17}$$

The coefficients $c_i$ are to be optimized. The number of individual plane-waves $e^{iKr}$ to be included into this sum can be truncated by an energy cut-off as

$$\frac{1}{2}|K|^2 < E_{\text{cut}} \tag{2.18}$$

where $K$ is the system's periodicity vector (see section 2.3).

### 2.1.2 Correlated Methods

Hartree-Fock theory includes a description of exchange correlation as electrons with equal spins avoid the same space (antisymmetry principle fulfilled in Slater determinant, Fermi correlation). A correction must be found for the energy contribution of the Coulomb correlation not represented in HF:[100]

$$E_{\text{exact}} - E_{\text{HF}} = E_{\text{correlation}} \tag{2.19}$$

One approach to include this interaction is to construct $n$-fold excited electron configurations from the HF single-determinant $\Psi_{SD}$ and consider the following sum as the system's correlated wave function.

$$\Psi = \Psi_{SD} + \sum_n c_n \Psi_n \tag{2.20}$$

In **coupled cluster theory**, those excited determinants are generated by an excitation operator

$$\hat{T} = \sum_n \hat{T}_n \tag{2.21}$$

that is expanded as exponential function in a Taylor series. The correlated wave function is described as

$$\Psi = e^{\hat{T}}\Psi_{SD} = \sum_{m} \frac{1}{m!}\hat{T}^{m}\Psi_{SD} \tag{2.22}$$

whereas the individual components are

$$\hat{T}_0 = 1, \tag{2.23}$$

$$\hat{T}_1 = \sum_{a,r} t_a^r \hat{a}_a^{\dagger}\hat{a}_r \tag{2.24}$$

and

$$\hat{T}_2 = \frac{1}{4}\sum_{ab,rs} t_{ab}^{rs}\hat{a}_a^{\dagger}\hat{a}_b^{\dagger}\hat{a}_r\hat{a}_s. \tag{2.25}$$

The operators $\hat{a}_a^{\dagger}$ (creation) and $\hat{a}_r$ (annihilation) populate individual electrons from/to occupied ($a$, $b$, ...) and virtual ($r$, $s$, ...) orbitals in order to generate the new (singly, doubly, ... excited) determinants from a single reference. The coefficients $t_a^r$, $t_{ab}^{rs}$,... are to be solved.

If the expansion goes to $n$=$\infty$, the resulting energy is exact (within BOA and neglecting relativistic effects at full basis set). However, even for finite $n$ the iterative solution of this huge number of determinants is difficult to compute so a gold standard of quantum chemistry is expanding to $n = 2$ and including the triple excitations perturbatively (CCSD(T)).[101]

A different approach is **Møller-Plesset perturbation theory**,[102] where excited configurations (determinants) are not explicitly generated. The correlation contribution is treated as perturbation $\lambda\hat{H}_1$ to the electronic Hamiltonian $\hat{H}_0$.

$$\hat{H}_1 = \sum_{i<j}\frac{1}{r_{ij}} - \sum_{i} v_{\mathrm{HF}}(i) \tag{2.26}$$

Again, a Taylor series expansion around $\lambda = 1$ is performed and the correlated wave function is

$$\Psi_n = \Psi_0^{(0)} + \lambda\Psi_0^{(1)} + \lambda^2\Psi_0^{(2)} + ... \tag{2.27}$$

and has the energy

$$E_n = E_0^{(0)} + \lambda E_0^{(1)} + \lambda^2 E_0^{(2)} + ... \tag{2.28}$$

A truncation of this expansion at first order results in the HF energy and wave function (double-counting of Coulomb correlation in 0th corrected by 1st order). Truncation at second order provides the energy correction

$$E_0^{(2)} = \frac{1}{4} \sum_{ab,rs} \frac{| \langle ab| |rs\rangle |^2}{\epsilon_a + \epsilon_b - \epsilon_r - \epsilon_s} \tag{2.29}$$

where all possible double excitations from occupied ($a$,$b$) to virtual ($r$,$s$) states are taken into account. The orbital energies $\epsilon$ are taken as references. In combination with HF (shifted Fock operator as $\hat{H}_0$), Equation 2.29 refers to the MP2 energy correction frequently applied in quantum-chemical applications.

## 2.2 Density Functional Theory

In density functional theory (DFT), the wave function is represented as a unique functional of the electron density

$$\Psi \overset{!}{=} \Psi[\rho(r)] \tag{2.30}$$

which has the ground-state energy

$$E_0 = E[\rho_o(r)]. \tag{2.31}$$

$E_0$ itself is a functional of the ground-state electron density (Hohenberg-Kohn theorem).[103] Thus, there is a one-to-one correspondence between $\Psi_0$ and $\rho_0$.
As for obtaining the energy, Kohn and Sham introduced a reference system of non-interacting electrons with the same density so that the energy is defined as[104]

$$E[\rho(r)] = T_0[\rho(r)] + \frac{1}{2} \int \int \frac{\rho(r)\rho(r')}{|r - r'|} \mathrm{d}r\mathrm{d}r' + \int \rho(r) V(r) \mathrm{d}r + E_{\mathrm{XC}}[\rho(r)] \tag{2.32}$$

where

$$T_0[\rho(r)] = \sum_i f_i \, \langle \psi_i| - \frac{1}{2} \nabla^2 |\psi_i\rangle \tag{2.33}$$

is the kinetic energy of the non-interacting electrons,[105,106] formally represented by the one-electron orbitals $\psi_i$ (Kohn-Sham orbitals, KS).[107,108]
The second term represents the Coulomb interaction between electron densities at two locations $r, r'$ (similar to the Hartree product) and V(r) is the Coulomb potential of $\rho$ with all nuclei.
$E_{\mathrm{XC}}[\rho(r)]$ is the exchange-correlation energy functional, which is not known exactly but can be approximated e.g. with reference to a uniform electron gas ($X\alpha$ local potential by Slater).[109] Similar to the kinetic energy $T_0$, $\rho$ can be represented by the

KS orbitals with occupation numbers $f_i$ as

$$\rho(r) = \sum_i f_i |\psi_i(r)|^2 \tag{2.34}$$

leading to one KS equation for each electron in the system:

$$\left(-\frac{1}{2}\nabla^2 + v(r) + \int \frac{\rho(r')}{|r-r'|}dr' + v_{XC}(r)\right)\psi_i(r) = \epsilon_i \psi_i(r). \tag{2.35}$$

The KS equations can be solved in an iterative, self-consistent way (as in the Hartree-Fock method).

KS-DFT suffers from the self-interaction error (one electron in the potential of the *full* density) and a lack of a description of long-range interactions. Together with the unknown exchange-correlation contribution this is the reason why DFT is reliable only for a description of ground-state properties. For instance, it fails for band gaps of materials and other properties involving excited states.

For practical use of DFT, good approximations for $E_{\mathrm{XC}}[\rho(r)]$ need to be found. One of them is the generalized-gradient approximation (GGA), where the energy contributions of electron exchange and electron correlation are represented as

$$E_{\mathrm{XC}}^{\mathrm{GGA}}[\rho(r)] = \int \rho(r) F[\rho(r), \nabla\rho(r)] dr \tag{2.36}$$

where F is a functional of a local electron density and its gradient. Perdew separated the energy contributions for correlation and exchange (as in $X\alpha$) so that[110]

$$F[\rho(r)] = \epsilon_{\mathrm{X}}[\rho(r), \nabla\rho(r)] + \epsilon_{\mathrm{C}}^{\mathrm{homogeneous}}[\rho(r), \nabla\rho(r)] \tag{2.37}$$

and fitted the energy $\epsilon_{\mathrm{C}}$ (later also $\epsilon_{\mathrm{X}}$) of this local density to numerical solutions (e.g. Monte Carlo methods) of the homogeneous electron gas. Becke later improved the description of exchange and fitted $\epsilon_{\mathrm{X}}$ to *exact* results from Hartree-Fock theory on noble gas atoms.[111] Perdew, Burke and Ernzerhof proposed a unified functional for $E_{\mathrm{XC}}^{\mathrm{GGA}}$ (PBE),[112,113] which is frequently applied in this work. Note that direct (vertical) transitions in electronic band structures of semiconductors are overestimated and fundamental gaps are underestimanted (overbinding) by the PBE functional.[114] In general KS-DFT, the $E_{\mathrm{XC}}$ suffers from the electronic self-interaction error which typically leads to an overestimation of molecular bonding energies and bond lengths.

Spin-resolved calculations are possible by extending the density coordinates to $(r, \alpha)$ and $(r, \beta)$.

Although there are (many more) approximations to the correlation interaction at short ranges, the description of long-range electronic correlation effects is often not included. An efficient way to correct for van-der-Waals type interactions is given by a pairwise atomic correction added to the total DFT energy. The general form of this has been known since 1924 with the formulation of the empirical Lennard-Jones interatomic potential[115] and Fritz London's definition of *dispersion* in 1930.[116] The attractive dispersion energy after Grimme et al. is given by

$$E_{\mathrm{DFT-D3}} = -\sum_{AB} \sum_{n=6,8,10} s_n f_n(R_{AB}) \frac{C_n}{R_{AB}^n} \tag{2.38}$$

as an implementation with specific parameters ($C_n$: dispersion coefficients, $f_n$: damping function, $s_n$: scaling) for common DFT XC-functionals.[117] In conjunction with the PBE functional this delivers reliable structures and energies for both molecular and extended systems.[118,119]

## 2.3 Extended Systems

In a periodic crystal the (static) nuclei create a potential that follows the translational symmetry of the structure (Born-von Karman, periodic boundary conditions, PBC).[120]

$$V_{\mathrm{nuclei}}(r) = V_{\mathrm{nuclei}}(r + R) \tag{2.39}$$

where $R$ is the translational periodicity vector in real space. The electrons affected by $V_{\mathrm{nuclei}}$ are well represented by a wave function adapted to the crystal's symmetry in reciprocal space. Each point in reciprocal space accords to a set of planes in real space (reflection in a scattering experiment). The lattice vectors in real space $a_v$ and reciprocal space $b_w$ can be transformed into one another by a Fourier transformation and follow the condition

$$a_v b_w = 2\pi\ \delta_{vw} \tag{2.40}$$

where $\delta_{vw}$ is the Kronecker delta.

Compared to finite size systems the electronic wave function has two new quantum numbers $n$ (band index) and $k$ (phase vector) representing different energetic states.

$$\Psi_n(k, r + R) = e^{(ikR)} \Psi_n(k, r) \tag{2.41}$$

This function fulfills Blochs theorem,[121] after that the product of a plane-wave $e^{ikr}$ with another translationally symmetric function $u_n(k,r) = u_n(k, r+R)$ yields, again,

a periodic function in the same lattice/potential.
$k$-points within $0 \leq k \leq \frac{\pi}{a_v}$ lie within the primitive cell in reciprocal space, the first Brillouin zone.
The total wave function $\Psi_n(k, r+R)$ is now constructed from one-electron plane-waves $\psi_i(r, k)$ according to Equation 2.17.
The energy of the electronic states $E_n(k)$ is then determined by solving one-electron Schrödinger equations as a sum (rather than an integral) over a dense mesh of $k$-points generated by e.g. the Monkhorst-Pack method.[122]

## 2.4 Approximations applied in periodic DFT

The VASP (version 5.3.5) software[123,124] was applied to calculate the electronic wave function and various properties of periodic systems in a plane-wave basis.
As systems with many electrons are treated, the introduction of pseudopotentials (effective core potentials) avoiding explicit calculation of low-lying electronic (core) states is an efficient approach to reduce computational effort. The core electrons are represented as pseudopotentials that account for core-valence Pauli repulsion and valence-nuclei Coulomb attraction and are hence small in amplitude.[125–128] Henceforth, any information on the core functions' nodal structure (orthonormality) is lost.
Alternatively, non-local pseudopotentials resolving angular momentum quantum numbers $l$ (s,p,d,f) of core functions can be used approximating a realistic description of the core region. However, the somewhat arbitrary separation of an atom's electrons into core and valence groups is critical for some systems.
In periodic systems the use of local pseudopotentials is inappropriate as (i) the periodic potential acting on the core electrons is not represented (pseudopotentials too "hard") and (ii) the core states are not properly resolved.
When using a plane-wave basis, the augmented-plane wave (APW) method[129,130] offers an improvement for this. The core region (atomic spheres) is represented by a physical, local potential acting on local basis functions (e.g. spherical harmonics) resulting in discrete core levels. The regions in between the core regions are correctly represented as an augmented plane-wave function (envelope) that connects inner and outer wave functions and the corresponding interactions ("muffin-tin" model).
In VASP, the projector-augmented wave (PAW) method[131] is applied which improves the deficiencies of APW and (older) pseudopotential approaches. The full (all electron, AE) wave function $|\Psi\rangle$ is mapped onto an auxiliary pseudo-wave function $|\tilde{\Psi}\rangle$ inside an augmentation region. $|\tilde{\Psi}\rangle$ is composed of an expansion of smooth

atomic orbitals ("partial waves") $|\tilde{\phi}_i\rangle$ representing pseudo-core states:

$$|\tilde{\Psi}\rangle = \sum_i c_i \, |\tilde{\phi}_i\rangle \tag{2.42}$$

The pseudo-functions $|\tilde{\phi}_i\rangle$ are obtained from a local potential (self-consistent with the pseudo-density) which coincides with the outside AE potential on the augmentation region boundary. The boundary radius is determined by the overlap with localized projector functions $\tilde{p}_i$.

Outside this region (atomic sphere, core region) the two wave functions $|\Psi\rangle$ and $|\tilde{\Psi}\rangle$ coincide. The AE wave function is composed of atomic orbitals $|\phi_i\rangle$, which correctly described the core states as they are imported from Schrödinger solutions of the isolated atom. $|\tilde{\Psi}\rangle$ and $|\Psi\rangle$ are connected by a linear transformation $T$ which reflects the local contributions of each atom, quantum numbers $l$,$m$ and the number of partial waves selected.

$$|\Psi\rangle = \sum_i c_i \, |\phi_i\rangle = T \, |\tilde{\Psi}\rangle \tag{2.43}$$

The coefficients $c_i$ can efficiently be determined and they remain identical in the AE and pseudo representations, respectively. The AE wave function is then obtained from $|\tilde{\Psi}\rangle$ as

$$|\Psi\rangle = |\tilde{\Psi}\rangle + \sum_i (|\phi_i\rangle - |\tilde{\phi}_i\rangle) \, \langle \tilde{p}_i | \tilde{\Psi}\rangle \, . \tag{2.44}$$

The linear transformations are performed with the projector functions $\tilde{p}_i$ for each inner partial wave $|\tilde{\phi}_i\rangle$.

## 2.5 Multi-scale Methods

*Ab initio* methods are limited in time and lengths scales being valid only within the quantum-mechanical regime but also due to limited computer capacities.

Even though it is desirable to follow the dynamics of elementary processes, e.g. in an *ab initio* molecular dynamics simulation, from first principles, large systems can only be addressed by introducing approximate methods.

Multi-scale methods like Monte Carlo (MC) simulations use information gained from the quantum level to describe the dynamics - the evolution of a mesoscopic system.[132,133]

Furthermore, MC models are advantageous for the simulation of growth as many processes involved exhibit a stochastic nature.[88]

A lattice-independent *kinetic MC* (KMC) program was developed as to deal with a variety of elementary gas phase (and many other types of) processes. The implemented algorithm together with some preliminary results is presented in the appendix.

In a lattice-dependent KMC simulation, the system is restricted to a finite number of configurations, often realized in a box with periodic boundary conditions (PBC). For the study of crystal growth the system is often represented by a surface lattice where species can adsorb, desorb and diffuse to and from specific lattice sites. The complexity of a simulation - i.e. the configurational space accessible - is then determined by the number of distinguishable lattice sites and the availability of specific processes in conjunction to the sites. The process energies and barriers are determined within one simulation step representing a snapshot configuration. Either, the activation energies can efficiently be approximated on-the-fly or a catalogue of pre-determined configuration-dependent activation energies is provided. These are typically accurate results e.g. from *ab initio* calculations of elementary processes occuring in the system modeled.

In lattice-independent KMC, the system is represented only by the population of individual species. Relative populations can serve as a measure for partial pressures of the species present. All possible processes are catalogued with pre-calculated reaction energies and barriers (activation energies $\Delta E^{\ddagger}$) which may use populated species as reactants and generate new product species. In the course of the KMC simulation the total population may change.

For both types, the rate of a process $i$ at a given simulation temperature $T$ and the activation energy $\Delta E^{\ddagger}$ is determined after Arrhenius as

$$k_i = A_{\text{preexp}}\ exp\frac{-\Delta E^{\ddagger}}{k_B T} \tag{2.45}$$

with the Boltzmann constant $k_B$ and a pre-exponential factor $A_{\text{preexp}}$. The attempt frequency is often set constant ($A_{\text{preexp}} = \frac{k_B T}{h}$, $h$ is Planck constant) for all processes, however, as it scales the process time step

$$\Delta t_i \propto \frac{1}{k_i} \tag{2.46}$$

more specific pre-factors are desired. If vibrational analyses are accessible for the processes studied, the sum of partition functions $Z_{\text{vib}}$ at reactant (*ed*) and transition states ($TS$) at simulation temperature $T$ should be applied:

$$A_{\text{preexp}}(T) = \frac{Z_{\text{vib}}^{TS}}{Z_{\text{vib}}^{ed}}. \tag{2.47}$$

The total rate constant of all possible events at one configuration (state) is then the sum

$$k_{\text{total}} = \sum_i k_i. \tag{2.48}$$

The probability $p_i$ of a process $i$ to occur at a given state can be defined as

$$p_i = \frac{k_i}{k_{\text{total}}} \tag{2.49}$$

which leads to the acceptance of $i$ in case

$$p_i > R \tag{2.50}$$

where $R \in [0, 1]$ is a random number. If process $i$ is successful, the system will be updated according to the consequences (e.g. chemical reaction) defined for $i$ and the simulation time evolves from $t_{\text{sys}}$ to $t_{\text{sys}-\text{new}}$ as

$$t_{\text{sys}-\text{new}} = t_{\text{sys}} + \Delta t. \tag{2.51}$$

Thus, the system evolves step-wise while, in most algorithms, one step per iteration is performed. The time step is determined as

$$\Delta t = -\frac{ln(R')}{k} \tag{2.52}$$

where $k$ is either $k_i$ (of the successful process $i$) or $k_{\text{total}}$ (after BKL[134,135]) depending on the algorithm. $R' \in ]0, 1]$ is another random number.

Different variants of KMC suitable to specific requirements were summarized in the literature.[136,137]

# Chapter 3

# Scope of Investigations Conducted

Elementary processes involved in the epitaxial growth of gallium phosphide (GaP) on silicon (Si) were investigated by quantum-chemical calculations. The studies were categorized according to the five phases of metal-organic vapour phase epitaxy (MOVPE) introduced in Figure 1.8. Different computational methodology was applied in order to accurately determine the kinetics of different chemical processes occuring in the gas phase, at the surface or at a film interface.

Besides, quantum-chemical analyses on reaction mechanisms and decomposition pathways were performed based on electronic structure calculations. The results provide an understanding of chemical processes not described before. Due to the sensitive reactor conditions in MOVPE (high purity, oxygen sensitivity, low pressure, inert gas environment) experimental analysis of elementary processes is limited. Thus, computational studies help to identify the bottleneck properties of specific III/V growth procedures relevant to optimize the materials quality and device performance. Indeed, new chemical pathways were explored and one fundamental elimination mechanism has been characterized for the first time. The knowledge gained was subsequently utilized to propose improved molecular properties specific for group 15 precursors applied in MOVPE.

Several studies on the gas phase reactivity according to phase 1 in Figure 1.8 were conducted. The focus was laid on the decomposition chemistry of triethylgallane (TEGa, $Ga(C_2H_5)_3$), *tert*-butylphosphine (TBP, $P(C_4H_9)H_2$) and related precursors and precursor fragments. Since experimental evidence is scarce, it was the aim of these studies to comprehend the decomposition networks to full extent so that reliable predictions on thermal decomposition products can be provided.

In the first study (3.1),[64] Gibbs free reaction energies were calculated for a large catalogue of decomposition pathways including 70 uni- and bimolecular reactions from seven mechanism classes. Wave function-based methods of advanced quality were applied in order to gain high-accuracy data on reaction energies and structures. The data was further used as benchmark for the accuracy reached by DFT with the GGA which was used as standard for the computations following. The main results of 3.1[64] suggest that the $\beta$-hydride elimination is the most likely pathway for TEGa as it is thermodynamically favourable and exhibits the lowest activation energies (thermal barriers). From the intermediates $GaH_3$ or $Ga(C_2H_5)H_2$ the elimination of $H_2$ is also possible, however, due to large barriers this was considered less likely. Alkane eliminations exhibit even larger barriers and homolytical cleavages are thermodynamically unfavourable in the gas phase. For TBP, on the other hand, the only accessible decomposition pathway with favourable thermodynamic properties is $\beta$-hydrogen elimination which exhibits large thermal barriers as computed by DFT. As this mechanism was not described in detail before, it was important to prove the mechanism proposed and fully understand the decomposition pathway that determines the candidates for adsorption.

For the characterization of the $\beta$-hydrogen elimination mechanism, a plethora of quantum-chemical analysis methods were applied. The results are presented in 3.2,[138] reporting three different mechanisms for amines, phosphines (and higher homologues) and metal *tert*-butyl compounds exhibiting either protic, neutral or hydridic hydrogen atoms transferred during the elimination, respectively. An analysis of the energy paths along an intrinsic reaction coordinate revealed also electron reorganization in reverse direction comparing hydridic and protic H transfer. The different nature of the elimination mechanisms explains the much larger energy barriers of group 15 in comparison to metal compounds. Partial charges, canonical molecular orbitals, EDA-NOCV and AIM were analyzed at the elimination transition states.

In 3.3[139] the insight gained from describing the $\beta$-hydrogen mechanism of group 15 CVD precursors was utilized in order to computationally design alternative compounds. Systematic precursor design is important as new precursor molecules are subject to chemical research aiming at higher elimination rates and complete decompositions. As was reported in 3.2,[138] the reaction transition state of TBP, *tert*-butylarsine (TBAs) and higher homologues is dominated by the heterolytical cleavage of the C-E bond (E = P, As, Sb, Bi) leaving a positive charge at the central carbon atom. By stabilizing this charge, precursors with elimination rates superior to TBP and TBAs were predicted exploiting the $\beta$-silyl effect. The results gained from the computational studies presented are useful to target precursor properties improving decomposition rates and yields.

By extensive studies on gas phase decomposition, the essential precursor fragments for adsorption were identified. The interaction of precursor fragments with the surface, adsorption processes and surface diffusion as illustrated in Figure 1.8, phase 2, were adressed in two independent research projects. Firstly, a MOVPE growth study of GaP on Si(001) is presented which was collaboratively conducted within the research training group GRK 1782 ($3.5^{96}$). Results from experimental growth and crystal structure analysis (TEM), kinetic modeling of the growth (KMC) as well as intrinsic stabilities of GaP-Si interfaces from perioidic density functional theory calculations were combined in order to explain the interface morphology observed. As growth is dominated by kinetically controlled surface transport, adatom diffusion barriers on different (001) surfaces present during growth were determined. The structural models applied resembled closely the settings for the KMC simulation assuming complete precursor decomposition to atomic species. The results gained lead to the conclusion that an intermixing of Si, Ga and P atoms occurs caused by a low mobility of P atoms during growth. As a consequence, the atomic structure rearranges during growth which leads to a nanoscopic faceting. The explicit calculation of interface formations in various crystal planes provided a rationale for GaP-Si to leave the [001] growth direction towards [111] and [112] where more stable interface configurations can be formed.

Secondly, the adsorption behaviour of TBP fragments on passivated Si(001)-H was studied focusing on multi-adsorption and surface activation effects (3.4). The stabilization of hydrogen vacancies by adsorbate interactions is introduced as a concept for the enhancement of adsorption. It was found that $P(C_4H_9)H$'s butyl group as well as the P atoms' lonepair coordinate towards a vacancy site in close surrounding which leads to stabilization in some structural configurations. This offers a kinetic argument for the agglomeration of multiple adsorbates at sub-monolayer coverage as vacancies are preferred adsorption sites. Furthermore, decomposition mechanisms of $P(C_4H_9)H$ as well as $Ga(C_2H_5)H$ adsorbed on Si(001)-H were investigated and compared to the mechanisms of the gas phase. The dominant channel is $\beta$-hydrogen elimination which was also found to occur at the surface from the above precursor fragments. In the environment of the Si(001)-H surface the reaction products (isobutene and ethylene) are slightly stabilized. While the $\beta$-hydride elimination barrier of adsorbed $Ga(C_2H_5)H$ is increased with respect to the gas phase equivalent, the barrier of $P(C_4H_9)H$'s $\beta$-hydrogen elimination was found to decrease. This is important as the gas phase decomposition of TBP is limited to this pathway which exhibits large barriers. The surface reactivity of CVD precursors needs to be studied in more detail in the future.

Study 3.5[96] investigated kinetic and thermodynamic properties of GaP epitaxy growth in order to understand the formation of the observed faceted GaP-Si interface morphology. Aspects of growth are represented in phase 4 in Figure 1.8. It was found that different thermal mobilites of adatoms on the surfaces present during growth lead to an intermixing of atoms in an interface region of eight atomic layers. In the same study, a formalism to determine absolute interface formation energies for different configurations was established. By combining two approaches of modeling periodic structure cells, the discrimination of Ga- and P-specific interfaces at multiple lattice planes was possible for the first time. Diverging stabilizations for interfaces with different atomic structure were found. The origin of this finding was investigated in detail in 3.6[140] applying further periodic DFT calculations and charge density analysis.

Various properties of GaP-Si interfaces were determined representing phase 5 in Figure 1.8. These included atomic partial charges, structural and energetic response to relaxation and electrostatic potentials. Based on those chemical properties, the observed stabilities of abrupt and atomically intermixed interfaces at (001), (111), (112) and (113) were discussed. The correlations found were also compared to established models on III/V-IV interface stabilities like the Electron Counting Model. Moreover, charges, electrostatic potential and strain-related forces were analyzed within the perspective of larger dimensions (sizes of the supercells) as those properties not only determine the local bonding situation at the interface but also indicate non-local behaviour of films in contact. Especially for thin film heterostructures, knowledge on those properties is essential for material integration and device performance. Specific questions addressed in 3.6[140] comprised (i) the potential offsets between the Si and GaP films, respectively, representing the electronic barrier for a conducting device, (ii) electrostatic polarization within the films and at the interface, resolving e.g. Ga- and P-polarized films and interfaces, and (iii) in how far local disturbances of partial charges, mechanical forces and local dipoles found at the interfaces extend over the material films. All calculations were performed on the GGA level of DFT with the D3 correction for dispersion forces applying large supercell models.

The final manuscript not only provides extensive insight into local and film-wide characteristics of the GaP-Si interface, it can also serve as a methodological reference for the determination and explanation of further III/V(-IV) interface stabilities.

In the following, short descriptions of the individual studies are presented next to the author's contributions to the research conducted as well as the compilation of the manuscripts. The articles compiled are attached in the appendix.

## 3.1 A quantum-chemical study on gas phase decomposition pathways of triethylgallane (TEG, $Ga(C_2H_5)_3$) and tert-butylphosphine (TBP, $PH_2(t\text{-}C_4H_9)$) under MOVPE conditions

Andreas Stegmüller, Phil Rosenow and Ralf Tonner*
Phys.Chem.Chem.Phys., 2014, 16,17018

*The gas phase decomposition reactions of precursor molecules relevant for metal-organic vapour phase epitaxy (MOVPE) of semiconductor thin films are investigated by computational methods on the density-functional level as well as on the ab initio (MP2, CCSD(T)) level. A comprehensive reaction catalogue of uni- and bimolecular reactions is presented for triethylgallium (TEG) as well as for tert-butylphosphine (TBP) containing thermodynamic data together with transition state energies. From these energies it can be concluded that TEG is decomposed in the gas phase under MOVPE conditions ($T$ = 400-675° C, $p$ = 0.05 atm) to $GaH_3$ via a series of β-hydride elimination reactions. For elevated temperatures, further decomposition to GaH is thermodynamically accessible. In the case of TBP, the original precursor molecule will be most abundant since all reaction channels exhibit either large barriers or unfavorable thermodynamics. Dispersion-corrected density functional calculations (PBE-D3) provide an accurate description of the reactions investigated in comparison to high level CCSD(T) calculations serving as benchmark values.*[64]

The author conducted all calculations leading to the presented results. The choice of methods was taken in collaboration with the supervisor. The manuscript's second author has identified some of the reaction mechanisms before (Master thesis) and performed preliminary calculations on the reaction energies. The interpretation of results were initially done by the author. Subsequently, the author refined formulations and interpretations together with the supervisor in an iterative way (regular meetings). In the same procedure, the manuscript was compiled (text formulation, manuscript structure, figure and table generation) between the two authors.

## 3.2 The $\beta$-hydrogen elimination mechanism in the absence of low-lying acceptor orbitals in $EH_2(t\text{-}C_4H_9)$ ($E = N\text{-}Bi$)

Andreas Stegmuüller and Ralf Tonner*
Inorg.Chem., DOI: 10.1021/acs.inorgchem.5b00687, 2015

*The $\beta$-hydrogen elimination reactions of group 15 alkyl compounds at the example of $EH_2(t\text{-}C_4H_9)$ ($E = N\text{-}Bi$) were investigated and compared to the group 13 example of $GaH_2(t\text{-}C_4H_9)$. With the aid of density functional theory-based extensive analysis of atomic and electronic structure at the transition state, we can derive three distinct reaction classes. The gallium compound follows the well-known $\beta$-hydride route with participation of an empty p-orbital at the metal in a concerted, synchronous fashion exhibiting low barriers. For compounds with group 15 elements, we find highly non-synchronous reactions with high reaction barriers. In the case of nitrogen, a protic hydrogen is transferred via attack of the nitrogen lone pair while, for the heavier homologues (P-Bi), the $E\text{-}C_\alpha$ bond breaking occurs first and the hydrogen atom remains rather neutral. The reaction barrier in group 15 homologues is thus determined by the $E\text{-}C_\alpha$ bond strength down the group. The results enable a rationale for ligand design for precursors involved in chemical vapour phase deposition processes.*

The author conducted all calculations leading to the presented results. The choice of methods was taken in collaboration with the supervisor, however, some methods were initiated by the author. Part of the inital research question arose from a discussion with Prof. Jörg Sundermeyer as acknowledged in the manuscript. The interpretation of results were initially done by the author. Subsequently, the author refined formulations and interpretations together with the supervisor in an iterative way (regular meetings). In the same procedure, the manuscript was compiled (text formulation, manuscript structure, figure and table generation) between the two authors.

## 3.3 A quantum-chemical descriptor for CVD precursor design: predicting decomposition rates of TBP and TBAs isomers and derivatives

Andreas Stegmüller, Ralf Tonner*
submitted to Chem.Vap.Depos., 2015

*As explained by recent findings, the β-hydrogen elimination mechanism is the major gas phase decomposition pathway for TBP and related CVD precursors. A quantum-chemical analysis revealed that the elimination barrier is mainly determined by the polarization between of the* $C_\alpha$*-E bond (E = P, As, Sb, Bi). Applying this hypothesis, six isomeric butyl-ligands were introduced in TBP and TBAs as to determine the direct dependency of the barrier with partial charge at the* $C_\alpha$ *atom. The correlation supports the hypothesis: positive inductive effects on* $C_\alpha$ *decrease the barrier. By introducing silyl groups in β-position to E, a positive charge at the transition state can be further stabilized and the elimination rate is estimated to increase about four orders of magnitude with respect to TBP and TBAs.*

The author conducted all calculations leading to the presented results. The choice of methods was taken in collaboration with the supervisor. The initial research question arose as a direct follow-up from a previous project and was initiated by the author. The introduction of the β-silyl effect for elimination barrier reduction was the supervisor's initiative. The interpretation of results were initially done by the author. Subsequently, the author refined formulations and interpretations together with the supervisor in an iterative way (regular meetings). In the same procedure, the manuscript was compiled (text formulation, manuscript structure, figure and table generation) between the two authors.

## 3.4 Adsorption of *tert*-butylphosphine on passivated Si(001)-H, surface vacancy stabilization and precursor decomposition

The following results will be published in two separate reports. Here, the preliminary results are summarized. The adsorption behaviour of TBP on the hydrogen-passivated Si(001)-H surface and its decomposition intermediates is currently under investigation. This project is carried out in collaboration with experimental researchers applying STM and TEM. Aspects of coverage-dependent adsorption and activation of the surface will be addressed.

A second article will adress decomposition mechanisms of relevant precursor fragments on the Si(001)-H surface. Reaction barriers and electronic rearrangements will be studied providing valuable kinetic data and insight into chemical mechanisms. These results might directly influence the choice of future precursor compounds and growth conditions applied in CVD. Furthermore, the influence of the surface on reaction mechanisms known from gas phase chemistry will be described.

### 3.4.1 Introduction

The adsorption and decomposition of precursors on a semiconductor substrate are essential processes for successful III/V material growth. At low pressures, surface processes are dominant over gas phase reactivity.[48]

The influence of the substrate on decomposition chemistry might change reaction kinetics significantly with respect to the gas phase, often circumventing slow mechanisms or creating new bottlenecks for growth.[92]

Decompositions of adsorbed GaP precursors have been investigated by temperature programmed desorption and time-resolved mass spectrometry experiments.[50,63,141] For the decomposition of triethylgallane (TEGa) and related fragments on a GaN(0001) substrate, the $\beta$-hydride elimination pathway was identified. This mechanism is not possible with trimethylgallane (TMGa) which is limited to homolysis.[50,141] The $\beta$-hydride elimination channel is often interpreted as a series of $\beta$-H elimination steps (as in Equation 3.1, [SAS] is a suitable *surface adsorption site*) and recombinative desorption of $H_2$ (Equation 3.2 or Equation 3.3) as has been reported for the gas phase.[64] This pathway leads to less carbon incorporation for TEGa compared to TMGa applied in MBE growth.[63]

$$[\mathrm{SAS}]\mathrm{-Ga(C_2H_5)H} \longrightarrow [\mathrm{SAS}]\mathrm{-GaH_2} + \mathrm{C_2H_4}\uparrow \tag{3.1}$$

$$[\mathrm{SAS}]\mathrm{-GaH_2} \longrightarrow [\mathrm{SAS}]\mathrm{-Ga} + \mathrm{H_2}\uparrow \tag{3.2}$$

$$[\mathrm{SAS}]\mathrm{-GaH_2} + [\mathrm{SAS}]\mathrm{-H} \longrightarrow [\mathrm{SAS}]\mathrm{-GaH}\cdot + [\mathrm{SAS}]\cdot + \mathrm{H_2}\uparrow \tag{3.3}$$

However, adsorbed TEGa also undergoes homolysis at similar reaction barriers as the $\beta$-hydride elimination. An ethyl group is transferred to the surface (Equation 3.4) where it undergoes rapid $\beta$-hydride elimination at 600 K in the case SAS = Ga. This corresponds to a surface-assisted instead of an adsorbate decomposition.

$$[\mathrm{SAS}]\mathrm{-Ga(C_2H_5)H} + [\mathrm{SAS}]\cdot \longrightarrow [\mathrm{SAS}]\mathrm{-GaH}\cdot + [\mathrm{SAS}]\mathrm{-C_2H_5} \tag{3.4}$$

After further recombinative desorption of hydrogen, this leaves a bare Ga atom on the surface (at 500-600 K).[65] At higher temperatures and under P-rich conditions, direct desorption of an ethyl group from the surface is slightly more favourable than $\beta$-hydride elimination.[63]

As for group 15 precursors, a cascade of homolytical bond dissociations of $NH_3$[142] and $PH_3$[68] on III/V(001) and Si(001) substrates was identified (Equation 3.5). The barriers of splitting H from $NH_3$ increase with the first, second and third hydrogen transferred to the surface (GaN(0001)). This is in accordance with alkyl amines while e.g. the Ge surface does not allow this mechanism due to decreased basicity of surface atoms.[143] Surface dangling bonds are saturated by the hydrogen atoms transferred.[68]

$$[\mathrm{Si}]\cdots \mathrm{PH_3} + [\mathrm{Si}]\cdot \longrightarrow [\mathrm{Si}]{-}\mathrm{PH_2} + [\mathrm{Si}]{-}\mathrm{H} \longrightarrow [\mathrm{Si}]{-}\mathrm{PH} + [\mathrm{Si}]{-}\mathrm{H_2} \tag{3.5}$$

On a hydrogen-passivated Si(001)-H, the barriers of the $PH_3$ dissociation cascade (Equation 3.5) are *decreasing* from the first to the third H transferred as was concluded from TBP, XPS and DFT investigations.[69] Adsorption and the first P-H bond homolysis steps are in accordance with the non-passivated surfaces. However, any further H transfer from $PH_2$ to the surface requires hydrogen vacancy sites at neighbouring dimers which raises the homolysis reaction energies.[69,144,145] Given a completed cascade (i.e. enough vacancies available to transfer all adsorbate H atoms to the surface), the incorporation of P into a Si-P heterodimer at the surface was reported to occur at about 600 K.[69] On the other hand, adsorbed PH is stable being symmetrically bonded on top of a Si-Si surface dimer. The H transfer reactions in Equation 3.5 might occur on one or two dimers (intra- vs. inter-dimer) and their equilibrium can be controlled by dosing the $PH_3$ gas phase pressure.

Further, it was concluded that neighbouring adsorbates may influence decomposition and desorption. The recombination of two $PH_n$ (n = 2, 1, 0) fragments is energetically favorable. This either leads to the formation of P-P surface dimers from two PH fragments (n = 1) or desorption of $PH_3$ ($n \geq 1$) and Si-P heterodimers.[69]

The decomposition chemistry of alkyl phosphines (e.g. *tert*-butylphosphine, TBP, and triethylphosphine, TEP) on GaP(001)(2x4) was studied by HREELS experiments. Temperature-dependent analysis of vibrational data suggested that a mechanism similar to $\beta$-hydride elimination[74] might occur for the $P(C_4H_9)H$ adsorbate although a detailed explanation on the mechanism (Equation 3.6) has not been provided yet. From a gas phase analysis, a $\beta$-hydrogen elimination mechanism with a protic instead of a hydridic hydrogen transfer was reported for TBP.[138]

$$[\mathrm{Si}]\mathrm{-P(C_4H_9)H} \longrightarrow [\mathrm{Si}]\mathrm{-PH_2 + C_4H_8}\uparrow \tag{3.6}$$

In addition to $\beta$-hydrogen eliminations of alkyl groups from the adsorbed fragment, it was also suggested that homolysis occurs and those groups are transferred to the surface.[65] LEED, HREELS and TPD experiments show signals of the $C_4H_9\cdot$ radical evolving at around 350-450 K (barrier approx 101 kJ/mol) originating from an adsorbed PBuH fragment.

In this study, aspects of adsorption and surface reactivity are addressed with the example of the PBuH and $Ga(C_2H_5)H$ fragments on Si(001). These fragments are likely candidates to adsorb onto the substrate during MOVPE growth of GaP on Si. We assume that the surface[61] as well as the precursor molecules[65] are thermally activated (Equation 3.7) prior to reaching the chemisorbed state our calculations refer to.

$$\mathrm{P(C_4H_9)H_2} \longrightarrow \mathrm{P(C_4H_9)H}\cdot + \mathrm{H}\cdot \tag{3.7}$$

$$2\,\mathrm{H-[Si-Si]-H} \longrightarrow 2\,\mathrm{H-[Si-Si]}\cdot + \mathrm{H_2}\uparrow \tag{3.8}$$

Activation of the hydrogen-passivated Si surface occurs at elevated temperatures (e.g. via inter-dimer recombinative desorption of $H_2$, Equation 3.8).[72] Hydrogen vacancies (unsaturated surface electrons) can diffuse on the surface[75] and are considered potential sites for adsorption, especially for radical species like $P(C_4H_9)H$ or $Ga(C_2H_5)H$. The energetics of molecular activation reactions (homolytical cleavage, e.g. Equation 3.7)[64] as well as several of the above surface reactions[146] were studied by DFT calculations.

Firstly, structural configurations of the PBuH fragment adsorbed on a hydrogen-passivated Si(001)c(4x4) surface cell are studied. Secondly, the coverage is increased applying surface slab supercells of different dimensions (i.e. (2x1), (2x2), (4x2) and (4x4)) and the stability of multiple adsorbates at different relative adsorption sites is evaluated. Thirdly, the stabilization of a hydrogen vacancy on neighbouring surface sites to the $P(C_4H_9)H$ adsorbate is analyzed. This is motivated by the finding that surface vacancies favor adsorption and decomposition processes.[144,145] An understanding of the underlying mechanism is important as it determines the nucleation phase of semiconductor growth from TBP.

Finally, the decomposition reactivity of $Ga(C_2H_5)H$ as well as $P(C_4H_9)H$ on Si(001)-H was investigated. We focus on the $\beta$-hydride elimination (Equation 3.1, SAS = Si) and the $\beta$-hydrogen elimination (Equation 3.6) mechanisms where reaction energies and barriers can directly be compared to the equivalent mechanisms in the gas phase.

For the $\beta$-hydrogen elimination barrier of $P(C_4H_9)H$, only preliminary results can be reported.

### 3.4.2 Method Section

Periodic DFT calculations on the GGA level were conducted as it has recently been reported that the convergence of non-periodic cluster model geometries is by no means trivial in order to get accurate energies for adsorption processes.[83]

We use the PBE functional,[110,147] the D3[148] correction for dispersion interactions and a plane-wave basis set with the PAW formalism.[131] [124,149] The expansion of basis functions was truncated at a kinetic energy limit of 400 eV and accurate convergence settings for the energies and structural relaxations (SCF energy: $< 10^{-6}$ eV, forces: $< 10^{-2}$ eV/Å) were used. $k$-Points were generated after the Monkhorst-Pack scheme ($\Gamma$-centered) and the following grids were applied for different Si supercell dimensions: $6x12x1$ (2x1), $6x6x1$ (2x2), $3x6x1$ (4x2) and $3x3x1$ (4x4).

Slab-type supercells were applied that are periodically repeated in three dimensions. The hydrogen-passivated surfaces enclose slabs of 6 atomic Si layers thickness and are separated by a vacuum of >11 Å. In geometry optimziations, the two bottom Si layers including the hydrogen atoms were kept constraint representing the substrate bulk structure (frozen double layer approach).

Adsorption energies were determined as

$$\Delta E_{\mathrm{ads}} = E_{[\mathrm{Si}]-\mathrm{mol}} - (E_{\mathrm{mol}\cdot} + E_{[\mathrm{Si}]\cdot}) \tag{3.9}$$

where $E_{[Si]-ads}$ is the total energy of the Si surface slab with an adsorbate and $E_{mol\cdot}$ and $E_{[Si]\cdot}$ are the total energies of the (activated) free molecule and surface slab, respectively.

### 3.4.3 Configurations of TBP adsorbed on Si(001)c(4x4)

The adsorbate configurations of one TBP fragment on Si(001)-H ($[Si]{-}P(C_4H_9)H$) were analyzed inside the (4x4) slab supercell. The geometries of the individual adsorbates were relaxed keeping the surface constraint. The adsorbate's P atom is four-fold coordinated so that each configuration has an enantiomeric isomer. All configurations were independently relaxed.

As can be seen in Figure 3.1 the three minima determined are similar in energy. Conf1 is slightly less stabilized (-2.927 eV, $R$) than conf2 (-2.945 eV, $R$) and conf3 (-2.942 eV, $R$). The differences between two enantiomers are within the expected

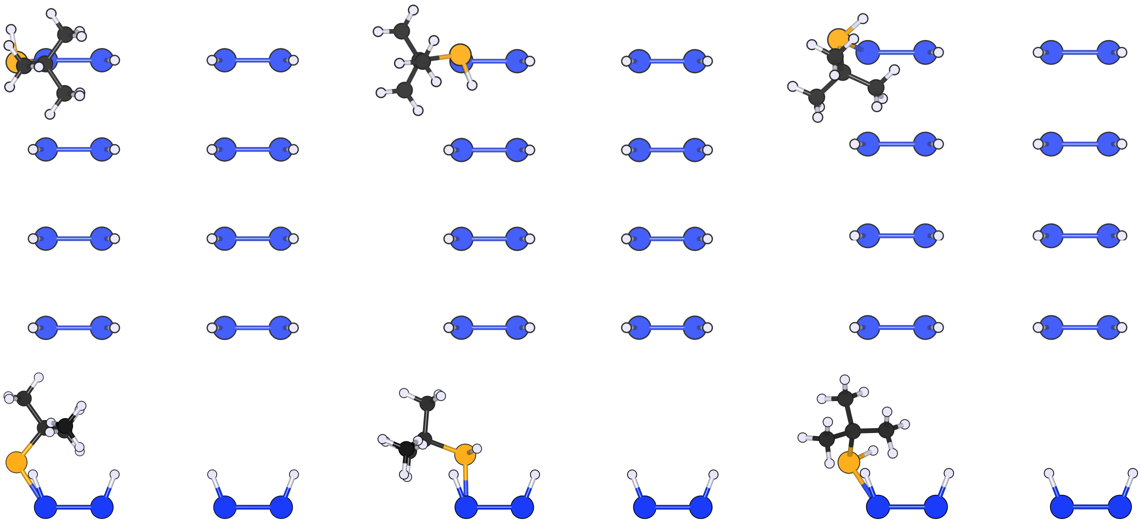

| | conf1 | conf2 | conf3 |
|---|---|---|---|
| $\Delta E_{\mathrm{ads}}$ ($R$ enantiomer) | -2.927 | -2.945 | -2.942 |
| $\Delta E_{\mathrm{ads}}$ ($S$ enantiomer) | -2.930 | -2.944 | -2.943 |

Figure 3.1: Minimum configurations of activated TBP on Si(001)-H in top-view (top) and side-view (bottom) perspective (R enantiomers shown). The adsorption energies (in eV) correspond to a coverage $\theta = \frac{1}{8}$ molecules per (4x4) unit cell.

methodological uncertainties. Thus, only one enantiomer per configuration is discussed in the following.

The orientation with respect to the Si-Si dimers can be observed by the top-view illustration on Figure 3.1. The butyl groups are aligned either parallel to and above the dimer the fragment is attached to (conf1), parallel and away from the dimer towards to trench between dimer rows (conf2) or perpendicular to the dimer bent towards the neighbouring dimer within the same dimer row (conf3). The $[\mathrm{Si}]{-}\mathrm{P}{-}(\mathrm{C_4H_9})$ bond angle is close to a tetrahedral arrangement supporting $sp^3$-hybridization at the P center. In conf1, the butyl group is arranged above the dimer at a large angle to the surface. In conf2 and conf3 it is bent over the trench at a low angle, and towards the neighbouring dimer at a mean angle. In all cases, two methyl groups point towards the surface maximizing attractive dispersion forces.

### 3.4.4 Multiple Adsorption and Coverage

Relative adsorption configurations were studied for coverages of two, four, six and eight molecules per (4x4) unit ($\theta$=$\frac{1}{4}$, $\frac{1}{2}$, $\frac{3}{4}$ and 1, respectively). The adsorption modes (ads. mode) are presented in a row:column nomenclature as introduced in Figure 3.2.

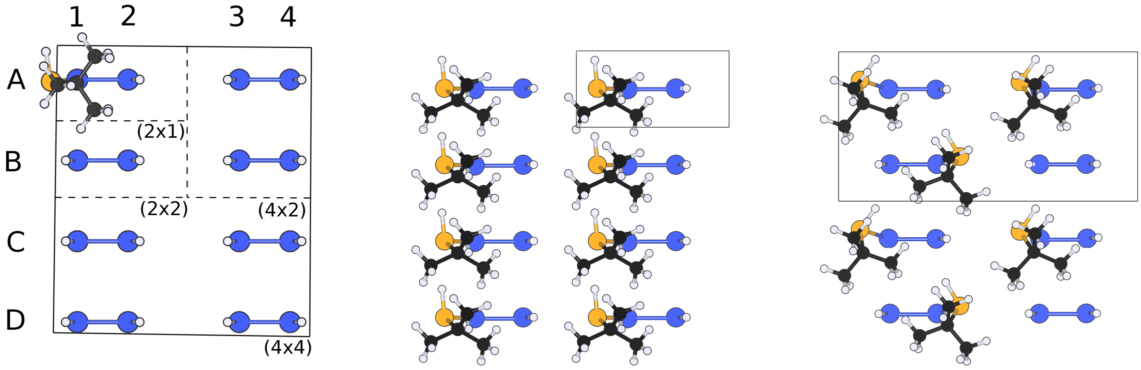

Figure 3.2: Left: Surface matrix nomenclature (row:column) for multiple adsorption on Si(001)-H in unit cells of dimensions (2x1), (2x2), (4x2) and (4x4). The cell sizes are given at bottom right-hand outside the respective cell boundary. Center, right: Illustrations of the mutliple adsorption mode in (2x1) and the most stable in (4x2).

Different supercell models were applied in order to generate various modes of adsorption relative to A:1. Each molecule was initiated as conf1 and subsequently relaxed in the presence of the other adsorbates. With this procedure, lateral interactions between the adsorbates as well as interactions with the surface are addressed on equal footing. The surface slab was kept constraint.

For low coverages (2 molecules per (4x4) unit cell, $\theta = \frac{1}{4}$), the adsorption energies (Table 3.1) are similar to the single adsorption modes ($\theta = \frac{1}{8}$ ) presented in Figure 3.1. Configurations with the molecules in large separation (e.g. A:1,C:1) as well as those with small separations (e.g. A1:A3) are amongst the most stable. This shows that lateral interactions are small for low coverages (neither repulsive nor attractive).

The configurations at coverage $\theta = \frac{1}{2}$ show increased stabilization. The adsorption of molecules on each dimer along a row was found to be favourable (A:1,B:2,C:1,D:2) leaving one dimer row completely uncovered. The adsorbates are subsequently positioned on the first (1) and second (2) Si atom of the dimers.

The most stable configuration was found for a coverage of $\frac{3}{4}$ (A:1,A:3,B:2,C:1,C:3,D:2) as shown in Figure 3.2, right. This corresponds to the configuration previously discussed with $\theta = \frac{1}{2}$ (one molecule on each dimer along one row) but with an additional adsorbate on every second dimer in the neighbouring row.

Only slightly lower in energy is one configuration at full coverage $\theta = 1$ where every dimer is covered by one adsorbate (A:1,A:3,B:1,B:3,C:1,C:3,D:1,D:3; center in Figure 3.2). Remarkably, all molecules are attached to the first Si atom on each dimer so that the butyl groups come rather close to each other. This points towards attractive lateral interactions for this specific configuration. Note that this configuration

Table 3.1: Relative configurations (adsorption modes) of multiple adsorbates at different coverages $\theta$. Adsorption energies $\Delta E_{\mathrm{ads}}$ are presented in eV per adsorbate molecule.

| $\theta^a$ | cell model | (2x1) | (2x2) | (4x2) | |
|---|---|---|---|---|---|
| 1 | ads. mode | A:1,A:3,B:1,B:3<br>C:1,C:3,D:1,D:3 | A:1,A:3,B:2,B:4<br>C:1,C:3,D:2,D:4 | A:1,A:4,B:2,B:3<br>C:1,C:4,D:2,D:3 | |
| | $\Delta E_{ads}$ | -3.086 | -2.603 | -2.650 | |
| $\frac{3}{4}$ | | (4x2) | | (4x2) | |
| | | A:1,A:4,B:2,C:1,C:4,D:2 | | A:1,A:3,B:2,C:1,C:3,D:2 | |
| | $\Delta E_{ads}$ | -2.896 | | -3.107 | |
| $\frac{1}{2}$ | | (2x2) | (4x2) | (4x2) | (4x2) |
| | | A:1,A:3,C:1,C:3 | A:1,B:3,C:1,D:3 | A:1,B:2,C:1,D:2 | A:1,A:3,C:1,C:3 |
| | $\Delta E_{ads}$ | -2.927 | -2.948 | -3.014 | -2.953 |
| $\frac{1}{4}$ | | (4x2) | (4x4) | (4x4) | (4x4) |
| | | A:1,C:1 | A:1,C:3 | A:1,B:2 | A:1,D:3 |
| | $\Delta E_{ads}$ | -2.947 | -2.931 | -2.927 | -2.935 |
| $\frac{1}{4}$ | | (4x2) | (4x4) | (4x4) | (4x4) |
| | | A:1,A:3 | A:1,B:3 | A:1,B:4 | A:1,C:4 |
| | $\Delta E_{ads}$ | -2.945 | -2.935 | -2.928 | -2.946 |

[a] Full coverage ($\theta = 1$) is defined as one adsorbate per Si dimer.

was computed applying the smallest supercell (2x1) and hence the adsorbates are aligned in a translationally symmetric fashion. The other adsorption modes at full coverage are significantly less stabilized than modes with lower coverages pointing towards repulsive inter-adsorbate interactions.

### 3.4.5 Hydrogen vacancy stabilization

As the relative configurations of multi-adsorbates were computed to be similar in energy it is not possible to accurately predict the adsorption mode to be observed from experiment (e.g. the nucleation phase of MOVPE growth of GaP) based on this energetic data. In the following, we study an aspect of kinetically controlled multi-adsorption motifs. Referring to the adsorption mechanism introduced above, a hydrogen vacancy will be the preferred adsorption site for TBP on Si(001)-H. If a hydrogen-vacancy was stabilized by an adsorbate, the secondary adsorption onto the vacancy close to the first adsorbate would be favoured. This would lead to regular patterns of multiple adsorbates agglomerated within small surface areas. Therefore, this situation can be modeled by periodic supercells of the dimensions introduced. The finding that lateral interactions are small, in most cases, supports this hypothesis.

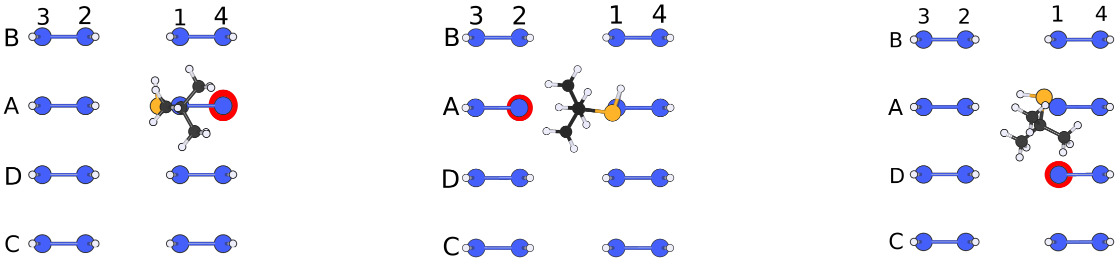

conf1 conf2 conf3-en

Figure 3.3: Most favourable hydrogen vacancy stabilization with conf1, conf2 and conf3-en. The vacancies are indicated by red circles.

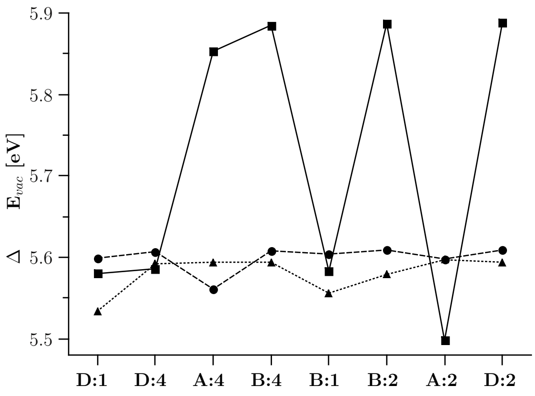

Figure 3.4: Vacancy formation energies of conf1 (points, dashed line), conf2 (squares, straight line) and conf3-en (triangles, dotted line). Positions are indicated in the format row:column as in Figure 3.3.

The vacancy formation energies were calculated as

$$E_{vac} = E_{[\mathrm{Si-P(C4H9)H}]\cdot} + E_{\mathrm{H}\cdot} - E_{[\mathrm{Si-P(C4H9)H}]} \tag{3.10}$$

where $E_{[\mathrm{Si-P(C4H9)H}]\cdot}$ is the energy of the surface slab with adsorbate and vacancy, $E_{[\mathrm{Si-P(C4H9)H}]}$ is the energy of the saturated surface slab with adsorbate, and $E_{\mathrm{H}\cdot}$ is the energy of a free hydrogen atom.

One molecule was placed in the large (4x4) supercell of Si(001)-H minimizing lateral interactions in the periodic system. Hydrogen vacancies were generated on surface Si atoms in the direct surrounding of the adsorbate (A:1) as illustrated in Figure 3.3. The three minimum configurations for $\theta = \frac{1}{8}$ coverage were considered here (only one enantiomer) and the hydrogen formation energy was calculated with the relaxed adsorbate ensuring optimal vacancy stabilization given this effect appears at all. All eight neighbouring surface sites of the adsorbate were considered and the most favourable motifs were identified as the ones shown in Figure 3.3. The energies of all vacancy positions relative to A:1 are presented in Figure 3.4.

The vacancy formation energies are positive indicating the large energy cost of creating a vacancy. Conf1 and conf3-en have similar energies that fluctuate only mildly about the average (5.58 eV). One motif is slightly favoured for vancancy formation with conf1 (A:4, 5.56 eV) and two can be identified with conf3-en (D:1, 5.53 eV and B:1, 5.56 eV). Conf2 is exceptional because it has the most favourable vacancy stabilization of all adsorbate configurations (A:2, 5.50 eV) and also exhibits the least favourable positions (A:4, B:4, B:2 and D:2, approx. 5.85 eV) which are significantly less stable than the remaining. These motifs exhibit the vacancy at a site inacessible for the P lonepair (B:4, A:4) or at large separation to the butyl group (B:2, D:2) excluding attractive interactions.

All configurations have in common that the most stabilized vacancy site is located in close contact to the butyl group of the adsorbate. Most favourable is a coordination of the adsorbate over the trench towards the vacancy site with conf2 (A:2), while coordinations within the same dimer (conf1) or to the next parallel dimer along the dimer row (conf3-en) is less favourable. The latter (D:1 with conf3-en) is slightly more stable than the prior case (A:2 with conf1). This might be caused by non-ideal overlap of the molecular orbitals as the inter-dimer separation within a dimer row (3.850 Å) is smaller than the inter-row separation (5.233 Å). Note that a coordination by two methyl groups gains the lowest vacancy formation energies.

The second best motif for vacancy stabilization with all adsorbate configurations corresponds to a coordination by the P lonepair. Conf1 and conf2 are similar in energy corresponding to a coordination across dimer rows (A:2, conf1) and within one dimer row (D:1, conf2), respectively.

In contrast, the stabilization by lonepair coordination with conf3-en (B:1) is more stable. As with conf2 it corresponds to a vacancy located at the neighbouring dimer within the same row but the distance between conf3-en's P atom to the vacancy is smaller due to a tilt towards this position. This is not the case in conf2 (D:1).

With conf1 (D:1) and conf2 (B:1) alternative motifs can be concluded where a hydrogen vacancy is stabilized by coordination of one (instead of two) methyl group. Those are almost identical in energy to the coordination by the P lonepair.

It can be concluded that vacancy stabilization via coordination of the butyl group (specifically two methyl groups) at suitable distance is most favourable. In conf1, the separation of the butyl group and the vacancy site is small (intra-dimer) resulting in less stabilization than in conf2 and conf3-en. Largest is the effect for a coordination across dimer rows (conf2, D:1) followed by coordination to the neighbouring dimer within the same row (conf3-en, D:1). A coordination by the P lonepair can also stabilize, where the effect is largest for small distances.

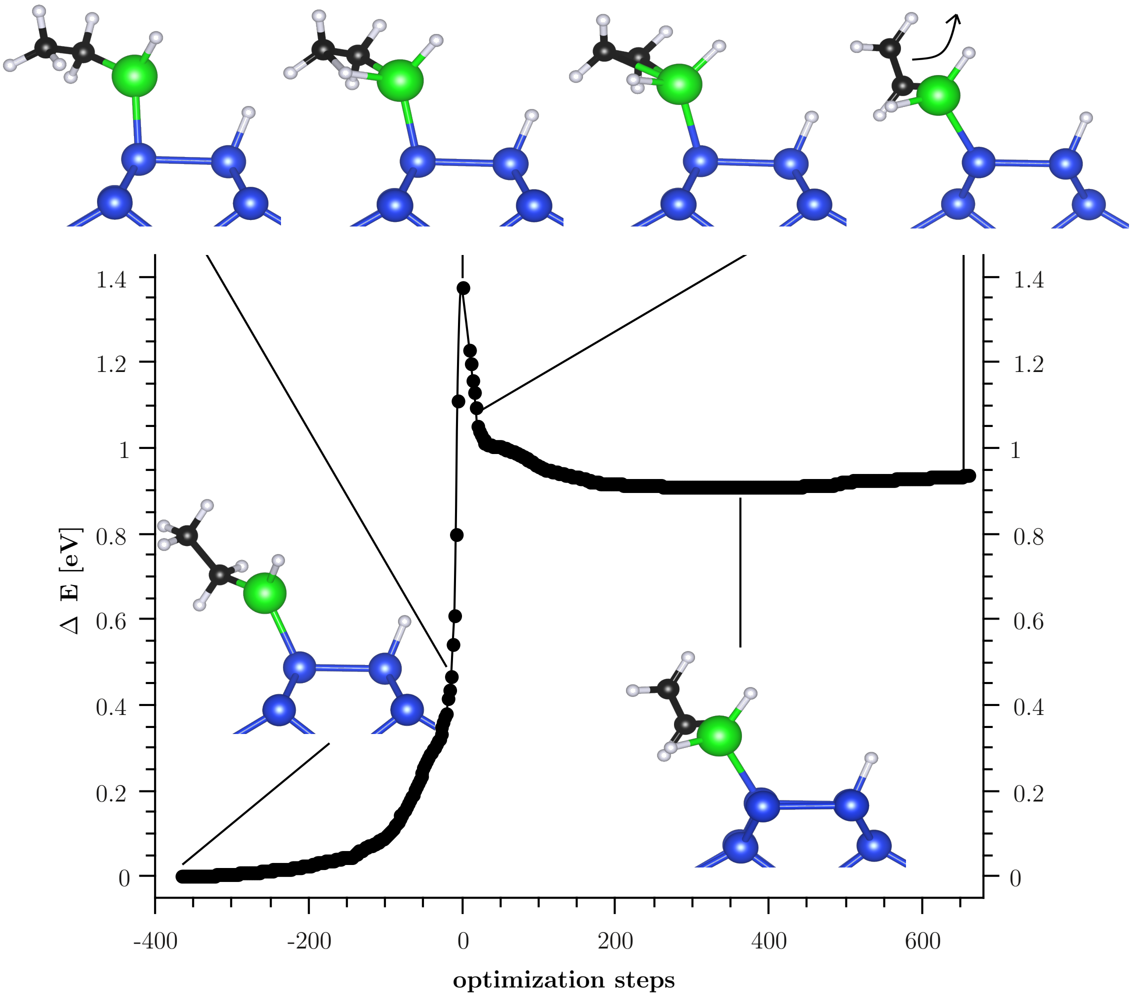

Figure 3.5: Reaction pathway of the $\beta$-hydride elimination of monoethylgallane on Si(001)(4x2). The reaction barrier is 1.397 eV and the $C_2H_4$ product is weakly bound in a precursor state (step 350) before complete desorption (step 650).

### 3.4.6 Decomposition Mechanisms: $\beta$-Hydrogen Elimination

A detailed analysis of the $\beta$-hydrogen elimination pathway of ethylgallane adsorbed on Si(001)(4x2) is presented in Figure 3.5. The transition state of the decomposition was identified by the dimer method[150] and the remaining data on the energy profile were computed by structure optimization. Initial and final states (steps -365 and 350, respectively) represent minima on the potential energy surface, complete desorption is indicated by a linear ascent of energy between steps 350 and 650.

Atomic rearrangements in the course of the reaction unveil a mechanism close to the $\beta$-hydride elimination of monoethylgallane $Ga(C_2H_5)H_2$ in the gas phase.[64] Initiated from the equilibrium configuration of the adsorbate (bottom, first structure in Figure 3.5) the ethyl group is rotated (top row, first structure) bringing the hydrogen

Table 3.2: Reaction energy $\Delta E$ and barrier $\Delta E^{\ddagger}$ (in eV) of the $\beta$-hydride and $\beta$-hydrogen elimination from monoethylgallane and *tert*-butylphosphane, respectively. Decompositions in the gas phase ($Ga(C_2H_5)H_2$, $P(C_4H_9)H_2$) and on a passivated Si(001)(4x2) surface ($[Si]{-}Ga(C_2H_5)H$, $[Si]{-}P(C_4H_9)H$) are compared.

| | $Ga(C_2H_5)H_2$ | $[Si]{-}Ga(C_2H_5)H$ | $P(C_4H_9)H_2$ | $[Si]{-}P(C_4H_9)H$ |
|---|---|---|---|---|
| $\Delta E$ | 1.397 [a] | 0.908 [b] | 1.004 [a] | 1.081 [b] |
| $\Delta E^{\ddagger}$ | 1.283 [a] | 1.375 [b] | 2.514 [a] | 2.391 [b,*] |

[a] PBE-D3/def2-TZVPP, turbomole v6.3.1[151]
[b] PBE-D3/plane-wave basis (cut-off 400 eV, $4x2x1$ $k$-points) , VASP v5.3.5[123,149]
* preliminary result

atom transferred into a coordination to the p(Ga)-orbital at the transition state (top row, second structure). Tetrahedral geometry indicates $sp^3$-hybridization at the Ga atom. Towards the final state,[A] the hydrogen atom transferred is detached from the ethylene product (top row, third structure), which itself is coordinated to the Ga atom by the evolving $\pi$ orbital (molecular plane parallel to the $[Si]{-}GaH_2$ plane, bottom, second structure) at the final state. In the course of the reaction, the $C_2H_4$ group is at first rotated towards the surface enabling a coordination of the hydride into the p(Ga) acceptor orbital. After the transition state towards desorption, the rotation is reversed recovering the initial orientation of the C.C axis relative to the surface.

The electronic reaction energies and barriers of the adsorbate $\beta$-hydrogen reactions of monoethylgallane and tert-butylphosphane ($[Si-]P(C_4H_9)H$) are compared to the equivalent gas phase mechanisms in Table 3.2. The same DFT functional and dispersion correction was applied in both cases ensuring comparability.

The products of $[Si]{-}Ga(C_2H_5)H$'s $\beta$-hydride elimination are more stabilized than $GaH_3$ and $C_2H_4$ in the gas phase. Note that $C_2H_4$ is bound in a $\pi$-coordinated precursor state as shown in Figure 3.5 which was not found in the gas phase. The barrier of the surface decomposition is increased with respect to the molecular mechanism. In contrast to the previous case, the reaction energy of the $\beta$-hydrogen elimination from the TBP fragment adsorbed to Si(001)(4x2) is slightly increased compared to the gas phase. The barrier, on the other hand, is decreased with respect to the gas phase decomposition from TBP. (Although preliminary results are presented, the barrier is expected to decrease further upon convergence.) These trends are another indication for fundamentally different mechanisms of the Ga and P fragments assuming identical surface effects for both adsorbates. Note that according to the Arrhenius law a small difference in energy barrier results already in a drastic change in the reaction rate. The differences of these mechanisms on the surface to the gas

---

[A] In surface science, this is called precursor state.

phase will be studied in detail in the future. Bonding analysis in the periodic system will be carried out similar to a previous gas phase study on TBP's $\beta$-hydrogen elimination.[138]

### 3.4.7 Summary and Conclusions

Under the assumption of a primary adsorption on an activated surface the adsorption behaviour of TBP on Si(001)-H was investigated. The activation of the surface can be achieved by the creation of a hydrogen vacancy from the passivated surface under MOVPE conditions. Dangling bonds on this surface are thermodynamically unstable, however, it was found that they can be locally stabilized by coordination of an adsorbate's butyl group or P lonepair towards a vacancy at suitable distance. Hydrogen vacancies can be considered preferred adsorption sites which might be localized to specific surface sites in the surrounding of an initial adsorbate. This mechanism might be able to explain an agglomeration of TBP adsorbates on Si(001) at sub-monolayer coverage. Lateral interactions between TBP adsorbates were found to be small and, hence, no preferred motif for multiple adsorption could be concluded. Thus, we propose a kinetically controlled mechanism of preferred adsorption of TBP on localized vacancy sites stabilized by an initial adsorbate.

Furthermore, the decomposition of ethylgallane on Si(001) was studied. The reaction energy, barrier and pathway are close to results from a gas phase analysis. It was concluded that the underlying mechanism is identical. $C_2H_4$ is weakly bound to a coordination state prior to complete desorption. It is stable enough to leave the surface under MOVPE conditions as reported from high-resolution electron energy loss spectroscopy[74] and in accordance to the shallow increase of energy upon removal from the surface. The reaction energy and barrier for $\beta$-hydrogen elimination of PBuH adsorbed on Si(001)-H is reported. The mechanism is similar to the one recently reported in the gas phase[138] although it is important to note that the barrier is decreased with respect to the gas phase. As this large barrier is generally considered unfavourable for efficient III/V material growth,[139] the findings are important for the design and understanding of precursor reactivity and will be studied in detail in the future.

## 3.5 Pyramidal Structure Formation at the Interface between III/V Semiconductors and Silicon

Andreas Beyer, Andreas Stegmüller, Jan O. Oelerich, Kakhaber Jandieri, Katharina Werner, Wolfgang Stolz, Sergei D.Baranovskii, Ralf Tonner*, Kerstin Volz*
submitted to Adv. Mat. Int., 2015

*An enhancement of computer performance following Moores law requires the miniaturization of semiconductor devices. Presently, their dimensions reach the nanoscale. Interfaces between materials become increasingly important as the volume is reduced. It is shown here how a pyramidal interface structure is formed irrespective of the conditions applied during the growth of two semiconductors. This drastically changes the common view of interfaces, which were assumed to be either atomically abrupt or interdiffused. Especially in semiconductor heteroepitaxy a simple surface segregation of one atomic species is often assumed. It is proven by first principles computations and kinetic modelling that the atom mobility during growth and the chemical environment at the interface are the decisive factors in the formation of the actual structure. Gallium phosphide grown on silicon was chosen as representative, nearly unstrained material combination to study the fundamental parameters influencing the interface morphology. Beyond that, this system has significant impact for cutting-edge electronic and optoelectronic devices. The findings derived in this study can be generalized to aid the understanding of further relevant semiconductor interfaces. This knowledge is crucial to comprehend current and steer future properties of miniaturized devices.*

The author conducted all DFT-related calculations leading to the presented results. All experimental (growth and microscopy, quantitative composition analysis) as well as the kinetic growth (kinetic Monte Carlo simulation) data were obtained by the co-authors. The choice of methods (within the DFT part) was taken in collaboration with the supervisor, however, some methods were initiated by the author (hopping model, definition of interface formation energy, construction of interface configurations). The initial research question arose from the experimental observation of non-abrupt, intermixed interface morphologies enabled by high-resolution transmission electron microscopy imaging. The interpretation of results (within DFT part) were initially done by the author. Subsequently, the author refined formulations and interpretations together with the supervisor in an iterative way (regular meetings). In the same procedure, the (DFT part of the) manuscript was compiled (text formulation, manuscript structure, figure and table generation) between the author and the supervisor. Subsequently, the full manuscript was revised by the author and the supervisor in an iterative way. All co-authors profited from the close collaboration enabled by the research training group (GRK 1782) framework. That is, in terms of compiling the above manuscript but also learning about the scientific content and different methodology applied.

## 3.6 Theoretical investigations on the stability of gallium phosphide - silicon interface structures by DFT

Andreas Stegmüller, Ralf Tonner*
manuscript in prep., 2015

*The morphology of the gallium phosphide - silicon interface is faceted and interdiffused about eight atomic layers which results from a combination of kinetic growth effects and thermodynamic stabilization of abrupt interfaces at (111) and intrinsically charge-compensated structures at (112) and (113). Different configurations of those are compared to (001) by computing absolute formation energies with periodic density functional theory applying both slab- and bulk-type supercells. As can be distinguished between specifically Ga- or P-terminated interfaces a detailed explanation on local interface properties is provided in an attempt to quantitatively explain the stabilities found. Simple counting of non-octet bonds is unable to severe divergence of formation energies of Ga- and P-dominated GaP-Si interfaces at (112) and (113). On the other hand, structural relaxation, averaged electrostatic potentials and partial charges based on natural bond orbitals (NPA) were used successfully support qualitative trends suggested by the Electron Counting Model for the stabilities of interfaces at (001) and (111). It was concluded that only periodic calculations from first principles quantitatively account for the chemical environment necessary to predict interface properties.*

The author conducted all calculations leading to the presented results. The choice of methods was taken in collaboration with the supervisor, however, some methods were initiated by the author (local potentials, summation of charges, definition of interface formation energy, construction of interface configurations, separation of local relaxation and cell elongation). The initial research question arose as a direct follow-up from a previous project. The interpretation of results were initially done by the author. Subsequently, the author refined formulations and interpretations together with the supervisor in an iterative way (regular meetings). In the same procedure, the manuscript was compiled (text formulation, manuscript structure, figure and table generation) between the two authors.

# Chapter 4

# Summary

A series of computational studies is presented that investigated growth aspects and chemical properties in chemical vapour deposition (CVD) of functional semiconductor materials. The system in focus is metal-organic vapour phase epitaxy (MOVPE) of gallium phosphide grown on silicon which is an important building block in quantum well heterostructures for optoelectronic devices.

The challenges arise not only in engineering the materials' electronic structure but also in finding the right growth conditions to steer the materials' composition and purity. A fundamental understanding of epitaxy procedures, which are largely kinetically driven, is necessary in order to systematically refine the growth parameters involving temperature, partial pressures of vaporized sources, choice of precursor species, substrate surface composition and growth dynamics such as the (intended) total growth rate. In CVD, a complex system of elementary chemical processes underlies these parameters. Experimental analysis of structural (TEM, electron diffraction, STM, AFM), electronic (XPS) or optical (SHG) properties can provide valuable but somewhat limited insight as *in situ* experiments are tedious. Methods from first principles, on the other hand, are reliable and computer capacities allow the treatment of many processes and realistic systems.

The research projects presented mainly apply density functional theory in the generalized-gradient approximation (PBE functional) with either local basis functions (for molecules) or plane waves for periodic systems. Well converged computational parameters suitable for the respective systems, including a reliable correction for dispersion interaction (D3) as shown in 3.1[64] were worked out. An extension to multi-scale methodology is desirable for growth studies, in general, and was developed, specifically, for gas phase decomposition kinetics by the Monte Carlo program *kmc-lists.py*. It was intended for dynamic simulation of elementary processes independent of any lattice constriction and is, thus, suited for gas phase processes. It is, however, flexible enough to address surface dynamics, adsorbate reactivity and various other systems, too.

As was presented in 3.1,[64] the relevant precursors for MOVPE of gallium phosphide (GaP) are triethylgallane (TEGa, $Ga(C_2H_5)_3$) and *tert*-butylphosphine (TBP, $P(C_4H_9)H_2$). Among seven different decomposition mechanisms formulated, homolytical bond cleavage is energetically unfeasible as highly reactive radical species are generated. Entropic contributions largely prevent bimolecular mechanisms although the carrier gas $H_2$ is available in the CVD reactor. For TEGa, $\beta$-hydride and, for TBP, $\beta$-hydrogen elimination are likely decomposition channels. Asides, the much less favourable $H_2$ and alkane eliminations are possible at high temperatures only. In MOVPE, non-equilibrium conditions are applied, hence elementary kinetics determine decomposition and growth rates. $GaH_3$ and TBP, in small quantities also $PH_3$ and GaH, were concluded to be produced and are likely candidates for adsorption on the substrate.

In 3.2,[138] the $\beta$-hydrogen elimination from TBP and related group 15 precursors $E(C_4H_9)H_2$ are investigated. For the first description of this mechanism in literature, an extensive quantum-chemical analysis was performed including partial charges, molecular orbitals, energy analysis along an intrinsic reaction coordinate, molecular structures, energy decomposition and natural orbitals of chemical valence concepts. For the groups with E = N and E = P, As, Sb, Bi different elimination mechanisms were discovered that exhibit protic and neutral hydrogen atoms transferred, respectively. This is significantly different to the metal compound (E = Ga) where a hydride is transferred and the electron flow during the reaction is reversed. Most relevant for compound semiconductor growth is the finding that for E = P, As, Sb, Bi the $C_\alpha$-E bond elongation and charge transfer to E is barrier-determining.

In 3.3[139] the insight gained from the mechanism analysis is applied for the construction of a quantum chemical descriptor of $\beta$-hydrogen eliminations of group 15 precursors. The hypothesis pursued is that the decomposition primarily follows the $\beta$-hydrogen channel for TBP and TBAs and the rate-determining property is represented by the partial charge at $C_\alpha$. A linear correlation in support for this hypothesis was found for six isomeric butyl derivates of TBP and TBAs which exhibit charges at $C_\alpha$ ranging between -0.6 $e$ and +0.2 $e$ and result in $\beta$-hydrogen elimination rates varying within four orders of magnitude. A significant increase of decomposition rates relative to TBP and TBAs was predicted for silylated derivatives where the above hypothesis still holds. At the transition states, hyperconjugation of silyl groups in $\beta$-position stabilize the positive $C_\alpha$ center and reduce the barrier by approx. 10-16 kJ mol$^{-1}$ per silyl group.

The adsorption behaviour of TBP and related fragments on Si(001)-H was investigated in 3.4. Activation of a hydrogen-passivated surface is crucial for adsorption and diffusion. No preferred adsorption motif for multiple adsorbates could be concluded from energetic arguments as inter-adsorbate interactions seem to be small for sub-monolayer coverages. However, the concept of stabilization of hydrogen vacancies (unsaturated electrons) on the surface by coordination of an adsorbate functional group was introduced. For the $P(C_4H_9)H$ fragment, some configurations were identified that stabilize a vacancy in direct surrounding by coordination of the butyl group or the P lonepair. This might deliver reasoning for clustered instead of randomly distributed adsorption motifs of multiple fragments. In accordance to gas phase decomposition, monoethylgallane undergoes $\beta$-hydride elimination and PBuH decomposes via $\beta$-hydrogen elimination on Si(001)-H. Electronic reaction energies, barriers and energy paths were reported for these mechanisms. Compared to the gas phase equivalents, decomposition of the TEGa fragment has a higher, and $P(C_4H_9)H$ a slightly lower barrier on the surface.

Study 3.5[96] presents a cooperation with TEM and MOVPE experiments. The interface morphology of GaP-Si was observed to be not abrupt but intermixed and faceted. Kinetic Monte Carlo simulation of the growth were performed including adsorption, desorption, atom mixing and diffusion events. Surface diffusion barriers for Ga, P and Si adatoms were calculated from periodic DFT assuming an ideal lattice of different surfaces present during growth (Si(001), Si/GaP(001) and Si/GaP-Ga(001)). It was found that atomic intermixing occurs during growth if one species is immobile on the surface. This was identified as the P atom in the system modeled. Originating from a flat Si(001) substrate, intermixing leads to a rough interface morphology during GaP growth. The calculation of absolute GaP-Si interface formation energies provided a thermodynamic reason why the (001) orientation is left during growth and facets at the crystal planes {111} and {112} appear instead. A large set of interface configurations was constructed in periodic slab and bulk supercell models. The formation energies obtained were in excellent agreement. Due to this approach it was possible to directly distinguish between Ga- and P-terminated interface configurations for the first time. With these findings, 3.5[96] provided the basis for a discussion on the bonding situation at the interface and in how far simple models of local electron counting (ECM) can quantify III/V-IV interface stabilities.

In 3.6 the discussion on stabilization effects of interface configurations and the influence of the chemical environment is extended. With abrupt GaP-Si(113) another intrinsically charge-compensated configuration was added so that abrupt and intermixed interfaces in the orientations (001), (111), (112) and (113) were distinguished. An explanation for the interface stabilization of abrupt GaP-Si at (111) can already be provided by the characteristic structure of zinc blende lattices. GaP-Si(111) is favourable if the terminal *bilayer* at the interface is exclusively comprised of Ga and P atomic layers in equal shares. It is destabilized if this balanced bonding situation is disturbed either by atomic intermixing or by splitting the GaP bilayer by the interface (GaP-Si(111)-sb). This is the reason for intermixed GaP-Si(111)-im and GaP-Si(111)-sb being considerably less stable than abrupt GaP-Si(111). GaP-Si(001), on the other hand, exhibits a different structure and is stabilized upon atomic intermixing at the interface. The intrinsically compensated configurations at (112) and (113) are favourable without intermixing in qualitative agreement with the ECM.

Partial charges (NPA), local average electrostatic potentials and the response upon structural relaxation were analyzed and provided a quantitative measure for (i) the interface stabilization and (ii) various properties relevant for integration into heterostructures. The latter comprise the electronic structure at the interface, e.g. the valence band offset represented by the average electrostic potentials and the accumulation of charge. Local partial charges and dipoles were calculated next to polarization fields along stacking direction. Furthermore, local distortions of atomic structure at the interfaces were calculated separately from strain, which was modeled by an elongation of the supercells with constraint relative atom positions. GaP and Si are almost lattice-matched and the experimentally determined mismatch was reproduced by the average of all orientations studied.

By means of these quantitative analyses the stability of III/V-IV interfaces can be predicted. Besides, local as well as extended electrostatic properties of thin films can be estimated and compared to related configurations and compositions.

With the series of projects conducted, it was possible to fulfill the following research goals in support of the development of novel III/V semiconductor materials and their integration in optoelectronic devices.

(i) For TEGa, TBP and related precursors, the decomposition networks were comprehensively elaborated and the most likely pathways were identified by thermodynamic and kinetic data.

(ii) The $\beta$-hydrogen elimination mechanism for group 15 compounds was identified as dominant decomposition channel and was described in detail for the first time.

(iii) A quantum-chemical descriptor for the prediction of decomposition rates of TBP, TBAs and related sources was proposed based on the findings on the $\beta$-

hydrogen mechanism. It enables the design of new compounds based on their ability to stabilize the elimination's transition state.

(iv) The reactivity of TBP on the Si(001) surface was investigated and a kinetic reasoning for sub-monolayer adsorption patterns was delivered next to $\beta$-hydrogen elimination barriers of $P(C_4H_9))H$ and $Ga(C_2H_5)H$ adsorbates.

(v) Essential growth processes of GaP epitaxy were determined by results from TEM and kinetic modeling. On the basis of kinetic as well as thermodynamic data , computed with DFT, the resulting GaP-Si interface morphology was explained.

(vi) Intrinsic III/V-Si interface formations were described by absolute energies of a large set of atomic configurations. Electrostatic and mechanical properties of those were calculated providing a rationale for the stabilities found and valuable insight into the relation between electronic and atomic structure at the interfaces.

# Chapter 5

# Zusammenfassung

Im Rahmen der vorliegenden Dissertation werden Studien vorgestellt, in denen mit computergestützten Methoden Aspekte des Wachstums der Chemischen Gasphasenabscheidung (Chemical Vapour Deposition, CVD) von funktionellen Halbleitermaterialien untersucht wurden. Der Fokus lag auf dem System Galliumphosphid (GaP), das in einer metall-organischen Gasphasenepitaxie (metal-organic vapour phase epitaxy, MOVPE) auf Siliziumsubstrate aufgebracht wird, um es als Dünnschicht in sog. Quantum-Well Heterostrukturen einzubringen und damit optisch aktive elektronische Bauteile zu konstruieren.

Die Herausforderungen dieser Entwicklung liegen nicht allein in der Anpassung der elektronischen Struktur der Halbleiter (band engineering), sondern zu großen Teilen auch im Verständnis der zugrundeliegenden Prozesse während des Wachstums. Zusammensetzung und Reinheit der Schichten sind für die Anwendung von großer Bedeutung, jedoch sensitiv abhängig von Wachstumstemperatur, Partialdrücken, der Auswahl der Vorläufersubstanzen, Oberflächenbeschaffenheit und Wachstumsgeschwindigkeit. In CVD-Verfahren finden chemische Elementarprozesse statt, die sich in einem komplexen Netzwerk gegenseitig bedingen und stark von den gewählten Wachstumsparametern abhängen. Experimentelle Analysemethoden zu Aufklärung der Struktur (TEM, Elektronenbeugung, STM, AFM), der elektronischen (XPS) oder optischen (SHG) Eigenschaften sind notwendig. Deren *in situ* Anwendung ist allerdings aufwendig und begrenzt. Methoden der *first principles* hingegen sind verlässlich für diese Systeme anwendbar und dank gesteigerter Computerleistungen können realistische Modelle der Prozesse und Strukturen berechnet werden.

Die vorgestellten Projekte wurden mit Dichtefunktionaltheorie in der GGA-Näherung betrachtet (PBE Funktional) unter Anwendung von atom-zentrierten Basisfunktionen (für Moleküle) oder ebenen Wellen für perioidische Modelle. Für die berechneten Systeme wurden passende und konvergierte Parameter ausgearbeitet, die unter anderem eine Korrektur für Dispersionswechselwirkungen (D3) beinhalten, wie in 3.1[64] vorgestellt wurde. Eine methodische Ausweitung zu Mehrskalenansätzen ist für Wachstumsstudien im Allgemeinen notwendig und wurde hier speziell für Gasphasenzerfallsreaktionen umgesetzt. Das Kinetic Monte Carlo Programm *kmc-lists.py* wurde für dynamische Simulationen von Elementarprozessen, die unabhängig von einem fixierten Strukturgitter ablaufen, entwickelt. Es ist allerdings derart gestaltet, dass auch Oberflächenprozesse, chemische Reaktivität von Adsorbaten und diverse weitere Systeme simuliert werden können.

In 3.1[64] wurden die für MOVPE-Anwendungen wichtigen Prekursoren Triethylgallan (TEGa, $Ga(C_2H_5)_3$) und *tert*-Butylphosphin (TBP, $P(C_4H_9)H_2$) untersucht, mit denen zum Beispiel GaP auf Si gewachsen wird. Es wurden sieben verschiedene Zerfallsmechanismen ausgearbeitet, wobei sich herausstellte, dass homolytische Bindungsspaltung energetisch unerreichbar ist, da radikalische Zwischenprodukte entstehen, die thermisch nicht stabil sind. Entropische Effekte verhindern das Ablaufen bimolekularer Reaktionen, obwohl das Trägergas $H_2$ mit hohen Partialdrücken im CVD Reaktor vorliegt. Für TEGa stellen $\beta$-Hydrid-, für TBP, $\beta$-Wasserstoffeliminierungen die wahrscheinlichsten Zerfallskanäle dar. Dagegen sind $H_2$- und Alkaneliminierungen energetisch deutlich weniger günstig und erst bei hohen Temperaturen zugänglich. Da MOVPE-Wachstumsbedingungen das Einstellen eines thermodynamischen Gleichgewichts häufig ausschließen, werden Zerfalls- und Wachstumsraten von der Kinetik ablaufender Elementarprozesse (i.e. Reaktionsbarrieren) bestimmt. Daher konnten $GaH_3$ und TBP als Hauptprodukte identifiziert werden, die das Substrat mit hoher Wahrscheinlichkeit als Adsorbate erreichen. Daneben erscheinen $PH_3$ and GaH, die nur auf Pfaden erreicht werden, die hohe Barrieren aufweisen.

Der Mechanismus der $\beta$-Wasserstoffeliminierung von TBP und verwandter Prekursoren der Gruppe 15 ($E(C_4H_9)H_2$, E = P und höhrere Homologe, sowie E = N) wurden in Studie 3.2[138] untersucht. Zur ersten quantenchemischen Beschreibung dieses Mechanismus wurden umfangreiche Analysen mit den folgenden Methoden unternommen: Partialladungen, Molekülorbitale, Energieanalyse entlang einer intrinsischen Reaktionskoordinate, Molekülstrukturen, Energiedekompositionsanalyse mit der Erweiterung der Natural Orbitals of Chemical Valence (EDA-NOCV). Die Gruppen mit E = Ga, E = N und E = P, As, Sb, Bi weisen unterschiedliche Eliminierungsmechanismen vor, wobei sich sowohl die Partialladung des transferierten Wasserstoffatoms als auch die Chronologie der Reaktionsschritte unterscheidet. Für die Anwendung als Wachstumsprekursoren für Halbleitermaterialien ist die Erkenntnis, dass die $C_\alpha$-E Bindungselongation sowie der Ladungstransfer zu E für die Gruppe (E = P, As, Sb, Bi) die Eliminierungsbarriere bestimmt, wichtig. Alkylverbindungen der Gruppe 15 unterlaufen $\beta$-Wasserstoffeliminierung, bei der ein Proton statt eines Hydrids übertragen wird.

Dieses Ergebnis wurde in Studie 3.3[139] als Grundlage dazu verwendet, einen quantenchemischen Deskriptor zu konstruieren, anhand dessen alternative MOVPE Prekursoren mit geringeren Barrieren vorhergesagt werden können. Unter der Annahme, dass $\beta$-Wasserstoffeliminierung geschwindigkeitsbestimmend für den Zerfall von TBP, *tert*-Butylarsin (TBAs) und ähnliche Prekursoren ist, wurde die Hypothese aufgestellt, dass die Zerfallsrate dieser Moleküle ausschließlich von der Partialladung des zentralen $C_\alpha$ abhängt (Bindungspolarisation).

Für jeweils sechs Derivate von TBP und TBAs mit isomeren Butylliganden und signifikant unterschiedlichen Partialladungen $q(C_\alpha)$ konnte eine lineare Korrelation festgestellt werden, die diese Hypothese stützt. Die berechneten $\beta$-Wasserstoffeliminierungsraten der Substanzen mit positiven $C_\alpha$ sind um vier Größenordnungen größer als die der Verbindungen mit negativen $C_\alpha$. Deutlich größere Raten konnten für TBP- und TBAs-Derivate vorhergesagt werden, die silylierte *tert*-Butylliganden enthalten, wobei der $\beta$-Silyleffekt (Hyperkonjugation) die positive Ladung am Übergangszustand der Eliminierung stabilisiert (ca. 10-16 kJ mol$^{-1}$ pro Silylgruppe).

Das Adsorptionsverhalten von TBP und seiner Fragmente auf Si(001)-H wurde in 3.4 untersucht. Dabei spielt die Aktivierung der mit Wasserstoff passivierten Oberfläche eine wichtige Rolle, die Adsorption und Diffusion beeinflusst. Auf der Grundlage energetischer Argumente konnte kein bevorzugtes Adsorptionsmuster mehrerer Fragmente festgestellt werden, da die intermolekularen Wechselwirkungen für Submonolagenbedeckung klein zu sein scheinen. Es wurde allerdings ein alternatives Konzept vorgeschlagen, nachdem die Lokalisierung von Wasserstofffehlstellen (ungesättigte Elektronen) auf der Oberfläche durch Koordination eines Adsorbats stabilisiert werden könnte. Für das $P^t(C_4H_9)H$-Fragment liegen einige Strukturkonfigurationen vor, die Fehlstellen in unmittelbarer Umgebung durch Koordination der Butylgruppe oder des freien Elektronenpaares (P) stabilisieren. Da Fehlstellen bevorzugte Adsorptionspositionen darstellen, könnte dieses Ergebnis eine agglomerierte Bedeckung mehrerer Moleküle gegenüber einer homogen verteilten erklären.

Wie aus den vorgestellten Ergebnissen zur Gasphase bekannt ist, kann Monoethylgallan via $\beta$-Hydrideliminierung und PBuH durch $\beta$-Wasserstoffeliminierung zerfallen. Beide Mechanismen kommen auch für Adsorbate auf der Si(001)-H Oberfläche vor. Es wurden elektronische Reaktionsenergien, -barrieren und Reak-

tionspfade für diese Mechanismen vorgestellt. Im Vergleich zu den Daten der Gasphasenzerfälle weist das TEGa-Fragment eine erhöhte und $P^t(C_4H_9)H$ eine leicht erniedrigte Zerfallsbarriere auf der Oberfläche auf.
In Studie 3.5[96] wird eine kooperative Arbeit vorgestellt, in der Ergebnisse aus TEM, MOVPE, dynamischer Simulationstechniken sowie DFT-Berechnungen kombiniert wurden, um die Grenzflächenmorphologie von GaP-Si aufzuklären. Die Struktur der Grenzfläche ist entgegen der bisherigen Erwartungen nicht abrupt, sondern über acht Atomlagen vermischt (intermixed) und facettiert. In einer kinetic Monte Carlo Simulation wurden Adsorption, Desorption, Einzelatomvermischung sowie Diffusionsprozesse berücksichtigt, wobei die Oberflächentransportbarrieren für Ga-, P- und Si-Adatome mit periodischer DFT und Modellen der unrekonstruierten Oberflächen Si(001), Si/GaP(001) und Si/GaP-Ga(001) berechnet wurden. Es wurde festgestellt, dass Vermischung von Atomen während des Wachstums vorkommt, falls eine Spezies eine geringere Mobilität vorweist. Dies führt dazu, dass die atomar flache Substratoberfläche Si(001) während des Wachstums von GaP aufgerauht wird und sich die Grenzflächenregion über mehrere Lagen ausdehnt. Im vorliegenden System konnte das P-Atom anhand der DFT Berechnungen als die immobile Spezies identifizert werden.
Mit der Berechnung von absoluten GaP-Si Grenzflächenbildungsenergien konnte außerdem ein thermodynamisches Argument diskutiert werden, warum die vorliegende Orientierung (001) während des Wachstums zu Gunsten der Kristallebenen {111} und {112} verlassen wird. Zu diesem Zweck wurden diverse Grenzflächenkonfigurationen konstruiert und mit slab- sowie bulk-artigen Superzellmodellen berechnet. Beide Zelltypen lieferten übereinstimmende Ergebnisse, wobei zum ersten Mal direkt zwischen Ga- und P-terminierten Grenzflächenkonfigurationen unterschieden werden konnte. Die Resultate zeigten unter anderem, dass abrupte Grenzflächen in {112} stabiler sind als {111} oder {001}. Darüber hinaus wurde in 3.5[96] die Grundlage zu einer Diskussion über den Ursprung der unterschiedlichen Stabilitäten bzw. die Bindungsverhältnisse der Grenzflächen geschaffen, die mit qualitativen Argumenten wie dem Electron Counting Model (ECM) verglichen wurden.
In Studie 3.6 wurde die Diskussion über den Ursprung der Stabilisierung bestimmter GaP-Si Grenzflächenkonfigurationen und deren chemische Umgebung weitergeführt. Mit der abrupten GaP-Si(113) wurde eine weitere intrinsisch ladungskompensierte Orientierung hinzugefügt, sodass nun zwischen abrupten und atomar vermischten (intermixed) Grenzflächen in den Orientierungen (001), (111), (112) und (113) unterschieden werden konnte. Die Stabilität von abrupter GaP-Si(111) kann mit einem

strukturellen Argument erklärt werden, da eine charakteristische Doppellagenabfolge entlang [111] in Zinkblende-Kristallstrukturen vorliegt, die eine Grenzfläche stabilisiert, falls die angrenzenden Doppellagen ausschließlich und vollständig durch Ga- und P-Atomlagen (sowie $Si_2$-Lagen) gebildet werden. Im Gegensatz dazu ist die ausgeglichene Bindungssituation innerhalb der Doppellagen gestört, falls atomares Vermischen innerhalb einer Atomlage (oder auch innerhalb einer Doppellage, GaP-Si(111)-sb) vorliegt, was zu Destabilisierung führt. Dadurch sind vermischte (intermixed) GaP-Si(111)-im und GaP-Si(111)-sb deutlich instabiler als abruptes GaP-Si(111). Dahingegen wird GaP-Si(001), das eine ganz andere Struktur vorweist, durch atomares Vermischen an der Grenzfläche stabilisiert.

Partialladungen (NPA), lokale elektrostatische Potentiale und das Verhalten bei Strukturrelaxation wurden als quantitative Indikatoren herangezogen, die (i) die Stabilisierung der Grenzflächenkonfigurationen sowie (ii) diverse Eigenschaften, die für die Integration der Materialien in Heterostrukturen von Bedeutung sind, beschreiben. Letztere repräsentieren vor allem die elektronische Struktur der Grenzfläche, zum Beispiel die relative Lage der Kanten der Valenzbänder sowie die Verdichtung von Ladung an den Grenzflächen.

Lokale Verzerrungen der atomaren Struktur wurden dem mechanischen Strain-Effekt, der anhand Elongation einer Superzellachse analysiert wurde, gegenübergestellt. Für die beinahe gittergleiche Kombination aus GaP und Si konnte der experimentell bekannte Gitterversatz reproduziert und eine geringe Strain-Energie abgeschätzt werden. Der Effekt von lokaler Relaxation (stress) der atomaren Struktur an den Grenzflächen is deutlich größer, wobei die Reihenfolge der relativen Stabilitäten nur in Ausnahmefällen (P-terminierte GaP-Si(111)) im Vergleich zum unrelaxierten Gitter verändert wird.

Neben atomaren Partialladungen wurden auch Polarisationsfelder (polarization fields) entlang der Wachstumsrichtung der Dünnschichten berechnet. Dabei zeigte sich, dass Überschussladung zur Destabilisierung der Grenzfläche beiträgt. Damit stehen quantitiative Methoden zur Verfügung, die Stabilität von Grenzflächen sowie lokale und ausgedehnte elektrostatische Eigenschaften von Dünnschichtstrukturen vorherzusagen. Es zeigte sich außerdem, dass einfache Modelle, die auf dem Auszählen von Non-Oktett-Bindungen beruhen, die Stabilitäten von Grenzflächenkonfigurationen qualitativ vorhersagen können.

Die durchgeführten Projekte konnten folgende Fragestellungen erfolgreich bearbeiten und die erzielten Ergebnisse werden die Entwicklung neuer III/V Halbleitermaterialien und deren Integration in optoelektronische Bauteile unterstützen.

(i) Die Zerfallsnetzwerke von TEG, TBP und verwandter Prekursoren konnten umfänglich aufgeklärt werden und anhand thermodynamischer sowie kinetischer Daten wurden die wahrscheinlichsten Produkte der Gasphase bestimmt.

(ii) Der Mechanismus der $\beta$-Wasserstoffeliminierung von Verbindungen der Gruppe 15 konnte aufgeklärt werden und wurde mit der $\beta$-Hydrideliminierung von Metallverbindungen (Ga) verglichen.

(iii) Basierend auf den Erkenntnissen der vorangegangenen Studien wurde ein quanten-chemischer Deskriptor vorgeschlagen, der es erlaubt, für die letztgenannte Prekursorengruppe alternative Derivate mit optimierten Zerfallsraten vorherzusagen.

(iv) Die Oberflächenreaktivität von TBP auf Si(001) wurde untersucht und ein kinetisches Argument zur Beschreibung von sub-monolagen Adsorptionsmustern konnte vorgestellt werden. Außerdem wurden Barrieren der $\beta$-Wasserstoffeliminierungen von $P(C_4H_9))H$ und $Ga(C_2H_5)H$ berechnet und mit Ergebnissen aus der Gasphase verglichen.

(v) Wesentliche Elementarprozesse des III/V-IV Wachstums wurden in einer Kombination aus TEM und kinetischer Simulation bestimmt und die resultierende Morphologie der GaP-Si Grenzfläche wurde erklärt.

(vi) Die Stabilitäten intrinsischer III/V-Si Grenzflächenstrukturen wurde anhand absoluter Bildungsenergien verschiedener Konfigurationen errechnet und anhand elektrostatischer sowie mechanischer Eigenschaften analysiert. Es konnten quantitative Argumente zur Grenzflächenstabilität sowie zur Beziehung von atomarer und elektronischer Struktur an der Grenzfläche gefolgert werden.

# Chapter 6

# Appendix

The following manuscripts represent substantial parts of research conducted by the author and to be considered for the cumulative part of this dissertation.

- **A quantum-chemical study on gas phase decomposition pathways of triethylgallane (TEG, $Ga(C_2H_5)_3$) and tert-butylphosphine (TBP, $PH_2(t\text{-}C_4H_9)$) under MOVPE conditions**
  Andreas Stegmüller, Phil Rosenow and Ralf Tonner
  Phys. Chem. Chem. Phys., 2014, 16, 17018-17029.

- **The $\beta$-hydrogen elimination mechanism in the absence of low-lying acceptor orbitals in $EH_2(t\text{-}C_4H_9)$ (E = N-Bi)**
  Andreas Stegmuüller and Ralf Tonner
  Inorg. Chem., 2015, 54, 6363-6372.

- **A quantum-chemical descriptor for CVD precursor design: predicting decomposition rates of TBP and TBAs isomers and derivatives**
  Andreas Stegmüller, Ralf Tonner
  accepted for publication, Chem. Vap. Depos., 2015.

- **Mysterious pyramidal structures at interfaces between III/V semiconductors and silicon**
  Andreas Beyer, Andreas Stegmüller, Jan O. Oelerich, Kakhaber Jandieri, Katharina Werner, Wolfgang Stolz, Sergei D.Baranovskii, Ralf Tonner, Kerstin Volz
  submitted, 2015

- **Theoretical investigations on the stability of gallium phosphide - silicon interface structures by DFT**
  Andreas Stegmüller, Ralf Tonner
  manuscript in prep., 2015

Next to the journal articles listed above the author contributed the following book chapters on high performance computing with the background of the *ab initio* description of GaP-Si growth. Please refer to the original publications (not printed here).

- **From Molecules to Thin Films: GaP Nucleation on Si Substrates.** in *High Performance Computing in Science and Engineering '13* (Eds.: W. E. Nagel, D. H. Kröner, M. Resch), Andreas Stegmüller, Ralf Tonner, pp. 185-199, Springer International Publishing, 2013, ISBN 978-3-319-02165-2.

- **GaP/Si: Studying Semiconductor Growth Characteristics with Realistic Quantum-Chemical Models.** in *High Performance Computing in Science and Engineering '14* (Eds.: W. Nagel, W. Jäger, M. Resch), Andreas Stegmüller, Ralf Tonner, pp. 205-220, Springer International Publishing, 2015, ISBN 978-3-319-10809-4.

- **Interfacial properties and growth dynamics of semiconductor interfaces**, submitted for consideration in *High Performance Computing in Science and Engineering '15*, Phil Rosenow, Andreas Stegmüller, Josua Pecher and Ralf Tonner, Springer International Publishing, 2015.

### Description of *kmc-lists.py*

In the course of the research projects described above the need for multi-scale methods describing the dynamics of elementary processes was frequently identified. A kinetic Monte Carlo program was developed that is independent of any lattice-restrictions which is usually applied for growth simulations.[133,152–154]
A catalogue of individual processes including necessary reactants and products to be generated, process barriers and process energies (free Gibbs energies are desirable) is supplied to the simulation. The processes are treated within Poisson statistics. Refer to Figure 6.1 for an overview on the algorithm.

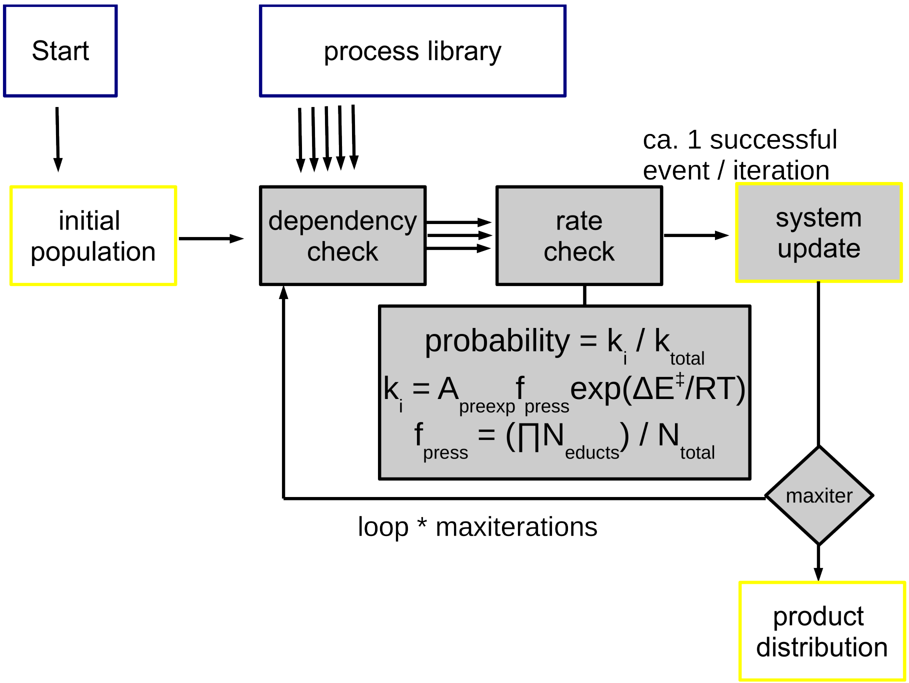

Figure 6.1: Illustration of the algorithm applied in the lattice-independent kinetic Monte Carlo code *kmc-lists.py*.

The initial population, the process library (catalogue), pre-exponential factors (determining absolute values for process rates $k$) and the simulation temperature are parameters to be provided by the user. The procedure determining probabilities of a process $i$ to be accepted $p_i$ is related to the Bortz-Kalos-Lebowitz algoritm[135] as the occurrence of *one* successful event per iteration is encouraged,

$$p_i = \frac{k_i}{\sum_i k_i}. \tag{6.1}$$

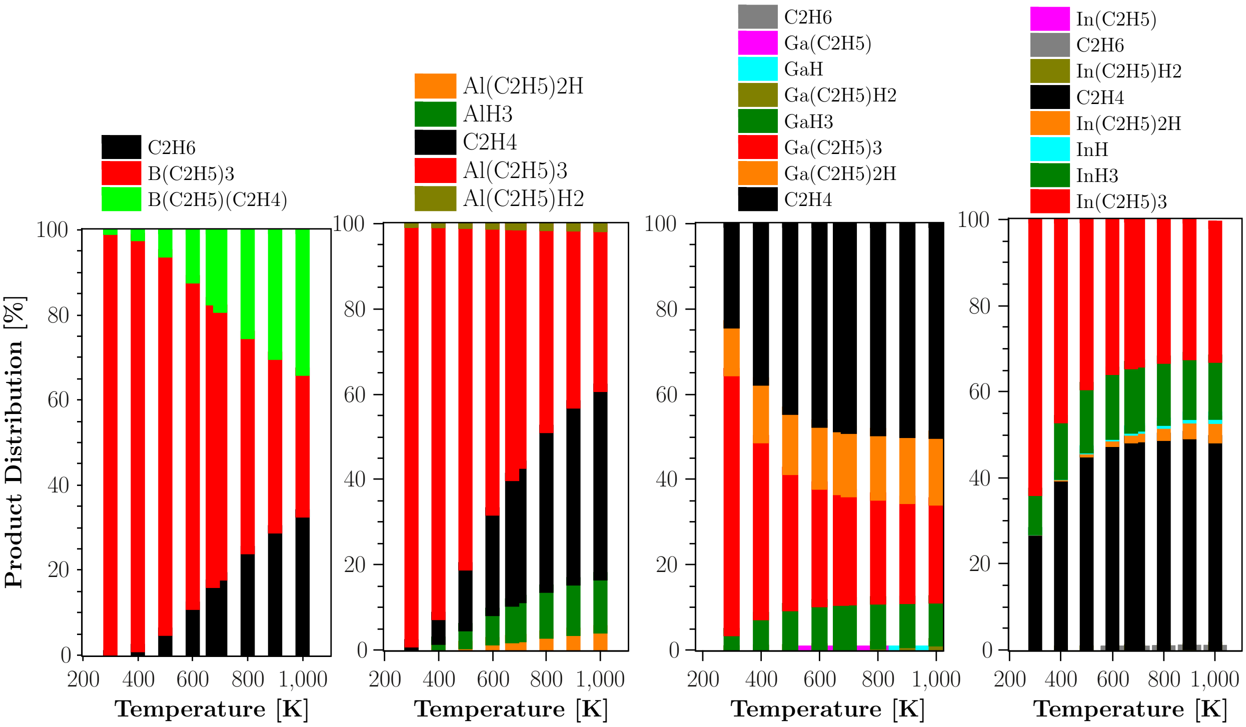

Figure 6.2: Product Distributions for (separated) $M(C_2H_5)_3$ (M = B-In) precursor decompositions from Kinetic Monte Carlo simulations with 100000 iterations at the given temperatures. The PBE-D3-based Gibbs reaction barriers and energies were provided for 673 K and 50 mbar of total pressure, which is the estimated total pressure ($H_2$ atmosphere) in the simulated CVD reactor.

The pressure factor reduces the probability of second (or third, fourth) order processes to occur as the product

$$f_{press} = \frac{\prod_i N_i}{N_{total}} \tag{6.2}$$

is smaller 1. Large relative populations $N_i$ of reactants $i$ lead to increased probabilities of occurrence.

The total pressure of the system, i.e. entire population, is determined by the user's input for the initial population and might change during simulation as species are annihilated or produced.

Preliminary results are presented in Figure 6.2. The equilibrium product distributions of uni- and bimolecular decomposition reactions of group 13 MOVPE precursors $M(C_2H_5)_3$ with M = B, Al, Ga, In in a $H_2$ atmosphere at 50 *mbar* are shown. The simulations were conducted at a temperature range from 200 to 1000 K and over 100000 iterations ensuring equilibrium distributions. The evolution of the original precursor species (red) and the side products with temperature can be followed.

Furthermore, some decomposition pathways become only available for the higher group 13 homologues and/or at higher temperatures. The dominant decomposition products for M = Al, Ga, In are the result of three consecutive β-hydride elimination steps, $MH_3$ (dark green) and the side product $C_2H_4$ (black).

Listing 6.1: Source code of kmc-lists.py

```
#!/usr/bin/python
# by Stegi 2015
# version 15 April 2015

import math
import random
from itertools import groupby
import collections
import sys
#import time # only from python 3.3
import timeit
initialtime = timeit.default_timer()
import datetime
from operator import itemgetter
from collections import Counter

########################
##### READ INPUT FROM FILES #####
########################
from processlibrary import processlibrary as originalprocesslibrary
N_original = len(originalprocesslibrary) # nu of processes
from kmcparameters import initialpopulation
     # the sum of the partial pressures will add up to p_total.

############ INPUT PARAMETERS #######################
from kmcparameters import inputparameters
A_preexp = (inputparameters['temperature']*1.3806*10**(-23) ) / 6.62607*10**(-34)
#A_preexp = inputparameters['A_preexp']
#A_preexp = 1   # in 1/second [1/s]
          # pre-exponential factor for Arrhenius
          # attempt frequency in [1/s] (=collision number*orientationfactor)
          # often given as k_B*T/h*c_0 = 6.25*10**(12) with c_0 = 1
          # weighing also according to p_partials/p_total
          # alternatively: partition sums of eigenmodes in TS and initial state; classical or
              quantum-mechanical
T = inputparameters['temperature']
#T = 700 # int(sys.argv[1]) # in Kelvin [K]
maxiterations = inputparameters['maxiterations']

     # N(least_frequent_species) = maxiterations = p_partial(least_frequent_species) *
          particlesscale
# particlesscale variable is thus dynamic with maxiterations and initial population. If problems
      occur,
# this can be changed to hard values here, e.g. via a particlesscale_default = 1.0
#####################################################


##### constants #####
k_B = float(1.3806488*10**(-23)) # in [m^2kg/s^2K] = [J/K]
N_Avogadro = 6.02214129 * 10**(23)  # this is 1 mol.
R_unigas = k_B * N_Avogadro  # Barriers in kJ/mol
#####################


##########################################
###### DEFINITIONS OF FUNCTIONS TO USE IN MAIN KERNEL #####
#########################################

def dependenycheck(availablespecies): # function takes the processlibrary and the catalogue of
     available species
    possibleprocesses = []
    for process in processlibrary:
        possibleprocesses.append(process) # inititally, all procs are possible
        i = 1
        while i <= 4:  # loop through all necessary educts
            if processlibrary[process]['educt%i' %i] is not '':
```

```
                if ('%s' %processlibrary[process]['educt%i' %i] in availablespecies) == False:
                      # if only one educt is not available, delete proc number from list  of
                           possibleprocesses
                      possibleprocesses.remove(process)
                      # print 'Necessary educt %s was not found and process %s was deleted from
                           possibleprocesses list for this iteration.' %(processlibrary[process
                           ]['educt%i' %i],process)
                      i = 4 # no need to look at the other educts
                else:
                    # print 'Educt %s was found. Process %s stays in.' %(processlibrary[process
                         ]['educt%i' %i],process)
                    pass    # the removal of the educt species happens after the proc was
                         successfull.
            i += 1
    return(possibleprocesses) # function returns the updated list of possible processes


def ratecheckrandom(availableprocesses,possibleprocesses,k_total,current_p_total):
    successfullprocesses = []
    random.shuffle(possibleprocesses) # consider each process in the library, but in shuffled
         chronology. This matters due to the dependencies
    for process in possibleprocesses:
        myrandomnum = random.uniform(0,1)
        pressurefactor = 1.0
        i = 1
        while i <= 4:  # include partial pressures of all necessary educts here.
            if processlibrary[process]['educt%s' %i] is not '':
                pressurefactor = pressurefactor * (float(collections.Counter(availablespecies)[(
                     processlibrary[process]['educt%s' %i])])/current_N_avail) # pressure only
                     represented as ratio between number of species in catalogue
            i += 1
        pressurefactor = pressurefactor * current_p_total/initial_p_total # this changes with
             the total pressure during simulation.
#        print 'current process %s pressurefactor is %s inside ratecheck' %(process,
     pressurefactor)
        rate = A_preexp * pressurefactor * math.exp(-float(processlibrary[process]['
             processbarrier'])*1000/(R_unigas*T))
## backrate needed
 #       print 'rate: %s' %rate
        probability = rate / k_total
        if probability >= myrandomnum:
            successfullprocesses.append(process)
            # print 'process %s with probab %s successful.' %(process,probability)
        else:
            # print 'process %s with probability %s failed the random check against k_i/k_total'
                 %(process,probability)
            pass
    return(successfullprocesses)


def deletetheeducts(successfullprocesses,availablespecies):
    correctedsuccessfullprocesses = successfullprocesses
    random.shuffle(successfullprocesses)  #  this is randomly shuffled. maybe this should also
         be weighed by k_i/k_total
    for process in successfullprocesses:
            i = 1
            while i <= 4:
                if processlibrary[process]['educt%s' %i] is not '':
                    try:
                        availablespecies['%s' %processlibrary[process]['educt%s' %i]]=
                             availablespecies['%s' %processlibrary[process]['educt%s' %i]]-1
                    except KeyError:
                        print 'Probability␣k_i/k_total␣fulfilled,␣but␣educt␣is␣missing.␣Process␣
                             rejected.'
                        correctedsuccessfullprocesses.remove(process)
                        i = 4 # if one educt is missing, process will be rejected. No checks on
                             other educts necessary.
                if processlibrary[process]['product%s' %i] is not '':
                    try:
                        availablespecies['%s' %processlibrary[process]['product%s' %i]]=
                             availablespecies['%s' %processlibrary[process]['product%s' %i]]+1
                    except KeyError:
                        availablespecies['%s' %processlibrary[process]['product%s' %i]] = 1.0
                i += 1
    return(correctedsuccessfullprocesses,availablespecies)
```

```
###########################################
##### SET UP INITIAL DISTRIBUTION OF SPECIES acc to PARTIAL PRESSURES #####
###########################################

print '               --------------------------------------------------------               '
print '-------------- Welcome to the list-based kinetic Monte Carlo simulation --------------'
print '               --------------------------------------------------------               \n'
print '       All processes are independent of each other (Poisson) and independent of     '
print '       any external constraints, e.g. lattices. The states are only comprised of     '
print '       distributions of species in a closed system, e.g. a reactor box. The in-     '
print '       itial population is as follows.                                               \n'
availablespecies = {}
initial_p_total = 0.0
for species in initialpopulation:
    print 'The partialpressure of %s is given as %s bar.' %(species,(float(initialpopulation[
        species])/10**5))
    availablespecies['%s' %species] = float(initialpopulation[species])
    initial_p_total = initial_p_total + float(initialpopulation[species])

particlesscale = maxiterations / availablespecies[min(availablespecies, key=availablespecies.get
    )]
for species in availablespecies:
    availablespecies['%s' %species] = availablespecies['%s' %species] * particlesscale

initial_N_avail  = 0
for species in availablespecies:
    initial_N_avail = initial_N_avail + availablespecies[species]

print '\nInitially, there are %i species in the system. Total pressure: %.4f bar.\n' %(
    initial_N_avail,(initial_p_total/10**5))
# The total numbers here are unphysical. However, the numbers can be interpreted as scales in
    the dimension of mols of particles. The scaling factor is particlescale.


########################################
##### update processlibrary with reverse processes / backrates #####
########################################

processlibrary = originalprocesslibrary
p = 0
while p < N_original:
    processlibrary[N_original+p] = {}
    processlibrary[N_original+p ]['processname'] = 'reverse-%s' %originalprocesslibrary[p]['
        processname']
    processlibrary[N_original+p ]['processbarrier']= '%s' %(float(originalprocesslibrary[p]['
        processbarrier'])-float(originalprocesslibrary[p]['processenergy']))
    processlibrary[N_original+p ]['processenergy']= '%s' %(-float(originalprocesslibrary[p]['
        processenergy']))
    processlibrary[N_original+p ]['educt1']= originalprocesslibrary[p]['product1']
    processlibrary[N_original+p ]['educt2']= originalprocesslibrary[p]['product2']
    processlibrary[N_original+p ]['educt3']= originalprocesslibrary[p]['product3']
    processlibrary[N_original+p ]['educt4']= originalprocesslibrary[p]['product4']
    processlibrary[N_original+p ]['product1']= originalprocesslibrary[p]['educt1']
    processlibrary[N_original+p ]['product2']= originalprocesslibrary[p]['educt2']
    processlibrary[N_original+p ]['product3']= originalprocesslibrary[p]['educt3']
    processlibrary[N_original+p ]['product4']= originalprocesslibrary[p]['educt4']
    p += 1

N_processlibrary = len(processlibrary)
if N_processlibrary == 2*N_original:
    print '       Process library has been extended with reverse processes.'
else:
    print '   Something went wrong with updating the processlibrary.'
#time.sleep(5)


########################################
############ MAIN KERNEL ############
########################################

iter = 0
listofpastevents = [] # global list
simulation_k_total = 0.0
simulation_time_total = 0.0
```

```
while iter < maxiterations:
    ##### one iteration corresponds to a configurational state #####
    currentpossibleprocesses = dependenycheck(availablespecies) # returns a list of process
         numbers. Need the library for everything.
    current_N_avail  = 0
    for species in availablespecies:
        current_N_avail = current_N_avail + availablespecies[species]
    current_p_total = initial_p_total*current_N_avail/initial_N_avail
 #   print '........ New Iteration %s has %s possible processes with fulfilled dependencies in
      the pool.' %(str(iter+1),str(current_N_avail))

    k_total = 0.0
    for process in currentpossibleprocesses: # in shuffled order from dependenycheck
        pressurefactor = 1.0
        i = 1
        while i <= 4:  # include partial pressures of all necessary educts here.
            if processlibrary[process]['educt%s' %i] is not '':
                pressurefactor = pressurefactor *(float(collections.Counter(availablespecies)[(
                     processlibrary[process]['educt%s' %i])])/current_N_avail) # pressure only
                     represented as ratio between number of species in catalogue
            i += 1
        pressurefactor = pressurefactor * current_p_total/initial_p_total # this changes with
             the total pressure during simulation.
#        print 'pressurefactor or process %s out of ratecheck is %s  ' %(process,pressurefactor)
        rate = A_preexp * pressurefactor * math.exp(-float(processlibrary[process]['
             processbarrier'])*1000/(R_unigas*T))
        k_total = k_total + rate # k_total=SUM(rates of all possible processes)

    simulation_k_total = simulation_k_total + k_total # just adding up all k_total's during
         simulation (maxiterations)
##### Poisson processes they all are. #MasterYoda #####
    listofsuccessfullprocesses = ratecheckrandom(availablespecies,currentpossibleprocesses,
         k_total,current_p_total)

##### Time steps: count the time of a successful event only. Weigh against random number. #####
    try:
        ratetemp = A_preexp * math.exp(-float(processlibrary[listofsuccessfullprocesses[0]]['
             processbarrier'])*1000/(R_unigas*T)) # just choose the first entry in the
             listofsuccessfullprocesses, pressurefactor=1 .
        currenttimestep = -1/(ratetemp)*math.log(random.uniform(0,1))
        #  currenttimestep = +1.0/float(ratetemp) # alternative definition
        simulation_time_total += currenttimestep
    except IndexError:
    ## jump iteration in this case without counting the time step.
        # print 'Currently no successful process'
        pass
#    print 'current time step is %.2e [sec].' %currenttimestep

    ##### Here, important updates are done to both lists!!!! # this deletes educts and adds the
         products.
    correctedsuccessfullprocesses,availablespecies = deletetheeducts(listofsuccessfullprocesses,
         availablespecies)

    for process in correctedsuccessfullprocesses:
        listofpastevents.append('%s' %process) # process number enters the list as str.

    iter += 1

#######################################



#################################################################
#####  O U T P U T  #####
#################################################################
print '\n␣␣␣␣␣␣␣␣␣␣—————————————————————————————————————␣␣␣␣␣␣␣␣␣␣'
print '␣␣␣␣␣␣␣␣␣␣␣—————————␣OUTPUT␣SECTION␣—————————————␣␣␣␣␣␣␣␣␣␣␣'
print '␣␣␣␣␣␣␣␣␣␣␣——————————————————————————————————————␣␣␣␣␣␣␣␣␣\n'

print '␣-␣General␣Information␣-␣\n'
print 'Average␣total␣rate␣constant␣k_total␣per␣iteration␣(over␣complete␣simulation)␣was␣%.2e' %(
    simulation_k_total / maxiterations)
print 'The␣pre-exponential␣factor␣for␣all␣rate␣constants␣was␣%.2e␣[1/sec].' %A_preexp
print 'Total␣simulation␣time␣ignoring␣pressurefactors␣␣%.2e␣[sec].' %(simulation_time_total) #
    counting only successful events, no pressurefactor
```

```
print 'Temperature:␣␣␣␣␣␣␣␣␣␣␣␣␣␣␣␣␣␣␣␣␣␣␣%s␣[K].' %T
print 'Initial␣total␣pressure:␣␣␣␣␣␣␣␣␣␣␣␣%s␣[bar].' %(initial_p_total/10**5)
print 'Initial␣number␣of␣species:␣␣␣␣␣␣␣␣␣%.2f␣␣␣␣(%.2e␣particels␣per␣1␣bar␣were␣assumed).' %(
    initial_N_avail,initial_N_avail*initial_p_total)
print 'Total␣pressure␣developed␣from␣%.6f␣to␣%.6f␣[bar]␣during␣simulation.' %((initial_p_total
    /10**5),(current_p_total/10**5))
# print 'The default pressurefactor applied was %s.' %pressurefactordefault

# usually one picks exactly one successfull process per iteration. Here, unlimited are tested
    and allowed to pass.
# Each iteration has a k_total = sum( k_i ). Then, there are no 'left-over processes' as in this
     case;
# i.e. a process was selected, had all dependencies fulfilled, the random number check (against
    k_i/k_total) was satisfied, but in his group/pool of selected processes, the available
# dependencies from past events were already used up by other successfull processes before
    within the iteration.
# Within this group/pool of successfull processes, the chronology of using up the available
    events and deleting them from the storage is shuffled.
#    However, this could (and should???) be weighted by k_i/k_total eventually.

#print '\n %s processes succeded the pressurefactor test, %s were kicked out by it.' %(
    succededpressurefactor,kickedoutbypressurefactor)
#print ' %s processes were used as dependencies.' %len(usedupdependencies)

##### file with all successfull events/processes. Total occurances #####
listofpasteventsfile = open('listofpastevents','w')
for entry in listofpastevents:
    listofpasteventsfile.write('%s\n' %(int(entry))) # in the original chronology, including
        deletions
listofpasteventsfile.close()

##### Total Occurances #####
listofpastevents.sort()
#collections.Counter(listofpastevents).items().sort(key=lambda x: x[0])
print '\n␣-␣Total␣occurances:␣-␣\n'
print '␣%s␣events␣occured␣within␣%s␣iterations.' %(len(listofpastevents), str(iter))
print '␣Warning:␣If␣events/iteration␣>>␣1.0,␣results␣are␣weighed␣randomly␣and␣not␣by␣k_i/k_total
    .'
for event in collections.Counter(listofpastevents).items():
    print '␣␣␣␣␣␣␣␣␣␣␣␣␣␣Event␣'+event[0]+'␣occured␣'+str(event[1])+'␣times␣in␣total.␣␣␣␣␣␣␣Name
        :␣%s' %processlibrary[int(event[0])]['processname']

##### Product distribution. Remaining available species #####
print '\n␣-␣Final␣Product␣Distribution:␣-␣\n'
totalproducts = 0
productspecies = 0
for productkey in collections.Counter(availablespecies):
    if productkey is not '':
        totalproducts += int(collections.Counter(availablespecies)[productkey])
        productspecies += 1
print '␣␣␣␣␣␣␣Species␣␣␣␣␣␣␣␣␣␣␣␣␣␣␣␣␣␣:␣␣␣␣␣Quantity␣␣␣␣:␣␣fraction␣of␣all␣products␣[%]␣'
print '-------------------------------------------------------------'
oldfraction = 0.0
SAD = 0
for productkey in collections.Counter(availablespecies):
    if productkey is not '':
        print '␣␣␣␣␣%s␣␣:␣␣␣%s␣␣:␣␣%.4f␣␣' %(productkey.ljust(25), str(collections.Counter(
            availablespecies)[productkey]).rjust(12), collections.Counter(availablespecies)[
            productkey]*100/float(totalproducts) )
        fraction = collections.Counter(availablespecies)[productkey] / float(totalproducts)
        SAD = SAD + abs( oldfraction - fraction )
        oldfraction = fraction
print '\n␣␣␣␣Total␣number␣of␣remaining␣species:␣%s␣' %totalproducts
print '␣␣␣␣Total:␣%s␣different␣species␣remain.' %productspecies
print '␣␣␣␣The␣sum␣of␣absolute␣differences␣(SAD)␣between␣product␣fractions␣of␣this␣simulation␣is
    ␣%.4f␣.' %(SAD)
print '␣␣␣␣(The␣lower␣this␣value,␣the␣more␣homogeneous␣is␣the␣distribution␣of␣products.)'
print '␣␣␣␣SAD␣/␣number␣of␣different␣products␣=␣%.4f␣.' %(SAD/productspecies)

##### Technicalities #####
print '\n␣-␣Technicalities␣-\n'
# print 'Sum of system and user CPU time: %s [sec]' %time.process_time() #from python 3.3
finaltime = timeit.default_timer()
print 'Wallclock␣time:␣%.1f␣[sec]' %(finaltime-initialtime)
print 'Date:␣␣␣␣␣␣␣␣␣␣␣%s␣␣' %datetime.datetime.now()
```

# Curriculum Vitae

## Education

| | | |
|---|---|---|
| 2007 | Abitur | Otto-Hahn Schule, Hanau |
| 2010 | B.Sc Chemistry | Goethe Universität, Frankfurt am Main |
| 2011 | M.Phil Chemistry | University of Cambridge |
| 2015 | Dr. rer. nat. (prospective) | Universität, Marburg |

## Awards and Scholarships

| | |
|---|---|
| 2007 | Cork Award (best graduand in sciences), Otto-Hahn Schule |
| 2008 | Scholarship Hessen state (tuition fees), Goethe-Universität |
| 2009 | Scholarship Studienstiftung des deutschen Volkes e.V. |
| 2010 | Dr. Albert Hloch Preis (group of best graduands), Goethe-Universität |
| 2010-11 | Scholarship Studienstiftung des deutschen Volkes e.V. (full, M.Phil) |
| 2012-15 | Scholarship (full, PhD) Beilstein-Institut, Frankfurt am Main. |

## Selected Talks

| | | |
|---|---|---|
| 10/2013 | Computational Surface Chemistry | HLRS, Stuttgart |
| 05/2014 | Growth Chemistry of Galliumphosphide epitaxially Grown on Si(001) | CECAM ETSF Meeting, Rome |
| 01/2015 | Gas Phase Decomposition Chemistry & Growth Effects in III/V Semiconductor MOVPE | CTPC Seminar, Auckland |

# Bibliography

[1] G. E. Moore, *Proceedings of the IEEE*, 1998, **86**, 82–85.

[2] J. A. del Alamo, *Nature*, 2011, **479**, 317–323.

[3] D. A. R. Barkhouse, O. Gunawan, T. Gokmen, T. K. Todorov and D. B. Mitzi, *Progress in Photovoltaics: Research and Applications*, 2012, **20**, 6–11.

[4] D. Liang and J. E. Bowers, *Nature Photonics*, 2010, **4**, 511–517.

[5] N. Koukourakis, C. Bückers, D. A. Funke, N. C. Gerhardt, S. Liebich, S. Chatterjee, C. Lange, M. Zimprich, K. Volz, W. Stolz, B. Kunert, S. W. Koch and M. R. Hofmann, *Applied Physics Letters*, 2012, **100**, 092107.

[6] M. Fuechsle, J. A. Miwa, S. Mahapatra, H. Ryu, S. Lee, O. Warschkow, L. C. L. Hollenberg, G. Klimeck and M. Y. Simmons, *Nature Nanotechnology*, 2012, **7**, 242–246.

[7] B. Kunert, K. Volz and W. Stolz, *Physica Status Solidi (B)*, 2007, **244**, 2730–2739.

[8] I. Vurgaftman and J. R. Meyer, *Journal of Applied Physics*, 2003, **94**, 3675–3696.

[9] C. Lange, S. Chatterjee, B. Kunert, K. Volz, W. Stolz, W. W. Rühle, N. C. Gerhardt and M. R. Hofmann, *Physica Status Solidi (C)*, 2009, **6**, 576–578.

[10] D. E. Aspnes and A. A. Studna, *Physical Review B*, 1983, **27**, 985–1009.

[11] P. J. Dean, G. Kaminsky and R. B. Zetterstrom, *Journal of Applied Physics*, 1967, **38**, 3551–3556.

[12] J. Barrau, T. Amand, M. Brousseau, R. J. Simes and L. Goldstein, *Journal of Applied Physics*, 1992, **71**, 5768.

[13] H. Carrère and X. Marie, in *Semiconductor Modeling Techniques*, ed. N. Balkan and M. Xavier, Springer Berlin Heidelberg, Berlin, Heidelberg, 2012, vol. 159, ch. 6, pp. 153–195.

[14] M. Silver and E. O'Reilly, *IEEE Journal of Quantum Electronics*, 1994, **30**, 547–533.

[15] A. Wilk, M. Gazouli, M. E. Skouri, P. Christol, P. Grech, A. N. Baranov and A. Joullié, *Applied Physics Letters*, 2000, **77**, 2298.

[16] J. Matthews and A. Blakeslee, *Journal of Crystal Growth*, 1974, **27**, 118–125.

[17] A. Beyer, I. Nemeth, S. Liebich, J. Ohlmann, W. Stolz and K. Volz, *Journal of Applied Physics*, 2011, **109**, 083529.

[18] E. Yablonovitch and E. Kane, *Journal of Lightwave Technology*, 1988, **6**, 1292–1299.

[19] Q. Dai, Q. Shan, J. Wang, S. Chhajed, J. Cho, E. F. Schubert, M. H. Crawford, D. D. Koleske, M. H. Kim and Y. Park, *Applied Physics Letters*, 2010, **97**, 133507.

[20] N. Hossain, S. R. Jin, S. Liebich, M. Zimprich, K. Volz, B. Kunert, W. Stolz and S. J. Sweeney, *Applied Physics Letters*, 2012, **101**, 011107.

[21] N. Hossain, S. J. Sweeney, S. Rogowsky, R. Ostendorf, J. Wagner, S. Liebich, M. Zimprich, K. Volz, B. Kunert and W. Stolz, *Electronics Letters*, 2011, **47**, 931.

[22] S. J. Sweeney, A. F. Phillips, A. R. Adams, E. P. O'Reilly and P. J. A. Thijs, *IEEE Photonics Technology Letters*, 1998, **10**, 1076–1078.

[23] T. Katoda and M. Kishi, *Journal of Electronic Materials*, 1980, **9**, 783–796.

[24] L. Desplanque, S. El Kazzi, C. Coinon, S. Ziegler, B. Kunert, a. Beyer, K. Volz, W. Stolz, Y. Wang, P. Ruterana and X. Wallart, *Applied Physics Letters*, 2012, **101**, 142111.

[25] K. Jandieri, M. K. Shakfa, S. Liebich, M. Zimprich, B. Kunert, C. Karcher, a. Chernikov, K. Volz, W. Stolz, M. Koch, S. Chatterjee, W. Heimbrodt, F. Gebhard and S. D. Baranovskii, *Physical Review B*, 2012, **86**, 125318.

[26] M. G. A. Bernard and G. Duraffourg, *Physica Status Solidi (B)*, 1961, **1**, 699–703.

[27] I. Nemeth, B. Kunert, W. Stolz, K. Volz and I. Németh, *Journal of Crystal Growth*, 2008, **310**, 1595–1601.

[28] P. Speier, *Microelectronic Engineering*, 1992, **18**, 1–31.

[29] K. Volz, A. Beyer, W. Witte, J. Ohlmann, I. Németh, B. Kunert and W. Stolz, *Journal of Crystal Growth*, 2011, **315**, 37–47.

[30] M. D. Dickey, R. C. Chiechi, R. J. Larsen, E. A. Weiss, D. A. Weitz and G. M. Whitesides, *Advanced Functional Materials*, 2008, **18**, 1097–1104.

[31] A. Mabbitt, *Journal of Materials Science*, 1970, **5**, 1043–1046.

[32] G. B. Stringfellow, *Organometallic Vapor-Phase Epitaxy: Theory and Practice*, Elsevier, 2012, pp. 80–83.

[33] A. S. Jordan, A. R. Von Neida, R. Caruso and C. K. Kim, *Journal of The Electrochemical Society*, 1974, **121**, 153.

[34] C. K. Gan, Y. P. Feng and D. J. Srolovitz, *Physical Review B*, 2006, **73**, 1–8.

[35] K. Volz, J. Koch, F. Höhnsdorf, B. Kunert and W. Stolz, *Journal of Crystal Growth*, 2009, **311**, 2418–2426.

[36] N. Waki, T. Nakano, M. Sugiyma, Y. Nakano and Y. Shimogaki, *Thin Solid Films*, 2006, **498**, 163–166.

[37] K. F. Jensen and D. I. Fotiadis, *Journal of Crystal Growth*, 1991, **107**, 1–11.

[38] M. Tirtowidjojo and R. Pollard, *Journal of Crystal Growth*, 1988, **93**, 108–114.

[39] R. A. Talalaev, E. V. Yakovlev and S. Y. Karpov, *Journal of Crystal Growth*, 2001, **230**, 232–238.

[40] P. Kratzer and M. Scheffler, *Computing in Science & Engineering*, 2001, **3**, 16–25.

[41] A. Brauers, *Journal of Crystal Growth*, 1991, **107**, 281–289.

[42] N. Bahlawane, F. Reilmann, L.-C. Salameh and K. Kohse-Höinghaus, *Journal of the American Society for Mass Spectrometry*, 2008, **19**, 947–54.

[43] A. Devi, *Coordination Chemistry Reviews*, 2013, **257**, 3332–3384.

[44] D. J. Emslie, P. Chadha and J. S. Price, *Coordination Chemistry Reviews*, 2013, **257**, 3282–3296.

[45] T. Hatanpää, M. Ritala and M. Leskelä, *Coordination Chemistry Reviews*, 2013, **257**, 3297–3322.

[46] M. von Hopffgarten and G. Frenking, *Wiley Interdisciplinary Reviews: Computational Molecular Science*, 2011, **2**, 43–62.

[47] J. H. Jensen, K. Morokuma and M. S. Gordon, *The Journal of Chemical Physics*, 1994, **100**, 1981.

[48] M. Weyers, *Journal of Crystal Growth*, 1991, **115**, 469–473.

[49] B. Kunert, K. Volz, J. Koch and W. Stolz, *Journal of Crystal Growth*, 2007, **298**, 121–125.

[50] K. Wong, B. McBurnett, R. Culp, a.H. Cowley and J. Ekerdt, *Surface Science*, 1998, **416**, 480–487.

[51] G. Fan, R. Hoare, M. Pemble, I. Povey, A. Taylor, J. O. Williams and A. Taylor, *Journal of Crystal Growth*, 1992, **124**, 49–55.

[52] N. Roberts and R. Needs, *Surface Science*, 1990, **236**, 112–121.

[53] D. Chadi, *Physical Review Letters*, 1979, **43**, 43–47.

[54] T. Sakamoto, T. Kawamura and G. Hashiguchi, *Applied Physics Letters*, 1986, **48**, 1612–1614.

[55] S. M. Mokler, W. Liu and B. Joyce, *Journal of Vacuum Science & Technology A: Vacuum, Surfaces, and Films*, 1992, **10**, 1846.

[56] W. G. Schmidt, S. Mirbt and F. Bechstedt, *Physical Review B - Condensed Matter and Materials Physics*, 2000, **62**, 8087–8091.

[57] H. Simka, B. G. B. Willis, I. Lengyel, K. F. Jensen, G. Britain, C. Engineering and M. Avenue, *Progress in Crystal Growth and Characterization of Materials*, 1997, **35**, 117–149.

[58] P. Kratzer, *Applied Surface Science*, 2003, **216**, 436–446.

[59] M. Rosini, R. Magri and P. Kratzer, *Physical Review B*, 2008, **77**, 1–11.

[60] U. Höfer, L. Li and T. Heinz, *Physical Review B*, 1992, **45**, 9485–9488.

[61] P. Bratu, W. Brenig, A. Groß, M. Hartmann, U. Höfer, P. Kratzer and R. Russ, *Physical Review B*, 1996, **54**, 5978–5991.

[62] J. M. Heitzinger, M. S. Jackson and J. G. Ekerdt, *Applied Physics Letters*, 1995, **66**, 352.

[63] I. Buchan and M. L. Yu, *Surface Science*, 1993, **280**, 383–92.

[64] A. Stegmüller, P. Rosenow and R. Tonner, *Physical Chemistry Chemical Physics*, 2014, **16**, 17018–17029.

[65] Y. Fukuda, T. Kobayashi and S. Mochizuki, *Applied Surface Science*, 2001, **176**, 218–222.

[66] J.-M. Lin and A. V. Teplyakov, *Theoretical Chemistry Accounts*, 2013, **132**, 1404.

[67] M. A. Filler and S. F. Bent, *Progress in Surface Science*, 2003, **73**, 1–56.

[68] H. Wilson, O. Warschkow, N. Marks, S. Schofield, N. Curson, P. Smith, M. Radny, D. McKenzie and M. Simmons, *Physical Review Letters*, 2004, **93**, 226102.

[69] H. Wilson, O. Warschkow, N. Marks, N. Curson, S. Schofield, T. Reusch, M. Radny, P. Smith, D. McKenzie and M. Simmons, *Physical Review B*, 2006, **74**, 195310.

[70] Y. Sun, D. C. Law and R. F. Hicks, *Surface Science*, 2003, **540**, 12–22.

[71] V. Narayanan, S. Mahajan, N. Sukidi, K. J. Bachmann, V. Woods and N. Dietz, *Philosophical Magazine A*, 2000, **80**, 555–572.

[72] M. Dürr, A. Biedermann, Z. Hu, U. Höfer and T. F. Heinz, *Science*, 2002, **296**, 1838–41.

[73] A. Aquino, *Applied surface science*, 1996, **105**, 304–311.

[74] G. Kaneda, N. Sanada and Y. Fukuda, *Applied Surface Science*, 1999, **142**, 1–6.

[75] C. Schwalb, M. Dürr and U. Höfer, *Physical Review B*, 2009, **80**, 085317.

[76] J. Wieferink, P. Krüger and J. Pollmann, *Physical Review B*, 2010, **82**, 1–11.

[77] G. Brocks, P. Kelly and R. Car, *Physical Review Letters*, 1991, **66**, 1729–1732.

[78] G. Brocks, P. Kelly and R. Car, *Surface Science*, 1992, **269-270**, 860–866.

[79] J. M. Bennett, O. Warschkow, N. A. Marks and D. R. McKenzie, *Physical Review B - Condensed Matter and Materials Physics*, 2009, **79**, 1–9.

[80] E. Kalered, H. Pedersen, E. Janzén and L. Ojamäe, *Theoretical Chemistry Accounts*, 2013, **132**, 1403.

[81] M. V. Lebedev, *Semiconductors*, 2011, **45**, 1519–1523.

[82] E. Penev, P. Kratzer and M. Scheffler, *Journal of Chemical Physics*, 1999, **110**, 3986.

[83] D. F. Tracey, B. Delley, D. R. McKenzie and O. Warschkow, *AIP Advances*, 2013, **3**, 042117.

[84] H. Vehkamäki, *Classical Nucleation Theory in Multicomponent Systems*, Springer Verlag, Berlin/Heidelberg, 2006, pp. 1–8.

[85] J. J. D. Yoreo and P. G. Vekilov, in *Classical Nucleation Theory in Multicomponent Systems*, ed. H. Vehkamäki, Springer Verlag, Berlin/Heidelberg, 2006, pp. 57–93.

[86] J. W. P. Schmelzer, *Nucleation theory and applications*, Wiley Online Library, Weinheim, 2005.

[87] J. Neugebauer, T. K. Zywietz, M. Scheffler, J. E. Northrup, H. Chen and R. M. Feenstra, *Physical Review Letters*, 2003, **90**, 056101.

[88] C. Ratsch and J. A. Venables, *Journal of Vacuum Science & Technology A: Vacuum, Surfaces, and Films*, 2003, **21**, S96.

[89] K. Werner, a. Beyer, J. Oelerich, S. Baranovskii, W. Stolz and K. Volz, *Journal of Crystal Growth*, 2014, **405**, 102–109.

[90] O. Romanyuk, T. Hannappel and F. Grosse, *Physical Review B*, 2013, **88**, 115312.

[91] P. Kratzer, E. Penev and M. Scheffler, *Applied Physics A: Materials Science & Processing*, 2002, **75**, 79–88.

[92] J. T. Tanskanen, J. R. Bakke, S. F. Bent and T. A. Pakkanen, *Langmuir*, 2010, **26**, 11899–11906.

[93] K. Gaul, *Bachelor of Science Thesis*, Philipps-University Marburg, 2014.

[94] R. P. Stoffel, C. Wessel, M.-W. Lumey and R. Dronskowski, *Angewandte Chemie (International ed. in English)*, 2010, **49**, 5242–5266.

[95] R. Dronskowski, *Computational Chemistry of Solid State*, Wiley-VCH Verlag GmbH & Co KGaA, Weinheim, 1st edn., 2005.

[96] A. Beyer, A. Stegmüller, J. O. Oelerich, K. Jandieri, K. Werner, W. Stolz, S. D. Baranovskii, R. Tonner and K. Volz, *submitted*, 2015.

[97] E. Schrödinger, *Annalen der Physik*, 1926, **79**, 498–527.

[98] A. Szabo and N. S. Ostlund, *Modern Quantum Chemistry: Introduction to Advanced Electronic Structure Theory*, McGraw-Hill, New York, 1989.

[99] N. Straumann, *arXiv:quant-ph*, 2008, **0403199v2**, 1–27.

[100] P. Löwdin, *Physical Review*, 1955, **97**, 1509–1520.

[101] J. Cizek, *Journal of Chemical Physics*, 1966, **45**, 4256.

[102] C. Mø ller and M. S. Plesset, *Physical Review*, 1934, **46**, 618–622.

[103] P. Hohenberg and W. Kohn, *Physical Review*, 1964, **136**, B864.

[104] W. Kohn and L. Sham, *Physical Review*, 1965, **140**, 1133–1138.

[105] L. H. Thomas, *Mathematical Proceedings of the Cambridge Philosophical Society*, 1927, **23**, 542–548.

[106] E. Fermi, *Zeitschrift der Physik*, 1928, **48**, 73–79.

[107] R. Stowasser and R. Hoffmann, *Journal of the American Chemical Society*, 1999, **121**, 3414–3420.

[108] D. P. Chong, O. V. Gritsenko and E. J. Baerends, *Journal of Chemical Physics*, 2002, **116**, 1760–1772.

[109] J. Slater, *Physical Review*, 1951, **81**, 385–390.

[110] J. P. Perdew, *Physical Review B*, 1986, **33**, 8822–8824.

[111] A. Becke, *Physical Review A*, 1988, **38**, 3098–3100.

[112] J. P. Perdew, K. Burke and M. Ernzerhof, *Physical Review Letters*, 1996, **77**, 3865–3868.

[113] J. P. Perdew, K. Burke and M. Ernzerhof, *Physical Review Letters*, 1997, **78**, 1396.

[114] P. V. Smith, M. W. Radny and G. A. Shah, *Journal of Computational Chemistry*, 2014, **35**, 1248–1254.

[115] J. E. Jones, *Proceedings of the Royal Society A: Mathematical, Physical and Engineering Sciences*, 1924, **106**, 463–477.

[116] R. Eisenschitz and F. London, *Zeitschrift für Physik*, 1930, **60**, 491–527.

[117] S. Grimme, *Wiley Interdisciplinary Reviews: Computational Molecular Science*, 2011, **1**, 211–228.

[118] S. Grimme and M. Steinmetz, *Physical Chemistry Chemical Physics*, 2013, **15**, 16031–16042.

[119] J. Möllmann and S. Grimme, *Physical Chemistry Chemical Physics*, 2010, **12**, 8500–8504.

[120] H. Ibach and H. Lüth, *Solid State Physics - An Introduction to Principles of Materials Science*, Springer Science & Business Media, Berlin, Heidelberg, 2003.

[121] F. Bloch, *Zeitschrift für Physik A*, 1929, 555–600.

[122] J. D. Pack and H. J. Monkhorst, *Physical Review B*, 1977, **16**, 1748–1749.

[123] G. Kresse and J. Furthmüller, *Physical Review B - Condensed Matter and Materials Physics Condensed Matter*, 1996, **54**, 11169–11186.

[124] J. Hafner, *Journal of Computational Chemistry*, 2008, **29**, 2044–2078.

[125] H. Hellmann, *Einführung in die Quantenchemie*, Verlag Franz Deuticke, Leipzig, Wien, 1937.

[126] H. Hellmann, *Acta Physicochimica U.R.S.S.*, 1934, **1**, 913–940.

[127] H. Hellmann, *Acta Physicochimica U.R.S.S.*, 1936, **4**, 225–244.

[128] H. Hellmann, *The Journal of Chemical Physics*, 1935, **3**, 61.

[129] J. Slater, *Physical Review*, 1937, **51**, 846.

[130] T. Loucks, *Augmented plane wave method a guide to performing electronic structure calculations*, Publisher W.A. Benjamin, New York, 1967.

[131] P. Blöchl, *Physical Review B*, 1994, **50**, 17953–17979.

[132] K. Reuter, D. Frenkel and M. Scheffler, *Physical Review Letters*, 2004, **93**, 1–4.

[133] K. Reuter, in *Modeling Heterogeneous Catalytic Reactions: From the Molecular Process to the Technical System*, ed. O. Deutschmann, Wiley-VCH, Weinberg, 2009, ch. 3, p. 72ff.

[134] A. F. Voter, in *Radiation Effects in Solids*, ed. K. Sickafus, Springer, 2007, pp. 1–23.

[135] A. Bortz, M. Kalos and J. Lebowitz, *Journal of Computational Physics*, 1975, **17**, 10–18.

[136] J. Amar, *Computing in Science & Engineering*, 2006, **8**, 9–19.

[137] A. Chatterjee and D. G. Vlachos, *Journal of Computer-Aided Materials Design*, 2007, **14**, 253–308.

[138] A. Stegmüller and R. Tonner, *Inorganic Chemistry*, 2015, **DOI: 10.1021/acs.inorgchem.5b00687**,.

[139] A. Stegmüller and R. Tonner, *Chemical Vapor Deposition*, 2015, **submitted**,.

[140] A. Stegmüller and R. Tonner, *manuscript in preparation*, 2015.

[141] K. C. Wong, M. T. McEllistrem, B. G. Mcburnett, R. D. Culp, A. H. Cowley and J. G. Ekerdt, *Surface Science*, 1998, **396**, 260–265.

[142] Y. S. Won, J. Lee, C. S. Kim and S.-S. Park, *Surface Science*, 2009, **603**, L31–L34.

[143] C. Mui, J. H. Han, G. T. Wang, C. B. Musgrave and S. F. Bent, *Journal of the American Chemical Society*, 2002, **124**, 4027–4038.

[144] S. F. Bent, J. S. Kachian, J. C. F. Rodríguez-Reyes and A. V. Teplyakov, *Proceedings of the National Academy of Sciences of the United States of America*, 2011, **108**, 956–960.

[145] P. W. Loscutoff and S. F. Bent, *Annual Review of Physical Chemistry*, 2006, **57**, 467–495.

[146] P. Rosenow, *Theoretische Untersuchungen zur Adsorption von GaP-Vorläufern auf der Si(001)-Oberfläche*, Philipps-Universität, Marburg, 2012.

[147] J. P. Perdew, *Physical Review B*, 1986, **34**, 7406.

[148] S. Grimme, S. Ehrlich and L. Goerigk, *Journal of Computational Chemistry*, 2011, **32**, 1456–1465.

[149] G. Kresse and D. Joubert, *Physical Review B*, 1999, **59**, 11–19.

[150] P. Xiao, D. Sheppard, J. Rogal and G. Henkelman, *The Journal of Chemical Physics*, 2014, **140**, 174104.

[151] *TURBOMOLE v6.3.1, a development of University of Karlsruhe and Forschungszentrum Karlsruhe GmbH, 1989-2015, TURBOMOLE GmbH, since 2007; available from* `http://www.turbomole.com`.

[152] G. Henkelman and H. Jonsson, *The Journal of Chemical Physics*, 2001, **115**, 9657.

[153] E. Antoshchenkova, M. Hayoun, F. Finocchi and G. Geneste, *Surface Science*, 2011, **606**, 605–614.

[154] D. T. Gillespie, *Journal of Computational Physics*, 1976, **22**, 403–434.

# Danksagung

Zuerst möchte ich Ralf Tonner danken, der die Durchführung der beschriebenen Projekte und das Verfassen dieser Dissertation vorbildlich begleitet hat.
Allen Mitgliedern und Studenten der Abteilung Theoretische Chemie an der Universität Marburg möchte ich für die angenehme und produktive Atmosphäre danken. Journal Club, Coffee and Cake und St. Pauli Principle sind wichtige Institutionen! Besonders hervorheben möchte ich Marc Raupach, Diego M. Andrada, Josua Pecher, Markus Hermann und Phil Rosenow, die wesentlich dazu beigetragen haben, dieses Projekt zu beginnen und zu Ende zu führen. Ohne Reuti und Andrea wäre vieles nicht möglich gewesen.

Ich möchte mich beim Beilstein Institut Frankfurt am Main bedanken, das mir mit einem Promotionsstipendium die notwendige finanzielle Unterstützung bereitgestellt hat, um sowohl die Forschungsarbeit als auch das Verfassen dieser Schrift durchzuführen. Ferner haben die beiden DFG Programme GRK 1782 und SFB 1083 die notwendige Infrastruktur geschaffen, um sich effizient und interdisziplinär mit anderen Wissenschaftler auszutauschen und gemeinsame Projekte durchzuführen.
Ich möchte diesbezüglich Andreas Beyer, Jan-Oliver Oelerich, Katharina Werner, Kerstin Volz, Gregor Witte, Marcel Reutzel und Wolfgang Stolz für ertragreiche Zusammenarbeit danken. Konstantin Gaul and Bernhard Leube haben diese Arbeit unterstützt, indem sie Berechnungen zu Vorläuferzerfällen durchgeführt haben.

Schließlich möchte ich mich bei Peter Schwerdtfeger bedanken, der mir es ermöglicht hat, am Centre for Theoretical Chemistry and Physics at Massey University wertvolle Zeit zu verbringen. Vielen Dank an Peter Albers für unermüdliche und treue Begleitung im Geiste.

Vielen Dank, Josua Pecher, Paul Jerabek, Diego M. Andrada, Marc Raupach und Wolfgang Stolz, für das Korrekturlesen von Teilen dieses Manuskripts. Katharina Werner und Phil Rosenow haben Abbildungsvorlagen bereitgestellt. Meinem Freund Basti Reichhold danke ich für das Anfertigen der großen Übersichtsgraphik.
Zum Schluß gebührt meiner Familie und meinen Freunden größter Dank, die während der Fertigstellung dieses Manuskripts viel Geduld bewiesen und mich unschätzbar unterstützt haben.

PCCP

PAPER

View Article Online
View Journal

Cite this: DOI: 10.1039/c4cp01584c

# A quantum chemical study on gas phase decomposition pathways of triethylgallane (TEG, $Ga(C_2H_5)_3$) and *tert*-butylphosphine (TBP, $PH_2(t\text{-}C_4H_9)$) under MOVPE conditions†

Andreas Stegmüller, Phil Rosenow and Ralf Tonner*

Received 11th April 2014,
Accepted 24th June 2014

DOI: 10.1039/c4cp01584c

www.rsc.org/pccp

The gas phase decomposition reactions of precursor molecules relevant for metal–organic vapour phase epitaxy (MOVPE) of semiconductor thin films are investigated by computational methods on the density-functional level as well as on the *ab initio* (MP2, CCSD(T)) level. A comprehensive reaction catalogue of uni- and bimolecular reactions is presented for triethylgallium (TEG) as well as for *tert*-butylphosphine (TBP) containing thermodynamic data together with transition state energies. From these energies it can be concluded that TEG is decomposed in the gas phase under MOVPE conditions ($T$ = 400–675 °C, $p$ = 0.05 atm) to $GaH_3$ *via* a series of β-hydride elimination reactions. For elevated temperatures, further decomposition to GaH is thermodynamically accessible. In the case of TBP, the original precursor molecule will be most abundant since all reaction channels exhibit either large barriers or unfavorable thermodynamics. Dispersion-corrected density functional calculations (PBE-D3) provide an accurate description of the reactions investigated in comparison to high level CCSD(T) calculations serving as benchmark values.

## 1. Introduction

Semiconductor materials composed of group 13 and group 15 elements (aka. III/V materials) grown on silicon surfaces have potential applications as highly efficient solar cells and lasers.[1] "Silicon photonics" aims at the combination of optical data processes with Si-based microelectronics technology, but is hampered by the indirect band gap of silicon and thus optically active overlayers have to be formed.[2] These materials are often deposited onto silicon substrates by a vapor phase epitaxy procedure from metal–organic precursor molecules (MOVPE). In order to tune the materials towards direct optical gaps, metastable quaternary group III/V materials were developed which exhibit lattice constants close to the Si bulk value.[3] However, these materials can be grown quasi-epitaxially on Si(001) applying a 40–50 nm buffer layer of GaP.[4,5] The quality of the III/V material's optoelectronic properties is highly dependent on the structural quality of the GaP nucleation layer which goes hand in hand with the cleanliness of the Si substrate surface, choice and purity of the precursors and the specific suitability of the applied growth conditions.[6] Crystal defects can be propagated by mechanical strain caused by the heterolayers' lattice mismatch to silicon or different thermal expansion coefficients. On the other hand, non-ideal reactor conditions lead to incomplete precursor decomposition and undesirable doping defects, *e.g.* carbon incorporation.[7] It is the declared goal of material scientists to minimize these defects during growth of promising III/V materials. Therefore, a detailed understanding of the chemical processes within the reactor is crucial and computational studies are used to complement experimental findings.[9–12] It is, for instance, difficult to obtain reaction-specific barriers from experiment (*e.g.* mass spectrometry) as the appearance of detected species can only be related to the overall temperature and reaction (growth) rate.[8,12,16]

One frequently applied precursor in the growth of III/V materials is trimethylgallane ($Ga(CH_3)_3$, TMG), which has a lower decomposition rate than triethylgallane ($Ga(C_2H_5)_3$, TEG) and pyrolyzes only at high temperatures (above 480 °C)[16] in the gas phase. Surface-assisted decomposition mechanisms, on the other hand, exhibit significantly lower barriers (<130 °C).[14] However, there is an increased tendency for carbon incorporation, because reactive and therefore uncontrollable radical species are formed from TMG, *e.g.* dimethylgallane and methyl radicals, which remain strongly bound to the Si surface.[12,14] By introducing ligands larger than methyl, decomposition temperatures (thermal barriers) were found to decrease: tri-*tert*-butylgallane, *e.g.*, undergoes clean decomposition *via* β-hydride elimination already at 260 °C (low barrier of 160 kJ $mol^{-1}$)[15]

---

*Fachbereich Chemie and Materials Sciences Center, Philipps-Universität Marburg, Hans-Meerwein-Strasse, 35032 Marburg, Germany.*
*E-mail: tonner@chemie.uni-marburg.de*

† Electronic supplementary information (ESI) available. See DOI: 10.1039/c4cp01584c

without carbon incorporation.[16] It has been found that this problem can be circumvented by using TEG as an epitaxy precursor, which delivers GaN layers with high intensity photoluminescence and higher electron mobility than those grown with TMG.[17] Some pathways for TEG were investigated previously but no barriers were reported.[13,15] Low-barrier β-hydride elimination seems to play a major role in successful growth procedures and precursors with larger ligands were addressed by experimental and theoretical studies.[15,16,18]

As a common source for group 15 elements *tert*-butylarsine ($AsH_2(t\text{-}C_4H_9)$ TBA) and *tert*-butylphosphine ($PH_2(t\text{-}C_4H_9)$, TBP)[19a] are used as MOVPE precursors. Some decomposition pathways for TBP were computed in an early computational study on the HF level,[19b] supporting the suggestion of breaking of the phosphorous–carbon bond in the initial step.[19c] A concise examination of decomposition pathways of TBP including barriers is not yet available. TEG and TBP fulfill general requirements for MOVPE precursor molecules such as lowered toxicity, suitable lab handling characteristics and, as investigated in this study, well-defined chemical stability.[9]

We want to briefly outline the experimental setup to set the stage for the computational investigations.[20] The original precursors are flushed into the reaction chamber in a hydrogen gas stream at 0.05 atm total pressure. TEG and TBP are kept separated in the gas phase by alternating the precursor flushes with pure hydrogen flushes, which rinse the reaction chamber. This procedure is referred to as flow-rate modulated epitaxy (FME) and was found to produce GaP layers of very high quality.[20] Hence, stable donor–acceptor complexes or oligomers of group 13 and 15 species, which have been extensively revised by Timoshkin and others,[21–25] will presumably not be of major importance for the decomposition. The partial pressures of Ga and P precursors are very low so that the formation of elemental Ga or P clusters[26,27] can be neglected.

The aim of this study is now to investigate a comprehensive reaction catalogue for the important MOVPE precursors TEG and TBP in the hydrogen gas atmosphere[28] *via* accurate computations on the DFT and *ab initio* level providing thermodynamic energies and barriers. To this end, 61 elementary reactions and reaction barriers for a rationally chosen subset of those were calculated on the MP2 and PBE-D3 levels of approximation and checked against benchmark calculations on the CCSD(T) level. The presented decomposition catalogue covers four mechanism classes (homolytical bond cleavage, β-hydrogen decomposition, $H_2$ and alkane elimination reactions) for unimolecular reactions and three classes (radical recombination, $H_2$ and alkane elimination reactions) for bimolecular reactions with several reactants. Primarily, this study aims at revealing the resulting decomposition products from the gas phase. Secondly, it presents the chemical mechanisms of the most prominent decomposition classes, showing thermodynamic and kinetic trends for those reactions under experimental conditions. Thirdly, the accurate benchmark data allow an error estimation for production type DFT calculations. This will help both experimental and theoretical scientists to understand the specific decomposition behavior and tune reactor conditions towards clean and complete decomposition.

For the presented results some assumptions had to be formulated which include the limitation of reactions with a maximum of two reaction partners (*e.g.* precursors + $H_2$), no agglomeration of multiple precursors of the same (due to low partial pressures) and of different types (due to separated input of Ga and P sources, respectively). Furthermore, reactor wall effects and the reactor layout are neglected in this study; however, processes related to the substrate surface will be investigated in future studies.

## 2. Computational details

Geometry optimizations without symmetry constraints were carried out using the Gaussian09 optimizer (standard convergence criteria)[30] combined with Turbomole (version 6.3.1)[31,32] energies and gradients (SCF convergence criterion $10^{-8}$ a.u., grid m4). Optimizations were carried out within the density functional approximation applying the GGA functional PBE[33] (widely used in materials science studies)[29] and on an *ab initio* level using the MP2 method. For the PBE calculations, dispersion effects were considered for the calculation of electronic reaction energies and molecular structure optimizations by applying the DFT-D3 method with an improved damping function (further called PBE-D3).[34,35]

One aim of this study is to establish a methodological standard for future studies on the gas phase and surface chemistry in these systems. Therefore, the geometries and energies derived at the MP2 level were used as the gas phase benchmark data for the PBE-D3 calculations of these molecular properties. Complementing the MP2 energies, CCSD(T)[36–39] energies of elementary reactions were derived based on MP2 geometries (on PBE-D3 geometries for transition states) to verify the accuracy of MP2 and PBE-D3. Minimum and transition state structures (the latter characterized by one imaginary mode) were confirmed by calculating the Hessian matrices on PBE-D3 (analytically[40]) and MP2 (numerically[41]). The reactants and products connected by a transition state were identified *via* an intrinsic reaction coordinate (IRC) calculation. Thermodynamic corrections were subsequently derived by statistical thermodynamics in the double harmonic approximation under the assumption of no hindered rotations.[12,42] The results regarding atomic species were complemented with entropic corrections applying the Sackur–Tetrode equation assuming an ideal gas and Maxwell–Boltzmann statistics.[43] The RI approximation was used for all PBE, MP2 and CCSD(T) calculations.[44,45] All methods were used together with a triple-ζ set of Gaussian basis functions (def2-TZVPP).[46] The levels of approximation are denoted PBE-D3/TZ, MP2/TZ and CCSD(T)/TZ in the following. Radical species are denoted by the symbol "$^\bullet$" and found to exhibit doublet spin states with the exception of $P^\bullet$ (quartet ground state). All other species involved in this study exhibit a singlet ground state with the exception of $P(t\text{-}C_4H_9)$ and PH (triplet ground state). Maximum deviation of the ideal values for the $\langle S^2 \rangle$ operator is $<0.03$ for the radical species, indicating a single-reference character suitable for the unrestricted Kohn–Sham/Hartree–Fock methods applied. The electronic states have been consistently confirmed by the presented PBE-D3, MP2 and CCSD(T) calculations in line with previous results on $GaCH_3$, PH and $PH_3$.[47,48] The accuracy of the methods applied was measured by comparing the energies to high level CCSD(T)/TZ data and will be presented in the Results section. To our knowledge, experimental thermodynamic data are unfortunately not available for the reactions investigated here. In the ESI,† the structures derived are compared to the available experimental data.[49–52]

## 3. Results

A catalogue of 61 elementary decomposition reactions was assembled and electronic reaction energies of these reactions were calculated using PBE-D3/TZ, MP2/TZ and CCSD(T)/TZ. Thermodynamic corrections were added for low pressure atmospheres (0.05 atm) and temperatures of 400 °C, 500 °C and 675 °C according to the experimental growth conditions. In the following sections, we present the data for the reaction energies of (i) decomposition of TEG, (ii) decomposition of TBP and (iii) selected transition state energies for TEG and TBP. In the first two sections, uni- and bimolecular reactions are considered separately. Higher order reactions were not considered here due to the low pressure environment. Furthermore, four different possible classes of decomposition reactions were considered for unimolecular reactions: (a) homolytical bond cleavage, (b) β-hydrogen elimination, (c) alkane elimination and (d) $H_2$ elimination. Three classes were considered for bimolecular decomposition reactions: alkane elimination with (a) a hydrogen radical ($H^\bullet$), (b) alkyl (ethyl, *tert*-butyl) radicals ($C_2H_5^\bullet$, $t\text{-}C_4H_9^\bullet$) or (c) molecular hydrogen ($H_2$) as reaction partners.

### 3.1 Thermodynamics of decomposition reactions of TEG

The reaction energies for unimolecular decomposition reactions of TEG are presented in Table 1. Four mechanism classes are listed with elementary reactions of the original precursors and their decomposition products. All reactions shown are endoenergetic ($\Delta E > 0$), while β-hydride and alkane elimination reactions are exergonic ($\Delta G < 0$) for elevated temperatures. This is due to entropic effects resulting in large differences between $\Delta E$ and $\Delta G$ values. Higher temperatures therefore favor these decomposition reactions. The general ordering (from the least to the most favorable reactions considering $\Delta E$) of the investigated decomposition mechanisms is homolytical cleavage reactions $\ll$ β-hydride elimination reactions $<$ $H_2$ elimination reactions $<$ alkane elimination reactions.

The reaction energies for bimolecular decomposition reactions of TEG are presented in Table 2. Here, all reactions listed are energetically accessible. Entropy effects are much smaller since the number of reactants does not change from educts to products (except BG2, BG5). For some radical species the MP2/TZ results deviate considerably from the CCSD(T)/TZ benchmark values (*e.g.* BG3, BG4, BG7) – the differences are mostly less on the PBE/TZ level. This is in line with the known difficulty of the MP2 method to describe radical species accurately. The energetic ordering of decomposition reactions with the following partners (from the least to the most favorable) is alkane elimination reactions with $H_2$ (BG15-19) $<$ alkane elimination reactions with alkyl radicals (BG12, BG14) $<$ $H_2$ elimination reactions with $H^\bullet$ radicals (BG9, BG11) $<$ alkane elimination reactions with $H^\bullet$

Table 1 Unimolecular decomposition reactions of TEG and related products. Changes in electronic ($\Delta E$) and Gibbs energy ($\Delta G$) for temperatures of 400 °C (a), 500 °C (b) and 675 °C (c) are given in kJ mol$^{-1}$. Mechanisms are grouped as homolytical bond cleavage reactions (AG1–AG10), β-hydrogen elimination reactions (AG11–AG14), alkane elimination reactions (AG15–AG17) and $H_2$ elimination reactions (AG18–AG20)

| | | PBE-D3/TZ | | | | MP2/TZ | | | | CCSD(T)/TZ |
|---|---|---|---|---|---|---|---|---|---|---|
| Reaction index | Reaction scheme | $\Delta E$ | $\Delta G$ (a) | $\Delta G$ (b) | $\Delta G$ (c) | $\Delta E$ | $\Delta G$ (a) | $\Delta G$ (b) | $\Delta G$ (c) | $\Delta E$ |
| AG1 | $Ga(C_2H_5)_3 \rightarrow (C_2H_5)_2Ga^\bullet + C_2H_5^\bullet$ | 292.3 | 144.3 | 124.6 | 90.4 | 329.4 | 192.8 | 174.6 | 143.2 | 313.1 |
| AG2 | $Ga(C_2H_5)_3 \rightarrow (C_2H_5)_2GaC_2H_4^\bullet + H^\bullet$ | 404.6 | 270.8 | 253.9 | 224.2 | 417.4 | 303.6 | 289.8 | 265.4 | 415.4 |
| AG3 | $Ga(C_2H_5)_3 \rightarrow (C_2H_5)_2GaCH_2^\bullet + CH_3^\bullet$ | 376.2 | 218.6 | 198.2 | 162.6 | 386.2 | 246.0 | 228.2 | 197.2 | 365.7 |
| AG4 | $(C_2H_5)_2GaC_2H_4^\bullet \rightarrow (C_2H_5)GaC_2H_4 + C_2H_5^\bullet$ | 201.4 | 99.4 | 82.5 | 53.2 | 243.9 | 108.7 | 89.7 | 58.2 | 245.6 |
| AG5 | $(C_2H_5)_2Ga^\bullet \rightarrow Ga(C_2H_5) + C_2H_5^\bullet$ | 144.8 | 15.3 | −1.8 | −31.1 | 167.5 | 44.5 | 28.4 | 0.6 | 145.1 |
| AG6 | $(C_2H_5)_2Ga^\bullet \rightarrow (C_2H_5)GaC_2H_4 + H^\bullet$ | 313.6 | 225.9 | 211.8 | 187.0 | 331.8 | 218.8 | 204.9 | 180.4 | 347.9 |
| AG7 | $(C_2H_5)GaC_2H_4 \rightarrow GaC_2H_4^\bullet + C_2H_5^\bullet$ | 231.2 | 62.5 | 43.8 | 11.4 | 250.6 | 118.5 | 101.1 | 70.9 | 210.0 |
| AG8 | $Ga(C_2H_5) \rightarrow GaC_2H_4^\bullet + H^\bullet$ | 400.1 | 273.1 | 257.3 | 229.5 | 414.9 | 292.8 | 277.6 | 250.7 | 412.8 |
| AG9 | $GaH_3 \rightarrow GaH_2^\bullet + H^\bullet$ | 337.8 | 226.9 | 212.3 | 186.6 | 346.8 | 235.0 | 220.3 | 194.5 | 356.7 |
| AG10 | $GaH \rightarrow Ga^\bullet + H^\bullet$ | 280.4 | 192.0 | 179.0 | 156.0 | 273.3 | 183.6 | 170.6 | 147.4 | 288.0 |
| AG11 | $Ga(C_2H_5)_3 \rightarrow Ga(C_2H_5)_2H + C_2H_4$ | 132.9 | −13.8 | −32.8 | −65.6 | 141.7 | 13.8 | −2.3 | −30.2 | 127.8 |
| AG12 | $Ga(C_2H_5)_2H \rightarrow Ga(C_2H_5)H_2 + C_2H_4$ | 133.7 | 12.3 | −2.9 | −29.1 | 140.4 | 11.9 | −4.3 | −32.3 | 126.8 |
| AG13 | $Ga(C_2H_5)H_2 \rightarrow GaH_3 + C_2H_4$ | 134.8 | 4.9 | −11.6 | −40.1 | 139.3 | 8.1 | −8.5 | −37.2 | 125.9 |
| AG14 | $Ga(C_2H_5) \rightarrow GaH + C_2H_4$ | 140.6 | 20.6 | 5.4 | −21.1 | 146.6 | 24.2 | 8.7 | −18.2 | 130.4 |
| AG15 | $Ga(C_2H_5)_3 \rightarrow Ga(C_2H_5) + n\text{-}C_4H_{10}$ | 54.5 | −47.1 | −61.0 | −84.8 | 86.3 | −0.6 | −12.4 | −32.4 | 68.5 |
| AG16 | $(C_2H_5)_2Ga^\bullet \rightarrow GaC_2H_4^\bullet + C_2H_6$ | 104.4 | −12.6 | −28.1 | −54.8 | 132.9 | 26.8 | 12.6 | −11.8 | 106.7 |
| AG17 | $Ga(C_2H_5)H_2 \rightarrow HGa + C_2H_6$ | 41.5 | −51.3 | −65.0 | −88.5 | 67.7 | −25.8 | −39.6 | −63.4 | 55.3 |
| AG18 | $Ga(C_2H_5)_2H \rightarrow (C_2H_5)GaC_2H_4 + H_2$ | 205.1 | 125.6 | 111.8 | 87.9 | 242.1 | 127.3 | 112.1 | 85.7 | 247.4 |
| AG19 | $Ga(C_2H_5)H_2 \rightarrow Ga(C_2H_5) + H_2$ | 73.4 | −29.4 | −44.0 | −69.4 | 93.2 | −10.1 | −24.7 | −50.1 | 85.4 |
| AG20 | $GaH_3 \rightarrow HGa + H_2$ | 79.3 | −13.7 | −27.1 | −50.4 | 100.6 | 6.0 | −7.5 | −31.2 | 94.8 |

Table 2 Bimolecular decomposition reactions of TEG and related products. Changes in electronic (Δ$E$) and Gibbs energy (Δ$G$) for temperatures of 400 °C (a), 500 °C (b) and 675 °C (c) are given in kJ mol$^{-1}$. Mechanisms are grouped as alkane or $H_2$ elimination reactions with $H^•$ (BG1–BG11), $C_2H_5^•$ (BG12–BG14) or $H_2$ (BG15–BG19) as a reaction partner

| | | PBE-D3/TZ | | | | MP2/TZ | | | | CCSD(T)/TZ |
|---|---|---|---|---|---|---|---|---|---|---|
| Reaction index | Reaction scheme | Δ$E$ | Δ$G$ (a) | Δ$G$ (b) | Δ$G$ (c) | Δ$E$ | Δ$G$ (a) | Δ$G$ (b) | Δ$G$ (c) | Δ$E$ |
| BG1 | $Ga(C_2H_5)_3 + H^• \rightarrow (C_2H_5)_2Ga^• + C_2H_6$ | −148.2 | −156.6 | −159.1 | −162.7 | −120.2 | −117.7 | −118.8 | −120.0 | −138.1 |
| BG2 | $(C_2H_5)_2Ga^• + H^• \rightarrow Ga(C_2H_5)_2H$ | −330.2 | −226.0 | −212.1 | −187.8 | −343.6 | −227.9 | −212.3 | −185.1 | −352.9 |
| BG3 | $(C_2H_5)_2Ga^• + H^• \rightarrow Ga(C_2H_5) + C_2H_6$ | −295.6 | −285.6 | −285.4 | −284.3 | −282.0 | −266.0 | −265.0 | −262.5 | −306.1 |
| BG4 | $Ga(C_2H_5)_2H + H^• \rightarrow Ga(C_2H_5)H^• + C_2H_6$ | −144.2 | −132.2 | −131.5 | −129.5 | −120.0 | −111.5 | −111.6 | −111.0 | −137.6 |
| BG5 | $Ga(C_2H_5)H^• + H^• \rightarrow Ga(C_2H_5)H_2$ | −333.4 | −224.4 | −209.9 | −184.5 | −345.0 | −235.9 | −221.5 | −196.2 | −354.4 |
| BG6 | $Ga(C_2H_5)H^• + H^• \rightarrow GaH + C_2H_6$ | −291.9 | −275.7 | −274.9 | −273.0 | −277.2 | −261.7 | −261.1 | −259.5 | −299.1 |
| BG7 | $Ga(C_2H_5)H_2 + H^• \rightarrow GaH_2^• + C_2H_6$ | −138.7 | −137.0 | −137.7 | −138.3 | −119.4 | −116.2 | −116.9 | −117.6 | −136.3 |
| BG8 | $Ga(C_2H_5) + H^• \rightarrow Ga^• + C_2H_6$ | −190.3 | −156.3 | −154.1 | −149.9 | −185.5 | −151.4 | −149.5 | −145.6 | −200.4 |
| BG9 | $GaH_3 + H^• \rightarrow GaH_2^• + H_2$ | −101.0 | −99.4 | −99.8 | −100.2 | −86.5 | −84.4 | −84.8 | −85.3 | −96.8 |
| BG10 | $GaH_2^• + H^• \rightarrow GaH + H_2$ | −258.5 | −240.6 | −239.4 | −237.1 | −246.2 | −229.0 | −227.8 | −225.6 | −261.8 |
| BG11 | $GaH + H^• \rightarrow Ga^• + H_2$ | −158.4 | −134.4 | −133.1 | −130.8 | −159.9 | −135.8 | -134.6 | −132.4 | −165.4 |
| BG12 | $Ga(C_2H_5)_3 + C_2H_5^• \rightarrow Ga(C_2H_5)_2^• + n\text{-}C_4H_{10}$ | −90.3 | −62.4 | −59.3 | −53.7 | −81.3 | −45.1 | −40.8 | −33.1 | −76.5 |
| BG13 | $(C_2H_5)_2Ga^• + C_2H_5^• \rightarrow (C_2H_5)GaC_2H_4 + C_2H_6$ | −126.8 | −75.0 | −71.9 | −66.2 | −117.7 | −91.6 | −88.5 | −82.7 | −103.3 |
| BG14 | $Ga(C_2H_5) + C_2H_5^• \rightarrow GaC_2H_4^• + C_2H_6$ | −40.4 | −27.8 | −26.3 | −23.7 | −34.6 | −17.7 | −15.8 | −12.4 | −38.4 |
| BG15 | $Ga(C_2H_5)_3 + H_2 \rightarrow Ga(C_2H_5)_2H + C_2H_6$ | −39.6 | −56.3 | −59.1 | −63.6 | −30.5 | −26.2 | −26.0 | −25.2 | −37.6 |
| BG16 | $Ga(C_2H_5)_2H + H_2 \rightarrow Ga(C_2H_5)H_2 + C_2H_6$ | −38.8 | −30.2 | −29.2 | −27.1 | −31.7 | −28.0 | −27.9 | −27.3 | −38.6 |
| BG17 | $Ga(C_2H_5)H_2 + H_2 \rightarrow GaH_3 + C_2H_6$ | −37.7 | −37.6 | −37.9 | −38.0 | −32.9 | −31.8 | −32.1 | −32.2 | −39.5 |
| BG18 | $Ga(C_2H_5) + H_2 \rightarrow GaH + C_2H_6$ | −31.9 | −21.9 | −21.0 | −19.1 | −25.5 | −15.7 | −14.9 | −13.3 | −30.1 |
| BG19 | $Ga(C_2H_5)\ _2^• + H_2 \rightarrow Ga(C_2H_5)H^• + C_2H_6$ | −35.7 | −31.9 | −31.5 | −30.4 | −30.3 | −20.0 | −18.8 | −16.3 | −37.1 |

radicals (BG1, BG4, BG7, BG8) ≪ radical recombinations (with or without elimination products; BG2, BG3, BG5, BG6, BG10, BG13). Reactions AG11–AG14 (β-hydride elimination reactions), AG19 and AG20 ($H_2$ elimination reactions), AG15 and AG17 (alkane elimination reactions) and BG15–BG18 (alkane elimination reactions with $H_2$) were chosen for subsequent investigation of reaction barriers under the condition of low $H^•$ concentration.

### 3.2 Thermodynamics of decomposition reactions of TBP

The reaction energies for unimolecular decomposition reactions of TBP are presented in Table 3. Most of the reactions are energetically and thermodynamically unfavorable. Only β-hydrogen elimination reactions (AP6 and AP7) are exothermic, although the entropy effects are very large for all unimolecular reactions. For the P-containing species a good agreement was found between the computational methods applied except for AP9 and AP12 which can be attributed to the difficulty of DFT dealing with atomic species. The reaction energies for bimolecular decomposition reactions of TBP are presented in Table 4. All elimination reactions are energetically (except BP8) and thermodynamically accessible. As for the bimolecular reactions with Ga species, entropic effects are small (except BP8, which results in three species). Reactions AP6 (β-hydrogen elimination) and BP8 (alkene + $H_2$ elimination with $H_2$) were chosen for the subsequent transition state analysis. No transition state could be found for reaction BP7.

Table 3 Unimolecular decomposition reactions of TBP and related products. Changes in electronic (Δ$E$) and Gibbs energy (Δ$G$) for temperatures of 400 °C (a), 500 °C (b) and 675 °C (c) are given in kJ mol$^{-1}$. Mechanisms are grouped as homolytical bond cleavage reactions (AP1–AP5), β-hydrogen elimination reactions (AP6 and AP7), alkane elimination reactions (AP8 and AP9) and $H_2$ elimination reactions (AP10–AP12)

| | | PBE-D3/TZ | | | | MP2/TZ | | | | CCSD(T)/TZ |
|---|---|---|---|---|---|---|---|---|---|---|
| Reaction index | Reaction scheme | Δ$E$ | Δ$G$ (a) | Δ$G$ (b) | Δ$G$ (c) | Δ$E$ | Δ$G$ (a) | Δ$G$ (b) | Δ$G$ (c) | Δ$E$ |
| AP1 | $P(t\text{-}C_4H_9)H_2 \rightarrow P(t\text{-}C_4H_9)H^• + H^•$ | 349.7 | 230.9 | 215.5 | 188.3 | 352.2 | 231.6 | 216.0 | 188.6 | 357.4 |
| AP2 | $P(t\text{-}C_4H_9)H_2 \rightarrow PH_2^• + t\text{-}C_4H_9^•$ | 279.3 | 119.9 | 99.1 | 62.9 | 314.4 | 156.6 | 135.8 | 99.8 | 289.2 |
| AP3 | $P(t\text{-}C_4H_9)H^• \rightarrow PH + t\text{-}C_4H_9^•$ | 266.1 | 126.6 | 108.0 | 75.8 | 281.4 | 143.7 | 125.3 | 93.2 | 260.7 |
| AP4 | $PH_3 \rightarrow H_2P^• + H^•$ | 356.9 | 239.9 | 224.8 | 198.2 | 353.3 | 234.6 | 219.4 | 192.7 | 360.1 |
| AP5 | $PH \rightarrow P^• + H^•$ | 313.8 | 218.9 | 205.6 | 181.9 | 277.6 | 181.6 | 168.2 | 144.4 | 295.8 |
| AP6 | $P(t\text{-}C_4H_9)H_2 \rightarrow PH_3 + i\text{-}C_4H_8$ | 96.9 | −48.7 | −67.6 | −100.5 | 111.7 | −36.3 | −55.7 | −89.3 | 96.3 |
| AP7 | $P(t\text{-}C_4H_9) \rightarrow PH + i\text{-}C_4H_8$ | 111.4 | −20.8 | −38.0 | −67.9 | 114.1 | −21.4 | −39.1 | −69.9 | 100.9 |
| AP8 | $P(t\text{-}C_4H_9)H_2 \rightarrow PH + i\text{-}C_4H_{10}$ | 205.9 | 90.6 | 73.3 | 46.2 | 199.0 | 81.6 | 65.0 | 36.3 | 184.4 |
| AP9 | $P(t\text{-}C_4H_9)H^• \rightarrow P^• + i\text{-}C_4H_{10}$ | 170.0 | 78.7 | 64.5 | 39.8 | 124.5 | 31.7 | 17.2 | −7.8 | 122.8 |
| AP10 | $P(t\text{-}C_4H_9)H_2 \rightarrow P(t\text{-}C_4H_9) + H_2$ | 239.9 | 123.2 | 107.4 | 79.9 | 236.8 | 119.0 | 103.1 | 75.5 | 231.0 |
| AP11 | $PH_3 \rightarrow PH + H_2$ | 254.5 | 151.1 | 137.1 | 112.5 | 239.2 | 133.9 | 119.7 | 94.9 | 235.7 |
| AP12 | $PH_2^• \rightarrow P^• + H_2$ | 211.5 | 130.2 | 117.9 | 96.1 | 163.5 | 80.9 | 68.5 | 46.7 | 171.4 |

Table 4 Bimolecular decomposition reactions of TBP and related products. Changes in electronic ($\Delta E$) and Gibbs energy ($\Delta G$) for temperatures of 400 °C (a), 500 °C (b) and 675 °C (c) are given in kJ mol$^{-1}$. Mechanisms are grouped as alkane/alkene and/or $H_2$ elimination reactions with $H^\bullet$ (BP1–BP5), $t$-$C_4H_9^\bullet$ (BP6) or $H_2$ (BP7–BP10) as a reaction partner

| | | PBE-D3/TZ | | | | MP2/TZ | | | | CCSD(T)/TZ |
|---|---|---|---|---|---|---|---|---|---|---|
| Reaction index | Reaction scheme | $\Delta E$ | $\Delta G$ (a) | $\Delta G$ (b) | $\Delta G$ (c) | $\Delta E$ | $\Delta G$ (a) | $\Delta G$ (b) | $\Delta G$ (c) | $\Delta E$ |
| BP1 | $P(t\text{-}C_4H_9)H_2 + H^\bullet \rightarrow P(t\text{-}C_4H_9)H^\bullet + H_2$ | −89.1 | −95.5 | −96.7 | −98.6 | −81.1 | −87.8 | −89.2 | −91.2 | −96.0 |
| BP2 | $P(t\text{-}C_4H_9)H_2 + H^\bullet \rightarrow PH_2^\bullet + \text{i-}C_4H_{10}$ | −130.6 | −147.0 | −150.1 | −154.9 | −120.1 | −137.1 | −140.5 | −145.8 | −144.6 |
| BP3 | $P(t\text{-}C_4H_9) + H^\bullet \rightarrow P^\bullet + \text{i-}C_4H_{10}$ | −159.0 | −140.0 | −139.6 | −138.7 | −193.4 | −175.2 | −175.1 | −174.6 | −204.2 |
| BP4 | $PH_3 + H^\bullet \rightarrow PH_2^\bullet + H_2$ | −81.9 | −86.5 | −87.3 | −88.6 | −80.0 | −84.8 | −85.7 | −87.1 | −93.4 |
| BP5 | $PH + H^\bullet \rightarrow P^\bullet + H_2$ | −125.0 | −107.4 | −106.6 | −105.0 | −155.7 | −137.8 | −136.9 | −135.4 | −157.7 |
| BP6 | $P(t\text{-}C_4H_9)H_2 + t\text{-}C_4H_9^\bullet \rightarrow P(t\text{-}C_4H_9)H^\bullet + \text{i-}C_4H_{10}$ | −60.2 | −36.0 | −33.7 | −29.6 | −82.4 | −62.1 | −60.3 | −57.0 | −76.3 |
| BP7 | $P(t\text{-}C_4H_9)H_2 + H_2 \rightarrow PH_3 + \text{i-}C_4H_{10}$ | −48.6 | −60.5 | −62.8 | −66.3 | −40.2 | −52.3 | −54.8 | −58.7 | −51.2 |
| BP8 | $P(t\text{-}C_4H_9)H_2 + H_2 \rightarrow PH_3 + \text{i-}C_4H_8 + H_2$ | 96.9 | −48.7 | −67.6 | −100.5 | 111.7 | −36.3 | −55.7 | −89.3 | 96.7 |
| BP9 | $P(t\text{-}C_4H_9)H^\bullet + H_2 \rightarrow PH_2^\bullet + \text{i-}C_4H_{10}$ | −41.5 | −51.5 | −53.4 | −56.3 | −39.0 | −49.2 | −51.3 | −54.5 | −48.6 |
| BP10 | $P(t\text{-}C_4H_9) + H_2 \rightarrow PH + \text{i-}C_4H_{10}$ | −34.1 | −32.6 | −33.1 | −33.7 | −37.8 | −37.4 | −38.2 | −39.3 | −46.5 |

To summarize the part of the study focusing on the reaction energies: unimolecular decomposition reactions exhibit much larger changes in $\Delta G$ upon considering increasing temperatures compared to bimolecular reactions. As expected, all reactions leading from radical species to saturated products are exergonic (see also ref. 10) while larger radical species tend to be more stabilized than small ones. All β-hydrogen elimination reactions (alkene elimination reactions) are exergonic (Ga and P species) and so are many uni- and bimolecular alkane and $H_2$ elimination reactions from Ga species. All unimolecular $H_2$ and alkane eliminations from P species are endergonic. This catalogue's bimolecular decomposition reactions are, generally, exergonic. Gas phase reactivity cannot be understood from the thermodynamic data alone. However, they give a strong hint on which reaction classes are relevant for the investigation of reaction kinetics in terms of transition state theory. This will be described for the reactions indicated in the previous paragraphs in the next section.

### 3.3 Transition states of TEG and TBP decomposition reactions

Several elementary decomposition reactions were identified from the catalogue presented in Tables 1–4, where the thermodynamic data indicate their importance for the gas phase decomposition chemistry of the MOVPE growth of GaP. For those reactions, transition states linking reactants and products of the reactions in Tables 1–4 were investigated. Subsequently, the possible decomposition pathways were formulated which determine the possible decomposition products. Furthermore, those pathways contain the structural data which provide rationalization of the underlying reaction mechanisms.

The selection criteria for the reactions considered in this section are the following: (i) elementary steps are exergonic, (ii) they do not depend on any other species than the carrier gas $H_2$ (which is present in sufficient concentration), and (iii) the reactant species will realistically be available either as original precursors or *via* exclusively exergonic preceding reactions. The transition states (TS) were optimized with PBE-D3/TZ.

Table 5 Transition state data for selected decomposition reactions of TEG, TBP and related products at PBE-D3/TZ. Electronic energies of activation ($\Delta E^{\#}$) and Gibbs energy of activation ($\Delta G^{\#}$) for temperatures of 400 °C (a), 500 °C (b) and 675 °C (c) are given in kJ mol$^{-1}$. The transition states' imaginary vibrational mode ($\nu_{\text{imag}}$) is given in cm$^{-1}$. Reactions AG11–AG14 and AP6 represent unimolecular β-hydrogen, AG15–AG17 and AG19–AG20 represent unimolecular alkane and $H_2$ elimination reactions, respectively. BG15–BG18 and BP8 represent bimolecular alkane and $H_2$ elimination reactions, respectively

| Reaction index | Reaction scheme | $\Delta E^{\#}$ | $\Delta G^{\#}$ (a) | $\Delta G^{\#}$ (b) | $\Delta G^{\#}$ (c) | $\nu_{\text{imag}}$ | $\Delta E^{\#}$ MP2/TZ//PBE-D3/TZ$^{a}$ | $\Delta E^{\#}$ CCSD(T)/TZ//PBE-D3/TZ$^{a}$ |
|---|---|---|---|---|---|---|---|---|
| AG11 | $Ga(C_2H_5)_3 \rightarrow Ga(C_2H_5)_2H + C_2H_4$ | 131.6 | 141.0 | 144.3 | 150.2 | i648 | 152.6 | 147.5 |
| AG12 | $Ga(C_2H_5)_2H \rightarrow Ga(C_2H_5)H_2 + C_2H_4$ | 128.1 | 149.9 | 155.1 | 164.2 | i686 | 150.7 | 145.3 |
| AG13 | $Ga(C_2H_5)H_2 \rightarrow GaH_3 + C_2H_4$ | 123.8 | 129.2 | 131.9 | 136.7 | i717 | 149.6 | 143.3 |
| AG14 | $Ga(C_2H_5) \rightarrow GaH + C_2H_4$ | 87.2 | 82.6 | 84.1 | 86.8 | i430 | 111.5 | 109.7 |
| AG15 | $Ga(C_2H_5)_3 \rightarrow Ga(C_2H_5) + n\text{-}C_4H_{10}$ | 312.3 | 326.2 | 329.4 | 335.1 | i377 | 375.3 | 360.1 |
| AG17 | $Ga(C_2H_5)H_2 \rightarrow HGa + C_2H_6$ | 194.7 | 199.8 | 202.2 | 206.7 | i713 | 234.2 | 236.9 |
| AG19 | $Ga(C_2H_5)H_2 \rightarrow Ga(C_2H_5) + H_2$ | 217.0 | 215.6 | 216.8 | 219.1 | i1140 | 271.2 | 255.7 |
| AG20 | $GaH_3 \rightarrow HGa + H_2$ | 211.5 | 200.5 | 200.5 | 200.4 | i1025 | 269.0 | 251.4 |
| BG15 | $Ga(C_2H_5)_3 + H_2 \rightarrow Ga(C_2H_5)_2H + C_2H_6$ | 96.7 | 208.5 | 225.2 | 254.5 | i1233 | 126.2 | 124.7 |
| BG16 | $Ga(C_2H_5)_2H + H_2 \rightarrow Ga(C_2H_5)H_2 + C_2H_6$ | 93.7 | 217.0 | 235.4 | 267.6 | i1258 | 124.3 | 122.8 |
| BG17 | $Ga(C_2H_5)H_2 + H_2 \rightarrow GaH_3 + C_2H_6$ | 92.1 | 204.7 | 221.5 | 251.0 | i1283 | 124.3 | 122.6 |
| BG18 | $Ga(C_2H_5) + H_2 \rightarrow GaH + C_2H_6$ | 67.3 | 169.2 | 184.8 | 212.0 | i1156 | 105.4 | 107.3 |
| AP6 | $P(t\text{-}C_4H_9)H_2 \rightarrow PH_3 + \text{i-}C_4H_8$ | 242.6 | 217.4 | 216.2 | 214.1 | i648 | 310.5 | 293.1 |
| BP8 | $P(t\text{-}C_4H_9)H_2 + H_2 \rightarrow PH_3 + \text{i-}C_4H_8 + H_2$ | 264.6 | 337.3 | 350.1 | 372.4 | i1120 | 365.8 | 354.0 |

[a] Energy calculations based on PBE-D3/TZ structures.

The electronic activation energies of the selected reactions and the frequencies of the transition state modes are given in Table 5. The energies vary from 67.3 (BG18) to 312.3 kJ mol$^{-1}$ (AG15), exemplifying the strong differences between barriers for different mechanisms. It becomes clear that the barriers for TEG and derived species are much lower compared to the two barriers investigated for decomposition reactions of TBP (except AG15). It is also striking that entropy has a much smaller influence on the barrier height compared to the reaction energies (Tables 1–4), except for the bimolecular reactions involving $H_2$ (BG15–BG18, BP8), where the barriers are drastically increased by the inclusion of entropic effects. This can be understood in terms of the entropy-lowering association of two species to one transition structure in the bimolecular case. The vibrational modes of the TS structures connecting educts and products can also be taken to distinguish the different mechanism classes: transition states containing $H_2$ exhibit much higher mode energies ($>$1100 cm$^{-1}$) compared to alkane elimination reactions (377–717 cm$^{-1}$). Before discussing the implications of the reaction catalogue introduced, an evaluation of the accuracy for the methods chosen will be presented.

### 3.4 Accuracy of PBE-D3/TZ and MP2/TZ *vs.* CCSD(T)/TZ

In order to validate the accuracy of the broadly applicable PBE-D3/TZ and MP2/TZ methods, statistical data regarding the deviations from the highly accurate CCSD(T)/TZ computations are given in Table 6. All presented deviation criteria of PBE-D3/TZ energies are of the same order as the respective deviations of MP2/TZ energies with respect to CCSD(T)/TZ//MP2/TZ. This validation of PBE-D3 is important as for calculations of larger systems the application of DFT-based methods will be preferred over the costly post-HF methods, especially for investigation of surface-assisted reactions where the MP2 method is currently only feasible for small systems. Energies of reactions where radical species are involved have a larger deviation and represent the respective maximum absolute deviations of this catalogue's reactions. This is known for species with an unpaired electron and mainly due to the inaccurate exchange contribution to the energy in GGA exchange–correlation functionals.[54] However, focusing on decomposition reaction energies, the description of even large radicals by PBE-D3/TZ seems to be of sufficient accuracy relative to CCSD(T)/TZ.

The relative and absolute deviations of the examined energy barriers are larger, as it is known for GGA functionals to underestimate reaction barriers.[55] Remarkably, RMS, RAD and MAE of PBE-D3/TZ are smaller compared to MP2/TZ with respect to CCSD(T)/TZ. This overestimation of activation energies is a known shortcoming of MP2. Similar trends of reaction energy deviations for DFT relative to CCSD(T)/TZ were also found in other studies on Ga precursor decomposition.[12] In conclusion, the accuracy of the methods is sufficient for the purpose of identifying relevant decomposition products and analyzing the respective mechanisms.

In the following, uni- and bimolecular decomposition schemes including mainly exergonic reactions are presented for TEG and TBP. From those schemes several pathways were assembled involving the reaction energies together with the reaction barriers presented above.

### 3.5 Decomposition scheme for TEG

In the light of the results given in Tables 1 and 2, the plethora of possible reactions is reduced to the following set: unimolecular β-hydride elimination reactions or homolytical bond cleavage reactions of Ga–C, C–C or C–H can be formulated for TEG. Furthermore, recombinative elimination reactions of alkanes or hydrogen are energetically accessible for some decomposition products. In the bimolecular case, alkane and $H_2$ elimination reactions are possible with reactants like $H_2$ or radicals ($H^\bullet$, $C_2H_5{}^\bullet$). This leads to the decomposition pathways of first (Fig. 1, top) and second (Fig. 1, bottom) order reactions. However, all homolytical cleavage reactions of saturated species are endoenergetic and endergonic and are not considered further in this study. Specifically, the bond energies for TEG were calculated to be 404.6 kJ mol$^{-1}$ for the terminal $C_\beta$–H bond, 376.2 kJ mol$^{-1}$ for the $C_\alpha$–$C_\beta$ bond and 292.3 kJ mol$^{-1}$ for the Ga–C bond (AG2, AG3, AG1 for PBE-D3/TZ in Table 1). As a consequence, the remaining pathways build a decomposition scheme for TEG. The major pathways are discussed in the following subsections in detail.

**Pathway 1, "β-hydride eliminations".** The possibility of reaction *via* β-hydride elimination is a significant advantage to TEG compared to, for instance, TMG which has been studied extensively for CVD applications.[12] Since a carbon atom in the β-position to gallium is absent in TMG, only endergonic homolytical cleavage reaction can occur, hence a decomposition reaction is less likely.[15] The suggested decomposition pathway 1 for TEG has four elementary steps and leads to

Table 6 Statistical deviation of PBE-D3/TZ and MP2/TZ reaction energies (Δ*E*) w.r.t. CCSD(T)/TZ energies and barriers (Δ*E*$^\#$) w.r.t. CCSD(T)/TZ and MP2/TZ energies. *Method1*//*method2* indicates an energy calculation by *method1* on the structure optimized with *method2*

| | Reaction energies | | | | | | Reaction barriers | |
|---|---|---|---|---|---|---|---|---|
| | PBE-D3 w.r.t. CCSD(T)//MP2 | | | MP2 w.r.t. CCSD(T)//MP2 | | | PBE-D3 w.r.t. CCSD(T)//PBE-D3 | PBE-D3 w.r.t. MP2//PBE-D3 |
| | All | Radicals | Non-rad. | All | Radicals | Non-rad. | All | All |
| RMS[a] | 17.7 | 19.5 | 13.6 | 14.4 | 15.8 | 11.0 | 40.8 | 48.7 |
| MAE[b] | −47.2 | −47.2 | 42.4 | −40.6 | −40.6 | −17.7 | 89.5 | 101.2 |
| RAD[c] | 12.0 | 12.0 | 11.9 | 12.0 | 10.3 | 14.4 | 20.4 | 22.3 |
| RMD[d] | −38.5 | −38.5 | 24.9 | −25.9 | −19.3 | −25.9 | 37.3 | 36.2 |

[a] Root mean square error in kJ mol$^{-1}$. [b] Maximum absolute error in kJ mol$^{-1}$. [c] Relative average deviation in %. [d] Relative maximum deviation in %.

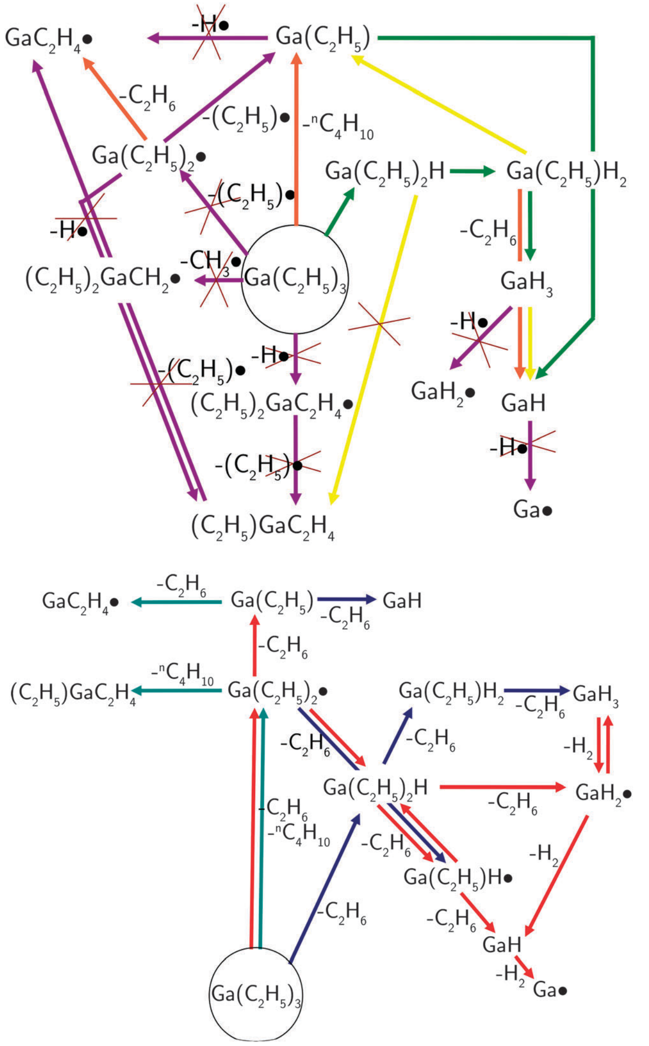

Fig. 1 Unimolecular (top) and bimolecular (bottom) decomposition reaction schemes for TEG considering information from Tables 1 and 2. Endergonic steps (at 400 °C) are crossed out or do not appear at all. Decomposition mechanisms are classified as radical cleavage reactions (magenta), alkane (orange), $H_2$ (yellow) and β-hydride (green) elimination reactions. Bimolecular elimination of alkanes or $H_2$ is considered with the $H^\bullet$ (red) or $C_2H_5^\bullet$ (turquoise) radicals or $H_2$ (blue) as reaction partners.

GaH as the smallest thermodynamically accessible Ga species (see Fig. 2). Firstly, ethylene is eliminated from TEG in a β-hydride elimination step with a Gibbs energy barrier of $\Delta G^{\#}_{400}$ = 141.0 kJ mol$^{-1}$. The transition state is rather symmetric with $d$(Ga–H) = 1.697 Å and $d$(C–H) = 1.718 Å. The same is true for the following further β-hydride elimination steps with barriers of $\Delta G^{\#}_{400}$ = 149.9 and $\Delta G^{\#}_{400}$ = 129.2 kJ mol$^{-1}$, respectively, leading to $GaH_3$. A reduction in the Ga–C, Ga–H and H–C bond lengths thereby points to slightly earlier transition states for the less substituted Ga species. And indeed, the trend in electronic barriers ($\Delta E^{\#}$ = 131.6, 128.1 and 123.8 kJ mol$^{-1}$, Table 1) confirms this assumption. Entropy covers this effect and leads to the observed different trend in $\Delta G^{\#}$. The fourth step within this pathway exhibits the highest barrier. The $H_2$ elimination from $GaH_3$ is slightly exergonic and has a barrier of $\Delta G^{\#}_{400}$ = 200.5 kJ mol$^{-1}$. The subsequent homolytical cleavage to Ga$^\bullet$ and H$^\bullet$ is highly endergonic in the gas phase ($\Delta G_{400}$ = 192.0 kJ mol$^{-1}$, see Table 1). Hence, *via* this pathway $GaH_3$ will likely be the main product with the possibility of GaH at elevated temperatures. From the graphical representation, it appears that the differences in the reaction profile with an increase in temperature might be due to entropy effects on the transition states. But a closer analysis of the numbers in Tables 1 and 5 reveals that the temperature effects of the intermediates are much stronger compared to the transition states.

**Pathway 2, "*n*-butane elimination".** A recombinative elimination of *n*-butane from TEG leads to monoethylgallium (Ga($C_2H_5$)) in a single step (Fig. 3), but the barrier for this reaction is very large ($\Delta G^{\#}_{400}$ = 326.2 kJ mol$^{-1}$) and unlikely to be surmounted even at elevated temperatures. If monoethylgallium can be formed by any (*e.g.* surface-assisted) process, a β-hydride elimination reaction may result in gallium monohydride (GaH) in a low barrier step ($\Delta G^{\#}_{400}$ = 82.6 kJ mol$^{-1}$). GaH is an interesting intermediate as it can be formed from many different sources (see Fig. 1).

**Pathway 3, "monoethylgallane decomposition processes".** Next to the low-barrier β-hydride elimination described in pathway 1, monoethylgallane can directly decompose to GaH (Fig. 4, reaction to the right) by the elimination of ethane ($\Delta G^{\#}_{400}$ = 199.8 kJ mol$^{-1}$). Furthermore, $H_2$ elimination to Ga($C_2H_5$) (Fig. 4, reaction to the left) can occur with a higher barrier of $\Delta G^{\#}_{400}$ = 215.6 kJ mol$^{-1}$. Since both processes are thermodynamically and kinetically less favorable than the β-hydride elimination (Fig. 2), they are not highly relevant gas phase reactions.

**Pathway 4, "2nd order pathway, ethane elimination".** The bimolecular decomposition reactions with a radical reactant or $H_2$ are exergonic. A highly interlinked decomposition network can be formulated (Fig. 1, bottom) leading to both radical and non-radical products. Formally, atomic Ga can be reached *via* an alkane elimination pathway with hydrogen radicals H$^\bullet$ as reactants (*e.g.* $\Delta G_{400}$(BG1) = −156.6 kJ mol$^{-1}$, Table 2). Assuming low concentrations of these radicals in the gas phase for thermodynamic reasons ($H_2$ dissociation: $\Delta G_{400}$ = 326.4 kJ mol$^{-1}$) no barrier was calculated for such elimination steps. Reactions with molecular hydrogen ($H_2$), which is used as a carrier gas and available in high concentrations, are more likely. The pathway shown in Fig. 5 contains three steps of $H_2$ addition reactions to saturated Ga species, which decompose under simultaneous ethane elimination in subsequent steps to Ga($C_2H_5$)$_2$H, Ga($C_2H_5$)$H_2$ and $GaH_3$, respectively. Note that electronic barriers are lower throughout compared to the corresponding unimolecular β-hydride elimination barriers of these species (Table 5), although an additional H–H bond is broken. However, upon applying thermodynamic corrections to the transition state energies of this bimolecular decomposition class the barriers are drastically increased. The very high initial barrier for the $H_2$-assisted reaction (BG1, $\Delta G^{\#}_{400}$ = 208.5 kJ mol$^{-1}$) indicates that the decomposition reactions *via* second-order reactions are less important.

Comparing uni- and bimolecular alkyl elimination from gallane species (Fig. 2 and 5), yet another trend can be

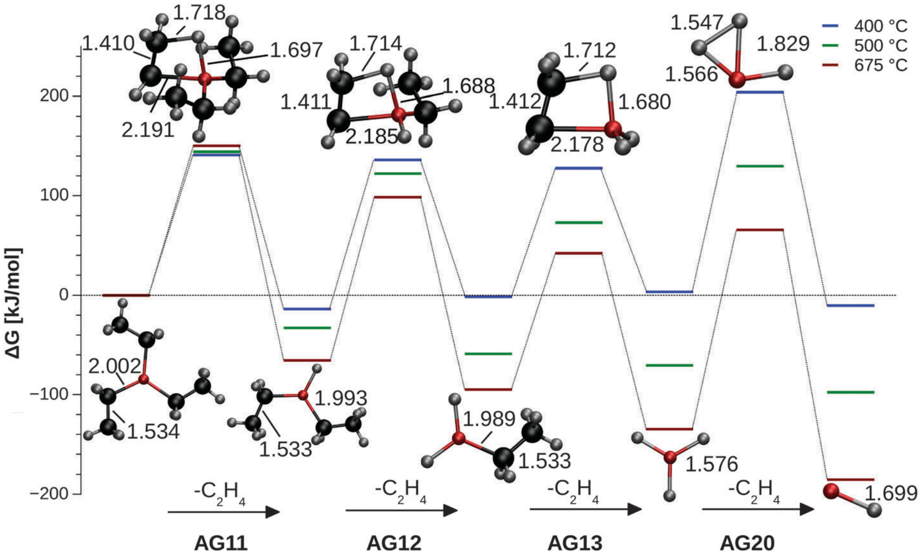

Fig. 2 Three-step β-hydride elimination from TEG to gallane ($GaH_3$), followed by a $H_2$ elimination step to GaH. Changes in Gibbs energy (Δ*G*) and barriers relative to the respective reactants (in kJ $mol^{-1}$) at experimental temperatures. Distances are given in Å.

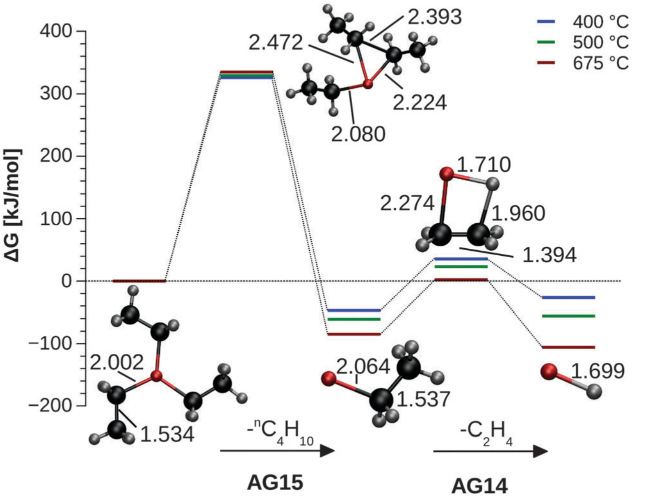

Fig. 3 Two-step decomposition of TEG to GaH *via* $Ga(C_2H_5)$. Changes in Gibbs energy (Δ*G*) and barriers relative to the respective reactants (in kJ $mol^{-1}$) at experimental temperatures. Distances are given in Å.

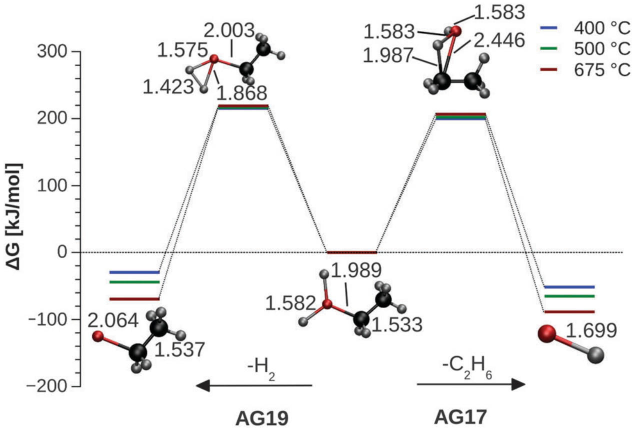

Fig. 4 Monoethylgallane (middle) decomposition to $Ga(C_2H_5)$ (left path) and GaH (right path). Changes in Gibbs energy (Δ*G*) and barriers (in kJ $mol^{-1}$) at experimental temperatures. Distances are given in Å.

observed: while the thermodynamics of unimolecular β-hydride elimination reactions strongly depend on temperature (Fig. 2), this is not the case for the bimolecular $C_2H_6$ elimination of the same species (Fig. 5). On the other hand, the barriers are significantly increasing with an increase in temperature for the bimolecular classes, whereas the unimolecular barriers are not affected by temperature (see also Table 5).

### 3.6 Decomposition scheme for TBP

Building upon the data presented in Tables 3 and 4, a decomposition scheme for TBP (Fig. 6) can be set up similar to TEG (Fig. 1). The reaction energies lead to the conclusion that TBP can decompose *via* homolytical bond cleavage and the elimination of hydrogen gas, alkane or alkene compounds, respectively. As it turns out, most unimolecular reactions (Fig. 6, left) can be neglected, since they are strongly endergonic (Table 3). Considering reactions with $H_2$, a hydrogen or an alkyl radical (*e.g.* $H^\bullet$, $t\text{-}C_4H_9^\bullet$), a bimolecular decomposition scheme of exclusively exergonic reactions can be formulated which involves radical and non-radical intermediate species. Within this scheme (Fig. 6, right), no P species smaller than the radical $PH_2^\bullet$ can be reached from TBP. If dehydrogenated $P(t\text{-}C_4H_9)$ is present, PH and atomic P can be reached on exergonic paths. The major pathways are discussed in the following.

**Pathway 5 "β-hydrogen elimination".** Fan *et al.* propose an "intramolecular β-hydrogen elimination" mechanism for TBP, confirmed by temperature-dependent FT-IR measurements performed during MOVPE in a $H_2$ atmosphere similar to the conditions in our study.[56] This exergonic alkene elimination ($i\text{-}C_4H_8$, isobutene) is the only unimolecular decomposition mechanism considered here as all other classes are highly

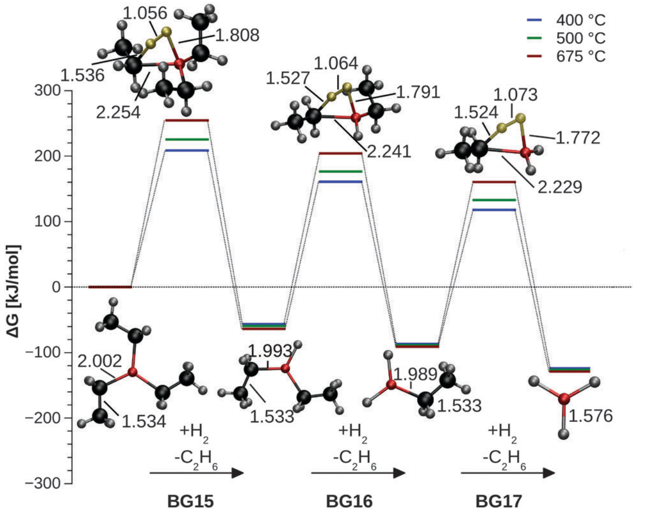

Fig. 5 Bimolecular $C_2H_6$ elimination reactions of $Ga(C_2H_5)_nH_{(3-n)}$ ($n$ = 3, 2, 1) with a reaction partner $H_2$. Changes in Gibbs energy ($\Delta G$) and barriers relative to the respective reactants (in kJ $mol^{-1}$) at experimental temperatures. Distances are given in Å.

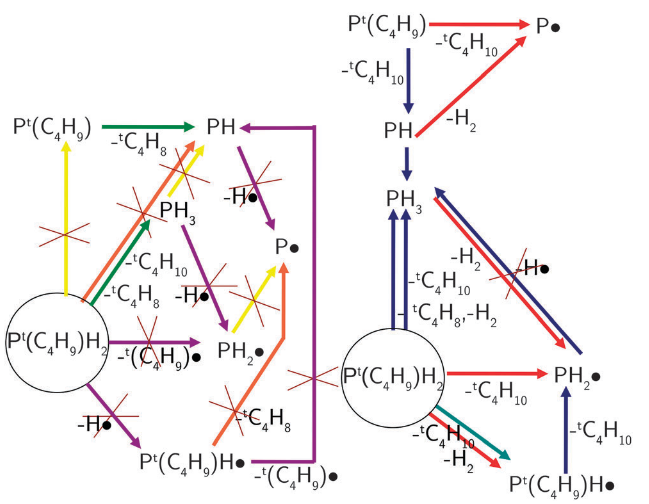

Fig. 6 Unimolecular (left) and bimolecular (right) decomposition reaction schemes for TBP considering information from Tables 3 and 4. Endergonic steps (at 400 °C) are crossed out or do not appear at all. Decomposition mechanisms are classified as radical cleavage reactions (magenta), alkane (orange), $H_2$ (yellow) and β-hydrogen (green) elimination reactions. Bimolecular elimination of alkanes and/or $H_2$ is considered with the $H^\bullet$ (red) or $t\text{-}C_4H_9^\bullet$ (turquoise) radicals or $H_2$ (blue) as reaction partners.

endergonic. It can be formulated for TBP as well as for the triplet species $P(t\text{-}C_4H_9)$ (AP6 and AP7). It involves the transfer of a hydrogen atom from a β-carbon atom of the butyl group to the phosphorous center. As the formal acceptor orbital of the P atom is occupied, the reaction cannot directly be compared to the β-hydride mechanism discussed for the Ga species (which exhibits an empty p-orbital).[57] A transition state with a rather large P–C distance was found (left path in Fig. 7). A detailed analysis of this reaction class is beyond the scope of this study and will be presented elsewhere.[58] The barrier for this reaction (AP6, $\Delta G^{\#}_{400}$ = 217.4 kJ $mol^{-1}$) is significantly higher than typical barriers of the calculated β-hydride elimination of Ga species (AG11–AG14, $\Delta G^{\#}_{400}$ = 82.6–149.9 kJ $mol^{-1}$). Furthermore, the trend of Gibbs energy barriers for the reaction with an increase in temperature is reversed with respect to the Ga β-hydride eliminations indicating differences in the mechanism. The equivalent decomposition from the triplet $P(t\text{-}C_4H_9)$ will not be discussed in detail here since its formation from TBP by eliminating $H_2$ is endergonic (AP10, $\Delta G_{400}$ = 123.2 kJ $mol^{-1}$).

**Pathway 6, "second order pathway, alkane elimination".** The bimolecular decomposition network of TBP is less interlinked compared to the bimolecular network of Ga species, since only a small number of decomposition products can be formulated. Reactions of TBP with a radical may lead to $P(t\text{-}C_4H_9)H^\bullet$ or $PH_2^\bullet$, from which recombination with further radical partners (*e.g.* $H^\bullet$) may lead to the original precursor or phosphine ($PH_3$). The most important bimolecular decomposition pathway for TBP is the exergonic concerted elimination of isobutene and $H_2$. A transition state can be found for this single-step reaction and is very high in energy (BP8, $\Delta E^{\#}$ = 264.6 kJ $mol^{-1}$). As expected for a bimolecular reaction, the unfavorable entropy factor increases this barrier even further to $\Delta G^{\#}_{400}$ = 337.3 kJ $mol^{-1}$ rendering it highly improbable that this barrier could be overcome at the given temperature (see the right path in Fig. 7). Several bimolecular reactions can be formulated for $P(t\text{-}C_4H_9)$, but applying the assumption given above (low reactant concentration due to missing decomposition pathways of TBP to this intermediate) no reaction barrier was calculated for these. Considering the thermodynamic schemes of both uni- and bimolecular decomposition pathways from TBP, only phosphine ($PH_3$) is likely to be formed in significant concentrations aside the original precursor in the gas phase. Notably, it is known from the experiment that the fraction of the original precursor finally arriving on the surface is very large for P species[4,56] in line with the large barriers presented here.

## 4. Discussion

The results presented in the previous sections will be discussed in the light of the assumptions presented earlier. In the first Results section, thermodynamic data were presented for many elementary reactions starting from the precursors TEG ($Ga(C_2H_5)_3$) and TBP ($PH_2(t\text{-}C_4H_9)$). Of course, it cannot be excluded that a reaction might be missing in the catalogue but considering the large amount of data and the various mechanism classes we are confident to have included the important reactions. Initially, all fragments were further investigated even when no direct route to this fragment was found. This enables a complete picture of the Ga and P species and a comprehensive evaluation of the methodology. The reaction channels described here encompass uni- and bimolecular reactions. As pointed out in the Introduction, unimolecular reactions are assumed to occur more likely than higher order reactions in a low-pressure atmosphere. Calculations of homolytical bond cleavage reactions (*e.g.* symmetric dissociation of

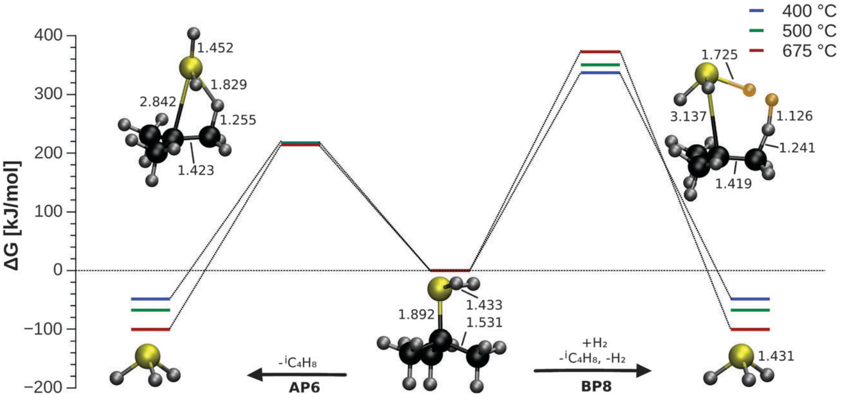

Fig. 7 Decomposition of TBP *via* β-hydrogen elimination of isobutene (reaction to the left) and bimolecular concerted elimination of isobutene and $H_2$ (reaction to the right) leading to phosphine, respectively. Changes in Gibbs energy ($\Delta G$) and barriers (in kJ mol$^{-1}$) at experimental temperatures. Distances are given in Å.

$H_2$, cleavage of $H^\bullet$, $CH_3^\bullet$, and $C_2H_5^\bullet$ from TEG) show that this decomposition class is consistently endergonic (for saturated reactants) and can therefore be neglected. Instead, β-hydride elimination reactions seem to be the dominant channel for TEG.

Additionally, some classes of bimolecular reactions have to be considered. These are reactions with the carrier gas $H_2$ which are thermodynamically accessible.[53] But also the radicals $H^\bullet$, $C_2H_5^\bullet$, $t$-$C_4H_9^\bullet$, *etc.* might be available in small concentrations as they can be produced in the course of a MOVPE procedure. Especially interesting is the formation of atomic hydrogen which can potentially be thermally desorbed from the substrate at 480–580 °C[16] as well as hydrogen (or carbon hydrates) *via* recombinative desorption.[59] As this work focused on pure gas phase reactions, the investigation of the latter reactions only becomes important when the surface is explicitly considered in the next phase of this study. Heterolytic dissociation reactions leading to ionic species are not considered as those will not occur in the gas phase and are of minor importance when focusing on relevant decomposition products. For example, an alternative (''barrierless'') mechanism for reaction AP6 involving an unstable, ionized intermediate step was proposed for the As-precursor TBA,[15] but the mechanism is probably surface-mediated. It becomes clear that the conclusions about viability of a reaction mechanism cannot be drawn from the thermodynamic data alone. Reaction barriers were calculated only for those exergonic reactions that were likely to occur based on the above assumptions. AP6, for instance, is strongly exergonic but exhibits a large barrier which will result in a very low reaction rate at all but the highest temperatures. Generally, transition state theory is valid here as large molecules and high temperatures are considered.[48]

The distribution of particles and temperature in the chamber are fluctuating irregularly. The Si-wafer is locally heated, so the highest temperature region is at and directly above the surface. The carrier gas flow induces a flux that transports the heated gas away from the wafer towards the gas outlet. As a consequence, the temperatures applied in this study (experimental surface temperatures of 400, 500 and 675 °C) represent upper bounds for the temperature in the gas phase. This has consequences in interpreting the calculated energies: since the change in Gibbs energy becomes more negative (or less positive) with an increase in temperature for all elementary reactions, a higher temperature means a more exergonic reaction. Thus, the presented thermodynamic values represent a lower bound for the discussed MOVPE precursors. In the real system, the reaction enthalpies will be less favorable due to colder local temperatures further away from the surface. The situation is different for the reaction barriers: as the barrier of a reaction generally *increases* with an increase in temperature (except AG20 and AP6), the calculated data are upper bounds for the barriers. In the real system, lower temperatures will result in smaller barriers. However, as the temperature dependence of Gibbs energy barriers is not strong, this effect will not be decisive. More important will be the higher kinetic energy of the molecules to overcome these (slightly raised) barriers at higher temperature.

Decomposition reactions on the surface have entirely different mechanisms and may lead to different inert and reactive intermediates. Catalytic effects of the surface might change the relevant barriers drastically, hence studies in this field have to be taken into account.[16,60] Thus we will continue our work in this field by applying periodic calculations to the GaP–Si system within the methodology validated here.

## 5. Conclusions

In this study, we present a comprehensive reaction catalogue for the gas phase decomposition reactions of triethylgallane ($Ga(C_2H_5)_3$, TEG) and *tert*-butylphosphine ($PH_2(t$-$C_4H_9)$, TBP) with thermodynamic and reaction barrier data based on DFT and *ab initio* (MP2, CCSD(T)) energies. From these data, conclusions can be drawn for the gas phase species relevant for the MOVPE growth of III/V-semiconductor GaP on silicon substrates. For TEG, we find a series of β-hydride elimination reactions as the most probable pathway leading to $GaH_3$ or even GaH at elevated temperatures (675 °C). Radical cleavage and other reactions as often proposed earlier are found to exhibit unfavorable thermodynamic characteristics. For TBP, a group 15 analogue of the β-hydride elimination reaction is found to be the energetically most accessible reaction. For all uni- and bimolecular TBP decomposition reactions, the computed barriers are very high leading to the conclusion of mainly the original precursor arriving at the surface. Methodologically, we could show that dispersion-corrected DFT computations at the PBE-D3 level perform well in comparison to MP2 and CCSD(T) benchmark data and can be used for further studies of these systems.

## Acknowledgements

We thank Prof. Kerstin Volz, Prof. Wolfgang Stolz and Dr. Andreas Beyer (Marburg) for fruitful discussions and insights into experimental details. Funding by the DFG through the Research Training Group "Functionalization of Semiconductors" (GRK 1782) is gratefully acknowledged. A.S. thanks the Beilstein Institut, Frankfurt am Main, for generous support *via* a PhD fellowship. Computational resources were kindly provided by HRZ Marburg, LOEWE-CSC Frankfurt and HLR Stuttgart.

## References

1 (*a*) B. Kunert, K. Volz, I. Németh and W. Stolz, *J. Lumin.*, 2006, **121**, 361; (*b*) N. Koukourakis, C. Buckers, D. A. Funke, N. C. Gerhardt, S. Liebich, S. Chatterjee, C. Lange, M. Zimprich, K. Volz, W. Stolz, B. Kunert, S. W. Koch and M. R. Hofmann, *Appl. Phys. Lett.*, 2012, **100**, 092107; (*c*) B. Kunert, K. Volz, J. Koch and W. Stolz, *Appl. Phys. Lett.*, 2006, **88**, 182108; (*d*) S. Liebich, M. Zimprich, A. Beyer, C. Lange, D. J. Franzbach, S. Chatterjee, N. Hossain, S. J. Sweeney, K. Volz, B. Kunert and W. Stolz, *Appl. Phys. Lett.*, 2011, **99**, 071109; (*e*) B. Kunert, K. Volz and W. Stolz, *Phys. Status Solidi B*, 2007, **244**, 2730.

2 D. Liang and J. E. Bowers, *Nat. Photonics*, 2010, **4**, 511.

3 B. Kunert, K. Volz, J. Koch and W. Stolz, *J. Cryst. Growth*, 2007, **298**, 121.

4 A. Beyer, J. Ohlmann, S. Liebich, H. Heim, G. Witte, W. Stolz and K. Volz, *J. Appl. Phys.*, 2012, **111**, 83534.

5 A. Beyer, I. Németh, S. Liebich, J. Ohlmann, W. Stolz and K. Volz, *J. Appl. Phys.*, 2011, **109**, 083529.

6 P. Gibart, *Rep. Prog. Phys.*, 2004, **67**, 667.

7 C. Wang, *J. Cryst. Growth*, 2004, **272**, 664.

8 M. Jacko and S. J. W. Price, *Can. J. Chem.*, 1963, **41**, 1560.

9 A. Brauers, *Prog. Cryst. Growth Charact. Mater.*, 1991, **22**, 1.

10 M. Trachtman and S. Beebe, *J. Phys. Chem.*, 1995, 15028.

11 D. Moscatelli, P. Caccioppoli and C. Cavallotti, *Appl. Phys. Lett.*, 2005, **86**, 91106.

12 R. Schmid and D. Basting, *J. Phys. Chem. A*, 2005, **109**, 2623.

13 J. Lee, Y. Kim and T. Anderson, *ECS Trans.*, 2009, **25**, 41.

14 T. R. Gow and R. Lin, *J. Cryst. Growth*, 1990, **106**, 577.

15 M. Boero, Y. Morikawa, K. Terakura and M. Ozeki, *J. Chem. Phys.*, 2000, **112**, 9549.

16 N. Bahlawane, F. Reilmann, L.-C. Salameh and K. Kohse-Höinghaus, *J. Am. Soc. Mass Spectrom.*, 2008, **19**, 947.

17 A. Saxler, D. Walker, P. Kung, X. Zhang, M. Razeghi, J. Solomon, W. C. Mitchel and H. R. Vydyanath, *Appl. Phys. Lett.*, 1997, **71**, 3272.

18 B. Wolbank and R. Schmid, *Chem. Vap. Deposition*, 2003, **9**, 272.

19 (*a*) S. H. Li, C. A. Larsen, N. I. Buchan and G. B. Stringfellow, *J. Electron. Mater.*, 1989, **18**, 457; (*b*) Y. S. Hiraoka, M. Mashita, T. Tada and R. Yoshimura, *Appl. Surf. Sci.*, 1992, **60–1**, 246; (*c*) C. H. Chen, D. S. Cao and G. B. Stringfellow, *J. Electron. Mater.*, 1988, **17**, 67.

20 K. Volz, A. Beyer, W. Witte, J. Ohlmann, I. Németh, B. Kunert and W. Stolz, *J. Cryst. Growth*, 2011, **315**, 37.

21 A. Y. Timoshkin, *Coord. Chem. Rev.*, 2005, **249**, 2094.

22 A. Y. Timoshkin and H. F. Schaefer III, *J. Phys. Chem. C*, 2008, **112**, 13816.

23 A. Y. Timoshkin, H. F. Bettinger and H. F. Schaefer III, *J. Cryst. Growth*, 2001, **222**, 170.

24 B. Mondal, D. Mandal, D. Ghosh and A. K. Das, *J. Phys. Chem. A*, 2010, **114**, 5016.

25 J. Schäfer, A. Simons, J. Wolfrum and R. A. Fischer, *Chem. Phys. Lett.*, 2000, **319**, 477.

26 A. Szabó, A. Kovács and G. Frenking, *Z. Anorg. Allg. Chem.*, 2005, **631**, 1803.

27 A. Y. Timoshkin and G. Frenking, *J. Am. Chem. Soc.*, 2002, **124**, 7240.

28 G. Zimmermann, A. Ougazzaden and A. Gloukhian, *Mater. Sci. Eng., B*, 1997, **44**, 37.

29 S. J. Hashemifar, P. Kratzer and M. Scheffler, *Phys. Rev. B: Condens. Matter Mater. Phys.*, 2010, **82**, 214417.

30 M. J. Frisch, G. W. Trucks, H. B. Schlegel, G. E. Scuseria, M. A. Robb, J. R. Cheeseman, G. Scalmani, V. Barone, B. Mennucci, G. A. Petersson, H. Nakatsuji, M. Caricato, X. Li, H. P. Hratchian, A. F. Izmaylov, J. Bloino, G. Zheng, J. L. H. Sonnenberg, M. Ehara, K. Toyota, R. Fukuda, J. Hasegawa, M. Ishida, T. Nakajima, Y. Honda, O. Kitao, H. Nakai, T. Vreven, J. A. Montgomery Jr., J. E. Peralta, F. Ogliaro, M. Bearpark, J. J. Heyd, E. Brothers, K. N. Kudin, V. N. Staroverov, R. Kobayashi, J. Normand, K. Raghavachari, A. Rendell, J. C. Burant, S. S. Iyengar, J. Tomasi, M. Cossi, N. Rega, N. J. Millam, M. Klene, J. E. Knox, J. B. Cross, V. Bakken, C. Adamo, J. Jaramillo, R. Gomperts, R. E. Stratmann, O. Yazyev, A. J. Austin, R. Cammi, C. Pomelli, J. W. Ochterski, R. L. Martin, K. Morokuma, V. G. Zakrzewski, G. A. Voth, P. Salvador, J. J. Dannenberg, S. Dapprich, A. D. Daniels, Ö. Farkas, J. B. Foresman, J. V. Ortiz, J. Cioslowski and D. J. Fox, *Gaussian 09, Rev. C.01*, Gaussian, Inc., Wallingford CT, 2009.

31 TURBOMOLE V6.3, a development of University of Karlsruhe and Forschungszentrum Karlsruhe GmbH, 1989–2007, TURBOMOLE GmbH, since 2007; available from www.turbomole.com, **2012**.

32 R. Ahlrichs, M. Bär, M. Häser, H. Horn and C. Kölmel, *Chem. Phys. Lett.*, 1989, **162**, 165.

33 J. P. Perdew, K. Burke and M. Ernzerhof, *Phys. Rev. Lett.*, 1996, **77**, 3865.

34 S. Grimme, J. Antony, S. Ehrlich and H. Krieg, *J. Chem. Phys.*, 2010, **132**, 154104.

35 S. Grimme, S. Ehrlich and L. Goerigk, *J. Comput. Chem.*, 2011, **32**, 1456.

36 O. Christiansen, H. Koch and P. Jørgensen, *Chem. Phys. Lett.*, 1995, **243**, 409.

37 C. Hättig and F. Weigend, *J. Chem. Phys.*, 2000, **113**, 5154.

38 F. Weigend, M. Häser, H. Patzelt and R. Ahlrichs, *Chem. Phys. Lett.*, 1998, **294**, 143.

39 C. Hättig, A. Hellweg and A. Köhn, *Phys. Chem. Chem. Phys.*, 2006, **8**, 1159.

40 P. Deglmann and F. Furche, *J. Chem. Phys.*, 2002, **117**, 9535.

41 P. Deglmann, F. Furche and R. Ahlrichs, *Chem. Phys. Lett.*, 2002, **362**, 511.

42 M. Tafipolsky and R. Schmid, *J. Comput. Chem.*, 2005, **26**, 1579.

43 O. Sackur, *Ann. Phys.*, 1911, **36**, 958.

44 K. Eichkorn, O. Treutler, H. Ohm, M. Häser and R. Ahlrichs, *Chem. Phys. Lett.*, 1995, **242**, 652.

45 F. Weigend, *Phys. Chem. Chem. Phys.*, 2006, **8**, 1057.

46 F. Weigend and R. Ahlrichs, *Phys. Chem. Chem. Phys.*, 2005, **7**, 3297.

47 B. C. Hoffman, C. D. Sherrill and H. F. Schaefer III, *J. Mol. Struct.*, 1996, **370**, 93.

48 H. Simka, B. G. Willis and I. Lengyel, *Prog. Cryst. Growth Charact. Mater.*, 1997, **35**, 117.

49 N. W. Mitzel, C. Lustig, R. J. F. Berger and N. Runeberg, *Angew. Chem., Int. Ed.*, 2002, **41**, 2519.

50 J. R. Durig, *J. Mol. Struct.*, 1977, **30**, 77.

51 (*a*) H. Oberhammer, R. Schmutzler and O. Stelzer, *Inorg. Chem.*, 1978, **17**, 1254; (*b*) J. Bruckmann and C. Krüger, *Acta Crystallogr., Sect. C: Cryst. Struct. Commun.*, 1995, **51**, 1152.

52 L. Bartell and H. Burgi, *J. Am. Chem. Soc.*, 1972, **531**, 5239.

53 Test calculations with different partial pressures for the carrier gas $H_2$ ($5 \times 10^{-2}$ atm) and the precursor molecules ($5 \times 10^{-4}$ atm) (for application of this approach, see E. Kalered, H. Pedersen, E. Janzén and L. Ojamäe, *Theor. Chem. Acc.*, 2013, **132**, 1) resulted in a constant shift of all reactions containing $H_2$ as a reactant or product. None of the conclusions regarding endo- or exothermicity of the reactions is affected by this shift.

54 D. R. B. Brittain, C. Y. Lin, A. T. B. Gilbert, E. I. Izgorodina, P. M. W. Gill and M. L. Coote, *Phys. Chem. Chem. Phys.*, 2009, **11**, 1138.

55 W. Koch and M. C. Holthausen, *A Chemist's Guide to Density Functional Theory*, Wiley-VCH, Weinheim, New York, 2nd edn, 2001.

56 G. H. Fan, R. D. Hoare, M. E. Pemble, I. M. Povey, A. G. Taylor and J. O. Williams, *J. Cryst. Growth*, 1992, **124**, 49.

57 (*a*) D. S. Matteson, *Organometallic Reaction Mechanisms*, Academic Press, New York and London, 1974, ch. 5; (*b*) J. E. Huheey, E. A. Keiter and R. L. Keiter, *Inorganic Chemistry, Principles of Structure and Reactivity*, Harber Collins College Publishers, 1993, 4th edn, p. 699.

58 A. Stegmüller and R. Tonner, in preparation.

59 C. Schwalb, M. Dürr and U. Höfer, *Phys. Rev. B: Condens. Matter Mater. Phys.*, 2009, **80**, 085317.

60 S. Salim, C. K. Lim and K. F. Jensen, *Chem. Mater.*, 1995, **7**, 507.

Supplementary Information

# Quantum Chemical Study on Gas Phase Decomposition Pathways of Triethylgallane (TEG, $Ga(C_2H_5)_3$) and Tertiarybutylphosphine (TBP, $PH_2(t\text{-}C_4H_9)$) under MOVPE Conditions

Andreas Stegmüller, Phil Rosenow, Ralf Tonner*

## Accuracy of structures investigated

For the title molecules, structural data from experiment were compared to PBE-D3/TZ and MP2/TZ results (see Figure SI-1). Solid TEG has four molecules in the unit cell, three triskel-shaped moieties and one exhibiting a rotated ethyl group. The triskel-shaped structure (more stable by ΔE(MP2/TZ) = 3.1 kJ $mol^{-1}$) will be prominently represented in the gas phase. Crystal packing effects cause the rotation of an ethyl group on one of the four units, as well as reduced mean bond lengths and disturbed molecular planarity as exhibited by the mean $C_\alpha$-Ga-$C_\alpha$-$C_\beta$ torsion angle (12.4°) on the three triskel-shaped molecules with respect to calculated values.[1] For TBP only data derived from vibrational spectroscopy are available,[2] so mean values of the structure of tri-*tert*-butylphosphine, $P(t\text{-}C_4H_9)_3$, determined by electron diffraction were used as a reference.[3a] One value (indicated by an asterisk) was taken from an X-ray diffraction study.[3b] $P(t\text{-}C_4H_9)_3$ was measured at 90 - 95 °C with assumed $C_3$ overall symmetry and internal $C_{3V}$ symmetry of the *tert*-butyl groups (with a possible deviation towards $C_3$ symmetry)[3], although “geometric constraints” might have a significant effect on the bond angles ($C_\beta$-$C_\alpha$-$C_\beta$) of tri-*tert*-butyl groups, as was shown by a study on tri-*tert*-butylmethane.[4] Bulky *tert*-butyl groups presumably cause slightly extended mean bond distances, larger *ligand-P-ligand* angles ($C_\alpha$-P-$C_\alpha$ as opposed to H-P-$C_\alpha$) and increased twist angles in $P^t(C_4H_9)_3$ as opposed to TBP. In this exemplary comparison, PBE-D3/TZ as well as MP2/TZ give good agreement to available experimental structures.

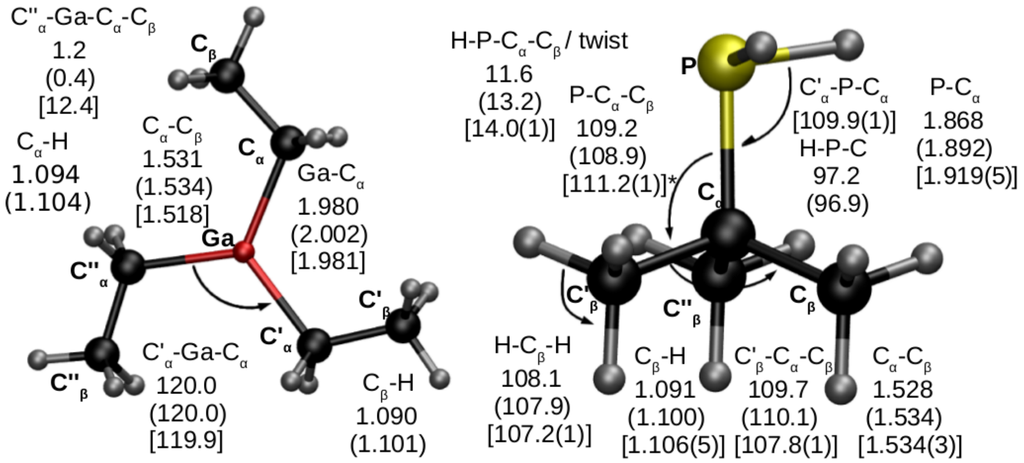

**Figure S1**: Optimized structures of TEG and TBP. Bond distances *A-B* (in Å), angles *A-B-C* (in °) and torsion angles *A-B-C-D* (in °) are given for MP2/TZ, PBE-D3/TZ (round brackets) and to averaged experimental values (in square brackets) of the three triskel-shaped molecules from X-ray diffraction results on TEG[1], electron diffraction data[3a] and X-ray analysis (designated by *)[3b] on P(*t*-Bu$_3$). Error of X-ray diffraction data approx. $3*10^{-4}$ Å and $2*10^{-2}$ °.

## References

[1] N. W. Mitzel, C. Lustig, R. J. F. Berger, N. Runeberg, *Angew. Chem. Int. Ed. Engl.*, **2002**, *41*, 2519.

[2] J. R. Durig, *J. Mol. Struc.*, **1977**, *30*, 77.

[3] a) H. Oberhammer, R. Schmutzler, O. Stelzer, *Inorg. Chem.*, **1978**, *17*, 1254; b) J. Bruckmann, C. Krüger, *Acta Cryst. C*, **1995**, *51*, 1152.

[4] L. Bartell, H. Burgi, *J. Am. Chem. Soc.*, **1972**, *531*, 5239.

**Table S1.** Absolute values for electronic and Gibbs Energies of the species investigated in kJ mol$^{-1}$.

| | PBE-D3/TZ | | | |
|---|---|---|---|---|
| | E | G (400 °C) | G (500 °C) | G (675 °C) |
| Ga(C2H5)3 | -5676287.9 | -5676141.8 | -5676214.6 | -5676352.7 |
| (C2H5)2Ga(C2H4)· | -5674571.6 | -5674463.4 | -5674536.6 | -5674674.9 |
| (C2H5)2Ga(CH2)· | -5571443.0 | -5571379.1 | -5571445.4 | -5571570.4 |
| HGaEt2 | -5470042.0 | -5470000.5 | -5470061.3 | -5470175.5 |
| Et2Ga' | -5468400.0 | -5468366.8 | -5468425.0 | -5468534.1 |
| EtGaC2H4 | -5466774.6 | -5466733.3 | -5466789.1 | -5466893.6 |
| H2GaEt | -5263795.3 | -5263833.0 | -5263878.1 | -5263961.8 |
| HgaEt' | -5262150.2 | -5262201.0 | -5262244.1 | -5262323.7 |
| GaEt | -5260659.6 | -5260720.8 | -5260761.7 | -5260837.2 |
| GaC2H4' | -5258947.8 | -5259040.0 | -5259080.3 | -5259154.1 |
| H3Ga | -5057547.6 | -5057673.0 | -5057703.5 | -5057759.0 |
| H2Ga' | -5055898.0 | -5056038.4 | -5056067.1 | -5056118.8 |
| GaH | -5054406.0 | -5054545.0 | -5054570.3 | -5054615.5 |
| Ga(0) | -5052813.9 | -5052945.4 | -5052967.1 | -5053005.8 |
| H2PBu | -1312975.7 | -1312879.4 | -1312932.6 | -1313033.2 |
| HPBu' | -1311314.2 | -1311240.9 | -1311293.0 | -1311391.3 |
| Pbu | -1309673.5 | -1309614.6 | -1309664.8 | -1309759.2 |
| PH3 | -900508.2 | -900609.8 | -900638.3 | -900638.3 |
| H2P' | -897191.4 | -897317.0 | -897340.9 | -897383.6 |
| HP | -897191.4 | -897317.0 | -897340.9 | -897383.6 |
| P(0) | -895565.8 | -895690.4 | -895711.2 | -895748.1 |
| isobutane | -415578.5 | -415471.8 | -415517.3 | -415603.4 |
| N-Butane | -415573.8 | -415468.1 | -415513.9 | -415600.3 |
| Bu' | -413856.8 | -413797.2 | -413844.1 | -413931.9 |
| isobutene | -412370.7 | -412318.3 | -412361.9 | -412443.6 |
| C2H6 | -209347.8 | -209339.3 | -209372.8 | -209434.8 |
| Et' | -207595.6 | -207630.7 | -207665.0 | -207728.1 |
| C2H4 | -206113.0 | -206155.2 | -206186.1 | -206242.8 |
| CH3' | -104468.6 | -104544.1 | -104571.0 | -104619.7 |
| H2 | -3062.3 | -3141.7 | -3160.4 | -3194.0 |
| H' | -1311.7 | -1407.7 | -1424.1 | -1453.6 |

| | MP2/TZ | | | | CCSD(T)/TZ//MP2/TZ |
|---|---|---|---|---|---|
| | E | G (400 °C) | G (500 °C) | G (675 °C) | E |
| Ga(C2H5)3 | -5672574.9 | -5672419.1 | -5672493.0 | -5672632.6 | -5672899.1 |
| (C2H5)2Ga(C2H4)· | -5670845.3 | -5670707.3 | -5670778.5 | -5670913.0 | -5671171.4 |
| (C2H5)2Ga(CH2)· | -5567860.9 | -5567773.2 | -5567838.0 | -5567960.1 | -5568139.1 |
| HGaEt2 | -5466592.5 | -5466527.7 | -5466586.9 | -5466697.9 | -5466826.8 |
| Et2Ga' | -5464936.7 | -5464891.7 | -5464949.9 | -5465058.8 | -5465161.7 |
| EtGaC2H4 | -5463292.6 | -5463264.7 | -5463320.4 | -5463424.3 | -5463501.5 |
| H2GaEt | -5260611.4 | -5260638.2 | -5260682.8 | -5260765.4 | -5260755.6 |
| HgaEt' | -5258954.2 | -5258994.2 | -5259036.7 | -5259115.2 | -5259088.9 |
| GaEt | -5257460.4 | -5257512.6 | -5257553.1 | -5257627.5 | -5257592.3 |
| GaC2H4' | -5255733.2 | -5255811.7 | -5255850.9 | -5255922.8 | -5255867.2 |
| H3Ga | -5054631.5 | -5054752.5 | -5054782.8 | -5054837.8 | -5054685.2 |

| | | | | | | |
|---|---|---|---|---|---|---|
| H2Ga' | -5052972.4 | -5053109.3 | -5053137.9 | -5053189.2 | | -5053016.3 |
| GaH | -5051473.1 | -5051610.8 | -5051635.9 | -5051681.0 | | -5051517.4 |
| Ga(0) | -5049887.5 | -895888.1 | -5050040.7 | -5050079.4 | | -5049917.2 |
| H2PBu | -1311576.9 | -1311461.8 | -1311513.9 | -1311612.6 | | -1311846.4 |
| HPBu' | -1309912.4 | -1309822.1 | -1309873.3 | -1309969.9 | | -1310176.7 |
| Pbu | -1308282.3 | -1308207.1 | -1308256.4 | -1308349.1 | | -1308537.5 |
| PH3 | -899638.8 | -899736.0 | -899764.3 | -899815.7 | | -899730.8 |
| H2P' | -897973.2 | -898093.2 | -898120.3 | -898168.9 | | -898058.5 |
| HP | -896341.8 | -896466.4 | -896490.2 | -896532.8 | | -896417.2 |
| P(0) | -894751.9 | -894876.6 | -894897.3 | -894934.3 | | -894809.2 |
| isobutane | -415036.0 | -414913.8 | -414958.7 | -415043.5 | | -415244.7 |
| N-Butane | -415028.2 | -414907.0 | -414952.3 | -415037.4 | | -415238.3 |
| Bu' | -413289.2 | -413211.9 | -413257.8 | -413343.9 | | -413498.7 |
| isobutene | -411826.4 | -411762.2 | -411805.3 | -411886.1 | | -412019.3 |
| C2H6 | -209070.6 | -209053.2 | -209086.5 | -209147.8 | | -209187.8 |
| Et' | -207308.8 | -207334.6 | -207368.4 | -207430.6 | | -207424.3 |
| C2H4 | -205840.7 | -205877.6 | -205908.4 | -205964.8 | | -205944.5 |
| CH3' | -104327.7 | -104399.8 | -104426.7 | -104475.3 | | -104394.3 |
| H2 | -3057.8 | -3135.7 | -3154.4 | -3188.0 | | -3077.9 |
| H' | -1312.3 | -1408.2 | -1424.6 | -1454.1 | | -1312.3 |

| | Transition States | | PBE-D3/TZ | | |
|---|---|---|---|---|---|
| | | E | G (400 °C) | G (500 °C) | G (675 °C) |
| AG11 | Ga(C2H5)3 → Ga(C2H5)2H + C2H4 | -5676156.3 | -5675950.1 | -5676019.4 | -5676151.3 |
| AG12 | Ga(C2H5)2H → Ga(C2H5)H2 + C2H4 | -5469913.9 | -5469818.3 | -5469874.0 | -5469979.1 |
| AG13 | Ga(C2H5)H2 → GaH3 + C2H4 | -5263671.5 | -5263688.6 | -5263731.1 | -5263810.2 |
| AG14 | Ga(C2H5) → GaH + C2H4 | -5260572.4 | -5260624.3 | -5260663.7 | -5260736.4 |
| AG15 | Ga(C2H5)3 → Ga(C2H5) + nC4H10 | -1312733.1 | -1312625.9 | -5675834.9 | -5675967.2 |
| AG17 | Ga(C2H5)H2 → HGa + C2H6 | -5263600.6 | -5263616.2 | -5263658.8 | -5263738.0 |
| AG19 | Ga(C2H5)H2 → Ga(C2H5) + H2 | -5263578.4 | -5263602.6 | -5263646.5 | -5263728.1 |
| AG20 | GaH3 → HGa + H2 | -5057336.1 | -5057469.3 | -5057499.9 | -5057555.4 |
| BG15 | Ga(C2H5)3 + H2 → Ga(C2H5)2H + C2H6 | -5679253.5 | -5679020.2 | -5679094.8 | -5679236.8 |
| BG16 | Ga(C2H5)2H + H2 → Ga(C2H5)H2 + C2H6 | -5473010.6 | -5472888.7 | -5472949.8 | -5473065.1 |
| BG17 | Ga(C2H5)H2 + H2 → GaH3 + C2H6 | -5266765.5 | -5266750.3 | -5266797.4 | -5266885.3 |
| BG18 | Ga(C2H5) + H2 → GaH + C2H6 | -5263654.6 | -5263674.9 | -5263719.0 | -5263800.7 |
| AP6 | P tC4H9H2 → PH3 + tC4H8 | -1312733.1 | -1312625.9 | -1312680.2 | -1312782.8 |
| BP8 | PtC4H9H2 + H2 → PH3 + tC4H8 + H2 | -1315773.4 | -1315644.2 | -1315703.8 | -1315816.7 |

| | Transition States | MP2/TZ//PBE-D3/TZ | CCSD(T)/TZ//PBE-D3/TZ |
|---|---|---|---|
| | | E | E |
| AG11 | Ga(C2H5)3 → Ga(C2H5)2H + C2H4 | -5672422.3 | -5672751.5 |
| AG12 | Ga(C2H5)2H → Ga(C2H5)H2 + C2H4 | -5466441.8 | -5466681.6 |
| AG13 | Ga(C2H5)H2 → GaH3 + C2H4 | -5260461.9 | -5260612.3 |
| AG14 | Ga(C2H5) → GaH + C2H4 | -5257348.9 | -5257482.5 |
| AG15 | Ga(C2H5)3 → Ga(C2H5) + nC4H10 | -1311266.4 | -1311553.3 |
| AG17 | Ga(C2H5)H2 → HGa + C2H6 | -5260377.2 | -5260518.7 |

| | | | |
|---|---|---|---|
| AG19 | Ga(C2H5)H2 → Ga(C2H5) + H2 | -5260340.2 | -5260499.9 |
| AG20 | GaH3 → HGa + H2 | -5054362.4 | -5054433.8 |
| BG15 | Ga(C2H5)3 + H2 → Ga(C2H5)2H + C2H6 | -5675506.4 | -5675852.3 |
| BG16 | Ga(C2H5)2H + H2 → Ga(C2H5)H2 + C2H6 | -5469526.0 | -5469782.0 |
| BG17 | Ga(C2H5)H2 + H2 → GaH3 + C2H6 | -5263544.9 | -5263710.9 |
| BG18 | Ga(C2H5) + H2 → GaH + C2H6 | -5260412.7 | -5260562.9 |
| AP6 | P tC4H9H2 → PH3 + tC4H8 | -1311266.4 | -1311553.3 |
| BP8 | PtC4H9H2 + H2 → PH3 + tC4H8 + H2 | -1314268.9 | -1314570.3 |

**Table S2.** Absolute values for entropies of the species investigated in kJ mol$^{-1}$ K$^{-1}$.

| | PBE-D3/TZ | | | MP2/TZ | | |
|---|---|---|---|---|---|---|
| | S (400 °C) | S (500 °C) | S (675 °C) | S (400 °C) | S (500 °C) | S (675 °C) |
| Ga(C2H5)3 | 0.7053 | 0.7512 | 0.8251 | 0.7159 | 0.7609 | 0.8333 |
| (C2H5)2Ga(C2H4)· | 0.7097 | 0.7541 | 0.8253 | 0.6899 | 0.7333 | 0.8031 |
| (C2H5)2Ga(CH2)· | 0.6444 | 0.6827 | 0.7439 | 0.6292 | 0.6667 | 0.7267 |
| HGaEt2 | 0.5915 | 0.6250 | 0.6789 | 0.5749 | 0.6077 | 0.6604 |
| Et2Ga' | 0.5667 | 0.5979 | 0.6479 | 0.5666 | 0.5971 | 0.6461 |
| EtGaC2H4 | 0.5437 | 0.5731 | 0.6201 | 0.5416 | 0.5704 | 0.6165 |
| H2GaEt | 0.4400 | 0.4612 | 0.4949 | 0.4349 | 0.4555 | 0.4885 |
| HgaEt' | 0.4210 | 0.4399 | 0.4700 | 0.4153 | 0.4337 | 0.4631 |
| GaEt | 0.4014 | 0.4177 | 0.4437 | 0.3966 | 0.4125 | 0.4380 |
| GaC2H4' | 0.3951 | 0.4099 | 0.4332 | 0.3851 | 0.3993 | 0.4219 |
| H3Ga | 0.3013 | 0.3100 | 0.3237 | 0.2989 | 0.3074 | 0.3207 |
| H2Ga' | 0.2839 | 0.2904 | 0.3005 | 0.2822 | 0.2885 | 0.2983 |
| GaH | 0.2501 | 0.2547 | 0.2617 | 0.2493 | 0.2538 | 0.2607 |
| Ga(0) | 0.2036 | 0.2065 | 0.2107 | 0.2049 | 0.2065 | 0.2107 |
| H2PBu | 0.5148 | 0.5478 | 0.6010 | 0.5050 | 0.5372 | 0.5893 |
| HPBu' | 0.5054 | 0.5364 | 0.5864 | 0.4970 | 0.5273 | 0.5762 |
| Pbu | 0.4874 | 0.5161 | 0.5624 | 0.4785 | 0.5066 | 0.5519 |
| PH3 | 0.2815 | 0.2892 | 0.3016 | 0.2799 | 0.2874 | 0.2995 |
| H2P' | 0.2685 | 0.2745 | 0.2837 | 0.2676 | 0.2734 | 0.2824 |
| HP | 0.2363 | 0.2406 | 0.2471 | 0.2359 | 0.2401 | 0.2466 |
| P(0) | 0.1935 | 0.1964 | 0.2006 | 0.1935 | 0.1964 | 0.2006 |
| isobutane | 0.4423 | 0.4692 | 0.5132 | 0.4362 | 0.4624 | 0.2006 |
| N-Butane | 0.4447 | 0.4715 | 0.5153 | 0.4390 | 0.4651 | 0.5079 |
| Bu' | 0.4553 | 0.4809 | 0.5225 | 0.4462 | 0.4711 | 0.5117 |
| isobutene | 0.4238 | 0.4474 | 0.4857 | 0.4197 | 0.4428 | 0.4803 |
| C2H6 | 0.3281 | 0.3424 | 0.3659 | 0.3253 | 0.3392 | 0.3620 |
| Et' | 0.3363 | 0.3495 | 0.3709 | 0.3318 | 0.3447 | 0.3655 |
| C2H4 | 0.3041 | 0.3151 | 0.3329 | 0.3026 | 0.3134 | 0.3309 |
| CH3' | 0.2653 | 0.2726 | 0.2839 | 0.2651 | 0.2722 | 0.2833 |
| H2 | 0.1851 | 0.1891 | 0.1951 | 0.1848 | 0.1888 | 0.1948 |
| H' | 0.1508 | 0.1537 | 0.1579 | 0.1508 | 0.1537 | 0.1579 |

| | Transition States | | | |
|---|---|---|---|---|
| | PBE-D3/TZ | S (400 °C) | S (500 °C) | S (675 °C) |
| AG11 | Ga(C2H5)3 → Ga(C2H5)2H + C2H4 | 0.6705 | 0.7161 | 0.7893 |
| AG12 | Ga(C2H5)2H → Ga(C2H5)H2 + C2H4 | 0.5404 | 0.5736 | 0.6267 |
| AG13 | Ga(C2H5)H2 → GaH3 + C2H4 | 0.4146 | 0.4353 | 0.4684 |

| | | | | |
|---|---|---|---|---|
| AG14 | Ga(C2H5) → GaH + C2H4 | 0.3861 | 0.4022 | 0.4279 |
| AG15 | Ga(C2H5)3 → Ga(C2H5) + nC4H10 | 0.5265 | 0.7191 | 0.7916 |
| AG17 | Ga(C2H5)H2 → HGa + C2H6 | 0.4157 | 0.4362 | 0.4689 |
| AG19 | Ga(C2H5)H2 → Ga(C2H5) + H2 | 0.4293 | 0.4497 | 0.4824 |
| AG20 | GaH3 → HGa + H2 | 0.3025 | 0.3106 | 0.3233 |
| BG15 | Ga(C2H5)3 + H2 → Ga(C2H5)2H + C2H6 | 0.7212 | 0.7707 | 0.8505 |
| BG16 | Ga(C2H5)2H + H2 → Ga(C2H5)H2 + C2H6 | 0.5916 | 0.6287 | 0.6884 |
| BG17 | Ga(C2H5)H2 + H2 → GaH3 + C2H6 | 0.4578 | 0.4825 | 0.5221 |
| BG18 | Ga(C2H5) + H2 → GaH + C2H6 | 0.4308 | 0.4508 | 0.4829 |
| AP6 | P tC4H9H2 → PH3 + tC4H8 | 0.5265 | 0.5593 | 0.6120 |
| BP8 | PtC4H9H2 + H2 → PH3 + tC4H8 + H2 | 0.5765 | 0.6143 | 0.6749 |

**Table S3.** Reaction entropies (changes) in kJ mol$^{-1}$ K$^{-1}$.

| Reaction Index | PBE-D3/TZ<br>dS | | | MP2/TZ<br>dS | | |
|---|---|---|---|---|---|---|
| | 673.15 K | 773.15 K | 948.15 K | 673.15 K | 773.15 K | 948.15 K |
| AG1 | 0.1977 | 0.1962 | 0.1937 | 0.1825 | 0.1809 | 0.1783 |
| AG2 | 0.1552 | 0.1566 | 0.1581 | 0.1247 | 0.1261 | 0.1277 |
| AG3 | 0.2044 | 0.2041 | 0.2027 | 0.1783 | 0.1780 | 0.1768 |
| AG4 | 0.1703 | 0.1685 | 0.1656 | 0.1825 | 0.1817 | 0.1789 |
| AG5 | 0.1710 | 0.1693 | 0.1666 | 0.1617 | 0.1601 | 0.1575 |
| AG6 | 0.1277 | 0.1288 | 0.1301 | 0.1257 | 0.1269 | 0.1283 |
| AG7 | 0.1877 | 0.1863 | 0.1840 | 0.1753 | 0.1736 | 0.1709 |
| AG8 | 0.1444 | 0.1458 | 0.1474 | 0.1393 | 0.1404 | 0.1417 |
| AG9 | 0.1334 | 0.1341 | 0.1347 | 0.1340 | 0.1348 | 0.1355 |
| AG10 | 0.1043 | 0.1055 | 0.1070 | 0.1051 | 0.1064 | 0.1080 |
| AG11 | 0.1903 | 0.1889 | 0.1866 | 0.1615 | 0.1602 | 0.1580 |
| AG12 | 0.1526 | 0.1512 | 0.1489 | 0.1626 | 0.1612 | 0.1590 |
| AG13 | 0.1653 | 0.1639 | 0.1616 | 0.1667 | 0.1653 | 0.1630 |
| AG14 | 0.1528 | 0.1521 | 0.1509 | 0.1553 | 0.1547 | 0.1535 |
| AG15 | 0.1408 | 0.1379 | 0.1339 | 0.1197 | 0.1168 | 0.1126 |
| AG16 | 0.1565 | 0.1544 | 0.1512 | 0.1437 | 0.1414 | 0.1378 |
| AG17 | 0.1382 | 0.1360 | 0.1327 | 0.1397 | 0.1375 | 0.1342 |
| AG18 | 0.1372 | 0.1372 | 0.1364 | 0.1515 | 0.1515 | 0.1509 |
| AG19 | 0.1465 | 0.1456 | 0.1439 | 0.1465 | 0.1458 | 0.1443 |
| AG20 | 0.1339 | 0.1338 | 0.1332 | 0.1351 | 0.1352 | 0.1348 |
| BG1 | 0.0388 | 0.0354 | 0.0308 | 0.0252 | 0.0217 | 0.0169 |
| BG2 | -0.1260 | -0.1265 | -0.1270 | -0.1425 | -0.1431 | -0.1436 |
| BG3 | 0.0121 | 0.0086 | 0.0037 | 0.0045 | 0.0010 | -0.0039 |
| BG4 | 0.0069 | 0.0036 | -0.0009 | 0.0149 | 0.0115 | 0.0068 |
| BG5 | -0.1318 | -0.1324 | -0.1330 | -0.1312 | -0.1319 | -0.1325 |
| BG6 | 0.0064 | 0.0036 | -0.0003 | 0.0085 | 0.0056 | 0.0017 |
| BG7 | 0.0212 | 0.0180 | 0.0135 | 0.0218 | 0.0185 | 0.0139 |

| | | | | | | |
|---|---|---|---|---|---|---|
| BG8 | -0.0204 | -0.0224 | -0.0250 | -0.0185 | -0.0205 | -0.0232 |
| BG9 | 0.0169 | 0.0159 | 0.0140 | 0.0172 | 0.0162 | 0.0145 |
| BG10 | 0.0005 | -0.0003 | -0.0016 | 0.0011 | 0.0005 | -0.0007 |
| BG11 | -0.0122 | -0.0128 | -0.0137 | -0.0117 | -0.0122 | -0.0130 |
| BG12 | -0.0302 | -0.0314 | -0.0328 | -0.0421 | -0.0434 | -0.0448 |
| BG13 | -0.0312 | -0.0319 | -0.0328 | -0.0315 | -0.0322 | -0.0331 |
| BG14 | -0.0145 | -0.0150 | -0.0155 | -0.0180 | -0.0188 | -0.0196 |
| BG15 | 0.0293 | 0.0271 | 0.0245 | -0.0005 | -0.0028 | -0.0057 |
| BG16 | -0.0084 | -0.0106 | -0.0132 | 0.0005 | -0.0018 | -0.0046 |
| BG17 | 0.0043 | 0.0021 | -0.0005 | 0.0046 | 0.0023 | -0.0006 |
| BG18 | -0.0082 | -0.0097 | -0.0113 | -0.0068 | -0.0083 | -0.0101 |
| BG19 | -0.0153 | -0.0137 | -0.0111 | -0.0168 | -0.0153 | -0.0128 |
| | -0.0026 | -0.0047 | -0.0072 | -0.0108 | -0.0130 | -0.0157 |

| | | | | | | |
|---|---|---|---|---|---|---|
| AP1 | 0.1414 | 0.1423 | 0.1433 | 0.1428 | 0.1438 | 0.1448 |
| AP2 | 0.2091 | 0.2076 | 0.2052 | 0.2088 | 0.2073 | 0.2049 |
| AP3 | 0.1862 | 0.1851 | 0.1832 | 0.1851 | 0.1840 | 0.1821 |
| AP4 | 0.1379 | 0.1389 | 0.1400 | 0.1385 | 0.1397 | 0.1409 |
| AP5 | 0.1080 | 0.1095 | 0.1115 | 0.1084 | 0.1099 | 0.1120 |
| AP6 | 0.1905 | 0.1889 | 0.1864 | 0.1946 | 0.1930 | 0.1905 |
| AP7 | 0.1727 | 0.1719 | 0.1704 | 0.1771 | 0.1764 | 0.1750 |
| AP8 | 0.1638 | 0.1620 | 0.1593 | 0.1670 | 0.1654 | 0.0000 |
| AP9 | 0.1304 | 0.1292 | 0.1274 | 0.1326 | 0.1315 | -0.4464 |
| AP10 | 0.1577 | 0.1575 | 0.1566 | 0.1583 | 0.1582 | 0.1575 |
| AP11 | 0.1399 | 0.1404 | 0.1406 | 0.1408 | 0.1415 | 0.1419 |
| AP12 | 0.1100 | 0.1111 | 0.1121 | 0.1107 | 0.1118 | 0.1130 |

| | | | | | | |
|---|---|---|---|---|---|---|
| BP1 | 0.0249 | 0.0241 | 0.0226 | 0.0260 | 0.0253 | 0.0238 |
| BP2 | 0.0453 | 0.0422 | 0.0380 | 0.0480 | 0.0449 | 0.0406 |
| BP3 | -0.0024 | -0.0042 | -0.0065 | 0.0004 | -0.0015 | -0.0038 |
| BP4 | 0.0214 | 0.0207 | 0.0193 | 0.0217 | 0.0211 | 0.0199 |
| BP5 | -0.0085 | -0.0087 | -0.0092 | -0.0084 | -0.0086 | -0.0091 |
| BP6 | -0.0224 | -0.0230 | -0.0239 | -0.0181 | -0.0186 | -0.0194 |
| BP7 | 0.0239 | 0.0216 | 0.0187 | 0.0262 | 0.0238 | 0.0208 |
| BP8 | 0.1905 | 0.1889 | 0.1864 | 0.1946 | 0.1930 | 0.1905 |
| BP9 | 0.0203 | 0.0181 | 0.0154 | 0.0220 | 0.0197 | 0.0168 |
| BP10 | 0.0061 | 0.0045 | 0.0027 | 0.0088 | 0.0071 | 0.0053 |

**Table S4.** Cartesian coordinates of structures investigated (PBE-TZ) in Å.

| | | | |
|---|---|---|---|
| GaEt3 | | | |
| | 22 | | |
| | -2161.9838898290 | | |
| C | -0.004562 | 0.034882 | -0.017162 |
| C | 0.025385 | -0.022435 | 1.514050 |
| Ga | 1.778538 | 0.015846 | -0.922255 |
| C | 3.452147 | -0.081353 | 0.168002 |
| C | 4.763555 | -0.088862 | -0.625012 |
| C | 1.887067 | 0.093963 | -2.917527 |
| C | 0.544795 | 0.156543 | -3.654560 |
| H | -0.080720 | -0.720841 | -3.434229 |
| H | -0.038870 | 1.041254 | -3.361020 |
| H | 0.669365 | 0.198966 | -4.748295 |
| H | 5.648033 | -0.144670 | 0.029297 |
| H | 4.816631 | -0.944469 | -1.314048 |
| H | 4.872217 | 0.817259 | -1.238823 |
| H | -0.984837 | -0.009281 | 1.953126 |
| H | 0.523787 | -0.933276 | 1.876723 |
| H | 0.574853 | 0.828933 | 1.941655 |
| H | -0.587751 | -0.806715 | -0.428550 |
| H | -0.536943 | 0.936856 | -0.364396 |
| H | 3.374766 | -0.979671 | 0.804100 |
| H | 3.428955 | 0.763454 | 0.877401 |
| H | 2.473937 | -0.780337 | -3.247107 |
| H | 2.515845 | 0.963188 | -3.175669 |

| | | | |
|---|---|---|---|
| Et2GaC2H4radical | | | |
| | 21 | | |
| | -2161.3301860120 | | |
| C | 0.019218 | -0.000946 | 0.011380 |
| Ga | -0.003840 | 0.022797 | 2.009401 |
| C | 1.708251 | 0.023455 | 2.958764 |
| C | 3.058047 | 0.009473 | 2.328537 |
| C | -1.360641 | -0.002800 | -0.656537 |
| C | -1.705770 | 0.046537 | 3.051568 |
| C | -1.541585 | 0.046913 | 4.575234 |
| H | 3.647963 | -0.867055 | 2.657687 |
| H | 3.025421 | -0.002115 | 1.230521 |

|  |  |  |  |
|---|---|---|---|
| H | 3.657311 | 0.886513 | 2.638893 |
| H | -2.510340 | 0.061495 | 5.099430 |
| H | -0.997599 | -0.842899 | 4.924529 |
| H | -0.972775 | 0.922351 | 4.921304 |
| H | -1.292720 | -0.015984 | -1.755908 |
| H | -1.954775 | -0.878989 | -0.358410 |
| H | -1.947148 | 0.885232 | -0.379067 |
| H | 0.603540 | -0.881881 | -0.303445 |
| H | 0.611079 | 0.867276 | -0.324060 |
| H | -2.305780 | -0.819033 | 2.724290 |
| H | -2.281214 | 0.927840 | 2.721823 |
| H | 1.726267 | 0.034823 | 4.056046 |

Et2GaCH2radical

18

-2122.050591769

|  |  |  |  |
|---|---|---|---|
| C | 0.015971 | -0.000636 | 0.011583 |
| C | -1.361393 | -0.002245 | -0.660980 |
| Ga | -0.006857 | 0.022293 | 2.005606 |
| C | -1.705317 | 0.045473 | 3.051476 |
| C | -1.540397 | 0.047846 | 4.574869 |
| C | 1.696508 | 0.022777 | 2.975645 |
| H | 2.674953 | 0.012461 | 2.484711 |
| H | -2.509240 | 0.061721 | 5.098598 |
| H | -0.995370 | -0.840816 | 4.925169 |
| H | -0.972876 | 0.924381 | 4.919961 |
| H | -1.288528 | -0.015313 | -1.759867 |
| H | -1.956622 | -0.878574 | -0.365612 |
| H | -1.948735 | 0.885971 | -0.386043 |
| H | 0.603116 | -0.881117 | -0.298920 |
| H | 0.610759 | 0.867384 | -0.318875 |
| H | -2.304209 | -0.821044 | 2.724529 |
| H | -2.281896 | 0.925357 | 2.719836 |
| H | 1.769221 | 0.033399 | 4.068060 |

GaEt2H

16

-2083.4289820670

|  |  |  |  |
|---|---|---|---|
| C | -0.004039 | -0.000016 | -0.013916 |
| C | 0.049164 | 0.000064 | 1.517707 |

| | | | |
|---|---|---|---|
| Ga | 1.760323 | -0.000004 | -0.941468 |
| C | 3.461866 | 0.000778 | 0.097767 |
| C | 4.752095 | -0.000401 | -0.728051 |
| H | 1.811272 | -0.000501 | -2.530513 |
| H | 0.577978 | -0.882356 | 1.906367 |
| H | 0.578031 | 0.882493 | 1.906274 |
| H | -0.955660 | 0.000115 | 1.968457 |
| H | 5.651976 | 0.000296 | -0.092904 |
| H | 4.814755 | -0.883102 | -1.380506 |
| H | 4.814938 | 0.880638 | -1.382730 |
| H | 3.426313 | 0.874316 | 0.771168 |
| H | 3.426011 | -0.871110 | 0.773270 |
| H | -0.565356 | 0.872965 | -0.388054 |
| H | -0.565372 | -0.873012 | -0.387981 |

GaEt2radical

15

-2082.8035811270

| | | | |
|---|---|---|---|
| Ga | 0.007241 | 0.016538 | 0.004989 |
| C | 0.006724 | 0.000733 | 2.038318 |
| C | 1.818476 | 0.006282 | -0.919108 |
| C | 1.829293 | 0.022641 | -2.446030 |
| C | -1.348928 | 0.004923 | 2.741167 |
| H | 1.306497 | -0.849807 | -2.863180 |
| H | 1.327040 | 0.915801 | -2.844153 |
| H | 2.853451 | 0.015124 | -2.851916 |
| H | -1.245653 | -0.004039 | 3.837971 |
| H | -1.938686 | 0.893977 | 2.476142 |
| H | -1.951028 | -0.871727 | 2.462903 |
| H | 0.614372 | 0.876544 | 2.325552 |
| H | 0.602021 | -0.887766 | 2.312094 |
| H | 2.351747 | 0.877915 | -0.501099 |
| H | 2.331514 | -0.886256 | -0.520290 |

EtGaC2H4

14

-2082.1748186060

| | | | |
|---|---|---|---|
| C | -0.016607 | 0.006097 | -0.018060 |
| C | 0.034436 | 0.003649 | 1.512747 |
| Ga | 1.716880 | -0.011321 | -0.950654 |

| | | | |
|---|---|---|---|
| C | 2.946881 | -0.087184 | -2.285785 |
| C | 3.827466 | 1.024386 | -2.797229 |
| H | 3.426147 | 2.023814 | -2.577487 |
| H | 4.857077 | 0.993698 | -2.400536 |
| H | 3.915942 | 0.955330 | -3.895880 |
| H | -0.978934 | 0.012397 | 1.942126 |
| H | 0.550072 | -0.885216 | 1.900535 |
| H | 0.566045 | 0.882015 | 1.903055 |
| H | -0.569410 | -0.866447 | -0.401979 |
| H | -0.553731 | 0.889405 | -0.399449 |
| H | 3.330474 | -1.103815 | -2.443761 |

GaEtH2

10

-2004.8737720130

| | | | |
|---|---|---|---|
| Ga | 0.010264 | 0.000562 | -0.006681 |
| H | -0.008002 | -0.000860 | 1.575376 |
| C | 1.737259 | -0.000606 | -0.989230 |
| C | 1.639889 | 0.013316 | -2.517961 |
| H | -1.362985 | 0.001847 | -0.794567 |
| H | 1.093043 | -0.861524 | -2.897580 |
| H | 1.106863 | 0.903007 | -2.882425 |
| H | 2.632616 | 0.009726 | -2.994235 |
| H | 2.313605 | 0.864972 | -0.620618 |
| H | 2.301459 | -0.880758 | -0.636289 |

HGaEtradical

9

-2004.2471676880

| | | | |
|---|---|---|---|
| Ga | 0.017522 | -0.001656 | -0.008273 |
| H | -0.015385 | 0.000655 | 1.610614 |
| C | 1.819876 | 0.000106 | -0.925576 |
| C | 1.839009 | -0.004782 | -2.451584 |
| H | 1.333033 | -0.890932 | -2.859885 |
| H | 1.327889 | 0.875747 | -2.865599 |
| H | 2.866702 | -0.003086 | -2.847552 |
| H | 2.334877 | 0.884687 | -0.512176 |
| H | 2.339802 | -0.878824 | -0.506367 |

GaEt_sing

8

-2003.6794457200

| | | | |
|---|---|---|---|
| Ga | -0.021750 | -0.189563 | 0.024547 |
| C | 1.885437 | -0.238396 | -0.764321 |
| C | 2.111085 | -1.473884 | -1.651043 |
| H | 1.968572 | -2.411688 | -1.091156 |
| H | 1.409426 | -1.502974 | -2.499659 |
| H | 3.125239 | -1.514161 | -2.079616 |
| H | 2.054553 | 0.690280 | -1.338601 |
| H | 2.613030 | -0.216442 | 0.066947 |

GaC2H4radical

7

-2003.0274501650

| | | | |
|---|---|---|---|
| C | 0.048350 | 0.122602 | -0.000942 |
| C | 0.029218 | 0.057658 | 1.491196 |
| Ga | 1.686265 | 0.363628 | -1.178388 |
| H | -0.406443 | -0.893912 | 1.850216 |
| H | 1.025906 | 0.157330 | 1.948079 |
| H | -0.614086 | 0.847495 | 1.923109 |
| H | -0.955396 | 0.021574 | -0.446614 |

GaH3

4

-1926.3181544450

| | | | |
|---|---|---|---|
| Ga | 0.000000 | -0.000000 | -0.000100 |
| H | 0.000000 | 0.000000 | 1.575510 |
| H | 1.364443 | 0.000000 | -0.788117 |
| H | -1.364443 | 0.000000 | -0.788117 |

H2Garadical

3

-1925.6898734640

| | | | |
|---|---|---|---|
| Ga | 0.009033 | 0.000000 | 0.005191 |
| H | -0.000957 | 0.000000 | 1.610990 |
| H | 1.401304 | 0.000000 | -0.794968 |

GaH

2

-1925.1215912030

|  |  |  |  |
|---|---|---|---|
| Ga | 0.000000 | 0.000000 | 0.002711 |
| H | 0.000000 | 0.000000 | 1.701799 |

H2PBu

16

-500.0860307843

|  |  |  |  |
|---|---|---|---|
| H | -0.010708 | -0.008076 | 0.019461 |
| C | -0.003819 | -0.006996 | 1.118061 |
| H | 1.048040 | -0.013736 | 1.450054 |
| H | -0.459134 | 0.932911 | 1.459057 |
| C | -0.745069 | -1.222480 | 1.681672 |
| C | -0.092705 | -2.519283 | 1.180803 |
| H | -0.095860 | -2.573056 | 0.082646 |
| H | 0.955506 | -2.565798 | 1.515602 |
| H | -0.610968 | -3.407921 | 1.567643 |
| C | -0.727210 | -1.188169 | 3.216824 |
| H | 0.311863 | -1.215812 | 3.580883 |
| H | -1.193171 | -0.270695 | 3.604032 |
| H | -1.258973 | -2.048721 | 3.646517 |
| P | -2.559999 | -1.276764 | 1.151599 |
| H | -2.340740 | -1.000405 | -0.237081 |
| H | -2.863582 | 0.093517 | 1.440332 |

HPBuradical

15

-499.4532169001

|  |  |  |  |
|---|---|---|---|
| H | -0.002141 | -0.009787 | 0.014563 |
| C | -0.002257 | -0.006740 | 1.113763 |
| H | 1.045598 | -0.013783 | 1.452346 |
| H | -0.459677 | 0.934551 | 1.449924 |
| C | -0.746653 | -1.226115 | 1.678766 |
| C | -0.086966 | -2.521274 | 1.181592 |
| H | -0.101910 | -2.588179 | 0.084754 |
| H | 0.966776 | -2.551738 | 1.506085 |
| H | -0.591749 | -3.409545 | 1.585729 |
| C | -0.735092 | -1.183783 | 3.214315 |
| H | 0.305512 | -1.186646 | 3.579964 |
| H | -1.222665 | -0.276728 | 3.598088 |
| H | -1.247531 | -2.055695 | 3.643592 |
| P | -2.525128 | -1.148219 | 1.060737 |

| | | | |
|---|---|---|---|
| H | -2.935401 | -2.355693 | 1.726672 |

PBu_triplett

14

-498.8282814328

| | | | |
|---|---|---|---|
| P | -0.000125 | 0.000000 | -0.348455 |
| C | -0.000018 | 0.000000 | 1.526729 |
| C | 1.455371 | -0.000000 | 2.023630 |
| C | -0.727675 | 1.260388 | 2.023623 |
| C | -0.727675 | -1.260388 | 2.023623 |
| H | -0.736370 | -1.275510 | 3.126339 |
| H | -1.770113 | -1.286948 | 1.677445 |
| H | -0.229523 | -2.176465 | 1.677356 |
| H | -0.736370 | 1.275510 | 3.126339 |
| H | -0.229523 | 2.176465 | 1.677356 |
| H | -1.770113 | 1.286948 | 1.677445 |
| H | 1.472722 | 0.000000 | 3.126374 |
| H | 1.999706 | -0.889481 | 1.677502 |
| H | 1.999706 | 0.889481 | 1.677502 |

H3P

4

-342.9854494715

| | | | |
|---|---|---|---|
| P | 0.002820 | 0.003049 | 0.002687 |
| H | 0.004650 | 0.004699 | 1.433405 |
| H | 1.432294 | 0.004539 | -0.056848 |
| H | -0.058935 | 1.431192 | -0.056633 |

H2Pradical

3

-342.3499143345

| | | | |
|---|---|---|---|
| P | 0.003934 | 0.000000 | 0.003879 |
| H | 0.003324 | 0.000000 | 1.439219 |
| H | 1.439124 | 0.000000 | -0.016758 |

HP

2

-341.7221444147

| | | | |
|---|---|---|---|
| P | 0.000000 | 0.000000 | 0.005751 |
| H | 0.000000 | 0.000000 | 1.445907 |

C4H10

14

-158.2854741665

| | | | |
|---|---|---|---|
| C | -0.002774 | 0.005456 | -0.001855 |
| C | 0.001095 | -0.001798 | 1.529095 |
| C | 1.425354 | -0.001889 | -0.553528 |
| C | -0.809293 | -1.173139 | -0.553447 |
| H | 1.431674 | 0.031841 | -1.652430 |
| H | 2.003124 | 0.857760 | -0.184725 |
| H | 0.554934 | 0.857528 | 1.933601 |
| H | -1.020583 | 0.032514 | 1.933773 |
| H | 0.480471 | -0.917268 | 1.910023 |
| H | -1.844900 | -1.159185 | -0.184491 |
| H | -0.357611 | -2.128898 | -0.244387 |
| H | -0.840788 | -1.159246 | -1.652345 |
| H | 1.954478 | -0.917104 | -0.244534 |
| H | -0.491251 | 0.937566 | -0.336019 |

Nbutane

14

-158.2837031436

| | | | |
|---|---|---|---|
| C | -0.017138 | 0.029674 | -0.059161 |
| C | -0.020896 | 0.036237 | 1.468848 |
| H | 1.010232 | 0.023368 | -0.452584 |
| H | -0.525615 | -0.863094 | -0.452529 |
| H | 0.465174 | 0.955110 | 1.837571 |
| H | -1.059691 | 0.075255 | 1.837591 |
| H | -0.526458 | 0.912074 | -0.470489 |
| C | 0.680293 | -1.179025 | 2.077256 |
| C | 0.676415 | -1.172218 | 3.605259 |
| H | 0.193607 | -2.097613 | 1.709034 |
| H | 1.719144 | -1.217387 | 1.709001 |
| H | 1.185630 | -2.054629 | 4.016962 |
| H | 1.185048 | -0.279551 | 3.998814 |
| H | -0.350938 | -1.165896 | 3.998889 |

C4H9radical

13

-157.6297195014

| | | | |
|---|---|---|---|
| C | 0.000032 | -0.000492 | 0.010780 |
| C | -0.003048 | -0.015540 | 1.500857 |
| C | 1.300233 | 0.000369 | 2.223208 |
| C | -1.230405 | 0.424808 | 2.222131 |
| H | -1.310093 | 1.532642 | 2.268336 |
| H | -2.146321 | 0.071014 | 1.725253 |
| H | 0.172280 | 1.020446 | -0.393989 |
| H | 0.798620 | -0.634319 | -0.403349 |
| H | -0.961923 | -0.337509 | -0.403977 |
| H | 2.051840 | -0.630900 | 1.725707 |
| H | 1.195157 | -0.339086 | 3.264724 |
| H | 1.735622 | 1.022075 | 2.272026 |
| H | -1.241473 | 0.071926 | 3.264394 |

C4H8

12

-157.0636885234

| | | | |
|---|---|---|---|
| C | -0.000711 | 0.000212 | 0.000407 |
| C | -0.001279 | -0.000122 | 1.503235 |
| C | 1.134034 | 0.000161 | -0.711947 |
| C | -1.354365 | 0.000574 | -0.652294 |
| H | 1.120828 | 0.000519 | -1.802758 |
| H | 2.110701 | -0.000268 | -0.225987 |
| H | -0.532407 | 0.882028 | 1.895819 |
| H | -0.534323 | -0.881231 | 1.895536 |
| H | 1.016285 | -0.001255 | 1.913103 |
| H | -1.939321 | 0.881750 | -0.342891 |
| H | -1.938889 | -0.881483 | -0.344563 |
| H | -1.281065 | 0.001599 | -1.746844 |

C2H6

8

-79.7363583008

| | | | |
|---|---|---|---|
| C | -0.000016 | -0.000019 | 0.003034 |
| C | 0.000012 | -0.000023 | 1.530375 |
| H | 1.022713 | -0.000167 | -0.399358 |
| H | -0.511521 | -0.885666 | -0.399311 |
| H | 0.511611 | 0.885568 | 1.932724 |
| H | -1.022711 | 0.000226 | 1.932788 |
| H | -0.511270 | 0.885775 | -0.399305 |

| | | | |
|---|---|---|---|
| H | 0.511167 | -0.885875 | 1.932719 |

C2H5radical

7

-79.0689847665

| | | | |
|---|---|---|---|
| C | -0.000222 | -0.000413 | 0.002743 |
| C | -0.003255 | -0.005852 | 1.485135 |
| H | 1.019979 | -0.000649 | -0.408530 |
| H | -0.499813 | -0.896991 | -0.418215 |
| H | -0.537259 | 0.867024 | -0.408499 |
| H | -0.848285 | 0.390277 | 2.045974 |
| H | 0.778658 | -0.515308 | 2.046019 |

C2H4

6

-78.5042915388

| | | | |
|---|---|---|---|
| C | 0.000000 | 0.000000 | 0.005728 |
| C | 0.000000 | -0.000000 | 1.338472 |
| H | 0.928304 | -0.000000 | -0.567736 |
| H | -0.928304 | -0.000000 | -0.567736 |
| H | -0.928293 | 0.000000 | 1.911926 |
| H | 0.928293 | 0.000000 | 1.911926 |

CH3radical

4

-39.7900020184

| | | | |
|---|---|---|---|
| C | -0.000222 | -0.000415 | 0.002744 |
| H | -0.002444 | -0.004398 | 1.088906 |
| H | 0.941537 | -0.000037 | -0.538421 |
| H | -0.939759 | 0.003197 | -0.542258 |

H2

2

-1.1663651729

| | | | |
|---|---|---|---|
| H | 0.000000 | 0.000000 | 0.008523 |
| H | 0.000000 | 0.000000 | 0.758969 |

Transition State Structures

AG11

22

| | | | |
|---|---|---|---|
| | | -2161.914820 | |
| C | -1.847611 | -1.062274 | 0.167494 |
| C | -2.974086 | -0.125181 | -0.271940 |
| Ga | -0.000015 | -0.322456 | -0.055618 |
| C | 0.000049 | 1.658417 | 0.891673 |
| C | 0.000021 | 1.963411 | -0.485411 |
| C | 1.847587 | -1.062276 | 0.167467 |
| C | 2.974057 | -0.125149 | -0.271910 |
| H | 2.885215 | 0.143531 | -1.334608 |
| H | 2.974953 | 0.813982 | 0.302074 |
| H | 3.966448 | -0.583082 | -0.133069 |
| H | -0.000031 | 0.573150 | -1.497462 |
| H | -0.917689 | 2.288130 | -0.975661 |
| H | 0.917719 | 2.288093 | -0.975706 |
| H | -3.966473 | -0.583120 | -0.133091 |
| H | -2.974999 | 0.813977 | 0.302000 |
| H | -2.885232 | 0.143451 | -1.334650 |
| H | -1.968328 | -1.345429 | 1.224222 |
| H | -1.884152 | -1.999605 | -0.408568 |
| H | -0.928001 | 1.734647 | 1.456488 |
| H | 0.928127 | 1.734606 | 1.456446 |
| H | 1.884148 | -1.999580 | -0.408637 |
| H | 1.968296 | -1.345476 | 1.224184 |

AG12

| | | | |
|---|---|---|---|
| | 16 | | |
| | -2083.367770 | | |
| C | -0.121262 | -0.396714 | -0.018805 |
| C | -0.075261 | -0.119300 | 1.484769 |
| Ga | 1.561382 | 0.042191 | -0.997798 |
| C | 3.218978 | -0.905912 | 0.070870 |
| C | 3.368609 | 0.464437 | 0.373355 |
| H | 2.015334 | 0.033417 | -2.495162 |
| H | 0.712017 | -0.701847 | 1.986994 |
| H | 0.120618 | 0.942127 | 1.695118 |
| H | -1.025756 | -0.379341 | 1.977070 |
| H | 2.176758 | 1.470719 | -0.343866 |
| H | 3.065384 | 0.845211 | 1.348595 |
| H | 4.129694 | 1.058291 | -0.132215 |
| H | 2.777199 | -1.570574 | 0.812089 |

|  |  |  |  |
|---|---|---|---|
| H | 3.857087 | -1.361336 | -0.683586 |
| H | -0.923809 | 0.187569 | -0.493375 |
| H | -0.351098 | -1.454900 | -0.213684 |

AG13

10

-2004.826600

|  |  |  |  |
|---|---|---|---|
| C | 1.336054 | -0.774959 | 0.000047 |
| C | 1.481974 | 0.629967 | 0.000115 |
| Ga | -0.709697 | -0.028486 | -0.000110 |
| H | -1.242230 | -0.265267 | 1.443306 |
| H | -1.242185 | -0.265968 | -1.443375 |
| H | 1.751948 | 1.151164 | -0.918312 |
| H | 1.751465 | 1.151127 | 0.918681 |
| H | 0.003302 | 1.492297 | -0.000478 |
| H | 1.472480 | -1.325704 | -0.928210 |
| H | 1.472089 | -1.325769 | 0.928300 |

AG14

8

-2003.646230

|  |  |  |  |
|---|---|---|---|
| C | 0.002391 | -0.000021 | -0.010060 |
| Ga | 0.004261 | 0.001635 | 2.264158 |
| C | 1.385111 | 0.000123 | 0.167321 |
| H | 1.706147 | 0.000724 | 2.100656 |
| H | 1.963318 | -0.921202 | 0.117751 |
| H | 1.963114 | 0.921558 | 0.116994 |
| H | -0.525755 | -0.921419 | -0.258388 |
| H | -0.525831 | 0.920951 | -0.259772 |

AG15

22

-2161.864940

|  |  |  |  |
|---|---|---|---|
| C | -0.143761 | 0.082583 | 0.520278 |
| Ga | 1.785981 | -0.229919 | 1.580512 |
| C | 3.434328 | 0.961390 | 1.142892 |
| C | 4.661684 | 0.218541 | 0.628648 |
| C | -1.109284 | -1.054969 | 0.758110 |
| C | 1.688194 | -0.596104 | -0.862333 |
| C | 2.041122 | 0.418247 | -1.897183 |

| | | | |
|---|---|---|---|
| H | 1.165241 | 1.041698 | -2.144067 |
| H | 2.853240 | 1.083047 | -1.574108 |
| H | 2.358411 | -0.046759 | -2.848729 |
| H | 4.477266 | -0.271615 | -0.339782 |
| H | 5.519917 | 0.893342 | 0.479278 |
| H | 4.984791 | -0.564666 | 1.330786 |
| H | -2.138694 | -0.745126 | 0.507416 |
| H | -0.878677 | -1.922637 | 0.123476 |
| H | -1.085621 | -1.396353 | 1.800822 |
| H | -0.255434 | 0.525993 | -0.474215 |
| H | -0.278794 | 0.905386 | 1.243725 |
| H | 3.111725 | 1.750974 | 0.446780 |
| H | 3.651276 | 1.439029 | 2.109833 |
| H | 0.888638 | -1.288575 | -1.133008 |
| H | 2.535360 | -1.146316 | -0.407455 |

AG17

10

| | | | |
|---|---|---|---|
| | -2004.799620 | | |
| C | -0.607514 | 0.544548 | 1.042911 |
| Ga | 1.715203 | -0.186195 | 0.808717 |
| C | -0.656718 | -0.888072 | 0.768584 |
| H | 1.033012 | 1.004818 | 0.020956 |
| H | 1.797305 | -0.358888 | 2.380474 |
| H | 0.382623 | -1.358331 | 0.315811 |
| H | -0.827002 | -1.518665 | 1.647095 |
| H | -1.302249 | -1.179549 | -0.069881 |
| H | -1.027511 | 1.229378 | 0.309930 |
| H | -0.631140 | 0.887418 | 2.074488 |

AG19

10

| | | | |
|---|---|---|---|
| | -2004.791130 | | |
| C | -0.219663 | 0.230132 | 0.639355 |
| C | -1.004302 | -1.062330 | 0.856024 |
| Ga | 1.759994 | 0.014218 | 0.858941 |
| H | 2.042388 | 1.823024 | 0.489344 |
| H | 3.070217 | 0.884276 | 0.783147 |
| H | -0.705189 | -1.846017 | 0.146508 |
| H | -0.855729 | -1.466222 | 1.866910 |

| | | | |
|---|---|---|---|
| H | -2.084243 | -0.891989 | 0.723980 |
| H | -0.370934 | 0.643644 | -0.368008 |
| H | -0.520228 | 1.020768 | 1.341536 |
| | | | |
| AG20 | | | |
| 4 | | | |
| | -1926.237590 | | |
| Ga | -0.000808 | 0.000000 | 0.000027 |
| H | -0.001268 | -0.000000 | 1.562202 |
| H | 1.790514 | 0.000000 | 0.369952 |
| H | 1.165194 | -0.000000 | -1.045495 |
| | | | |
| BG15 | | | |
| 24 | | | |
| | -2163.113440 | | |
| C | 0.975617 | 1.002698 | -2.024817 |
| C | -0.288845 | 1.842659 | -1.867779 |
| Ga | 1.716290 | -0.069107 | -0.186031 |
| C | 0.164102 | -0.275157 | 1.037121 |
| C | -0.231419 | 0.993054 | 1.800136 |
| C | 3.285502 | -1.152181 | -0.740661 |
| C | 4.247319 | -0.416898 | -1.677643 |
| H | 5.117341 | -1.038169 | -1.941407 |
| H | 4.630093 | 0.505898 | -1.218553 |
| H | 3.756220 | -0.129484 | -2.617981 |
| H | -1.105576 | 0.821306 | 2.447637 |
| H | 0.588061 | 1.351648 | 2.438139 |
| H | -0.486695 | 1.815340 | 1.117836 |
| H | -0.742786 | 2.100976 | -2.836718 |
| H | -1.052428 | 1.313856 | -1.280239 |
| H | -0.081394 | 2.789390 | -1.345238 |
| H | 0.749450 | 0.036727 | -2.506713 |
| H | 1.706473 | 1.485128 | -2.692752 |
| H | 0.405132 | -1.087313 | 1.739668 |
| H | -0.680825 | -0.640409 | 0.431938 |
| H | 3.807083 | -1.485055 | 0.169102 |
| H | 2.901430 | -2.066626 | -1.220044 |
| H | 2.353282 | 1.604783 | 0.064190 |
| H | 1.832408 | 1.490631 | -0.847300 |

BG16

18

-2084.559640

| | | | |
|---|---|---|---|
| C | 0.816086 | 0.774260 | -2.174410 |
| Ga | 1.650437 | 0.567311 | -0.105083 |
| C | 3.235057 | -0.619113 | -0.153912 |
| C | 4.181710 | -0.332638 | -1.322765 |
| C | -0.452021 | 1.615482 | -2.293852 |
| H | 0.431779 | 0.815660 | 0.834243 |
| H | 5.056473 | -1.001012 | -1.311117 |
| H | 4.557237 | 0.700203 | -1.293520 |
| H | 3.682093 | -0.467861 | -2.292454 |
| H | -0.950641 | 1.481253 | -3.265614 |
| H | -1.176149 | 1.357311 | -1.509123 |
| H | -0.234542 | 2.689452 | -2.185930 |
| H | 0.585725 | -0.302723 | -2.215362 |
| H | 1.508125 | 0.947855 | -3.013441 |
| H | 3.761157 | -0.524565 | 0.807354 |
| H | 2.865924 | -1.655714 | -0.197726 |
| H | 2.226858 | 2.199385 | -0.564681 |
| H | 1.695837 | 1.706415 | -1.344821 |

BG17

12

-2006.005060

| | | | |
|---|---|---|---|
| C | 0.899693 | 0.921297 | -2.209024 |
| C | -0.496928 | 1.535418 | -2.265439 |
| Ga | 1.859571 | 0.864128 | -0.197559 |
| H | 3.264026 | 0.213283 | -0.321555 |
| H | 0.695456 | 0.825924 | 0.829411 |
| H | -1.005838 | 1.315103 | -3.215610 |
| H | -1.131173 | 1.156767 | -1.452235 |
| H | -0.462767 | 2.630908 | -2.160964 |
| H | 0.853147 | -0.177749 | -2.254244 |
| H | 1.522382 | 1.214984 | -3.068424 |
| H | 2.076763 | 2.571355 | -0.620025 |
| H | 1.614113 | 1.997469 | -1.399608 |

BG18

10

-2004.820170

| | | | |
|---|---|---|---|
| C | 0.075888 | 0.142156 | 2.167328 |
| C | 0.707281 | -1.189363 | 2.574881 |
| Ga | -0.424993 | -0.345372 | -0.087037 |
| H | 0.821997 | 0.558209 | 0.908988 |
| H | 1.251794 | 0.562430 | -0.014461 |
| H | -0.963134 | 0.231394 | 2.511126 |
| H | 0.616789 | 0.989691 | 2.620682 |
| H | 0.926824 | -1.241622 | 3.652626 |
| H | 0.055037 | -2.044371 | 2.339209 |
| H | 1.664345 | -1.360227 | 2.051769 |

AP6

16

-499.993642

| | | | |
|---|---|---|---|
| C | 0.356405 | -0.020454 | 1.346927 |
| C | -0.536902 | -1.180948 | 1.641025 |
| C | -1.483984 | -1.100385 | 2.700341 |
| C | -0.211677 | -2.491271 | 1.001722 |
| P | -2.974843 | -0.343103 | 0.444485 |
| H | 0.645658 | 0.019308 | 0.289293 |
| H | 1.290631 | -0.114120 | 1.934820 |
| H | -0.110956 | 0.932482 | 1.623850 |
| H | 0.033267 | -2.382748 | -0.062622 |
| H | 0.682494 | -2.926286 | 1.489936 |
| H | -1.027110 | -3.216942 | 1.110141 |
| H | -1.797635 | -2.050996 | 3.144570 |
| H | -1.307107 | -0.308346 | 3.438073 |
| H | -2.547062 | -0.666391 | 2.193122 |
| H | -4.127222 | -0.250407 | -0.434583 |
| H | -3.091253 | -1.767455 | 0.489517 |

BP8

18

-501.151633

| | | | |
|---|---|---|---|
| C | 1.501772 | -0.259123 | 1.377282 |
| C | 1.274749 | 0.320059 | 0.015714 |
| C | 1.487383 | 1.790973 | -0.139306 |
| C | 1.281623 | -0.531469 | -1.119505 |
| P | -1.781072 | 0.817341 | 0.515731 |

|  |  |  |  |
|---|---|---|---|
| H | 1.050977 | 0.350521 | 2.173027 |
| H | 2.588781 | -0.292930 | 1.583334 |
| H | 1.121462 | -1.285379 | 1.459565 |
| H | 0.956793 | 2.371446 | 0.629377 |
| H | 2.564537 | 2.019072 | -0.021375 |
| H | 1.178961 | 2.151406 | -1.128460 |
| H | 1.626951 | -0.077693 | -2.055881 |
| H | 1.682055 | -1.539657 | -0.957547 |
| H | 0.106955 | -0.806853 | -1.410324 |
| H | -0.723468 | 1.147727 | 1.412687 |
| H | -1.493758 | 1.927098 | -0.339868 |
| H | -1.017822 | -0.856106 | -1.415996 |
| H | -1.313078 | -0.328286 | -0.685321 |

Inorganic Chemistry
Article
pubs.acs.org/IC

# $\beta$-Hydrogen Elimination Mechanism in the Absence of Low-Lying Acceptor Orbitals in $EH_2(t\text{-}C_4H_9)$ (E = N−Bi)

Andreas Stegmüller and Ralf Tonner*

Fachbereich Chemie and Material Sciences Center, Philipps-Universität Marburg, Hans-Meerwein-Straße, 35032 Marburg, Germany

*Supporting Information*

**ABSTRACT:** The $\beta$-hydrogen elimination reactions of group 15 alkyl compounds at the example of $EH_2(t\text{-}C_4H_9)$ (element E = N−Bi) were investigated and compared to the group 13 example of $GaH_2(t\text{-}C_4H_9)$. With the aid of extensive density functional theory based analysis of atomic and electronic structures at the transition state, we can derive three distinct reaction classes. The gallium compound follows the well-known $\beta$-hydride route with participation of an empty p orbital at the metal in a concerted, synchronous fashion, exhibiting a low barrier. For compounds with group 15 elements, we find highly nonsynchronous reactions with high reaction barriers. In the case of nitrogen, a proton-like H atom is transferred via attack of the nitrogen nonbonding electron pair. For the heavier homologues (P−Bi), E−$C_\alpha$ bond breaking occurs first and the H atom does not carry charge at the transition state. The reaction barrier in group 15 homologues is thus determined by the E−$C_\alpha$ bond strength down the group. The results enable a rationale for ligand design for precursors involved in chemical vapor-phase deposition processes because a good ligand needs to stabilize the positive charge at $C_\alpha$.

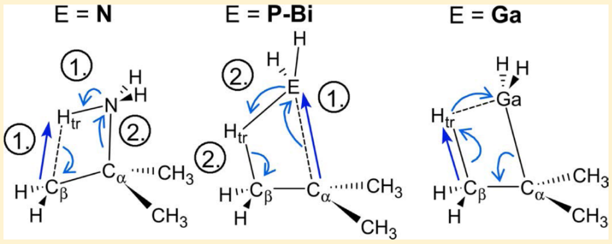

## INTRODUCTION

The understanding of reaction mechanisms for the formation and decomposition of inorganic compounds is of vital importance for progress in many research fields in material sciences. An excellent example is gas-phase chemistry, which can be crucial, e.g., for the conduction of chemical vapor deposition (CVD) techniques like organometallic vapor-phase epitaxy. Here, a clean and well-defined decomposition of the precursor molecules is essential for defect-free thin films.[1−3] Specifically, the growth of compound semiconductors of groups 13 and 15 (also known as III/V materials) is relevant for optoelectronic device applications.[4,5] In the current development toward the growth of metastable materials,[6] lower deposition temperatures are desired. This was not possible with precursor molecules of the first generation that carry hydrogen or methyl substituents because they exhibit large reaction barriers for bond breaking.[7] The advent of *tert*-butyl-substituted compounds paved the way for improved CVD procedures because of their much lower decomposition temperatures.[8,9] Typical precursor molecules of this second generation carry larger alkyl ligands like ethyl or *tert*-butyl, e.g., $M(C_2H_5)_3$ (M = B−In) or $EH_2(t\text{-}C_4H_9)$ (E = P, As). After long-standing discussions in the literature about the relative importance of homolytic dissociation and $\beta$-hydrogen elimination channels,[10−15] the latter was found to be responsible for the low-temperature decomposition characteristics.[3,9,16−18] In a recent computational study, we have shown that $\beta$-hydrogen elimination reactions are indeed the kinetically most favorable gas-phase decomposition pathways under CVD conditions for both group 13 and 15 compounds.[19] Thus, an understanding of this mechanism is crucial for further advancement in this research field.

$\beta$-Hydride elimination of transition-metal[20,21] and group 13 compounds is well understood and was investigated experimentally[11,12,22,23] and by quantum-chemical calculations.[24,25] It can be described as an interaction of the $\sigma(C_\beta{-}H_{tr})$ bond with the empty p-type orbital at the metal center (see Figure 1a). Thereby, the $C_\beta{-}H_{tr}$ bond is activated, a hydridic H atom is transferred, and the products are formed. However, how can we understand the respective mechanism from group 15 sources, which exhibit a filled p orbital at the central atom (Figure 1b)? Here, the interaction sketched for group 13 elements (the same

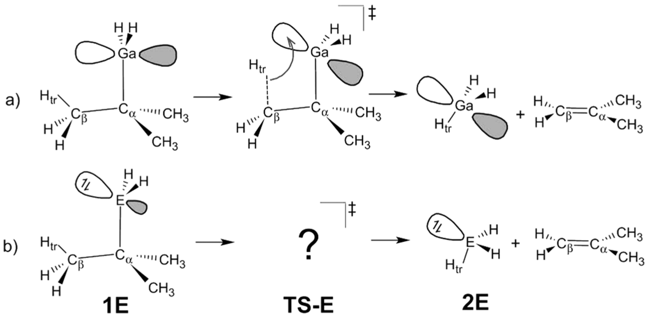

**Figure 1.** (a) Established mechanism of the $\beta$-hydride elimination exemplified for $GaH_2(t\text{-}C_4H_9)$. (b) Educt and products of $\beta$-hydrogen elimination from mono-*tert*-butylpnictogens (E = N−Bi) with the unknown TS structure indicated.

**Received:** March 26, 2015
**Published:** June 22, 2015

DOI: 10.1021/acs.inorgchem.5b00687
*Inorg. Chem.* 2015, 54, 6363−6372

mechanism is found for transition-metal compounds) is not possible because no empty orbital is available to activate the $C_\beta$−$H_{tr}$ bond. Also, the $H_{tr}$ atom is assumed to not be of hydridic nature; therefore, the usual term to describe this reaction is "β-hydrogen elimination".[9] As an example, the barrier for the reaction of $PH_2(t\text{-}C_4H_9)$ were found to be around twice as large as the barrier in $Ga(C_2H_5)_3$, which is already an indication for a different reaction mechanism.[19] It was also suggested in a computational study that β-hydrogen elimination for $AsH_2(t\text{-}C_4H_9)$ proceeds in a concerted and more complicated way than the group 13 analogue,[24] while early studies at the HF/6-31G level for $PH_2(t\text{-}C_4H_9)$ only focused on homolytic dissociation.[26]

Up to now, there is no conclusive picture of the β-hydrogen elimination reaction in group 15 compounds. It is crucial to have a detailed analysis of this mechanism for an optimization of precursor molecules for decomposition processes but also for a fundamental understanding of the underlying chemistry. Currently, ternary and quaternary compound semiconductors are heavily investigated for new optoelectronic devices, thus creating the need for reliable precursors also for heavier atoms.[5,27] The inclusion of group 15 elements other than P and As is thus timely and also enables us to discuss trends in the group. In this study, we present a quantum-chemical analysis of the β-hydrogen elimination reaction for $EH_2(t\text{-}C_4H_9)$ (E = N, P, As, Sb, Bi) in comparison to a group 13 precursor $[GaH_2(t\text{-}C_4H_9)]$. Via analysis of the structural and electronic contributions along the path of this intriguing reaction, we shed light on the underlying mechanism. These quantitative analyses are further translated into a model that highlights the differences between β-hydride and β-hydrogen elimination reaction mechanisms and also provides hints toward ligand optimization.

## ■ METHODS

Density functional theory with the generalized gradient approximation Perdew−Burke−Ernzerhof (PBE) functional[28,29] was applied together with the def2-TZVPP[30] basis set and effective core potentials for Sb and Bi[31] for unconstrained optimization of all structures. All subsequent analysis is based on these structures. It was shown that this computational level provides good accuracy in comparison to CCSD(*T*) benchmark values.[19] The nature of stationary points was confirmed via computation of the Hessian, also enabling the derivation of thermodynamic contributions to reaction energies and barriers ($p$ = 1 and 0.05 atm; $T$ = 298 and 675 K). The transition state (TS) structures, which connect reactant and product states via a single imaginary vibrational mode, were confirmed by intrinsic reaction coordinate (IRC) calculations. Partial charges were derived via atoms in molecules (AIM)[32] as well as natural population analysis (NPA).[33−35] The topological AIM[36] analysis was performed with AIMExt,[37] next to Wiberg bond indices (WBI)[38−40] on the basis of natural atomic orbitals (NAOs)[33−35] as implemented in *Gaussian09*.[41] Energy decomposition analysis with natural orbitals for chemical valence (EDA-NOCV)[42] calculations were performed with *ADF*[43] applying the BP86 functional[44,45] and the TZ2P+ Slater-type basis set[46] including scalar relativistic corrections[47] and frozen core approximation. Molecular orbital (MO) analysis was carried out with this method. EDA-NOCV analysis[48,49] allows the decomposition of bond energy into electrostatic, Pauli repulsion, and orbital relaxation contributions, subsequent to a structural fragment preparation energy:

$$\Delta E_{\text{bond}} = \Delta E_{\text{prep}} + \Delta E_{\text{elstat}} + \Delta E_{\text{Pauli}} + \Delta E_{\text{orb}} \tag{1}$$

This provides valuable insight into the nature of interactions between two fragments. With the NOCV extension, the orbital relaxation step in the procedure can be quantified by pairs of NOCVs and interpreted by their respective deformation density contributions $\Delta\rho$. This allows the determination of localized interactions stemming from fragment orbitals together with a quantification of their donating/accepting character by the NOCV eigenvalues $\pm\,\nu$.[42] The isosurface value for plotting densities was adjusted to emphasize the nature of MOs and NOCVs.

Analysis of the reaction force $F(\zeta)$ and reaction force constant $\kappa(\zeta)$[50,51] was carried out by numerical differentiation (centered finite differences) from high-resolution IRC calculations along a reaction coordinate $\zeta$ with

$$F(\zeta) = -\partial E/\partial\zeta \tag{2}$$

and

$$\kappa(\zeta) = \partial E^2/\partial^2\zeta \tag{3}$$

Points of inflection along the IRC can be observed as extrema of $F(\zeta)$, where $\kappa(\zeta) = 0$. Those points separate the IRC into reactant, transition, and product regions. The synchronicity of a reaction can already by evaluated by the symmetry of those regions with respect to the TS.

## ■ RESULTS

**Structures and Energies.** The electronic ($\Delta E$) and Gibbs ($\Delta G$) reaction energies for the β-hydrogen elimination reaction (Figure 1) of mono-*tert*-butyl compounds $EH_2(t\text{-}C_4H_9)$ (E = N−Bi, Ga) are shown in Table 1. All reactions are endothermic or very slightly exothermic at room temperature (E = N). It already turns out that three groups of elements can be distinguished: Energies within the group E = P−Bi (**1E** with E = P−Bi) are similar to each other, and E = Ga (**1Ga**) has the most positive and E = N (**1N**) the least positive reaction energy (even a negative $\Delta G$ value). Note that in CVD processes higher temperatures and lower total pressures are used.[52,53] Thus, these reactions will become thermodynamically more favorable under deposition conditions, as shown by Gibbs energies for typical conditions of $T$ = 675 K and $p$ = 0.05 atm in Table 1.[19] The reaction barriers almost linearly decrease within group 15 ($\Delta E^\ddagger$ = 275.8–171.2 kJ mol$^{-1}$), while the barrier for **1Ga** is significantly lower ($\Delta E^\ddagger$ = 120.1 kJ mol$^{-1}$). This generalizes previous findings for **1P**.[19]

**Table 1. Electronic Reaction Energies $\Delta E$, Gibbs Energies $\Delta G$, Reaction Barriers $\Delta E^\ddagger$ and $\Delta G^\ddagger$ in kJ mol$^{-1}$, and Imaginary Modes $\nu_{imag}$ in cm$^{-1}$ of the Reactions Introduced in Figure 1 at PBE/def2-TZVPP**

| | | $\Delta G$ | | | $\Delta G^\ddagger$ | | |
|---|---|---|---|---|---|---|---|
| E | $\Delta E$ | *a* | *b* | $\Delta E^\ddagger$ | *a* | *b* | $\nu_{imag}$ |
| N | 58.8 | −1.2 | −81.5 | 275.8 | 253.4 | 249.5 | 1402.3 |
| P | 82.6 | 17.0 | −63.1 | 238.8 | 218.0 | 213.2 | 606.3 |
| As | 80.7 | 15.1 | −64.3 | 213.2 | 193.9 | 188.8 | 435.7 |
| Sb | 80.9 | 14.9 | −71.3 | 187.2 | 168.8 | 166.4 | 295.0 |
| Bi | 81.4 | 14.9 | −70.8 | 171.2 | 152.6 | 150.0 | 253.1 |
| Ga | 87.3 | 26.0 | −49.0 | 120.1 | 115.1 | 122.3 | 810.8 |

[a] $T$ = 298 K and $p$ = 1 atm. [b] $T$ = 675 K and $p$ = 0.05 atm.

The vibrational frequencies $\nu_{imag}$ of the imaginary modes of the TS structure are highest for E = N (**TS-N**) with 1402.3 cm$^{-1}$ and decrease from 606.3 to 253.1 cm$^{-1}$ for **TS-P** to **TS-Bi**. Notably, $\nu_{imag}$(**TS-N**) is more than twice as large and $\nu_{imag}$(**TS-Ga**) only 204.5 cm$^{-1}$ larger than $\nu_{imag}$(**TS-P**), although the atomic mass of Ga is 5.00 times larger than that of N and 2.25 times larger than that of P. This is a first indication that the imaginary modes of **TS-E** (E = P−Bi) are constituted by an increasing contribution of molecular distortion including the heavy atom E, while **TS-N** and **TS-Ga** are dominated by the $C_\beta$−$H_{tr}$ stretch mode.

The TS structures for the *β*-hydrogen elimination reaction for $EH_2(t\text{-}C_4H_9)$ (E = N−Bi, Ga) are shown in Figure 2 together with selected structural parameters of the reactants. Again, three groups can be distinguished: **TS-N**, **TS-E** (E = P−Bi), and **TS-Ga**. The most pronounced difference is the $C_\alpha$−E distance, which is reactant-like for **TS-Ga**, slightly elongated for **TS-N**, and already considerably lengthened by >1 Å in **TS-E** (E = P−Bi). Additionally, **TS-Ga** exhibits a nearly tetrahedral arrangement at the Ga atom, while the ligand arrangement for the N atom in **TS-N** is closer to trigonal-planar. Another feature is the shape of the four-membered ring as indicated by the E−$C_\alpha$−$C_\beta$ angle. For **TS-Ga** and **TS-N**, the ring structure is distinct, while **TS-E** (E = P−Bi), on the other hand, show a very distorted ring structure. A further interesting measure is the $C_\beta$−$H_{tr}$ bond distance, which is very long for **TS-N** (1.653 Å) and **TS-Ga** (1.658 Å), while being close to the bond lengths in the reactants for **TS-E** (E = P−Bi), with decreasing bond lengths toward the heavier central atoms (1.245 Å for **TS-P** and 1.201 Å for **TS-Bi**). For all structures, the $C_\alpha$−$C_\beta$ distance shortens by 70−110 pm, leading to values midway between a typical C−C single and a C=C double bond. The $EH_2$ group in **TS-E** (E = P−Bi) exhibits a rotation of approximately 30° away from the alkyl ligand, which is later shown to be connected to the formation of nonbonding electron pairs at E.

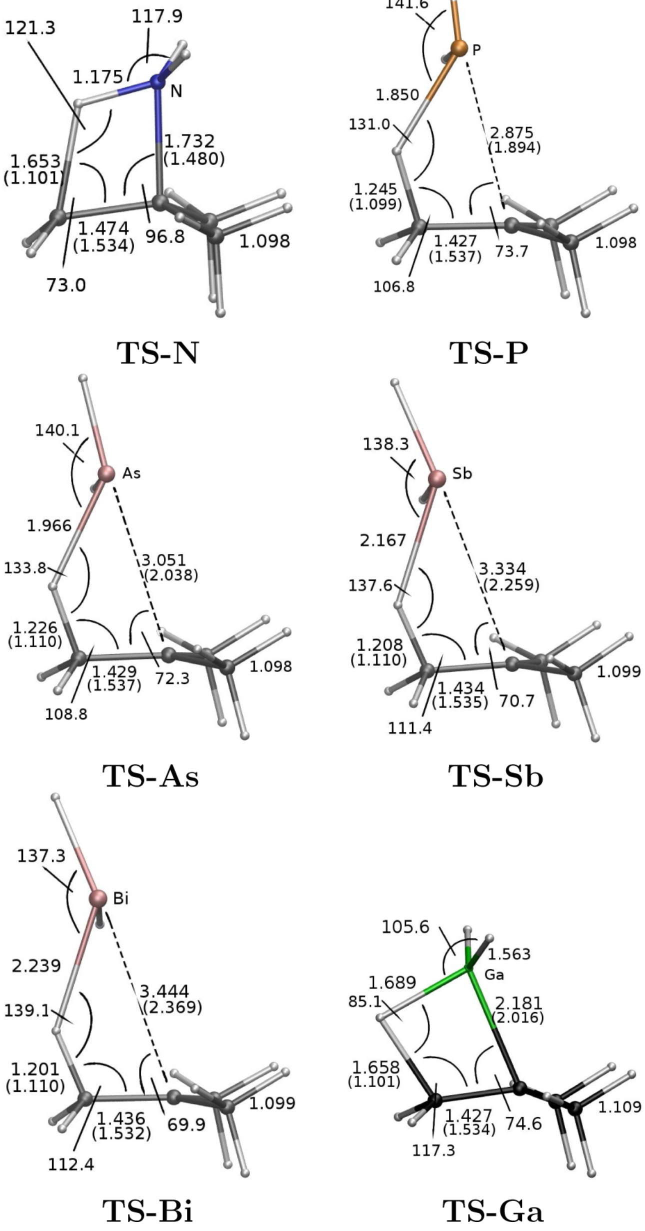

**Figure 2.** TS structures of $EH_2(t\text{-}C_4H_9)$ for *β*-H elimination reactions with selected bond lengths (in Å) and angles (in degree) for E = N−Bi, Ga. Selected reactant parameters are given in parentheses.

**Analysis along the Reaction Coordinate.** The reactant, TS (shaded area), and product regions were identified for the *β*-H elimination reactions of **1E** (E = N, P, Ga) by analysis of the reaction coordinate and are indicated in Figure 3. For **1As**−**1Bi**, features similar to those of **1P** were found. The TS region is marked by the two extrema in the force (magenta curves) where most of the bond rearrangements take place.

All molecules investigated undergo concerted elimination mechanisms, as proven by one minimum in the reaction force constant curve (blue curves). This is in line with the vibrational analysis exhibiting one imaginary mode. However, analysis reveals multiple steps during the reactions, indicating a nonsynchronous behavior of bond making and bond breaking.[51] In particular for **1N** and **1P**, asymmetric shapes of $E(\zeta)$ (black curves) and $F(\zeta)$ (magenta curves) can be observed, which is an indication of nonsynchronicity. The minimum of the force constant $\kappa(\zeta)$ (blue curves) does not coincide with the TS position, which has the same cause. For **TS-N** (Figure 3, left), we observe a slow energy increase in the first part of the reaction together with small forces because the rotations of the $NH_2$ and $C_\beta H_3$ groups taking place there do not require much energy. Then, a sharp increase of the energy curve, a maximum of the force curve, and a deep minimum of $\kappa(\zeta)$ mark breaking of the $C_\beta$−$H_{tr}$ bond, which is much more energy-intensive. After the TS, the energy decreases rather slowly with small forces, indicative of bond rearrangements that do not require much energy but take a number of steps, in this case mainly the final breaking of the N−$C_\alpha$ bond.

In the energy curve for **TS-P**, on the other hand, a steady increase before the TS is observed that can be traced back to the energy-intensive elongation of the P−$C_\alpha$ bond. This is not compensated for by a new bond forming simultaneously. The TS region is very broad here and also includes rotation of the $PH_2$ group. After the TS, a rapid energy decrease is associated with breaking of the $C_\beta$−$H_{tr}$ bond, which is compensated for by formation of the P−$H_{tr}$ bond at the same time.

For **TS-Ga**, the curves and the TS region appear much more symmetric, indicative of a higher synchronicity of bond making/bond breaking events. The extrema in the reaction force curve have similar heights, which underlines that processes before and after the TS have similar energetic measures. Here, it transpires that, in the case of the group 13 element, bond breaking and bond making occur at similar regions of the reaction coordinate. Thus, an energetic balancing is possible in contrast to the group 15 elements, where bond formation and bond cleavage are more separated events along the reaction coordinate. The structures at the points marking the TS regions are given in the Supporting Information (SI).

**Bonding Analysis.** Following the discussion of the structural features, we will now shed light on the bonding

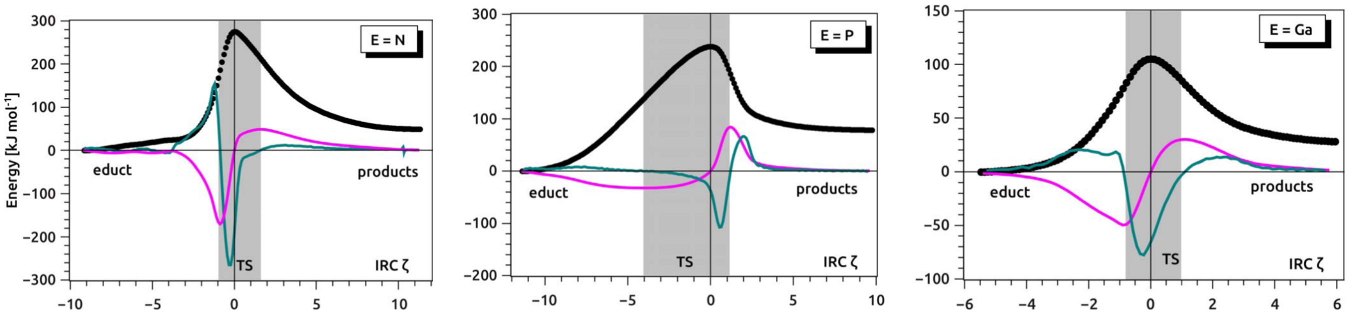

**Figure 3.** Energy $E(\zeta)$ along an IRC with $\zeta$ steps (black dots), reaction force $F(\zeta)$ (magenta curve), and reaction force constant $\kappa(\zeta)$ (blue curve) of the $\beta$-H elimination reactions of $EH_2(t\text{-}C_4H_9)$ with E = N (left), P (center), and Ga (right). The position of the TSs are set to $\zeta = 0$, and the transition regions are separated from the reactant (educt) and product regions by shaded areas as determined by extrema of the reaction force $F(\zeta)$, where $\kappa(\zeta) = 0$.

situation along the reaction path with complementary analysis methods. MO and partial charge analyses are followed by topological analysis of the electron density (AIM) and WBIs before we conclude with an energy decomposition analysis (EDA-NOCV). The combination of these methods leads to a conclusive picture of the reaction mechanism. It should be noted that bonding analysis at the TS is rarely conducted and leads to great insights if an informed choice of methods is applied.[54]

*MOs.* Selected MOs for **TS-N**, **TS-P**, and **TS-Ga** are shown in Figure 4. Again, **TS-P** represents the series of heavier group 15 homologues. The character of the highest occupied molecular orbital (HOMO) of **TS-N** is determined by the overlap of atomic orbitals (AOs) at $C_\beta$ and $H_{tr}$ with $\sigma(C_\beta{-}H_{tr})$-bonding character and the p(N) orbital, which has lone-pair (LP) character. In the HOMO−2, the second p(N) orbital with LP character is dominant and an overlap to the $\sigma(C_\beta{-}C_\alpha)$ bond can be identified. The HOMO−3 has N−$C_\alpha$-bonding character. Both the HOMO and HOMO−1 of **TS-P** have LP character at P with only minor contributions from the alkyl ligand [$p(C_\alpha)$ in the HOMO and $\sigma(C_\beta{-}H_{tr})$ in HOMO−1]. Only in the HOMO−7 are major contributions from the AOs of $C_\beta$ and $H_{tr}$ found. For **TS-Ga**, the HOMO exhibits contributions from $s(H_{tr})$ and $p(C_\alpha)$, while the HOMO−2 stems from the AOs $p(C_\beta)$ and $s(H_{tr})$. Information about the nature of the TS can be found here. For **TS-N**, we find MOs with bonding contributions between all atoms constituting the ring structure. A transformation of the $\sigma(C_\beta{-}H_{tr})$ and $\sigma(N{-}C_\alpha)$ bonds to a $\pi(C_\beta{-}C_\alpha)$ bond can be sketched. Furthermore, an orbital with bonding character between $H_{tr}$ and E was found in **TS-N** (HOMO−2) and **TS-Ga** (HOMO), but not among the MOs of **TS-E** (E = P−Bi). Orbital overlap between $H_{tr}$ and $C_\beta$ can be found in the HOMO−2 for **TS-Ga** and the HOMO−1 of **TS-P**. Furthermore, a partially empty $s(H_{tr})$ orbital is available in **TS-N** (LUMO+1) and **TS-P** (LUMO), which is not the case in **TS-Ga**, where it is fully occupied (contributions in HOMO and HOMO−2) in line with the interpretation of hydridic character. The $s(H_{tr})$ orbital can thus serve as a transit orbital for electron density flowing from the LP(E) toward the developing $\pi(C_\beta{-}C_\alpha)$ bond during the reaction. **TS-N** exhibits one MO with LP character (HOMO−2) at N, while **TS-P** exhibits two (HOMO and HOMO−1). The latter can be connected to the out-of-plane rotation of the $EH_2$ group found in the discussion of the TS structures above. While MO analysis thus gives qualitative insight, more quantitative measures are needed for a full description.

*Partial Charges.* Partial charge analysis gives information about the charge rearrangement in the course of the reaction. In Table 2, we present the absolute partial charges $q$ for important fragments ($H_{tr}$, $EH_2$, and $C_4H_8$) as well as charge shifts $\Delta q$ during the elimination reaction. The latter values are given for the steps reactant → TS and TS → products. The natural-orbital-based NPA charges were chosen, but similar trends are obtained by the electron-density-based AIM scheme (see the SI, Table S1).

First, we look at the charge shifts in the step from reactants to the TS (third column). We see that the $\beta$-hydrogen atom $H_{tr}$ gets positively charged by +0.43 e for **1N**, while it receives a significant amount of negative charge for **1Ga** (−0.27 e). For **1E** (E = P−Bi), $H_{tr}$ remains essentially neutral. A look at the other fragments shows that for **1N** the charge is shifted from $H_{tr}$ to the $C_4H_8$ fragment (−0.46 e), while for **1Ga**, the same fragment donates the charge (+0.25 e) to $H_{tr}$. Thus, we have the picture of a hydridic H atom for **1Ga**, while it seems more proton-like for **1N**. For **1E** (E = P−Bi), the charge shift as indicated by NPA is found to flow from the $C_4H_8$ fragment to the $EH_2$ fragment with less charge shifted for the heavier homologues (−0.52 e for **1P** to −0.33 e for **1Bi**). This leads to the $EH_2$ fragment being partially negatively charged at the TS and can be understood as an heterolytic cleavage of the E−$C_\alpha$ bond in **1E** (E = P−Bi) toward the TS. This is also found in the MO analysis, resulting in two MOs with LP character at E (see above).

The charge shift from the TS to the product is also found in Table 2 (fifth column). For **1N**, only small values are found in this step, and mainly the surplus charge at the $C_4H_8$ fragment (−0.13 e) is shifted toward the resulting product **2N**. This is in line with analysis of the reaction path and the finding that the majority of rearrangements is found from **1N** to **TS-N**. Similar conclusions can be drawn for **1Ga**. For **1E** (E = P−Bi), the charge is shifted from $EH_2$ to $H_{tr}$ and somewhat less to $C_4H_8$. Note that the $GaH_2$ fragment remains positively charged throughout the reaction, while the $NH_2$ fragment stays negatively charged. This is in accordance with the electronegativities of the atoms. Because these are the main determining factors for the observed partial charges, the interpretation of charge shifts can be limited, especially for H atoms.[55,56] We therefore decided to employ further methods to underline our arguments.

*AIM and WBIs.* The AIM method enables a topological analysis of the electron density and is thus independent of the choice of orbitals. Analysis of the bond paths and bond (or ring) critical points (BCPs and RCPs) helps to identify the

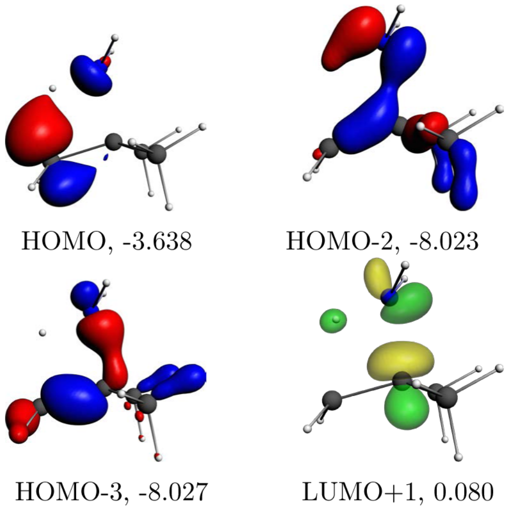

HOMO, -3.638 HOMO-2, -8.023

HOMO-3, -8.027 LUMO+1, 0.080

**TS-N**

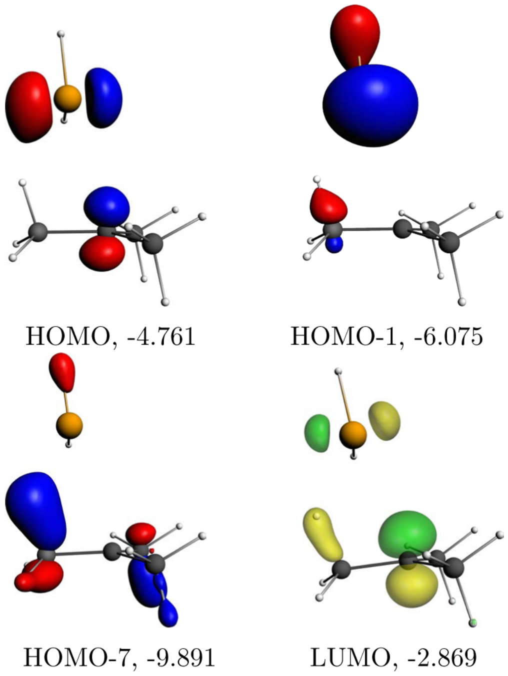

HOMO, -4.761 HOMO-1, -6.075

HOMO-7, -9.891 LUMO, -2.869

**TS-P**

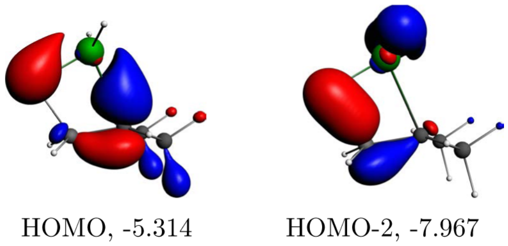

HOMO, -5.314 HOMO-2, -7.967

**TS-Ga**

**Figure 4.** Selected MOs for **TS-N** (top), **TS-P** (center), and **TS-Ga** (bottom) with orbital eigenvalues in electronvolts.

character of an interatomic interaction (Table 3).[36] Moreover, the second derivative (Laplacian, $\nabla^2\rho$) of the electron density indicates areas of charge accumulation and depletion. Nevertheless, a bond path should not be taken as proof for a chemical bond.[57,58] We combine the AIM with a second measure for the breaking and forming of bonds during the elimination reactions. WBIs based on NAOs were calculated for the TS structures, giving an estimate of the number of electrons that populate bonding orbitals.

**Table 2. NPA Partial Charges $q$ for the Fragments $H_{tr}$, $EH_2$, and $C_4H_8$ at the Educt State, TS, and Product (prd.) State and Charge Shifts ($\Delta q_{frag}$) for 1E → TS-E and TS-E → 2E + $C_4H_8$**

| $H_{tr}$ | $q$(reactant) | $\Delta q_{frag}$ → | $q$(TS) | $\Delta q_{frag}$ → | $q$(prd.) |
|---|---|---|---|---|---|
| N | −0.01 | *+0.43* | 0.41 | *−0.08* | 0.33 |
| P | 0.00 | *+0.08* | 0.09 | *−0.55* | −0.46 |
| As | 0.00 | *+0.07* | 0.07 | *−0.33* | −0.27 |
| Sb | 0.00 | *+0.03* | 0.02 | *−0.33* | −0.30 |
| Bi | −0.01 | *+0.02* | 0.01 | *−0.28* | −0.27 |
| Ga | −0.01 | *-0.27* | −0.28 | *−0.12* | −0.40 |
| $EH_2$ | $q$(reactant) | $\Delta q_{frag}$ → | $q$(TS) | $\Delta q_{frag}$ → | $q$(prd.) |
| N | −0.32 | *+0.04* | −0.28 | *−0.05* | −0.33 |
| P | 0.31 | *−0.52* | −0.21 | *+0.67* | 0.46 |
| As | 0.20 | *−0.38* | −0.18 | *+0.45* | 0.27 |
| Sb | 0.25 | *−0.39* | −0.14 | *+0.44* | 0.30 |
| Bi | 0.21 | *−0.33* | −0.12 | *+0.39* | 0.27 |
| Ga | 0.38 | *+0.02* | 0.41 | *−0.01* | 0.40 |
| $C_4H_8$ | $q$(reactant) | $\Delta q_{frag}$ → | $q$(TS) | $\Delta q_{frag}$ → | $q$(prd.) |
| N | 0.33 | *-0.46* | −0.13 | *+0.13* | 0 |
| P | −0.31 | *+0.43* | 0.12 | *-0.12* | 0 |
| As | −0.20 | *+0.31* | 0.12 | *-0.12* | 0 |
| Sb | −0.24 | *+0.36* | 0.12 | *-0.12* | 0 |
| Bi | −0.20 | *+0.31* | 0.11 | *-0.11* | 0 |
| Ga | −0.37 | *+0.25* | −0.13 | *+0.13* | 0 |

The molecular graph for **TS-N** in Figure 5 shows a RCP, which necessitates BCPs between all atoms in the ring. The N atom shows an accumulation of charge toward the $C_\alpha$ atom, in line with the bond lengths and the MO picture of the still significant bonding interactions between the two atoms. This is reflected in a considerable density at the BCP (0.12 au) and the largest WBI in the series (0.61). The $C_\beta$−$H_{tr}$ bond is already weak here (WBI: 0.30) and strongly polarized toward the $C_\beta$ atom (BCP lying very close to $H_{tr}$). The $H_{tr}$−N bond exhibits already significant values for the density at the BCP (0.20 au) and the WBI (0.48) midway between the reactant and product. Again, the bond is strongly polarized toward the N atom. The $C_\beta$−$C_\alpha$ bond exhibits values still closer to a single bond (WBI: 1.23).

The heavier homologues **TS-E** (E = P−Bi; **TS-P** is shown in Figure 5) exhibit significant differences. While the change of the $C_\beta$−$C_\alpha$ bond order is similar to that of **TS-N**, the $C_\beta$−$H_{tr}$ bond is still much stronger (WBI: 0.57−0.80) but again polarized toward the C atom. The results for the $H_{tr}$−E and $C_\alpha$−E bonds differ for AIM and WBI analysis. While the WBIs indicate slightly lower order for the former bond in comparison to **TS-N** and a significant $C_\alpha$−E bond order, the AIM results indicate a low density at the BCPs for $H_{tr}$−E, and for $C_\alpha$−E, no bond paths are found. Regarding the dependence of the WBIs on orbital partitioning and the erratic trend for **TS-Sb** and **TS-Bi**, we prefer to discuss the AIM results in this case. Thus, a negligible $C_\alpha$−E interaction is found in accordance with the large bond lengths. The contour plot shows electron

**Table 3. Electron Densities at BCPs ($\rho$[BCP], in au) Together with WBIs for the Four Bonds in the Ring of the TS Structures (Figure 5)**

| bond analysis | | reactant[a] | TS-N | TS-P | TS-As | TS-Sb | TS-Bi | TS-Ga | product[a] |
|---|---|---|---|---|---|---|---|---|---|
| $C_\alpha$–E | $\rho$[BCP] | | 0.12 | | | | | 0.07 | |
| | WBI | 1 | 0.61 | 0.52 | 0.53 | 0.43 | 0.57 | 0.44 | 0 |
| $C_\beta$–$H_{tr}$ | $\rho$[BCP] | | 0.09 | 0.18 | 0.19 | 0.20 | 0.20 | 0.08 | |
| | WBI | 1 | 0.30 | 0.57 | 0.61 | 0.80 | 0.78 | 0.38 | 0 |
| $H_{tr}$–E | $\rho$[BCP] | | 0.20 | 0.07 | 0.06 | 0.05 | 0.04 | 0.08 | |
| | WBI | 0 | 0.48 | 0.37 | 0.34 | 0.15 | 0.50 | 0.47 | 1 |
| $C_\beta$–$C_\alpha$ | $\rho$[BCP] | | 0.27 | 0.29 | 0.29 | 0.29 | 0.28 | 0.29 | |
| | WBI | 1 | 1.23 | 1.30 | 1.29 | 1.14 | 1.08 | 1.31 | 2 |

[a]Ideal reactant and product WBIs are given to discuss trends. Calculated reactant and product WBIs are provided in the SI.

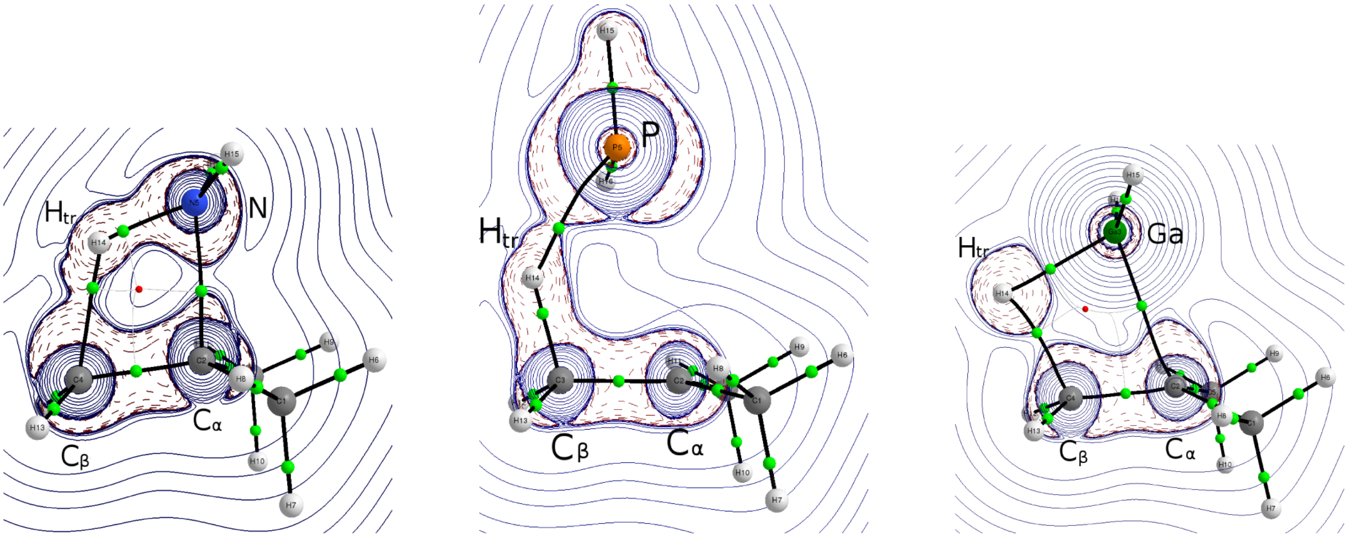

**TS-N** **TS-P** **TS-Ga**

**Figure 5.** Contour plot of $\nabla^2\rho$ within the $H_{tr}$–$C_\beta$–$C_\alpha$–E plane for **TS-E** (E = N, P, Ga) with BCPs and bond paths from AIM analyses. Dashed red lines indicate areas of electron accumulation (positive $\nabla^2\rho$). Filled blue lines indicate areas of density depletion (negative $\nabla^2\rho$). BCPs are marked by green dots and RCPs by red dots.

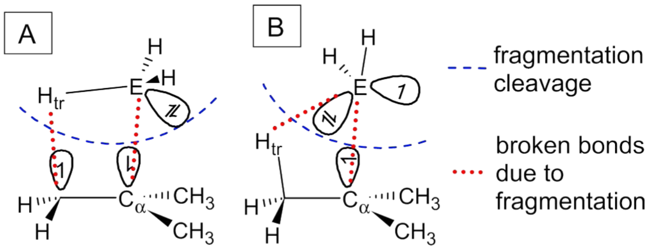

**Figure 6.** Schemes for EDA-NOCV analysis of **TS-E** separating into (a) $EH_3$ and $C_4H_8$ (E = Ga, N) or (b) $EH_2^\bullet$ and $C_2H_9^\bullet$) (E = P–Bi) fragments.

accumulation at the P atom, which is in line with the two MOs found exhibiting LP character.

The representative of group 13, **TS-Ga**, shows RCPs and BCPs similar to those of **TS-N**; however, significant quantitative differences can be observed. No electron accumulation is found around the Ga atom, in accordance with the absence of a nonbonding electron pair. The $C_\alpha$–Ga, $H_{tr}$–Ga, and $C_\beta$–$H_{tr}$ bonds are less polarized and leave much more density at the $H_{tr}$ atom, again underlining the hydridic character.

*Energy Decomposition Analysis.* Previous analyses gave insight into charge rearrangement and electron distribution. What is missing as the last piece of the puzzle is analysis of the energetic consequences of this charge flow at the TS. This can be achieved by applying the EDA-NOCV method.[54] The critical step in every decomposition method is the choice of fragments. The main criterion is a low value for the orbital interaction term ($\Delta E_{orb}$), meaning that the fragments' electronic structures are close to the one in the final molecule.[59] We tested various schemes and concluded that the fragmentations shown in Figure 6 should be used. The corresponding EDA results are found in the SI (Tables S3–S5). Note that, for E = P–Bi, fragmentation B with charged ($EH_2^-$ and $C_4H_9^+$) or neutral ($EH_2^\bullet$ and $C_2H_9^\bullet$) fragments leads to very similar results. These fragmentations indicate heterolytic and homolytic cleavage of the E–$C_\alpha$ bond, respectively. While the charged fragments are in line with the interpretation of an already broken E–$C_\alpha$ bond (see above), neutral decomposition leads to smaller orbital energy values and is thus presented subsequently.

While analysis of the EDA results can lead to great insight in many occasions,[60] here we will focus on partitioning of the orbital interaction term $\Delta E_{orb}$ in NOCV components. It should, nevertheless, be noted that the same grouping as that observed in the previous sections results from EDA: **TS-N** and **TS-Ga** show similar results, and **TS-E** (E = P–Bi) represent a separate group with only mild quantitative differences toward heavier homologues. The discussion will focus on the comparison of compounds analyzed with the same fragmentation to avoid ambiguities.

The results of EDA-NOCV analysis are given in Table 4 for fragmentation A (**TS-N** and **TS-Ga**) and in Table 5 for fragmentation B [**TS-E** (E = P−Bi)]. For all TSs, one major NOCV component is found that enables unambiguous interpretation of the orbital contribution to the bond energy. In the case of **TS-N**, the first deformation density ($\Delta\rho_1$) delivers by far the largest contribution to the orbital relaxation energy (−497.8 kJ mol$^{-1}$) and can be identified as a charge shift from the N atom into the region of the $C_\beta$−$H_{tr}$ bond combined with density accumulation between N and $C_\alpha$ from both atoms.

**Table 4. Most Significant NOCV Deformation Densities ($\Delta\rho$), Eigenvalues for NOCV Orbitals ($\nu$), and Corresponding Energies ($\Delta E$ in kJ mol$^{-1}$) for TS-N (Top) and TS-Ga (Bottom)**[a]

| | | | | |
|---|---|---|---|---|
| | 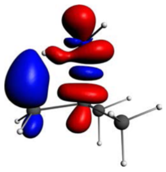 | | 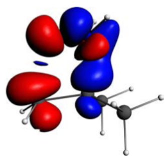 | |
| | $\Delta\rho_1$ | | $\Delta\rho_2$ | |
| **TS-N** | $\Delta E_1$ | $\nu_1$ | $\Delta E_2$ | $\nu_2$ |
| | -497.8 | ±0.586 | -43.9 | ±0.151 |
| | 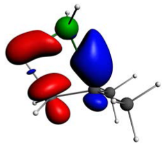 | | 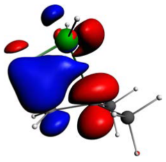 | |
| | $\Delta\rho_1$ | | $\Delta\rho_2$ | |
| **TS-Ga** | $\Delta E_1$ | $\nu_1$ | $\Delta E_2$ | $\nu_2$ |
| | -369.8 | ±0.544 | -68.5 | ±0.198 |

[a] The fragmentation is shown in Figure 6. Charge flow is from red to blue areas.

**Table 5. Most Significant NOCV Deformation Densities ($\Delta\rho$), Eigenvalues for NOCV Orbitals ($\nu$), and Corresponding Energies ($\Delta E$ in kJ mol$^{-1}$) for TS-E (E = P−Bi)**[a]

| | | | | | | |
|---|---|---|---|---|---|---|
| | 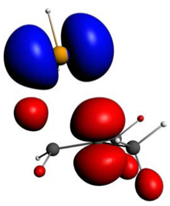 | | 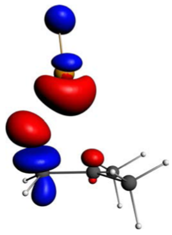 | | 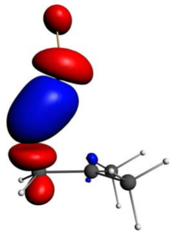 | |
| | $\Delta\rho_1^{\beta-\alpha}$ | | $\Delta\rho_2^{\alpha+\beta}$ | | $\Delta\rho_3^{\alpha+\beta}$ | |
| | $\Delta E_1$ | $\nu_1^{\beta-\alpha}$ | $\Delta E_2$ | $\nu_2^{\alpha+\beta}$ | $\Delta E_3$ | $\nu_3^{\alpha+\beta}$ |
| **TS-P** | -137.2 | ±0.173 | -23.3 | ±0.208 | -26.5 | ±0.174 |
| **TS-As** | -111.2 | ±0.163 | -15.3 | ±0.169 | -19.0 | ±0.147 |
| **TS-Sb** | -81.2 | ±0.144 | -12.0 | ±0.146 | -14.3 | ±0.133 |
| **TS-Bi** | -68.7 | ±0.119 | -10.4 | ±0.129 | -10.7 | ±0.116 |

[a] The fragmentation is shown in Figure 6. Charge flow is from red to blue areas.

The second component ($\Delta\rho_2$) shows reverse electron flow: from the $C_\beta$−$H_{tr}$ region toward the N atom, together with charge shifted to the $C_\alpha$ atom. This contributes far less to the orbital energy (−43.9 kJ mol$^{-1}$).

For **TS-Ga** (Table 4, bottom), essentially the same components are found but with inverse energy ordering. The first deformation density ($\Delta\rho_1$) shows the charge flow from the $C_\beta$ and $H_{tr}$ atoms into the Ga−$C_\alpha$ bonding region and delivers a stabilization of −369.8 kJ mol$^{-1}$. The second one ($\Delta\rho_2$) now is the inverse charge flow from the $C_\alpha$ and Ga atomic orbitals toward the $C_\beta$−$H_{tr}$ bond and into the ring structure. This contributes −68.5 kJ mol$^{-1}$ to the orbital energy. We can thus quantify the results from the partial charge and MO analysis above and conclude that the charge shift in the TS is reverse for **TS-N** in comparison to **TS-Ga**. While N is donating, Ga is accepting electron density at the TS.

The results for **TS-E** (E = P−Bi) are found in Table 5. Because of the unrestricted fragments, we have $\alpha$- and $\beta$-NOCV components. As is often observed, these spin densities can have either the same charge flow or a reversed one. Here, the first deformation density ($\Delta\rho_1$) shows the latter behavior. Thus, we subtracted the respective energies and eigenvalues as well as the densities. It appears that the net charge flow is from the p($C_\alpha$) and the $H_{tr}$ region to the LP region of E. This delivers stabilization energies of up to −137.2 kJ mol$^{-1}$ for **TS-P** and still −68.7 kJ mol$^{-1}$ for **TS-Bi**. For the other two major deformation densities, both spins exhibit the same charge shift pattern and are thus added up. Some more energy is gained by donation from LP(E) and $H_{tr}$ to $C_\beta$ ($\Delta\rho_2$) and into the E−$H_{tr}$ bonding region ($\Delta\rho_3$). The absence of charge donation between $C_\alpha$ and E supports the above analyses in the finding that this bond is already broken. The resulting picture is a slowly evolving E−$H_{tr}$ bond with density mainly stemming from E and a strong charge accumulation at E.

## ■ DISCUSSION

We will now discuss the observations from the analysis methods employed and arrive at a comprehensive picture of the $\beta$-H elimination mechanisms for the three distinct groups identified above: **1N**, **1E** (E = P−Bi), and **1Ga**.

**$\beta$-Proton Elimination of 1N.** **1N** exhibits the largest reaction barrier in the series. Analysis of the reaction path (Figure 3) shows a sharp increase in the reaction force close to the TS connected to this energy increase and a narrow transition region. From the reactant to the TS, the following changes in the chemical bonds can be identified:

(i) Breaking of the $\sigma(C_\beta-H_{tr})$ bond. The increased bond length (1.653 Å), a low WBI (0.30), and electron density at the BCP ($\rho$[BCP] = 0.09 au) are strong indicators for bond cleavage. The electrons are shifted from the bonding region toward the $C_\beta$ atom at the TS, which can be seen in the charge shift analysis [$\Delta q(H_{tr})$ = +0.41 e and $\Delta q(C_4H_8)$ = −0.46 e] and the HOMO, which has mainly $C_\beta$ character.

(ii) Formation of the $\sigma(N-H_{tr})$ bond. The N−$H_{tr}$ distance (1.175 Å) is already close to the distance in **2N** (1.022 Å). WBI (0.48) and $\rho$[BCP] (0.20 au) exhibit significant values underlined by the HOMO−2 with bonding character between the atoms. The electrons for the bond stem from LP(N), as can be seen qualitatively in the polar bond of the AIM analysis and quantitatively in the deformation density $\Delta\rho_1$ of EDA-NOCV analysis ($\Delta E_1$ = −497.8 kJ mol$^{-1}$).

Because the 1s($H_{tr}$) orbital has contributions to both the $\sigma(C_\beta-H_{tr})$ and $\sigma(H_{tr}-N)$ bonds, it can be understood as being an "electron transit orbital" for the charge flow between these regions. The $H_{tr}$ atom exhibits substantial positive partial charge at the TS ($q$ = +0.41 e). It can thus best be interpreted as being proton-like. It appears as if the nonbonding electron pair of the N atom pushes the electron density via the s($H_{tr}$) orbital toward the $C_\beta$ atom. Additionally, it is found that the $\sigma$(N$-$$C_\alpha$) bond is only moderately weakened (slight bond elongation, high WBI, and BCP and MOs with bonding character) and the $\pi$($C_\beta$$-$$C_\alpha$) bond only starts to form (increased WBI and bond shortening).

After the TS, the reaction force analysis shows a broader transition region with more rearrangements toward the products. The reaction energy is the only exothermic at ambient conditions ($\Delta G$ = $-1.2$ kJ mol$^{-1}$). The only major change in chemical bonds is as follows:

(i) $\sigma$(N$-$$C_\alpha$) bond breaking. The charge is shifted from $C_4H_8$ to $NH_3$, as indicated by the partial charge analysis. The $\pi$($C_\beta$$-$$C_\alpha$) bond constitutes mainly the electron density from the $C_\alpha$ atom.

***β*-Hydrogen Elimination of 1E (E = P−Bi).** The reaction barriers for **1E** (E = P−Bi) are between **1N** and **1Ga**, with values decreasing toward heavier homologues. All reactions are equally endothermic at ambient conditions and only become viable at CVD conditions. The reaction path analysis shows an extended transition region before the TS with rather small forces and a smooth change in the force constant. This can be understood by the only significant bond change from the reactant to TS:

(i) Breaking of the $\sigma$(E$-$$C_\alpha$) bond. The E$-$$C_\alpha$ bond lengths increase by approximately 1 Å. This is accompanied by rotation of the $EH_2$ moiety. All electronic indicators (WBI, $\rho$[BCP], MO, EDA-NOCV) provide evidence for complete cleavage of this bond at the TS. The charge is shifted to the E atom, which can be deduced from the partial charge [$\Delta q(EH_2)$ = $-0.52$ to $-0.31$ e] and MO analysis [HOMO and HOMO−1 with LP(E) character]. This charge stems from the $C_4H_8$ fragment, as found by partial charge shifts and EDA-NOCV ($\Delta E_1$ = $-137.2$ to $-68.7$ kJ mol$^{-1}$). The trend observed for the reaction barriers (lower for heavier homologues) can thus be understood from the decreasing E$-$$C_\alpha$ bond strength from P to Bi, which makes it increasingly easy to cleave the E$-$$C_\alpha$ bonds.

All other bonds are only mildly changed from the reactant to TS, as can be seen from the bond lengths being close to the reactant and the small changes in the electronic indicators. The interaction between E and $H_{tr}$ is still quite weak; e.g., the bond length for **TS-P** (1.850 Å) is still much longer than that for **2P** (1.431 Å), underlined by electronic analysis (small $\rho$[BCP] and no bonding MO). $H_{tr}$ is essentially neutral at the TS [$\Delta q(EH_2)$ = +0.08 to +0.02 e]. Thus, the H atom transferred is best understood to be a neutral H atom.

From the TS to product, the changes indicated by reaction path analysis point toward a quite rapid development to the products: (i) The E$-$$H_{tr}$ bond formed is initiated by the electrons from LP(E). (ii) The $\pi$($C_\beta$$-$$C_\alpha$) bond is formed with electron density from the $\sigma$($C_\beta$$-$$H_{tr}$) bond. The 1s($H_{tr}$) orbital can act as a transit orbital for the electronic rearrangement because it is partially occupied in the TS.

***β*-Hydride Elimination of 1Ga.** The reaction barrier for **1Ga** is the lowest in the series, while the reaction is also the most endothermic one. Reaction path analysis reveals rather symmetric changes before and after the TS (synchronous reaction). The $\sigma$($C_\beta$$-$$H_{tr}$) bond is strongly elongated ($d$ = 1.658 Å) and small WBI (0.38) and $\rho$[BCP] (0.09 au) are observed. It is not completely broken, as a bonding MO (HOMO−2) indicates. The charge is shifted from the region of the $\sigma$($C_\beta$$-$$H_{tr}$) bond toward the Ga and $C_\alpha$ atoms, as shown by EDA-NOCV ($\Delta E_1$ = $-369.8$ kJ mol$^{-1}$).

$H_{tr}$ receives a negative partial charge ($\Delta q$ = $-0.27$ e) before the TS, which stems almost entirely from the $C_4H_8$ fragment ($\Delta q$ = +0.25 e). This indicates the transfer of a $H_{tr}$ atom with hydridic character, as commonly assumed. The TS exhibits a tetrahedral arrangement at the Ga atom, enabling the transfer of this hydridic $H_{tr}$ to the $GaH_2$ fragment.

All other bonds in the system are about to form [Ga$-$$H_{tr}$ and $\pi$($C_\beta$$-$$C_\alpha$)] or break (Ga$-$$C_\alpha$) simultaneously at the TS. The formation of the Ga$-$$H_{tr}$ bond is completed by electron transfer from the $C_4H_8$ fragment [$\Delta q$(TS → product) = +0.13 e], and the elimination closes by breaking the Ga$-$$C_\alpha$ bond. The rearrangements necessary for these two processes are revealed in the reaction path analysis.

## ■ CONCLUSION

*β*-H elimination reactions for group 15 alkyl species differ significantly from the respective group 13 compounds. For the example of $EH_2(t\text{-}C_4H_9)$ with E = N−Bi and Ga, we find three distinct mechanisms summarized in Figure 7.

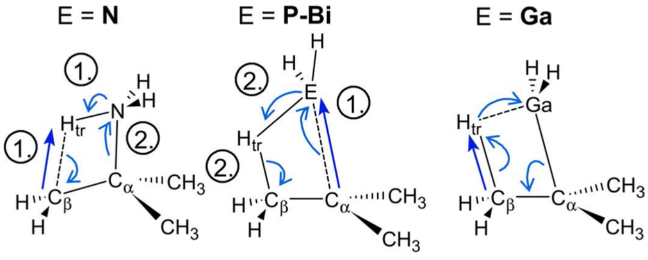

**Figure 7.** Chronology of the reaction steps for *β*-H elimination reactions for $EH_2(t\text{-}C_4H_9)$ with E = N (left), E = P−Bi (center), and E = Ga (right). Electron shifts (bent arrows) and bond-length elongations (straight arrows) before (1.) and after (2.) the TS are highlighted.

The H atom transferred ($H_{tr}$) has either protic (E = N), neutral (E = P−Bi), or hydridic (E = Ga) character at the TS. For group 15 elements, we find a nonsynchronous sequence of the reaction steps, while it is synchronous for group 13. Furthermore, the chronologies of the steps during the reaction differ for the three species. For E = N, the $C_\beta$$-$$H_{tr}$ bond is elongated in conjunction with electron transfer out of $\sigma$($C_\beta$$-$$H_{tr}$) toward $\pi$($C_\beta$$-$$C_\alpha$). In this process, the LP(N) "attacks" the protic H atom. The charge flow is clockwise in Figure 7. After the TS, the N$-$$C_\alpha$ bond is broken, and the products are formed.

For E = P−Bi, the barrier is exclusively determined by cleavage of the E$-$$C_\alpha$ bond along with electron transfer, leading to two LPs at E. All other bond rearrangements occur after the TS.

For E = Ga, the reaction is found to proceed rather symmetrically around the TS. Before the TS, all bonds are stretched, with the majority change in $C_\beta$$-$$H_{tr}$. Charge accumulation at the $H_{tr}$ atom renders it hydridic. After the TS, synchronous bond making/bond breaking is observed.

The main reason for the higher barrier of *β*-H elimination reactions in group 15 compounds is thus the nonsynchronicity of the reaction steps, in contrast to a synchronous bond rearrangement in group 13 alkyls. The filled p orbital at E requires bond breaking to occur before new bonds are formed. This leads to energetically high-lying TSs. The reason that this reaction can still occur although no acceptor orbital is available lies in the protic character of the transferred $H_{tr}$ atom (E = N) or the possibility of accommodating E−$C_\alpha$ bond breaking before E−$H_{tr}$ bond formation occurs (E = P−Bi). The trend in group 15 is thus determined by the E−$C_\alpha$ bond strengths, which is weaker for the heavier homologues, in line with lower-lying TSs. The last mechanism requires a good ability of the $C_\alpha$ atom to stabilize the positive partial charge occurring in the TS. This knowledge can be used to design new group 15 precursors containing ligands that stabilize this charge at $C_\alpha$ even better than the *tert*-butyl ligand.[61]

## ■ ASSOCIATED CONTENT

### Ⓢ Supporting Information

Absolute partial charges (NPA and AIM), reactant and product WBI, structures at inflection points along the IRC, EDA results from different fragmentations, Cartesian coordinates, and absolute energies for all species calculated. The Supporting Information is available free of charge on the ACS Publications website at DOI: 10.1021/acs.inorgchem.5b00687.

## ■ AUTHOR INFORMATION

### Corresponding Author

*E-mail: tonner@chemie.uni-marburg.de. Phone: +49 (0) 6421-2825418. Fax: +49 (0) 6421-2821826.

### Notes

The authors declare no competing financial interest.

## ■ ACKNOWLEDGMENTS

We thank the DFG (Research Training Group 1782) for funding and Prof. Jörg Sundermeyer (Marburg) for raising our interest in this issue. A.S. thanks the Beilstein Institut, Frankfurt/Main, Germany, for support. Computational support from HRZ Marburg, LOEWE-CSC Frankfurt, and HLR Stuttgart is acknowledged.

## ■ REFERENCES

(1) Brauers, A. *Prog. Cryst. Growth Charact.* **1991**, *22*, 1−18.
(2) Brauers, A. *J. Cryst. Growth* **1991**, *107*, 281−289.
(3) Russell, D. K. *Chem. Vap. Deposition* **1996**, *2*, 223−233.
(4) Liang, D.; Bowers, J. E. *Nat. Photonics* **2010**, *4*, 511−517.
(5) Liebich, S.; Zimprich, M.; Beyer, A.; Lange, C.; Franzbach, D. J.; Chatterjee, S.; Hossain, N.; Sweeney, S. J.; Volz, K.; Kunert, B.; Stolz, W. *Appl. Phys. Lett.* **2011**, *99*, 071109-1−071109-4.
(6) Kunert, B.; Volz, K.; Nemeth, I.; Stolz, W. *J. Lumin.* **2006**, *121*, 361−364.
(7) Manasevit, H. M. *Appl. Phys. Lett.* **1968**, *12*, 156−159.
(8) Stringfellow, G. B. *J. Electron. Mater.* **1988**, *17*, 327−335.
(9) Stringfellow, G. B. *Mater. Sci. Eng., B* **2001**, *87*, 97−116.
(10) Speckman, D. M.; Wendt, J. P. *J. Appl. Phys.* **1991**, *69*, 3316−3323.
(11) Murrell, A. J.; Wee, A. T. S.; Fairbrother, D. H.; Singh, N. K.; Foord, J. S.; Davies, G. J.; Andrews, D. A. *J. Appl. Phys.* **2013**, *68*, 4053−4063.
(12) Buchan, I.; Yu, M. L. *Surf. Sci.* **1993**, *280*, 383−392.
(13) Li, S. H.; Larsen, C. A.; Buchan, N. I.; Stringfellow, G. B. *J. Electron. Mater.* **1989**, *18*, 457−464.
(14) Paputa, M. C.; Price, S. J. W. *Can. J. Chem.* **1979**, *57*, 3178−3181.
(15) Lee, P. W.; Omstead, T. R.; Mckenna, D. R.; Jensen, K. F. *J. Cryst. Growth* **1987**, *85*, 165−174.
(16) Bahlawane, N.; Reilmann, F.; Salameh, L.-C.; Kohse-Höinghaus, K. *J. Am. Soc. Mass Spectrom.* **2008**, *19*, 947−954.
(17) Fan, G.; Hoare, R.; Pemble, M.; Povey, I.; Taylor, A. *J. Cryst. Growth* **1992**, *124*, 49−55.
(18) Larsen, C. A.; Buchan, N. I.; Li, S. H.; Stringfellow, G. B. *J. Cryst. Growth* **1989**, *94*, 663−672.
(19) Stegmüller, A.; Rosenow, P.; Tonner, R. *Phys. Chem. Chem. Phys.* **2014**, *16*, 17018−17029.
(20) Elschenbroich, C.; Salzer, A. *Organometallics: A Concise Introduction*; Wiley-VCH: Weinheim, Germany, 1992; p 198.
(21) Housecroft, C. E.; Sharpe, A. *Inorganic Chemistry*; Pearson/Prentice Hall: New York, 2005; p 721.
(22) Lee, J.; Kim, Y.; Anderson, T. *ECS Trans.* **2009**, *25*, 41−49.
(23) Banse, B. A.; Creighton, J. R. *Surf. Sci.* **1991**, *257*, 221−229.
(24) Boero, M.; Morikawa, Y.; Terakura, K.; Ozeki, M. *J. Chem. Phys.* **2000**, *112*, 9549−9556.
(25) Ryan, C.; de Lewis, A. K.; Caddick, S.; Kaltsoyannis, N. *Theor. Chem. Acc.* **2011**, *129*, 303−312.
(26) Hiraoka, Y. S.; Mashita, M.; Tada, T.; Yoshimura, R. *Appl. Surf. Sci.* **1992**, *60*−*61*, 246−250.
(27) Koukourakis, N.; Buckers, C.; Funke, D. A.; Gerhardt, N. C.; Liebich, S.; Chatterjee, S.; Lange, C.; Zimprich, M.; Volz, K.; Stolz, W.; Kunert, B.; Koch, S. W.; Hofmann, M. R. *Appl. Phys. Lett.* **2012**, *100*, 092107-3.
(28) Perdew, J.; Burke, K.; Ernzerhof, M. *Phys. Rev. Lett.* **1996**, *77*, 3865−3868.
(29) Perdew, J.; Burke, K.; Ernzerhof, M. *Phys. Rev. Lett.* **1997**, *78*, 1396.
(30) Weigend, F.; Ahlrichs, R. *Phys. Chem. Chem. Phys.* **2005**, *7*, 3297−3305.
(31) Metz, B.; Stoll, H.; Dolg, M. J. *Chem. Phys.* **2000**, *113*, 2563−2569.
(32) Biegler-König, F. W.; Bader, R. F. W.; Tang, T.-h. *J. Comput. Chem.* **1982**, *3*, 317−328.
(33) Weinhold, F.; Landis, C. *A Natural Bond Orbital Donor−Acceptor Perspective*; Cambridge University Press: Cambridge, U.K., 2005.
(34) Reed, A. E.; Weinstock, R. B.; Weinhold, F. *J. Chem. Phys.* **1985**, *83*, 735−746.
(35) Reed, A. E.; Weinhold, F. *J. Chem. Phys.* **1983**, *78*, 4066−4073.
(36) Weinhold, R. *Atoms in Molecules—A Quantum Theory*; Oxford University Press: Oxford, U.K., 1990.
(37) KeithT. A.*AIMExt Professional*; TK Gristmill Software: Overland Park, KS, 2015. aim.tkgristmill.com (accessed June 16, 2015).
(38) Wiberg, K. *Tetrahedron* **1968**, *24*, 1083−1096.
(39) Borisova, N.; Semenov, S. *Vestn. Leningr. Univ.* **1973**, *16*, 119.
(40) de Giambiagi, M.; Grempel, D.; Heyman, C. *J. Chim. Phys.* **1975**, *72*, 15−22.
(41) Frisch, M. J.; et al. *Gaussian09*, revision C.01; Gaussian Inc.: Wallingford, CT, 2010.
(42) Mitoraj, M. P.; Michalak, A.; Ziegler, T. *J. Chem. Theory Comput.* **2009**, *5*, 962−975.
(43) *ADF 2010.02*: Baerends, F.; et al. *J. Comput. Chem.* **2010**, *22* (9), 931−967.
(44) Becke, A. *Phys. Rev. A* **1988**, *38*, 3098−3100.
(45) Perdew, J. *Phys. Rev. B* **1986**, 8822−8824.
(46) Chong, D. *J. Comput. Chem.* **2004**, *25*, 1030−1036.
(47) Lenthe, E. V.; Baerends, E. J.; Snijders, J. G. *J. Chem. Phys.* **1993**, *99*, 4597−4610.
(48) Ziegler, T.; Rauk, A. *Theor. Chim. Acta* **1977**, *46*, 1−10.
(49) Kitaura, K.; Morokuma, K. *Int. J. Quantum Chem.* **1976**, *10*, 325−340.
(50) Politzer, P.; Toro-Labbé, A. *J. Chem. Sci.* **2005**, *117*, 467−472.
(51) Politzer, P.; Murray, J.; Jaque, P. *J. Mol. Model.* **2013**, 4111−4118.
(52) Kunert, B.; Volz, K.; Koch, J.; Stolz, W. *J. Cryst. Growth* **2007**, *298*, 121−125.
(53) Beyer, A.; Ohlmann, J.; Liebich, S.; Heim, H.; Witte, G.; Stolz, W.; Volz, K. *J. Appl. Phys.* **2012**, *111*, 083534-1−083534-6.
(54) Hermann, M.; Goedecke, C.; Jones, C.; Frenking, G. *Organometallics* **2013**, *32*, 6666−6673.

(55) Martin, F.; Zipse, H. *J. Comput. Chem.* **2005**, *26*, 97−105.

(56) Guerra, C. F. *J. Comput. Chem.* **2004**, *25*, 189−210.

(57) Bader, R. F. W. *J. Phys. Chem. A* **2009**, *113*, 10391−10396.

(58) Cerpa, E.; Krapp, A.; Vela, A.; Merino, G. *Chem.—Eur. J.* **2008**, *14*, 10232−10234.

(59) Tonner, R.; Frenking, G. *Chem.—Eur. J.* **2008**, *14*, 3260−3272.

(60) Hopffgarten, M. v.; Frenking, G. *WIREs Comput. Mol. Sci.* **2012**, *2*, 43−62.

(61) Stegmüller, A.; Tonner, R. *Chem. Vap. Deposition* submitted, 2015.

# The $\beta$-hydrogen elimination mechanism in the absence of low-lying acceptor orbitals in $EH_2(t\text{-}C_4H_9)$ (E = N-Bi)

Andreas Stegmüller and Ralf Tonner*

*Fachbereich Chemie and Material Sciences Center, Philipps-Universität Marburg,*
*Hans-Meerwein-Straße, Germany*

E-mail: tonner@chemie.uni-marburg.de
Phone: +49 (0) 6421-2825418. Fax: +49 (0) 6421-2821826

Supporting Information

**Supporting Information Available:** This material is available free of charge via the Internet at `http://pubs.acs.org/`.

## Absolute Partial Charges, NPA and AIM

Table S1: Absolute AIM and NPA charges for the educt, TS and product structures of *tert*-butyl-$EH_2$ summed into the fragments $H_{tr}$, $EH_2$ and $C_4H_8$.

| q(educt) | | N | P | As | Sb | Bi | Ga |
|---|---|---|---|---|---|---|---|
| $H_{tr}$ | AIM | 0.21 | 0.22 | 0.22 | 0.23 | 0.23 | 0.22 |
| | NPA | -0.01 | 0.00 | 0.00 | 0.00 | -0.01 | -0.01 |
| $EH_2$ | AIM | -0.12 | 0.20 | 0.22 | 0.07 | 1.21 | 0.47 |
| | NPA | -0.32 | 0.31 | 0.20 | 0.25 | 0.21 | 0.38 |
| $C_4H_8$ | AIM | -0.09 | -0.43 | -0.44 | -0.29 | -1.44 | -0.68 |
| | NPA | 0.33 | -0.31 | -0.20 | -0.24 | -0.20 | -0.37 |
| q(transition state) | | | | | | | |
| $H_{tr}$ | AIM | 0.41 | 0.22 | 0.22 | 0.21 | -0.09 | -0.04 |
| | NPA | 0.41 | 0.09 | 0.07 | 0.02 | 0.01 | -0.28 |
| $EH_2$ | AIM | -0.18 | -0.21 | -0.19 | -0.17 | 0.10 | 0.27 |
| | NPA | -0.28 | -0.21 | -0.18 | -0.14 | -0.12 | 0.41 |
| $C_4H_8$ | AIM | -0.24 | -0.02 | -0.02 | -0.04 | 0.00 | -0.23 |
| | NPA | -0.13 | 0.12 | 0.12 | 0.12 | 0.11 | -0.13 |
| q(product) | | | | | | | |
| $H_{tr}$ | AIM | 0.35 | 0.02 | -0.01 | -0.09 | -0.11 | -0.28 |
| | NPA | 0.33 | -0.46 | -0.27 | -0.30 | -0.27 | -0.40 |
| $EH_2$ | AIM | -0.35 | -0.02 | 0.01 | 0.09 | 0.11 | 0.28 |
| | NPA | -0.33 | 0.46 | 0.27 | 0.30 | 0.27 | 0.40 |
| $C_4H_8$ | AIM | 0 | 0 | 0 | 0 | 0 | 0 |
| | NPA | 0 | 0 | 0 | 0 | 0 | 0 |

## Educt and Product WBI

Table S2: Wiberg Bond Indices for the four bonds in the educt (**1E**) and product (**2E**, $C_4H_8$) structures .

| | educt | | | | | | product | | | | | |
|---|---|---|---|---|---|---|---|---|---|---|---|---|
| | N | P | As | Sb | Bi | Ga | N | P | As | Sb | Bi | Ga |
| $C_\alpha$-E | 1.00 | 0.93 | 0.90 | 0.91 | 1.58 | 0.64 | 0 | 0 | 0 | 0 | 0 | 0 |
| $C_\beta$-$H_{tr}$ | 0.93 | 0.93 | 0.93 | 0.92 | 0.91 | 0.93 | 0 | 0 | 0 | 0 | 0 | 0 |
| $H_{tr}$-E | 0.00 | 0.00 | 0.00 | 0.01 | 0.04 | 0.00 | 0.88 | 1.01 | 1.00 | 0.99 | 0.99 | 0.86 |
| $C_\beta$-$C_\alpha$ | 1.00 | 1.01 | 1.02 | 1.02 | 0.99 | 1.02 | 1.90 | 1.90 | 1.90 | 1.90 | 1.90 | 1.90 |

## Structures at Inflection Points along the IRC

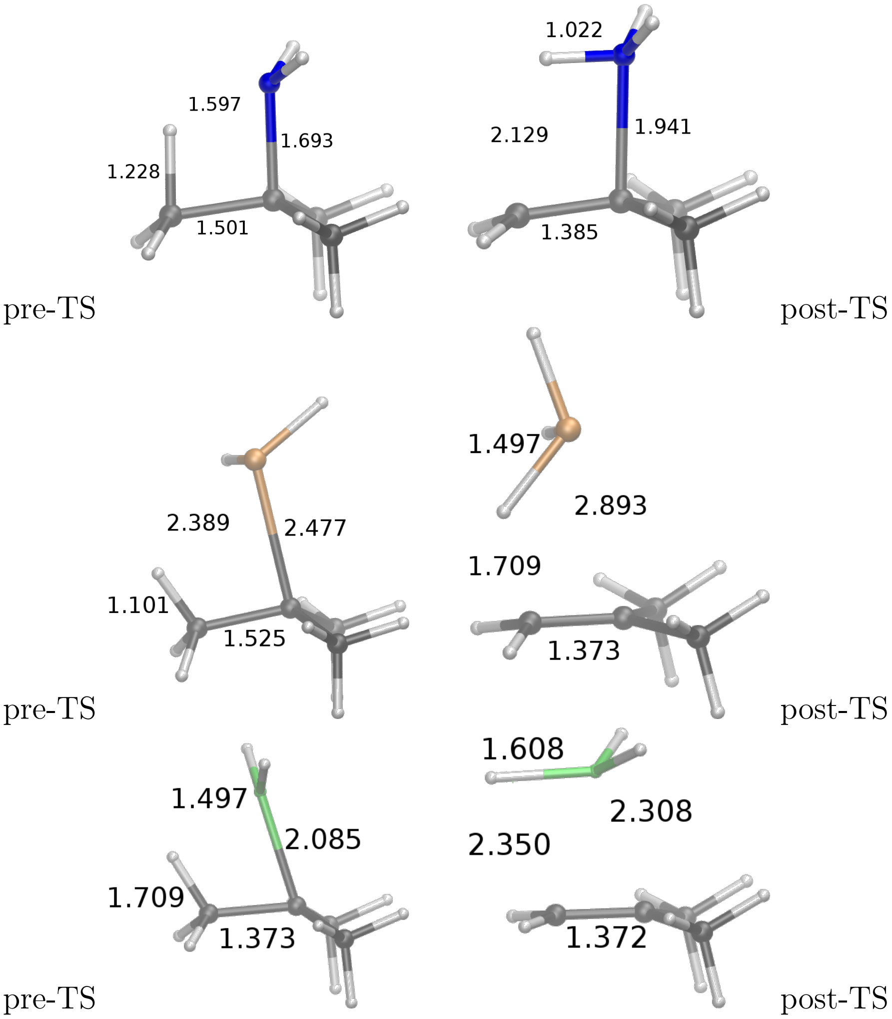

Figure S1: Structures at the inflection points identified by an analysis on the reaction force along the IRC's of $\beta$-hydrogen elimination reactions from $E(C_4H_9)H_2$ with E = N (top), P (center), Ga (bottom). The lengths of the four bonds being formed or broken during the reaction are provided in Å.

## EDA analysis with different fragmentations

Table S3: EDA results in kJ mol$^{-1}$ for fragmentation A neutral. The negative dissociation energy is ΔE = -$D_e$ = $\Delta E_{int}$+$\Delta E_{prep}$.

| | N | P | As | Sb | Bi | Ga |
|---|---|---|---|---|---|---|
| $\Delta E_{int}$ | 56.1 | -114.4 | -124.0 | -123.9 | -120.1 | -63.5 |
| $\Delta E_{Pauli}$ | 1168.0 | 629.5 | 657.7 | 713.7 | 749.1 | 857.1 |
| $\Delta E_{elstat}$ | -533.6 | -229.7 | -242.6 | -261.6 | -278.7 | -445.4 |
| | 48.0% | 30.9% | 31.0% | 31.2% | 32.1% | 48.4% |
| $\Delta E_{orb}$ | -578.2 | -514.3 | -539.1 | -575.9 | -590.5 | -475.1 |
| | 52.0% | 69.1% | 69.0% | 68.8% | 67.9% | 51.6% |
| $\Delta E_{prep}$ | 174.6 | 277.4 | 264.2 | 237.7 | 217.3 | 111.9 |
| $\Delta E$ | 230.7 | 162.9 | 140.2 | 113.8 | 97.2 | 48.4 |

Table S4: EDA results in kJ mol$^{-1}$ for fragmentation B neutral. The negative dissociation energy is ΔE = -$D_e$ = $\Delta E_{int}$+$\Delta E_{prep}$.

| | N | P | As | Sb | Bi | Ga |
|---|---|---|---|---|---|---|
| $\Delta E_{int}$ | -355.5 | -61.1 | -48.4 | -31.9 | -23.6 | -263.3 |
| $\Delta E_{Pauli}$ | 1620.8 | 232.1 | 184.2 | 146.5 | 130.0 | 1173.9 |
| $\Delta E_{elstat}$ | -710.5 | -100.2 | -82.4 | -67.3 | -61.4 | -621.5 |
| | 36.0% | 34.2% | 35.4% | 37.7% | 39.9% | 42.4% |
| $\Delta E_{orb}$ | -1265.7 | -193.1 | -150.2 | -111.1 | -92.3 | -845.7 |
| | 64.1% | 65.9% | 64.6% | 62.3% | 60.1% | 57.6 |
| $\Delta E_{prep}$ | 263.8 | 31.4 | 25.3 | 19.8 | 17.7 | 157.0 |
| $\Delta E$ | -91.7 | -29.7 | -23.1 | -12.2 | -5.9 | -136.2 |

Table S5: EDA results in kJ mol$^{-1}$ for fragmentation B charged EH$_2^-$ + C$_4$H$_9^+$. The negative dissociation energy is ΔE = -$D_e$ = $\Delta E_{int}$+$\Delta E_{prep}$.

| | N | P | As | Sb | Bi | Ga |
|---|---|---|---|---|---|---|
| $\Delta E_{int}$ | -912.4 | -580.2 | -567.8 | -540.7 | -540.5 | -947.4 |
| $\Delta E_{Pauli}$ | 1663.2 | 317.4 | 250.8 | 202.6 | 180.4 | 1853.1 |
| $\Delta E_{elstat}$ | -1403.8 | -520.3 | -473.8 | -418.4 | -395.5 | -1287.0 |
| | 54.5% | 58.0% | 57.9% | 56.3% | 54.9% | 46.0% |
| $\Delta E_{orb}$ | -1171.8 | -377.3 | -344.8 | -324.8 | -325.4 | -1513.4 |
| | 45.5% | 42.0% | 42.1% | 43.7% | 45.1% | 54.0% |
| $\Delta E_{prep}$ | 239.7 | 32.6 | 28.1 | 24.8 | 24.4 | 300.7 |
| $\Delta E$ | -672.7 | -547.7 | -539.7 | -515.9 | -516.1 | -646.7 |

Table S6: SCF energies in kJ mol $^{-1}$ and Cartesian coordinates in Å for $E(C_4H_9)H_2$ educt structures E = N, P, As, Sb, Bi, Ga.

| | | | |
|---|---|---|---|
| Energy | = | -560777.01 | |
| C | 0.026662 | -0.2288 | 0.112513 |
| C | 0.002092 | -0.225813 | 1.634094 |
| C | 1.347684 | 0.124333 | 2.252906 |
| C | -1.195733 | 0.33691 | 2.282762 |
| N | -0.277577 | -1.876196 | 2.080157 |
| H | 0.813947 | -0.875131 | -0.304681 |
| H | 0.212541 | 0.796914 | -0.236815 |
| H | -0.945098 | -0.541246 | -0.295523 |
| H | 2.169138 | -0.509732 | 1.885838 |
| H | 1.587982 | 1.167218 | 2.001496 |
| H | 1.305048 | 0.054637 | 3.349136 |
| H | -1.007127 | 0.986523 | 3.143066 |
| H | -1.960829 | 0.73032 | 1.606492 |
| H | -1.183876 | -1.294509 | 2.550699 |
| H | -0.472274 | -2.528044 | 1.308266 |
| H | 0.411603 | -2.302597 | 2.714274 |
| Energy | = | -1312935.7 | |
| C | 0.364291 | -0.020263 | 1.348256 |
| C | -0.533089 | -1.179832 | 1.638568 |
| C | -1.486695 | -1.097458 | 2.696516 |
| C | -0.2023 | -2.492672 | 1.005059 |
| P | -3.005622 | -0.340458 | 0.435437 |
| H | 0.650322 | 0.026882 | 0.289643 |
| H | 1.301955 | -0.123548 | 1.930057 |
| H | -0.094441 | 0.934159 | 1.635424 |
| H | 0.059778 | -2.387529 | -0.055959 |
| H | 0.683692 | -2.930163 | 1.507158 |
| H | -1.020218 | -3.217603 | 1.102134 |
| H | -1.793026 | -2.049074 | 3.145344 |
| H | -1.305207 | -0.30769 | 3.436494 |
| H | -2.543791 | -0.670839 | 2.196154 |
| H | -4.160064 | -0.246578 | -0.439596 |
| H | -3.122875 | -1.765389 | 0.479921 |
| Energy | = | -6286506.07799 | |
| C | 0.409742 | -0.026127 | 1.367848 |
| C | -0.489929 | -1.183281 | 1.655791 |
| C | -1.470922 | -1.089884 | 2.690555 |
| C | -0.167023 | -2.497693 | 1.024344 |
| As | -3.108013 | -0.283613 | 0.372293 |
| H | 0.702497 | 0.018625 | 0.310555 |
| H | 1.346483 | -0.126272 | 1.952526 |
| H | -0.047631 | 0.930485 | 1.651101 |
| H | 0.119758 | -2.393747 | -0.030739 |
| H | 0.700826 | -2.955083 | 1.541243 |
| H | -0.999456 | -3.208662 | 1.100512 |
| H | -1.77299 | -2.041231 | 3.144299 |
| H | -1.290568 | -0.302903 | 3.434537 |
| H | -2.520668 | -0.6832 | 2.20553 |
| H | -4.412694 | -0.20807 | -0.473159 |
| H | -3.206704 | -1.8174 | 0.403372 |
| Energy | = | -1047841.52972 | |
| C | 0.493114 | -0.033241 | 1.402872 |
| C | -0.431398 | -1.179439 | 1.675152 |
| C | -1.443607 | -1.071373 | 2.695149 |
| C | -0.12664 | -2.500962 | 1.040751 |
| Sb | -3.282382 | -0.186605 | 0.274938 |
| H | 0.805867 | 0.013714 | 0.340272 |
| H | 1.432749 | -0.148762 | 1.999688 |
| H | 0.051774 | 0.942026 | 1.688303 |
| H | 0.207663 | -2.399293 | -0.011633 |
| H | 0.712832 | -3.001498 | 1.585957 |
| H | -0.990033 | -3.193991 | 1.075993 |
| H | -1.746453 | -2.02962 | 3.159969 |
| H | -1.259611 | -0.282728 | 3.451648 |
| H | -2.499337 | -0.679975 | 2.233685 |
| H | -4.830101 | -0.192309 | -0.552087 |
| H | -3.301728 | -1.923999 | 0.289951 |
| Energy | = | -980649.70 | |
| C | 0.531189 | -0.035961 | 1.41945 |
| C | -0.403165 | -1.175879 | 1.684494 |
| C | -1.430564 | -1.059986 | 2.690871 |
| C | -0.105592 | -2.499982 | 1.052249 |
| Bi | -3.354018 | -0.166706 | 0.235733 |
| H | 0.849819 | 0.012392 | 0.358163 |
| H | 1.469638 | -0.157199 | 2.017517 |
| H | 0.097838 | 0.942728 | 1.706717 |
| H | 0.26065 | -2.400492 | 0.010074 |
| H | 0.706649 | -3.023883 | 1.616917 |
| H | -0.984446 | -3.17475 | 1.057313 |
| H | -1.725713 | -2.016 | 3.16609 |
| H | -1.252676 | -0.267373 | 3.444853 |
| H | -2.488808 | -0.693591 | 2.232085 |
| H | -5.01141 | -0.165372 | -0.554544 |
| H | -3.366683 | -1.986001 | 0.212626 |
| Energy | = | -5469980.72925 | |
| C | 0.041317 | -0.009288 | 0.034704 |
| C | 0.003974 | 0.014473 | 1.554036 |
| Ga | 2.011823 | 0.00063 | 2.404471 |
| C | 0.11066 | -1.22541 | 2.252393 |
| C | -0.854457 | 1.11097 | 2.16293 |
| H | 0.39255 | 0.945988 | -0.379745 |
| H | -0.970383 | -0.186595 | -0.373364 |
| H | 0.700806 | -0.798281 | -0.350855 |
| H | -0.538898 | 2.109414 | 1.829415 |
| H | -1.910036 | 0.987177 | 1.859879 |
| H | -0.817627 | 1.102444 | 3.260463 |
| H | -0.396467 | -1.346982 | 3.211571 |
| H | 0.240256 | -2.151815 | 1.689581 |
| H | 1.559316 | -1.511208 | 3.00709 |
| H | 2.99572 | -0.292893 | 1.233965 |
| H | 1.991334 | 0.962275 | 3.629189 |

Table S7: SCF energies in kJ mol $^{-1}$ and Cartesian coordinates in Å for $\beta$-H elmination TS structures E = N, P, As, Sb, Bi, Ga in $E(C_4H_9)H_2$.

| | | | |
|---|---|---|---|
| Energy | = | -560501.19 | |
| C | 0.026662 | -0.2288 | 0.112513 |
| C | 0.002092 | -0.225813 | 1.634094 |
| C | 1.347684 | 0.124333 | 2.252906 |
| C | -1.195733 | 0.33691 | 2.282762 |
| N | -0.277577 | -1.876196 | 2.080157 |
| H | 0.813947 | -0.875131 | -0.304681 |
| H | 0.212541 | 0.796914 | -0.236815 |
| H | -0.945098 | -0.541246 | -0.295523 |
| H | 2.169138 | -0.509732 | 1.885838 |
| H | 1.587982 | 1.167218 | 2.001496 |
| H | 1.305048 | 0.054637 | 3.349136 |
| H | -1.007127 | 0.986523 | 3.143066 |
| H | -1.960829 | 0.73032 | 1.606492 |
| H | -1.183876 | -1.294509 | 2.550699 |
| H | -0.472274 | -2.528044 | 1.308266 |
| H | 0.411603 | -2.302597 | 2.714274 |
| Energy | = | -1312696.9 | |
| C | 0.364291 | -0.020263 | 1.348256 |
| C | -0.533089 | -1.179832 | 1.638568 |
| C | -1.486695 | -1.097458 | 2.696516 |
| C | -0.2023 | -2.492672 | 1.005059 |
| P | -3.005622 | -0.340458 | 0.435437 |
| H | 0.650322 | 0.026882 | 0.289643 |
| H | 1.301955 | -0.123548 | 1.930057 |
| H | -0.094441 | 0.934159 | 1.635424 |
| H | 0.059778 | -2.387529 | -0.055959 |
| H | 0.683692 | -2.930163 | 1.507158 |
| H | -1.020218 | -3.217603 | 1.102134 |
| H | -1.793026 | -2.049074 | 3.145344 |
| H | -1.305207 | -0.30769 | 3.436494 |
| H | -2.543791 | -0.670839 | 2.196154 |
| H | -4.160064 | -0.246578 | -0.439596 |
| H | -3.122875 | -1.765389 | 0.479921 |
| Energy | = | -6286292.9 | |
| C | 0.409742 | -0.026127 | 1.367848 |
| C | -0.489929 | -1.183281 | 1.655791 |
| C | -1.470922 | -1.089884 | 2.690555 |
| C | -0.167023 | -2.497693 | 1.024344 |
| As | -3.108013 | -0.283613 | 0.372293 |
| H | 0.702497 | 0.018625 | 0.310555 |
| H | 1.346483 | -0.126272 | 1.952526 |
| H | -0.047631 | 0.930485 | 1.651101 |
| H | 0.119758 | -2.393747 | -0.030739 |
| H | 0.700826 | -2.955083 | 1.541243 |
| H | -0.999456 | -3.208662 | 1.100512 |
| H | -1.77299 | -2.041231 | 3.144299 |
| H | -1.290568 | -0.302903 | 3.434537 |
| H | -2.520668 | -0.6832 | 2.20553 |
| H | -4.412694 | -0.20807 | -0.473159 |
| H | -3.206704 | -1.8174 | 0.403372 |

| | | | |
|---|---|---|---|
| Energy | = | -1047654.5 | |
| C | 0.493114 | -0.033241 | 1.402872 |
| C | -0.431398 | -1.179439 | 1.675152 |
| C | -1.443607 | -1.071373 | 2.695149 |
| C | -0.12664 | -2.500962 | 1.040751 |
| Sb | -3.282382 | -0.186605 | 0.274938 |
| H | 0.805867 | 0.013714 | 0.340272 |
| H | 1.432749 | -0.148762 | 1.999688 |
| H | 0.051774 | 0.942026 | 1.688303 |
| H | 0.207663 | -2.399293 | -0.011633 |
| H | 0.712832 | -3.001498 | 1.585957 |
| H | -0.990033 | -3.193991 | 1.075993 |
| H | -1.746453 | -2.02962 | 3.159969 |
| H | -1.259611 | -0.282728 | 3.451648 |
| H | -2.499337 | -0.679975 | 2.233685 |
| H | -4.830101 | -0.192309 | -0.552087 |
| H | -3.301728 | -1.923999 | 0.289951 |
| Energy | = | -980478.71 | |
| C | 0.531189 | -0.035961 | 1.41945 |
| C | -0.403165 | -1.175879 | 1.684494 |
| C | -1.430564 | -1.059986 | 2.690871 |
| C | -0.105592 | -2.499982 | 1.052249 |
| Bi | -3.354018 | -0.166706 | 0.235733 |
| H | 0.849819 | 0.012392 | 0.358163 |
| H | 1.469638 | -0.157199 | 2.017517 |
| H | 0.097838 | 0.942728 | 1.706717 |
| H | 0.26065 | -2.400492 | 0.010074 |
| H | 0.706649 | -3.023883 | 1.616917 |
| H | -0.984446 | -3.17475 | 1.057313 |
| H | -1.725713 | -2.016 | 3.16609 |
| H | -1.252676 | -0.267373 | 3.444853 |
| H | -2.488808 | -0.693591 | 2.232085 |
| H | -5.01141 | -0.165372 | -0.554544 |
| H | -3.366683 | -1.986001 | 0.212626 |
| Energy | = | -5469860.6 | |
| C | 0.041317 | -0.009288 | 0.034704 |
| C | 0.003974 | 0.014473 | 1.554036 |
| Ga | 2.011823 | 0.00063 | 2.404471 |
| C | 0.11066 | -1.22541 | 2.252393 |
| C | -0.854457 | 1.11097 | 2.16293 |
| H | 0.39255 | 0.945988 | -0.379745 |
| H | -0.970383 | -0.186595 | -0.373364 |
| H | 0.700806 | -0.798281 | -0.350855 |
| H | -0.538898 | 2.109414 | 1.829415 |
| H | -1.910036 | 0.987177 | 1.859879 |
| H | -0.817627 | 1.102444 | 3.260463 |
| H | -0.396467 | -1.346982 | 3.211571 |
| H | 0.240256 | -2.151815 | 1.689581 |
| H | 1.559316 | -1.511208 | 3.00709 |
| H | 2.99572 | -0.292893 | 1.233965 |
| H | 1.991334 | 0.962275 | 3.629189 |

Table S8: SCF energies in kJ mol $^{-1}$ and Cartesian coordinates in Å for product structures $EH_3$ with E = N, P, As, Sb, Bi, Ga and $C_4H_8$.

| | | | |
|---|---|---|---|
| Energy | = | -148369.01 | |
| N | 0.2093102505 | -1.5498905415 | 1.6283274514 |
| H | 0.4603380894 | -1.2296474033 | 0.6910373373 |
| H | -0.6899493669 | -2.0255186718 | 1.5324978925 |
| H | 0.8875727705 | -2.2749806702 | 1.8697013468 |
| Energy | = | -900503.96 | |
| P | -2.4499032854 | -0.6879197314 | -0.0980466076 |
| H | -1.3333980385 | -1.0678569649 | 0.7118906152 |
| H | -1.7658767625 | -1.0329946672 | -1.3063177406 |
| H | -3.0426738634 | -1.9858163396 | 0.0066285373 |
| Energy | = | -5874076.18 | |
| As | -2.424220813 | -0.6352781532 | -0.1168190446 |
| H | -1.2277160351 | -1.2075366122 | 0.6570843653 |
| H | -1.762416116 | -0.9835188261 | -1.4579508095 |
| H | -3.1367682338 | -1.9950767108 | -0.0802951785 |
| Energy | = | -635413.16 | |
| Sb | -2.5740115682 | -0.5944806308 | -0.1538528316 |
| H | -1.1976793611 | -1.1639649687 | 0.7159161678 |
| H | -1.8152019923 | -0.9930558474 | -1.6507200809 |
| H | -3.2924496591 | -2.1605258446 | -0.0778939031 |
| Energy | = | -568220.96 | |
| Bi | -2.8476242057 | -0.5831523057 | -0.1301092824 |
| H | -1.3433153701 | -1.1491963303 | 0.6943977779 |
| H | -2.1054847189 | -0.9630811388 | -1.7326556717 |
| H | -3.5178319462 | -2.2587474161 | -0.0471842712 |
| Energy | = | -5057544.23 | |
| Ga | 0.015198 | -1.714803 | 2.115518 |
| H | 0.690379 | -1.122945 | 0.821801 |
| H | -1.318192 | -2.544635 | 1.999412 |
| H | 0.673064 | -1.476314 | 3.526796 |
| Energy | = | -412349.19 | |
| C | 0.0322683374 | -0.0954636031 | 0.0832228169 |
| C | 0.0124609213 | 0.1773178282 | 1.5621007718 |
| C | 1.3576739143 | 0.2572286641 | 2.2297641594 |
| C | -1.1312230344 | 0.3390248252 | 2.2415032746 |
| H | 0.5437010912 | -1.0472007366 | -0.1348188706 |
| H | 0.5935869038 | 0.686768214 | -0.4533627588 |
| H | -0.9799526136 | -0.1440241954 | -0.3376405725 |
| H | 1.9182108912 | -0.6825052838 | 2.0972064788 |
| H | 1.9744255456 | 1.0511748351 | 1.7779916115 |
| H | 1.2697318915 | 0.4582377517 | 3.3048872339 |
| H | -1.1330709152 | 0.537099542 | 3.3145177313 |
| H | -2.1015059331 | 0.2784741587 | 1.7459111237 |

# A quantum chemical descriptor for CVD precursor design: predicting decomposition rates of TBP and TBAs isomers and derivatives

Andreas Stegmüller, Ralf Tonner*

*M.Phil Andreas Stegmüller and Dr. Ralf Tonner, Philipps-Universität Marburg, Fachbereich Chemie and Material Sciences Center,*
*Hans-Meerwein-Straße 4, 35032 Marburg, Germany*
email: tonner@chemie.uni-marburg.de, phone: +49 (0) 6421-2825418, fax: +49 (0) 6421-2821826

Silicon microelectronics is approaching fundamental physical limits impeding further performance enhancement of devices.[1,2] One way to improve on the current situation is to move toward optoelectronic applications by combination of novel III/V compound materials and silicon substrates.[3,4] This requires the growth of metastable III/V materials on the Si surface at low temperatures.[5] Thus, precursor molecules for metal-organic chemical vapor deposition (MOCVD or MOVPE) need well-defined decomposition channels for the production of high-quality films.[6] In recent years, *tert*-butyl phosphane (TBP) and arsane (TBAs) have become common as MOCVD precursors due to their much lower decomposition temperatures compared to molecules with hydrogen- or methyl-ligands. The main reaction channel for TBP and TBAs is $\beta$-hydrogen elimination.[7] In a recent study, we could reveal the details of this mechanism.[8] Nevertheless, the large decomposition barriers leave room for improvement by fine-tuning of substituents. An enhanced gas phase reactivity then has a direct influence on the material's growth rate.[9] Here we show the derivation of an easy descriptor for the prediction of decomposition rates in precursors dominated by $\beta$-hydrogen elimination and propose a new precursor class based on the theoretical concepts outlined.

Ab initio quantum chemical approaches are an established tool for the prediction of precursor chemistry[10] or describing even all steps of CVD processes.[11] They are also often used to complement experimental investigations.[12] However, for the prediction of decomposition channels, tedious computation of reaction barriers and transition states for every compound accessible is necessary.[9] Establishing reliable predictors for the quick assessment of relative barriers and thus decomposition rates is highly desirable. For the $\beta$-hydrogen elimination in group 15 compounds it was shown that the breaking of the E-$C_\alpha$ bond (E = P, As) determines the barrier height.[8] In this rate-determining step, electron transfer from $C_\alpha$ to E occurs. This leads to the hypothesis that the barrier can be estimated by the polarity of the E-$C_\alpha$ bond. The transition state energy should then depend on the ability of the $C_\alpha$ atom to stabilize the resulting positive partial charge (Scheme 1).

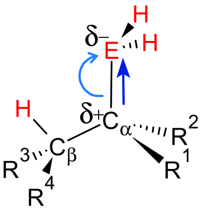

E = P, As

|  | 1E | 2E | 3E | 4E |
|---|---|---|---|---|
| $R^1$ = | $CH_3$ | H | H | $CH_3$ |
| $R^2$ = | $CH_3$ | H | H | H |
| $R^3$ = | H | $CH_3$ | $C_2H_5$ | $CH_3$ |
| $R^4$ = | H | $CH_3$ | H | H |

Scheme 1: CVD precursors investigated. The reaction step that determines the decomposition barrier is marked with arrows (straight arrow: bond stretch, curved arrow: electronic rearrangement).

In this study, we show that better stabilization of positive charge at $C_\alpha$ indeed leads to a lowering of the energy barrier in a series of alkyl ligands relevant for CVD applications. This easy-to-derive quantity can serve as a descriptor in the future avoiding tedious transition state analyses. We also propose a modification of the *tert*-butyl ligand to further reduce the decomposition barrier.

The substituents in $EH_2C_\alpha R^1R^2(C_\beta R^3R^4)$ (E = P, As) were chosen to include the *tert*-butyl group as in TBP (**1P**) and TBAs (**1As**) and the isomeric groups isobutyl (**2E**), *n*-butyl (**3E**) and *sec*-butyl (**4E**) (Scheme 1). This choice reflects tertiary, secondary and primary alkyl ligands, which exert different inductive effects on $C_\alpha$. Still, these isomers carry the same atom numbers, which renders them a comparable test set for the leading hypothesis.

The possible $\beta$-hydrogen elimination reactions of these ligands are outlined in Figure 1. The *sec*-butyl ligand in **4E** can decompose to three

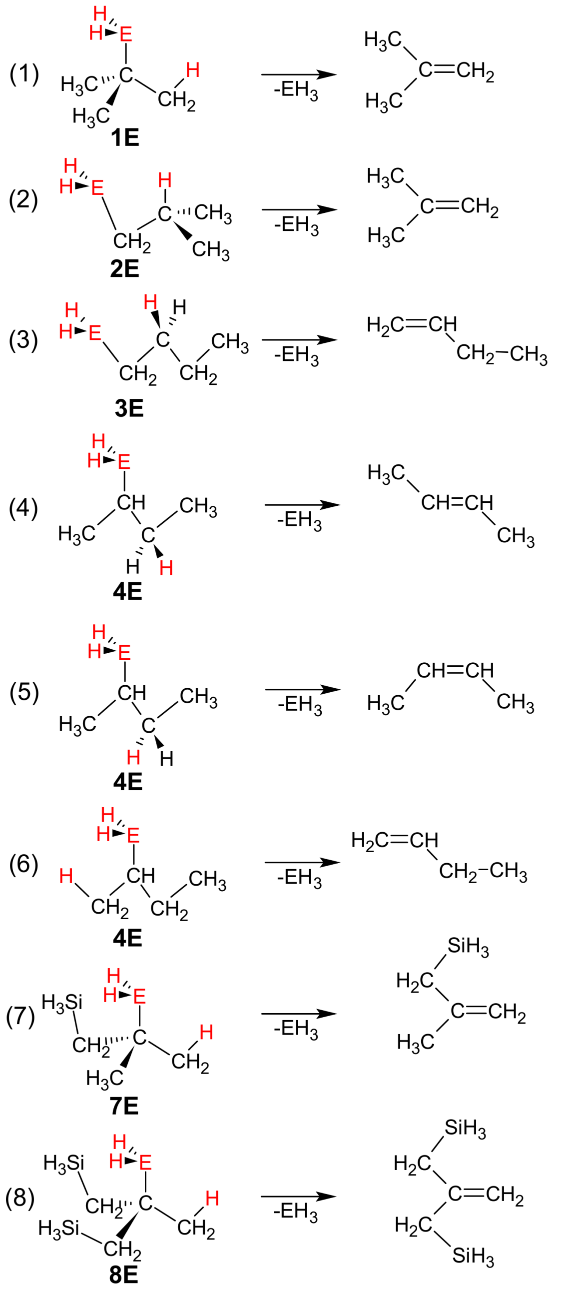

Figure 1: $\beta$-H elimination reactions of **1E-4E, 7E** and **8E** with E = P, As. Atoms constituting the $EH_3$ group to be eliminated are highlighted in red.

Table 1: Energies, rates and partial charges for the reactions investigated.[a]

| # | $\Delta E^b$ | $\Delta E^{\ddagger c}$ | $\Delta E^{\ddagger c}_{rel}$ | $\nu^d_{imag}$ | $-lg(k)^e$ | $q(C_\alpha^{reac})^f$ | $q(C_\alpha^{TS})^f$ |
|---|---|---|---|---|---|---|---|
| | | | | E = P | | | |
| (1) | 82.6 | 238.8 | 0 | 606.3 | 29.0 | -0.23 | 0.17 |
| (2) | 82.4 | 258.7 | +19.9 | 1095.0 | 32.5 | -0.66 | -0.35 |
| (3) | 95.1 | 259.6 | +10.7 | 1071.4 | 30.9 | -0.67 | -0.35 |
| (4) | 79.9 | 244.9 | +6.1 | 828.7 | 30.1 | -0.44 | -0.07 |
| (5) | 84.5 | 248.3 | +9.4 | 827.1 | 30.7 | -0.44 | -0.07 |
| (6) | 95.1 | 249.5 | +10.6 | 865.1 | 30.9 | -0.44 | -0.07 |
| (7) | 73.2 | 222.7 | -16.2 | 455.9 | 26.2 | -0.38 | 0.20 |
| (8) | 67.5 | 212.8 | -26.0 | 362.0 | 24.5 | -0.34 | 0.20 |
| | | | | E = As | | | |
| (1) | 80.7 | 213.2 | 0 | 435.7 | 24.5 | -0.20 | 0.17 |
| (2) | 80.7 | 235.3 | +22.2 | 782.8 | 28.4 | -0.66 | -0.31 |
| (3) | 93.6 | 236.0 | +22.8 | 791.1 | 28.5 | -0.66 | -0.34 |
| (4) | 77.9 | 220.2 | +7.0 | 575.3 | 25.8 | -0.42 | -0.07 |
| (5) | 82.6 | 223.7 | +10.5 | 567.3 | 26.4 | -0.42 | -0.07 |
| (6) | 93.1 | 225.5 | +12.4 | 600.8 | 26.7 | -0.43 | -0.07 |
| (7) | 71.1 | 196.6 | -16.5 | 338.6 | 21.7 | -0.20 | 0.18 |
| (8) | 65.6 | 186.4 | -26.7 | 274.7 | 19.9 | -0.19 | 0.18 |

[a] Energies in kJ $mol^{-1}$ (PBE/def2-TZVPP)
[b] Reaction energies for reactions outlined in Figure 1
[c] Activation energies absolute and relative to reaction (1)
[d] Imaginary modes of TS in $cm^{-1}$
[e] Negative decadic logarithm of Arrhenius reaction rates $k$
[f] Natural partial charges $q(C_\alpha)$ of reactant and TS in $|e|$

different products (reactions (4)-(6)), while the other ligands only exhibit one decomposition channel each (reactions (1), (2) and (3)).

Reaction energies and barrier heights for the $\beta$-hydrogen elimination reactions (1)-(6) of **1E - 4E** (E = P, As) are presented in Table 1. All reactions are energetically unfavourable. Inclusion of enthalpic and entropic corrections (Gibbs energies) leads to less endothermic reactions and additionally lowers the reaction barriers. These reactions will thus occur under MOCVD conditions.[8] Nevertheless, the corrections have little effect on the relative energies of the reactions (see Table SI-1 in the Supporting Information). We will thus focus on the discussion of electronic energies here.

The reactions exhibit large barriers which decrease in the following order:

$$\text{(3) } n\text{-butyl} \geq \text{(2) isobutyl} >$$
$$\text{(4) } sec\text{-butyl} > \text{(1) } tert\text{-butyl.}$$

The *Bell-Evans-Polanyi* principle[13,14] is fulfilled for reactions (3)-(6) for both central atoms P and As. This means that reaction barriers correlate with the reaction energies: Energetically high-lying products (ΔE) follow large reaction barriers ($\Delta E^\ddagger$). This gives a first hint, that ground-state properties determine the barriers here.

Transition states (TS) for reactions (1)-(6) were found in accordance with the previously investigated[8] $\beta$-hydrogen elimination mechanism and the resulting structures are shown in Figure 2. The

TSs exhibit 4-membered rings, which involve the bonds being formed and broken during the reaction. All compounds **1E-4E** follow the same reaction mechanism, however structural differences can be found. The E-C$_\alpha$ bond length is a good indicator for the location of the TS on the potential energy surface (early or late TS). While an early TS exhibits a short bond length and a high barrier, a late TS shows larger E-C$_\alpha$ distance and a lower barrier. The trend for the bond lengths at the TS thereby follows the trend in the barriers outlined above with reaction (2) having the smallest bond lengths (2.525 Å for E = P and 2.740 Å for E = As) and reaction (1) the largest (2.875 Å for E = P and 3.036 Å for E = As).

The origin of this trend can be found in the charge distribution. Partial charges q(C$_\alpha$) of reactant and TS structures are presented in the last two columns of Table 1. We find a good correlation of this descriptor with the reaction barriers. The negative proportionality of q($C_\alpha^{reac}$) and barrier height is shown in Figure 3 for E = P and E = As. This supports the initial hypothesis. The partial charges at the TS q($C_\alpha^{TS}$) correlate in a similar fashion with the barrier height (see Figure SI-1 in the SI). Since this quantity requires a TS search it is less efficient to compute. Note that for MOCVD applications, knowledge of the stereochemistry of the fragments (products of reactions (4)-(6)) is not important.

Although the differences in reaction barriers seem not very large (maximum difference 22.8 kJ mol$^{-1}$ between reactions (1) and (3) for E = As), this leads to huge changes in the rate constant. We estimated this with an Arrhenius-type approach (see Computational Details) and give the negative decadic logarithm of the rate constant in Table 1. The above-mentioned difference in barriers then translates to a four orders of magnitude change in the rate constant. This has a significant impact on the gas phase chemistry.

The values of q($C_\alpha^{reac}$) (which are comparable to previous results[15]) are largely determined by the inductive effect of the alkyl substituents at C$_\alpha$. Can this predictor be used to tune the barrier height for decomposition of CVD precursors? The inductive effects are maximized by the *tert*-butyl substituent, which is an explanation for the success of TBP and TBAs. Thus we need to employ other mechanisms for the stabilization of positive charge at C$_\alpha$.

In organic chemistry, the stabilization of carbocations can be achieved by a silyl-group in $\beta$-position. This is due to an orbital-interaction effect, which can be described by an overlap of the $\sigma$(Si-C$_\beta$)-bond with the partially empty p(C$_\alpha$)-orbital. This so-called hyperconjugation leads to a stabilization

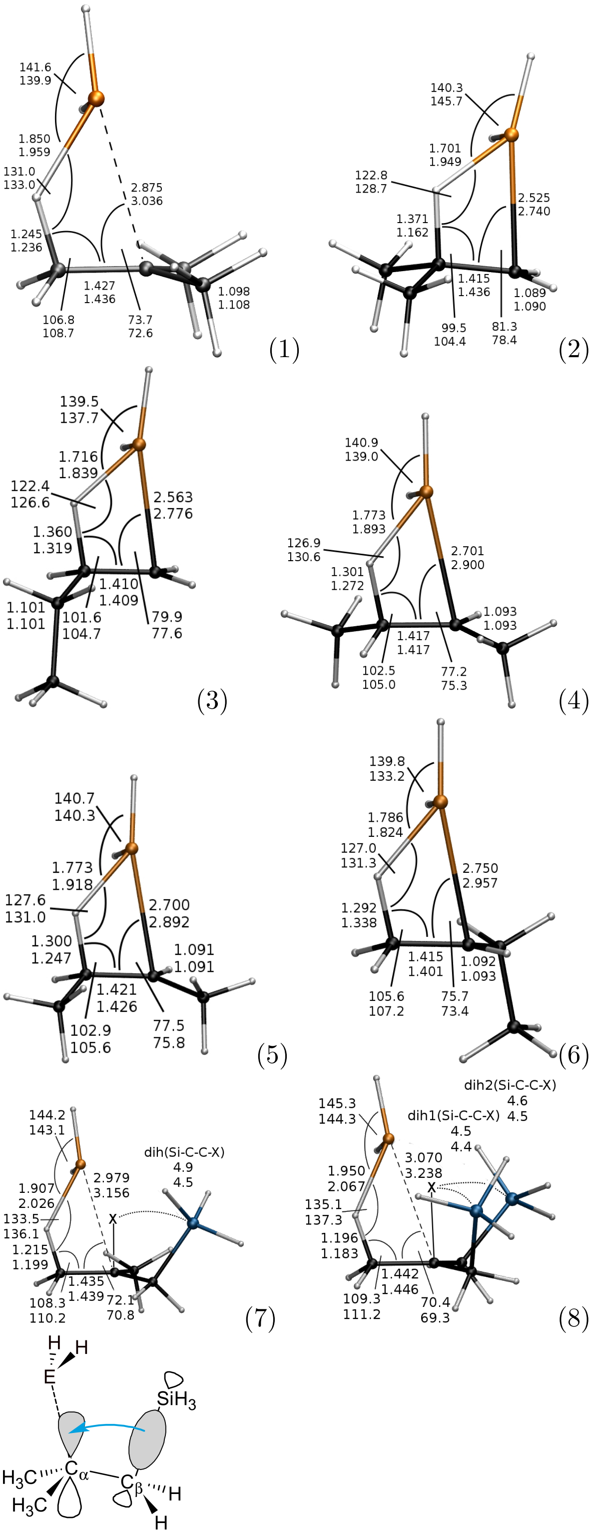

Figure 2: Transition state structures of reactions (1)-(8). Bond lengths in Å and angles in degrees are presented for E = P (top value) and E = As (bottom value). An orbital scheme of the $\beta$-silyl effect in (7) is presented (bottom).

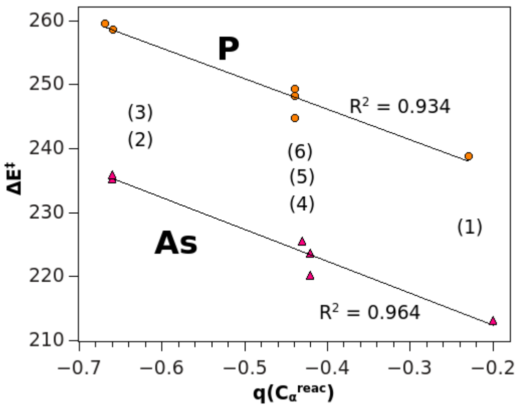

Figure 3: Energy barriers of reactions (1)-(6) w.r.t. partial charges at $C_\alpha$ in the reactant. The straight lines were interpolated for the groups with E = P (orange) and E = As (red), respectively.

of positive charge at $C_\alpha$ and should thus reduce the decomposition barrier toward $\beta$-hydrogen elimination. The required orbital overlap can occur if the respective atoms are aligned properly.[16]

We investigated the mono- and di-silylated derivatives of **1E**, where one (**7E**) or two (**8E**) hydrogen atoms at $C_\beta$ (i.e. $R^3$, $R^4$ in Scheme 1) are substituted by a $SiH_3$ group. We find drastically reduced decomposition barriers for these compounds, which are approx. 16 kJ mol$^{-1}$ (**7E**) and 26 kJ mol$^{-1}$ (**8E**) lower compared to **1E**. As proposed from our model, this correlates with a slightly more positive partial charge at $C_\alpha$ at least for the TS structures. Also, the E-$C_\alpha$ bond lengths at the TS are even larger compared to **1E**. The TS structures (Figure 2) show why the energetic effect is so large and additive. In both cases, the Si-$C_\beta$ bond lies in the same plane as the partially empty p-orbital of the $C_\alpha$ atom. This can be measured by the dihedral angle Si-$C_\beta$-$C_\alpha$-X, where X is a dummy atom at the position of the p-orbital. This angle is close to 0° for the $SiH_3$-groups in both precursors. Note, that the $EH_2$ group is already bent away from the $C_\alpha$ atom.

In conclusion, the barriers of the $\beta$-hydrogen elimination reaction from TBP and TBAs as well as isomeric alkyl ligands correlate linearly with the partial charge at $C_\alpha$: the more positive q($C_\alpha$), the lower the reaction barrier. This is due to the heterolytic breaking of the E-$C_\alpha$ bond being the rate-determining step. The polarity of the E-$C_\alpha$ bond can be influenced by changing the inductive effect of the substituent. The barriers exhibit a range of more than 20 kJ mol$^{-1}$, which translates to a four orders of magnitude change in the rate constant. As the $\beta$-hydrogen elimination determines the gas phase reactivity for TBP, TBAs and related molecules, the descriptor presented is suitable for the design of future CVD precursors. We propose silylated derivatives of the *tert*-butyl ligand, which exploit hyperconjugative stabilization effects and exhibit a drastic reduction in decomposition barriers. The $SiH_3$ group proposed contains no unwanted elements for MOCVD applications on silicon substrates, although doping effects might need to be monitored. The reaction investigated might also be relevant for surface-assisted precursor decomposition and the transferability of the approach described here will be investigated in the future.

## Computational Details

Unconstrained structural optimization of all compounds was carried out with density functional theory methods using the GGA functional PBE[17] together with the def2-TZVPP basis set.[18] This level of approximation has been previously established.[9] Reaction pathways were confirmed via analytical computation of the Hessian matrix and optimizing the intrinsic reaction coordinate (IRC) following the imaginary mode for the TS structures. Free energies were computed via a statistical thermodynamics approach at 1 atm and 273 K. Reaction rates based on an Arrhenius-type approach were calculated with constant pre-exponential factors from activation energies $\Delta E^\ddagger$ as

$$k_i = \frac{k_B T}{h} \exp \frac{\Delta E_i^\ddagger}{k_B T}$$

with $k_B$ and $h$ being the Boltzmann and Planck constants, respectively. Partial charges were derived by natural population analysis (NPA)[19] (similar results were derived for the density-based atoms in molecules scheme[20,21] as shown in the SI). All computations were carried out with the program package Gaussian09.[22]

We thank the DFG for support via RTG 1782 "Functionalization of Semiconductor". A. S. thanks the Beilstein Institut, Frankfurt/Main, for support. The HRZ Marburg, LOEWE-CSC Frankfurt and HLRS Stuttgart are acknowledged for computing time.

# References

[1] G.E. Moore, *P. IEEE* **1998**, *86*, 82.

[2] R. Chen, T.T.D. Tran, K.W. Ng, W.S. Ko, L.C. Chuang, F.G. Sedgwick, and C. Chang-Hasnain, *Nat. Photonics* **2011**, *5*, 170.

[3] D. Liang and J.E. Bowers, *Nat. Photonics* **2010**, *4*, 511.

[4] F. Dimroth, *Phys. Status Solidi C* **2006**, *3*, 373.

[5] K. Volz, J. Koch, F. Höhnsdorf, B. Kunert, and W. Stolz, *J. Crys. Growth* **2009**, *311*, 2418.

[6] A. Brauers, *J. Crys. Growth* **1991**, *107*, 281.

[7] M. Boero, Y. Morikawa, K. Terakura, and M. Ozeki, *J. Chem. Phys.* **2000**, *112*, 9549.

[8] A. Stegmüller and R. Tonner, *Inorg. Chem.,* DOI: 10.1021/acs.inorgchem.5b00687.

[9] A. Stegmüller, P. Rosenow, and R. Tonner, *Phys. Chem. Chem. Phys.* **2014**, *16*, 17018.

[10] I. Kazadojev, D.J. Otway, and S.D. Elliott, *Chem. Vap. Deposition* **2013**, *19*, 117.

[11] H. Pedersen and S.D. Elliott, *Theor. Chem. Acc.* **2014**, *133*, 1476.

[12] V. Miikkulainen, M. Suvanto, and T.A. Pakkanen, *Chem. Vap. Deposition* **2008**, *14*, 71.

[13] R.P. Bell, *P. Roy. Soc. A - Math Phy.* **1936**, *154*, 414.

[14] M. Evans and M. Polanyi, *T Faraday Soc.* **1938**, *34*, 11.

[15] J. Levy, *Struct. Chem.* **1999**, *10*, 121.

[16] K.N. Houk, M.N. Paddon-Row, N.G. Rondan, Y.D. Wu, F.K. Brown, D.C. Spellmeyer, J.T. Metz, Y. Li, and R.J. Loncharich, *Science* **1986**, *231*, 1108.

[17] J.P. Perdew, K. Burke, and M. Ernzerhof, *Phys. Rev. Lett.* **1996**, *77*, 3865.

[18] F. Weigend and R. Ahlrichs, *Phys. Chem. Chem. Phys.* **2005**, *7*, 3297.

[19] A.E. Reed, R.B. Weinstock, and F. Weinhold, *J. Chem. Phys.* **1985**, *83*, 735.

[20] T.A. Keith (2013), AIMExt Professional.

[21] R. Bader (1990) *Atoms in Molecules - A Quantum Theory*, Oxford University Press.

[22] M.J. Frisch, G.W. Trucks, H.B. Schlegel, G.E. Scuseria, M.A. Robb, J.R. Cheeseman, G. Scalmani, V. Barone, B. Mennucci, G.A. Petersson, H. Nakatsuji, M. Caricato, X. Li, H.P. Hratchian, A.F. Izmaylov, J. Bloino, G. Zheng, J.L. Sonnenberg, M. Hada, M. Ehara, K. Toyota, R. Fukuda, J. Hasegawa, M. Ishida, T. Nakajima, Y. Honda, O. Kitao, H. Nakai, T. Vreven, J.A. Montgomery Jr., J.E. Peralta, F. Ogliaro, M. Bearpark, J.J. Heyd, E. Brothers, K.N. Kudin, V.N. Staroverov, T. Keith, R. Kobayashi, J. Normand, K. Raghavachari, A. Rendell, J.C. Burant, S.S. Iyengar, J. Tomasi, M. Cossi, N. Rega, J.M. Millam, M. Klene, J.E. Knox, J.B. Cross, V. Bakken, C. Adamo, J. Jaramillo, R. Gomperts, R.E. Stratmann, O. Yazyev, A.J. Austin, R. Cammi, C. Pomelli, J.W. Ochterski, R.L. Martin, K. Morokuma, V.G. Zakrzewski, G.A. Voth, P. Salvador, J.J. Dannenberg, S. Dapprich, A.D. Daniels, O. Farkas, J.B. Foresman, J.V. Ortiz, J. Cioslowski, and D.J. Fox (2010), Gaussian 09 Rev C.01.

## Table of contents

Easily accessible information from quantum chemical computations can be used to predict decomposition barriers for phosphorous and arsenic precursor molecules for CVD. Based on the mechanistic description of the $\beta$-hydrogen elimination reaction, a precursor with a very low decomposition barrier is suggested.

# Supporting Information

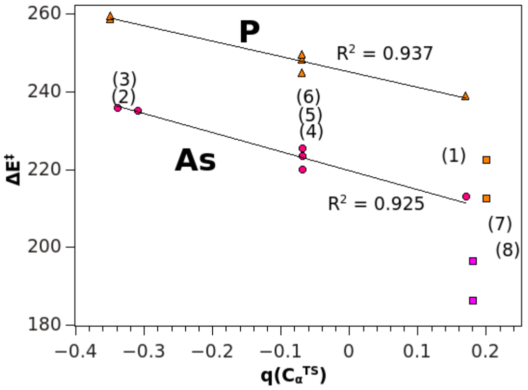

Figure SI-1: Correlation of energy barriers for reactions (1)-(8) with partial charges at $C_\alpha$ at the TS. Linear interpolations are presented for (1)-(6) for E = P (orange) and E = As (red).

Table SI-1: Electronic reaction energies ΔE, barriers $\Delta E^\ddagger$, free reaction energies ΔG and barriers $\Delta G^\ddagger$ (in kJ $mol^{-1}$) at 273 K and 1 atm for E = P and E = As (PBE/def2-TZVPP).

| reaction | E = P | | | | E = As | | | |
|---|---|---|---|---|---|---|---|---|
| index, ligand | ΔE | $\Delta E^\ddagger$ | ΔG | $\Delta G^\ddagger$ | ΔE | $\Delta E^\ddagger$ | ΔG | $\Delta G^\ddagger$ |
| (1) *tert*-butyl | 82.6 | 238.8 | 17.0 | 218.0 | 80.7 | 213.2 | 15.1 | 193.9 |
| (2) isobutyl | 82.4 | 258.7 | 17.1 | 239.5 | 80.7 | 235.3 | 15.6 | 217.0 |
| (3) *n*-butyl | 95.1 | 259.6 | 31.2 | 241.2 | 93.6 | 236.0 | 29.6 | 218.0 |
| (4) *sec*-butyl | 79.9 | 244.9 | 15.2 | 225.9 | 77.9 | 220.2 | 12.9 | 201.8 |
| (5) *sec*-butyl | 84.5 | 248.3 | 19.4 | 229.1 | 82.6 | 223.7 | 17.2 | 205.5 |
| (6) *sec*-butyl | 95.1 | 249.5 | 31.6 | 231.1 | 93.1 | 225.5 | 29.3 | 207.7 |
| (7) mono-silyl-butyl | 73.2 | 222.7 | 6.7 | 206.2 | 71.1 | 196.6 | 4.0 | 179.8 |
| (8) di-silyl-butyl | 67.5 | 212.8 | 3.7 | 199.1 | 65.6 | 186.4 | -0.1 | 172.2 |

Table SI-2: NPA and AIM partial charges (in $|e|$) for $C_\alpha$ at reactant and transition states for E = P and E = As (PBE/def2-TZVPP).

| | E = P | | | | E = As | | | |
|---|---|---|---|---|---|---|---|---|
| | $q(C_\alpha^{reactant})$ | | $q(C_\alpha^{TS})$ | | $q(C_\alpha^{reactant})$ | | $q(C_\alpha^{TS})$ | |
| reaction index, ligand | NPA | AIM | NPA | AIM | NPA | AIM | NPA | AIM |
| (1) *tert*-butyl | -0.23 | -0.32 | 0.17 | -0.01 | -0.20 | -0.20 | 0.17 | -0.01 |
| (2) isobutyl | -0.66 | -0.43 | -0.35 | -0.09 | -0.66 | -0.28 | -0.31 | -0.11 |
| (3) *n*-butyl | -0.67 | -0.43 | -0.35 | -0.09 | -0.66 | -0.28 | -0.34 | -0.10 |
| (4) *sec*-butyl | -0.44 | -0.37 | -0.07 | -0.04 | -0.42 | -0.23 | -0.07 | -0.05 |
| (5) *sec*-butyl | -0.44 | -0.37 | -0.07 | -0.04 | -0.42 | -0.23 | -0.07 | -0.05 |
| (6) *sec*-butyl | -0.44 | -0.37 | -0.07 | -0.05 | -0.43 | -0.23 | -0.07 | -0.05 |
| (7) mono-silyl-butyl | -0.38 | -0.32 | 0.20 | -0.01 | -0.20 | -0.20 | 0.18 | -0.01 |
| (8) di-silyl-butyl | -0.34 | -0.32 | 0.20 | 0.00 | -0.19 | -0.19 | 0.18 | -0.01 |

Table SI-3: SCF energies in kJ mol $^{-1}$ and Cartesian cordinates in Å for reactant structures **1E-4E** with E = P.

Energy = -1312935.72

| | | | |
|---|---|---|---|
| C | 0.196872813 | 0.0588332458 | 1.2649710167 |
| C | -0.8249714672 | -1.0857212127 | 1.3594452568 |
| C | -0.1498123105 | -2.4238008985 | 1.0386798049 |
| C | -1.4333857136 | -1.1254026013 | 2.7706161404 |
| P | -2.2316439205 | -0.669242199 | 0.1610793422 |
| H | 0.647332849 | 0.1169379545 | 0.2631917003 |
| H | 1.0115650168 | -0.1034937233 | 1.9886839133 |
| H | -0.2631443637 | 1.032259541 | 1.4877748979 |
| H | 0.2869615477 | -2.4218240272 | 0.0301428621 |
| H | 0.6621956152 | -2.6244933336 | 1.7581752822 |
| H | -0.8636658308 | -3.2574905248 | 1.0963268879 |
| H | -2.1742110317 | -1.9324288619 | 2.8682899436 |
| H | -0.6424533361 | -1.3057129625 | 3.516120009 |
| H | -1.9272331487 | -0.1768713748 | 3.0259346974 |
| H | -1.5282363841 | -0.9817140769 | -1.0477039247 |
| H | -2.8738773348 | -1.9502329447 | 0.19139317 |

Energy = -1312935.53

| | | | |
|---|---|---|---|
| C | -1.344585 | -0.679232 | 1.24918 |
| C | -1.794272 | -0.789061 | 2.715854 |
| C | -2.017884 | -2.244787 | 3.137227 |
| C | -0.777867 | -0.103785 | 3.636299 |
| P | -2.645721 | -1.263551 | 0.029041 |
| H | 0.20323 | -0.599965 | 3.573058 |
| H | -1.162766 | 0.378683 | 1.001926 |
| H | -0.393349 | -1.212568 | 1.10135 |
| H | -2.756887 | -0.255718 | 2.810389 |
| H | -1.884998 | -1.009375 | -1.156433 |
| H | -2.309898 | -2.65497 | 0.013213 |
| H | -1.103626 | -0.14236 | 4.68592 |
| H | -0.636808 | 0.952341 | 3.364553 |
| H | -2.331511 | -2.307127 | 4.188935 |
| H | -2.793851 | -2.73308 | 2.530227 |
| H | -1.089685 | -2.828038 | 3.028787 |

Energy = -1312931.53

| | | | |
|---|---|---|---|
| C | -1.440722 | -0.545061 | 1.507816 |
| P | -2.559488 | -1.392273 | 0.2649 |
| C | -1.910698 | -0.80119 | 2.943919 |
| C | -1.13159 | -0.015193 | 4.008603 |
| C | 0.340378 | -0.412561 | 4.134406 |
| H | -1.493727 | 0.533459 | 1.286702 |
| H | -0.397386 | -0.855657 | 1.367028 |
| H | -1.836418 | -1.880061 | 3.165187 |
| H | -2.980878 | -0.54813 | 3.021685 |
| H | -1.714172 | -1.235042 | -0.880539 |
| H | -2.098758 | -2.729392 | 0.495443 |
| H | -1.628617 | -0.159516 | 4.98125 |
| H | -1.207138 | 1.06259 | 3.786126 |
| H | 0.835542 | 0.147163 | 4.940048 |
| H | 0.441887 | -1.48435 | 4.36305 |
| H | 0.899327 | -0.216536 | 3.208613 |

Energy = -1312931.5

| | | | |
|---|---|---|---|
| C | -1.478035 | -0.472432 | 1.524358 |
| C | -1.962634 | -0.775197 | 2.952866 |
| C | -1.101787 | -0.147905 | 4.052358 |
| H | -0.054505 | -0.475311 | 3.971345 |
| P | -2.530157 | -1.462366 | 0.313145 |
| C | -1.578465 | 1.011783 | 1.156749 |
| H | -0.430124 | -0.797698 | 1.430944 |
| H | -1.985237 | -1.867488 | 3.099601 |
| H | -3.006602 | -0.433119 | 3.055772 |
| H | -1.688423 | -1.293667 | -0.833529 |
| H | -1.979366 | -2.751424 | 0.608752 |
| H | -1.465378 | -0.439806 | 5.047447 |
| H | -1.113167 | 0.949798 | 4.009284 |
| H | -1.220152 | 1.19763 | 0.134397 |
| H | -2.620531 | 1.361993 | 1.214904 |
| H | -0.975654 | 1.634289 | 1.833282 |

Table SI-4: SCF energies in kJ mol $^{-1}$ and Cartesian cordinates in Å for silylated reactant structures with E = P.

Energy = -2075748.21

| | | | |
|---|---|---|---|
| H | -0.577878 | -1.065282 | -1.770512 |
| Si | -0.700445 | -1.177638 | -0.330077 |
| P | -0.619987 | -1.494516 | 2.450771 |
| C | 0.009237 | 0.011728 | 1.976108 |
| C | 1.327185 | 0.012617 | 2.693384 |
| H | -2.102584 | -1.156671 | 0.038793 |
| C | -0.017867 | -0.065024 | 0.301332 |
| H | 0.159576 | -2.344928 | -0.312847 |
| C | -1.018797 | 0.690236 | 2.691352 |
| H | 0.990931 | 0.232207 | -0.021129 |
| H | -0.505316 | 0.828464 | -0.115889 |
| H | 1.938715 | -0.870118 | 2.46353 |
| H | 1.915005 | 0.895744 | 2.379073 |
| H | 1.204018 | 0.085394 | 3.784656 |
| H | -0.703218 | 1.305292 | 3.544396 |
| H | -1.825948 | 1.142877 | 2.102118 |
| H | -1.95961 | 0.223561 | 3.412721 |
| H | 0.284991 | -2.545815 | 2.011108 |
| H | -0.074737 | -1.846135 | 3.72345 |

Energy = -2838559.48

| | | | |
|---|---|---|---|
| C | 1.327185 | 0.012617 | 2.693384 |
| C | 0.009237 | 0.011728 | 1.976108 |
| C | -1.018797 | 0.690236 | 2.691352 |
| P | -0.619987 | -1.494516 | 2.450771 |
| C | -0.017867 | -0.065024 | 0.301332 |
| Si | -0.700445 | -1.177638 | -0.330077 |
| H | -0.577878 | -1.065282 | -1.770512 |
| H | -2.102584 | -1.156671 | 0.038793 |
| H | 0.159576 | -2.344928 | -0.312847 |
| H | 0.990931 | 0.232207 | -0.021129 |
| H | -0.505316 | 0.828464 | -0.115889 |
| Si | 1.917937 | -0.989557 | 3.558924 |
| H | 2.132137 | 0.274574 | 1.980876 |
| H | 1.413653 | 0.853246 | 3.398513 |
| H | -0.703218 | 1.305292 | 3.544396 |
| H | -1.825948 | 1.142877 | 2.102118 |
| H | -1.95961 | 0.223561 | 3.412721 |
| H | -0.201291 | -2.50618 | 1.492257 |
| H | -0.074737 | -1.846135 | 3.72345 |
| H | 2.892066 | -0.644209 | 3.902039 |
| H | 1.268808 | -1.15605 | 4.417313 |
| H | 2.036613 | -1.92108 | 3.007469 |

Table SI-5: SCF energies in kJ mol $^{-1}$ and Cartesian cordinates in Å for reactant structures **1E-4E** with E = As.

Energy = -6286506.08

| | | | |
|---|---|---|---|
| C | 0.2566545518 | 0.0502721424 | 1.2842955036 |
| C | -0.7705984237 | -1.0850690465 | 1.368301815 |
| C | -0.1139993966 | -2.4265549175 | 1.0394817747 |
| C | -1.4025645366 | -1.1257884318 | 2.7648061493 |
| As | -2.2582540597 | -0.6258074716 | 0.0639060428 |
| H | 0.7200832868 | 0.1078671572 | 0.2884361434 |
| H | 1.0640974243 | -0.1181353559 | 2.0164347201 |
| H | -0.1950976377 | 1.0280241002 | 1.5064488515 |
| H | 0.3367846404 | -2.4227343518 | 0.0372823647 |
| H | 0.6872158104 | -2.6438550225 | 1.7678647297 |
| H | -0.8373347188 | -3.2527165574 | 1.0818311463 |
| H | -2.1498752715 | -1.9282022836 | 2.8496853807 |
| H | -0.625029649 | -1.3146109201 | 3.523838123 |
| H | -1.8924288417 | -0.174969613 | 3.0204964129 |
| H | -1.4617693025 | -1.0186150832 | -1.1936087103 |
| H | -2.921942876 | -2.0142303449 | 0.1186835527 |

Energy = -6286506.09

| | | | |
|---|---|---|---|
| C | -1.277171 | -0.679675 | 1.256675 |
| C | -1.76219 | -0.781252 | 2.708308 |
| C | -2.024767 | -2.231738 | 3.125767 |
| C | -0.751331 | -0.118153 | 3.652818 |
| As | -2.653806 | -1.270778 | -0.081408 |
| H | 0.219621 | -0.63588 | 3.610222 |
| H | -1.061432 | 0.368472 | 1.001699 |
| H | -0.35052 | -1.252934 | 1.112823 |
| H | -2.714459 | -0.22667 | 2.787162 |
| H | -1.766271 | -0.981114 | -1.303573 |
| H | -2.248583 | -2.754498 | -0.104152 |
| H | -1.101183 | -0.150223 | 4.695059 |
| H | -0.581283 | 0.93459 | 3.384971 |
| H | -2.360706 | -2.2878 | 4.170914 |
| H | -2.797322 | -2.705445 | 2.502847 |
| H | -1.106961 | -2.833933 | 3.035121 |

Energy = -6286502.22

| | | | |
|---|---|---|---|
| C | -1.464166 | -0.497341 | 1.537619 |
| As | -2.656492 | -1.400306 | 0.201886 |
| C | -1.905535 | -0.798306 | 2.970193 |
| C | -1.11392 | -0.0328 | 4.042373 |
| C | 0.362336 | -0.423456 | 4.132988 |
| H | -1.542338 | 0.580836 | 1.329605 |
| H | -0.425769 | -0.798435 | 1.356618 |
| H | -1.81593 | -1.881444 | 3.163088 |
| H | -2.976054 | -0.557762 | 3.079058 |
| H | -1.720192 | -1.178336 | -0.998896 |
| H | -2.076738 | -2.80764 | 0.433256 |
| H | -1.593698 | -0.204626 | 5.019342 |
| H | -1.200021 | 1.049502 | 3.847587 |
| H | 0.868835 | 0.121841 | 4.941476 |
| H | 0.474144 | -1.499278 | 4.33648 |
| H | 0.903081 | -0.2042 | 3.201569 |

Energy = -6286501.8

| | | | |
|---|---|---|---|
| C | -1.480797 | -0.450183 | 1.543694 |
| C | -1.961577 | -0.761848 | 2.96745 |
| C | -1.097434 | -0.139019 | 4.068646 |
| H | -0.05017 | -0.464851 | 3.981491 |
| As | -2.61001 | -1.502803 | 0.242328 |
| C | -1.571672 | 1.031133 | 1.176341 |
| H | -0.443762 | -0.797685 | 1.427465 |
| H | -1.982933 | -1.854415 | 3.111143 |
| H | -3.004826 | -0.419388 | 3.079328 |
| H | -1.65258 | -1.319403 | -0.948504 |
| H | -1.980556 | -2.865342 | 0.583744 |
| H | -1.456986 | -0.436953 | 5.063521 |
| H | -1.110249 | 0.95886 | 4.031191 |
| H | -1.219294 | 1.216028 | 0.151811 |
| H | -2.608913 | 1.394555 | 1.244043 |
| H | -0.958461 | 1.650396 | 1.847981 |

Table SI-6: SCF energies in kJ mol $^{-1}$ and Cartesian cordinates in Å for silylated reactant structures with E = As.

Energy = -7049318.39

| | | | |
|---|---|---|---|
| C | -0.327906 | -2.611271 | 1.122289 |
| C | -0.986389 | -1.265508 | 1.43114 |
| As | -2.530509 | -0.864906 | 0.165188 |
| C | 0.029062 | -0.104736 | 1.345093 |
| C | -1.597698 | -1.296391 | 2.839795 |
| Si | 0.923204 | 0.262531 | -0.287222 |
| H | 0.818858 | -0.281829 | 2.0999 |
| H | -0.457924 | 0.838192 | 1.648145 |
| H | 0.090947 | -2.647092 | 0.107898 |
| H | 0.496746 | -2.801068 | 1.83197 |
| H | -1.047728 | -3.435754 | 1.217779 |
| H | -2.324495 | -2.114842 | 2.947865 |
| H | -0.803566 | -1.452401 | 3.588974 |
| H | -2.105445 | -0.35257 | 3.086634 |
| H | -1.845314 | -1.409654 | -1.099963 |
| H | -3.222206 | -2.21761 | 0.41148 |
| H | 1.879107 | 1.389151 | -0.048939 |
| H | 1.705102 | -0.910269 | -0.789013 |
| H | -0.033677 | 0.680283 | -1.358814 |

Energy = -7812129.71

| | | | |
|---|---|---|---|
| C | -0.290747 | -2.50063 | 1.144983 |
| C | -0.957118 | -1.147909 | 1.459976 |
| As | -2.523878 | -0.696424 | 0.237203 |
| C | 0.072948 | 0.001385 | 1.339472 |
| C | -1.52769 | -1.143436 | 2.886098 |
| Si | 0.898646 | 0.374692 | -0.327506 |
| H | 0.889999 | -0.191862 | 2.060355 |
| H | -0.391066 | 0.947619 | 1.668468 |
| H | 0.233992 | -2.448353 | 0.176408 |
| H | 0.504746 | -2.672259 | 1.896482 |
| Si | -1.318435 | -4.095269 | 1.080811 |
| H | -2.267426 | -1.941303 | 3.039145 |
| H | -0.712843 | -1.295866 | 3.613636 |
| H | -2.007438 | -0.182876 | 3.123878 |
| H | -1.941161 | -1.343333 | -1.030954 |
| H | -3.307214 | -1.977718 | 0.575603 |
| H | 1.860038 | 1.503259 | -0.126791 |
| H | 1.66184 | -0.794386 | -0.866722 |
| H | -0.106832 | 0.788422 | -1.355219 |
| H | -0.36772 | -5.247394 | 1.190143 |
| H | -2.298989 | -4.202603 | 2.206526 |
| H | -2.063884 | -4.23408 | -0.206978 |

Table SI-7: SCF energies in kJ mol $^{-1}$ and Cartesian cordinates in Å for TS structures with E = P reactions (1)-(4).

| | | | |
|---|---|---|---|
| Energy | = | -1312696.87 | |
| C | 0.3658002582 | -0.0162012233 | 1.3467099133 |
| C | -0.5343065576 | -1.1797843539 | 1.6385114387 |
| C | -1.4889151327 | -1.0987224475 | 2.70542354 |
| C | -0.2001869789 | -2.4969163861 | 1.0036856623 |
| P | -2.9968892628 | -0.3443497191 | 0.4362902209 |
| H | 0.6550493388 | 0.0332543146 | 0.278627 |
| H | 1.3126727734 | -0.1181630566 | 1.9322250769 |
| H | -0.0950079566 | 0.9483946985 | 1.6348992872 |
| H | 0.0570598332 | -2.3943411026 | -0.0692615046 |
| H | 0.6997458538 | -2.9338273005 | 1.5027774429 |
| H | -1.0185644301 | -3.2355330795 | 1.1074480319 |
| H | -1.7982548722 | -2.0581377263 | 3.1605962269 |
| H | -1.3104430813 | -0.2992600052 | 3.4504006121 |
| H | -2.5540769066 | -0.6678033504 | 2.1985564791 |
| H | -4.1573914096 | -0.2283626577 | -0.4477305638 |
| H | -3.143583069 | -1.7783037044 | 0.4714498361 |
| Energy | = | -1312676.81 | |
| C | -0.71465 | -1.091032 | 1.348761 |
| C | -1.396392 | -1.07359 | 2.588181 |
| C | -1.093648 | 0.078105 | 3.54074 |
| H | -0.140163 | -0.092359 | 4.064105 |
| P | -2.994027 | -0.384697 | 0.521939 |
| H | -0.138666 | -0.23057 | 1.011773 |
| H | -0.572018 | -2.017386 | 0.793368 |
| C | -1.727714 | -2.405839 | 3.245919 |
| H | -2.629643 | -0.653214 | 2.161553 |
| H | -4.153951 | -0.314642 | -0.387319 |
| H | -3.119208 | -1.805497 | 0.559861 |
| H | -1.879203 | 0.184242 | 4.302096 |
| H | -1.015374 | 1.029348 | 2.996409 |
| H | -2.557664 | -2.305276 | 3.95947 |
| H | -2.008945 | -3.16125 | 2.49951 |
| H | -0.857376 | -2.790502 | 3.801099 |
| Energy | = | -1312682.01 | (trans-TS) |
| C | -0.664814 | -1.164586 | 1.407833 |
| C | -1.432404 | -1.086363 | 2.588557 |
| C | -1.140691 | 0.008602 | 3.607252 |
| C | 0.078688 | -0.301636 | 4.482184 |
| P | -2.889347 | -0.336024 | 0.441492 |
| H | -0.025443 | -0.33649 | 1.102271 |
| H | -0.547363 | -2.096149 | 0.857494 |
| H | -1.757502 | -2.046867 | 3.010339 |
| H | -2.628703 | -0.653378 | 2.107883 |
| H | -4.002597 | -0.193093 | -0.510117 |
| H | -3.066591 | -1.751349 | 0.44055 |
| H | -2.023442 | 0.160685 | 4.24727 |
| H | -0.983808 | 0.956377 | 3.067003 |
| H | 0.253933 | 0.499621 | 5.214181 |
| H | -0.061239 | -1.239408 | 5.039444 |
| H | 0.985403 | -0.411554 | 3.870939 |
| Energy | = | -1312686.56 | |
| C | -0.198832 | -2.723289 | 0.518522 |
| C | -0.480443 | -1.415403 | 1.176405 |
| C | -1.035737 | -1.306583 | 2.475179 |
| C | -1.835746 | -0.070955 | 2.856371 |
| P | 1.684248 | -0.910947 | 2.711647 |
| H | -1.430284 | -2.25355 | 2.874123 |
| H | -0.404089 | -0.513094 | 0.564651 |
| H | 0.022784 | -1.248953 | 3.23001 |
| H | 1.104123 | 0.387007 | 2.571059 |
| H | 2.926321 | -0.319068 | 3.202408 |
| H | 0.618317 | -2.65552 | -0.20988 |
| H | 0.050579 | -3.50066 | 1.254305 |
| H | -1.095788 | -3.072433 | -0.028112 |
| H | -1.916891 | 0.034068 | 3.9466 |
| H | -1.357912 | 0.83874 | 2.466441 |
| H | -2.854361 | -0.116204 | 2.4436 |

Table SI-8: SCF energies in kJ mol $^{-1}$ and Cartesian cordinates in Å for TS structures with E = P reactions (5)-(8).

| | | | |
|---|---|---|---|
| Energy | = | -1312683.22 | |
| C | -1.199084 | -1.181027 | 2.451924 |
| C | -0.699796 | -1.338393 | 1.130551 |
| C | -0.232964 | -2.702367 | 0.641386 |
| C | -1.540258 | -2.316203 | 3.356263 |
| P | -3.377906 | -0.679022 | 0.938949 |
| H | 0.654157 | -3.043907 | 1.195275 |
| H | -1.172966 | -0.183736 | 2.893135 |
| H | -0.092247 | -0.494084 | 0.779458 |
| H | -1.753483 | -1.137045 | 0.396783 |
| H | -4.603813 | -0.060608 | 0.440331 |
| H | -2.724533 | 0.590904 | 0.965017 |
| H | 0.025937 | -2.663788 | -0.424433 |
| H | -1.015465 | -3.463802 | 0.763774 |
| H | -2.185396 | -1.998292 | 4.183404 |
| H | -2.037218 | -3.138088 | 2.823156 |
| H | -0.618209 | -2.741199 | 3.798791 |
| Energy | = | -1312682.01 | |
| C | -0.536556 | -1.328798 | 1.1366 |
| C | -1.185637 | -1.340051 | 2.39282 |
| H | -1.251561 | -0.409998 | 2.962017 |
| P | -3.177749 | -0.730534 | 0.635792 |
| H | 0.108324 | -0.47527 | 0.906109 |
| H | -0.150967 | -2.29159 | 0.779104 |
| C | -1.586687 | -2.598483 | 3.092208 |
| H | -1.492598 | -1.154882 | 0.268922 |
| H | -2.553918 | 0.535342 | 0.854283 |
| H | -4.323818 | -0.082848 | 0.006424 |
| H | -1.799324 | -3.383762 | 2.35033 |
| C | -0.480716 | -3.087144 | 4.052297 |
| H | -2.510968 | -2.437374 | 3.664716 |
| H | -0.797512 | -4.006137 | 4.56546 |
| H | 0.450365 | -3.299648 | 3.509217 |
| H | -0.258136 | -2.33082 | 4.818016 |
| Energy | = | -2075525.54 | |
| Si | 1.443971 | -0.20175 | -0.40148 |
| C | 0.215861 | -1.265356 | 0.621776 |
| C | -1.220087 | -0.975368 | 0.400437 |
| C | -1.853654 | -1.551366 | -0.825946 |
| C | -2.032762 | -0.356811 | 1.408801 |
| P | -1.299166 | 1.95065 | -0.152302 |
| H | 2.741278 | -0.962589 | -0.458779 |
| H | 1.69609 | 1.108516 | 0.257076 |
| H | 0.931169 | -0.037683 | -1.792491 |
| H | 0.444044 | -2.301871 | 0.313214 |
| H | 0.500161 | -1.158948 | 1.678688 |
| H | -1.197605 | -1.479716 | -1.704482 |
| H | -2.047588 | -2.629538 | -0.662519 |
| H | -2.814695 | -1.076585 | -1.057791 |
| H | -3.098607 | -0.610207 | 1.359027 |
| H | -1.633138 | -0.417806 | 2.428417 |
| H | -2.03361 | 0.842805 | 1.214758 |
| H | -1.418416 | 3.230925 | -0.815525 |
| H | -2.445353 | 1.443185 | -0.844086 |
| Energy | = | -2838346.6819 | |
| C | -1.087836 | -0.208613 | -1.280265 |
| C | 0.049248 | 0.672945 | -0.906697 |
| P | 0.085484 | 0.762977 | 2.16221 |
| Si | -2.234757 | -0.882994 | 0.101549 |
| C | 1.427418 | 0.202104 | -1.19896 |
| Si | 2.040707 | -1.316635 | -0.206264 |
| C | -0.206152 | 2.020246 | -0.45967 |
| H | -3.344349 | -1.584189 | -0.628368 |
| H | -2.838776 | 0.227194 | 0.891375 |
| H | -1.521911 | -1.855805 | 0.973956 |
| H | -0.745148 | -1.09005 | -1.842806 |
| H | -1.787267 | 0.346019 | -1.932037 |
| H | 1.477151 | -0.136379 | -2.252509 |
| H | 2.1663 | 1.006763 | -1.075613 |
| H | 0.609139 | 2.725491 | -0.657796 |
| H | -1.179674 | 2.418869 | -0.774238 |
| H | -0.311787 | 2.02769 | 0.73146 |
| H | 0.382112 | 0.616484 | 3.567845 |
| H | 1.406146 | 1.242361 | 1.887522 |
| H | 3.165533 | -1.950676 | -0.973442 |
| H | 2.513658 | -0.887031 | 1.139748 |
| H | 0.943494 | -2.32095 | -0.079945 |

Table SI-9: SCF energies in kJ mol $^{-1}$ and Cartesian cordinates in Å for TS structures with E = As reactions (1)-(4).

Energy = -6286292.93

| | | | |
|---|---|---|---|
| C | 0.4102920507 | -0.0219459129 | 1.3650413334 |
| C | -0.493073396 | -1.1827798093 | 1.6527925979 |
| C | -1.4744429378 | -1.090705209 | 2.6972605238 |
| C | -0.1654914021 | -2.5017992288 | 1.0215218678 |
| As | -3.0993811263 | -0.289533859 | 0.3767020696 |
| H | 0.710486612 | 0.0239737148 | 0.2994302989 |
| H | 1.3541092317 | -0.1204314839 | 1.9569691494 |
| H | -0.0493002946 | 0.945388932 | 1.6472288817 |
| H | 0.1200177195 | -2.4009145672 | -0.0447292889 |
| H | 0.7148346324 | -2.9584225609 | 1.5387971761 |
| H | -0.9988519923 | -3.2265557727 | 1.1023155973 |
| H | -1.7806366439 | -2.0498111716 | 3.1563810581 |
| H | -1.2953735003 | -0.2954547072 | 3.447328874 |
| H | -2.5340136983 | -0.6788664799 | 2.2109858604 |
| H | -4.4048477412 | -0.1927458414 | -0.4771780459 |
| H | -3.2216185135 | -1.827452043 | 0.3997590466 |

Energy = -6286270.78

| | | | |
|---|---|---|---|
| C | -0.62753 | -1.106704 | 1.377915 |
| C | -1.396204 | -1.063043 | 2.589963 |
| C | -1.077286 | 0.079912 | 3.557577 |
| H | -0.156098 | -0.122734 | 4.124001 |
| As | -3.083571 | -0.327471 | 0.446941 |
| H | -0.046648 | -0.2445 | 1.049859 |
| H | -0.48771 | -2.036946 | 0.828542 |
| C | -1.714347 | -2.404198 | 3.25531 |
| H | -2.455346 | -0.730322 | 2.247695 |
| H | -4.332179 | -0.295427 | -0.526596 |
| H | -3.182254 | -1.857536 | 0.504555 |
| H | -1.897551 | 0.214857 | 4.275926 |
| H | -0.943156 | 1.025003 | 3.013814 |
| H | -2.5605 | -2.299119 | 3.947642 |
| H | -1.979881 | -3.16094 | 2.505818 |
| H | -0.850945 | -2.779074 | 3.825437 |

Energy = -6286266.25

| | | | |
|---|---|---|---|
| C | -0.602071 | -1.134947 | 1.214817 |
| C | -1.337433 | -1.148445 | 2.417052 |
| H | -1.03603 | -0.382 | 3.147401 |
| As | -3.065184 | -0.124307 | 0.421375 |
| H | 0.005209 | -0.280349 | 0.92297 |
| H | -0.554516 | -2.015312 | 0.573002 |
| C | -1.755709 | -2.479004 | 3.034399 |
| H | -2.490884 | -0.586703 | 2.108827 |
| H | -4.434759 | 0.052541 | -0.334953 |
| H | -3.244753 | -1.647088 | 0.374612 |
| H | -2.618235 | -2.321047 | 3.699772 |
| H | -2.103997 | -3.146354 | 2.229851 |
| C | -0.621156 | -3.150192 | 3.815273 |
| H | -0.95735 | -4.095424 | 4.264215 |
| H | 0.235129 | -3.366403 | 3.161342 |
| H | -0.26223 | -2.502799 | 4.628828 |

Energy = -6286281.65

| | | | |
|---|---|---|---|
| C | -0.253378 | -2.748324 | 0.487388 |
| C | -0.533417 | -1.439303 | 1.140128 |
| C | -1.033485 | -1.320651 | 2.461018 |
| C | -1.830113 | -0.081738 | 2.849129 |
| As | 1.80525 | -0.887042 | 2.763412 |
| H | -1.434276 | -2.263211 | 2.866408 |
| H | -0.447006 | -0.535219 | 0.531931 |
| H | 0.00051 | -1.258024 | 3.199606 |
| H | 1.157085 | 0.493357 | 2.582848 |
| H | 3.061419 | -0.214514 | 3.409647 |
| H | 0.551853 | -2.681057 | -0.254636 |
| H | 0.00975 | -3.521504 | 1.22347 |
| H | -1.153943 | -3.109733 | -0.046386 |
| H | -1.889453 | 0.029203 | 3.940054 |
| H | -1.35949 | 0.825086 | 2.444841 |
| H | -2.855017 | -0.134169 | 2.454469 |

Table SI-10: SCF energies in kJ mol $^{-1}$ and Cartesian cordinates in Å for TS structures with E = As reactions (5)-(8).

Energy = -6286278.12

| | | | |
|---|---|---|---|
| C | -1.160227 | -1.204919 | 2.490158 |
| C | -0.709837 | -1.352515 | 1.144739 |
| C | -0.216832 | -2.709211 | 0.652141 |
| C | -1.493964 | -2.343879 | 3.389112 |
| As | -3.506027 | -0.651759 | 0.892489 |
| H | 0.709404 | -3.0067 | 1.165716 |
| H | -1.145836 | -0.205507 | 2.927192 |
| H | -0.098914 | -0.506373 | 0.799558 |
| H | -1.714313 | -1.158902 | 0.43182 |
| H | -4.760661 | 0.041133 | 0.263847 |
| H | -2.766024 | 0.69355 | 0.91829 |
| H | -0.013448 | -2.675929 | -0.425972 |
| H | -0.962668 | -3.496626 | 0.823421 |
| H | -2.10284 | -2.024585 | 4.242795 |
| H | -2.025411 | -3.149314 | 2.862698 |
| H | -0.56913 | -2.799651 | 3.795447 |

Energy = -6286276.28

| | | | |
|---|---|---|---|
| C | -0.536814 | -1.450356 | 1.142573 |
| C | -0.951229 | -1.47865 | 2.495277 |
| C | -0.916615 | -0.281716 | 3.38642 |
| C | 0.395078 | -0.217416 | 4.200676 |
| As | -3.40803 | -1.309762 | 0.905254 |
| H | 0.050062 | -0.573516 | 0.83942 |
| H | -0.17204 | -2.390501 | 0.715534 |
| H | -1.203144 | -2.439399 | 2.950541 |
| H | -1.572419 | -1.264924 | 0.426708 |
| H | -3.067656 | -2.806738 | 0.905705 |
| H | -4.775484 | -1.609784 | 0.210683 |
| H | -1.765773 | -0.300973 | 4.084663 |
| H | -1.013651 | 0.634892 | 2.783641 |
| H | 0.394361 | 0.662691 | 4.859329 |
| H | 0.515568 | -1.111462 | 4.82815 |
| H | 1.268813 | -0.151344 | 3.537997 |

Energy = -7049121.74

| | | | |
|---|---|---|---|
| Si | 1.470179 | -0.249796 | -0.388729 |
| C | 0.230398 | -1.309309 | 0.627663 |
| C | -1.200906 | -1.003415 | 0.408872 |
| C | -1.844844 | -1.563933 | -0.818718 |
| C | -2.00644 | -0.363609 | 1.41482 |
| As | -1.321944 | 2.096421 | -0.172795 |
| H | 2.773255 | -0.999271 | -0.435723 |
| H | 1.694277 | 1.066001 | 0.269337 |
| H | 0.958835 | -0.08783 | -1.780536 |
| H | 0.450632 | -2.344359 | 0.307864 |
| H | 0.517353 | -1.215234 | 1.685088 |
| H | -1.184365 | -1.511093 | -1.695593 |
| H | -2.070555 | -2.636705 | -0.658073 |
| H | -2.791166 | -1.062224 | -1.055362 |
| H | -3.06789 | -0.64082 | 1.382502 |
| H | -1.597888 | -0.419459 | 2.431484 |
| H | -2.049683 | 0.818458 | 1.2208 |
| H | -1.566246 | 3.477379 | -0.837761 |
| H | -2.515109 | 1.499284 | -0.938345 |

Energy = -7811943.28

| | | | |
|---|---|---|---|
| C | -1.102187 | -0.209659 | -1.314795 |
| C | 0.034689 | 0.664908 | -0.926209 |
| As | 0.093164 | 0.811249 | 2.308148 |
| Si | -2.236443 | -0.909709 | 0.064459 |
| C | 1.414808 | 0.191823 | -1.202921 |
| Si | 2.02077 | -1.347028 | -0.236678 |
| C | -0.216946 | 2.014438 | -0.470925 |
| H | -3.349111 | -1.622209 | -0.647754 |
| H | -2.833383 | 0.195439 | 0.867773 |
| H | -1.495324 | -1.86648 | 0.932102 |
| H | -0.759666 | -1.080554 | -1.893974 |
| H | -1.807154 | 0.354623 | -1.952431 |
| H | 1.481709 | -0.131459 | -2.261035 |
| H | 2.154385 | 0.991978 | -1.055854 |
| H | 0.596125 | 2.716053 | -0.69354 |
| H | -1.189813 | 2.412433 | -0.789532 |
| H | -0.302836 | 2.058154 | 0.708199 |
| H | 0.45056 | 0.772083 | 3.815624 |
| H | 1.515219 | 1.281912 | 1.959655 |
| H | 3.197369 | -1.924844 | -0.968644 |
| H | 2.398523 | -0.955046 | 1.151072 |
| H | 0.944276 | -2.382282 | -0.205685 |

DOI: 10.1002/ ((please add manuscript number))
**Article type: Full Paper**

# Pyramidal Structure Formation at the Interface between III/V Semiconductors and Silicon

*Andreas Beyer, Andreas Stegmüller, Jan O. Oelerich, Kakhaber Jandieri, Katharina Werner, Wolfgang Stolz, Sergei D. Baranovskii, Ralf Tonner*, Kerstin Volz**

*Dr. Andreas Beyer,*
*Faculty of Physics and Material Sciences Centre, Philipps-Universität Marburg, Hans-Meerwein Str. 6, D-35032 Marburg, Germany*

*Andreas Stegmüller,*
*Faculty of Chemistry and Material Sciences Centre, Philipps-Universität Marburg, Hans-Meerwein Str., D-35032 Marburg, Germany*

*Jan O. Oelerich,*
*Faculty of Physics and Material Sciences Centre, Philipps-Universität Marburg, Hans-Meerwein Str. 6, D-35032 Marburg, Germany*

*Dr. Kakhaber Jandieri,*
*Faculty of Physics and Material Sciences Centre, Philipps-Universität Marburg, Hans-Meerwein Str. 6, D-35032 Marburg, Germany*

*Katharina Werner,*
*Faculty of Physics and Material Sciences Centre, Philipps-Universität Marburg, Hans-Meerwein Str. 6, D-35032 Marburg, Germany*

*Prof. Dr. Wolfgang Stolz,*
*Faculty of Physics and Material Sciences Centre, Philipps-Universität Marburg, Hans-Meerwein Str. 6, D-35032 Marburg, Germany*

*Prof. Dr. Sergei D. Baranovskii,*
*Faculty of Physics and Material Sciences Centre, Philipps-Universität Marburg, Hans-Meerwein Str. 6, D-35032 Marburg, Germany*

*Dr. Ralf Tonner,*
*Faculty of Chemistry and Material Sciences Centre, Philipps-Universität Marburg, Hans-Meerwein Str., D-35032 Marburg, Germany*
*Tel: +49 – 6421 - 2825418*
*Email: ralf.tonner @chemie.uni-marburg.de*

*Prof. Dr. Kerstin Volz*
*Faculty of Physics and Material Sciences Centre, Philipps-Universität Marburg, Hans-Meerwein Str. 6, D-35032 Marburg, Germany*
*Tel: +49 – 6421 - 2822297*
*Email: kerstin.volz@physik.uni-marburg.de*

**Keywords:** III/V on silicon, interface formation, atomic resolution transmission electron microscopy, density functional theory, kinetic Monte Carlo

**Abstract text.**

An enhancement of computer performance following Moore's law requires the miniaturization of semiconductor devices. Presently, their dimensions reach the nanoscale. Interfaces between materials become increasingly important as the volume is reduced. It is shown here how a pyramidal interface structure is formed irrespective of the conditions applied during the growth of two semiconductors. This drastically changes the common view of interfaces, which were assumed to be either atomically abrupt or interdiffused. Especially in semiconductor heteroepitaxy a simple surface segregation of one atomic species is often assumed. It is proven by first principles computations and kinetic modelling that the atom mobility during growth and the chemical environment at the interface are the decisive factors in the formation of the actual structure. Gallium phosphide grown on silicon was chosen as representative, nearly unstrained material combination to study the fundamental parameters influencing the interface morphology. Beyond that, this system has significant impact for cutting-edge electronic and optoelectronic devices. The findings derived in this study can be generalized to aid the understanding of further relevant semiconductor interfaces. This knowledge is crucial to comprehend current and steer future properties of miniaturized devices.

## 1. Introduction

The aim to satisfy Moore's law requires the semiconductor industry to maximize the density of integrated circuits to continue the ongoing performance increase of microelectronic devices[1]. Fundamental questions on how to achieve this are, as yet, unanswered and the "Red Brick Wall" – meaning necessary technological solutions not being found – is approaching. This industry is currently following two approaches to reach their performance goals: downscaling of device dimensions and extending beyond the state-of-the-art silicon (Si) complementary metal–oxide–semiconductor (CMOS) technology[1,2]. Both approaches necessitate the development of new architectures and new materials. Downscaling, for example, requires new high-*k* compounds to prevent tunnelling processes[3]. Progress beyond current CMOS technology, on the other hand, also needs materials that overcome silicon's fundamental limitation of not enabling optical excitations due to an indirect band-gap. So-called III/V semiconductors, mixtures of elements in the third and fifth group of the periodic table, are highly promising, e.g. for conducting channels[4] or even laser applications[5]. Monolithic integration of these materials with Si is desired to enable seamless integration with current CMOS technologies. This can be achieved with up-scalable growth techniques, specifically metal organic vapor phase epitaxy (MOVPE). However, the requirements regarding the quality (lack of defects) of the films deposited is very high, resulting in major experimental challenges[6]. The difference in lattice constants and polarity between Si and III/V semiconductors leads to misfit dislocations, stacking faults, twins and antiphase boundaries, which severely impede the resulting device performance. In addition, thermal expansion coefficients of both materials differ, which results in cracking for thicker layer stacks. This can be avoided by using lattice-matched material combinations or strain-balancing at growth temperature[7]. Deterioration of electronic properties via atoms moving into the neighboring material (cross-doping) also requires suitable growth conditions. On a microscopic level, it is usually assumed that the morphology and the defect structure of III/V layers grown on group IV (here: silicon) substrates are mainly determined by the charge neutrality of the interface. This charge distribution is expected to be the outcome of carefully choosing the growth conditions.

One way of remedying several of the issues mentioned above is to provide an interlayer of gallium phosphide (GaP) between Si and the optically or electrically active III/V device. Gallium phosphide is the only III/V semiconductor which is nearly lattice-matched to Si at room temperature, with a remaining lattice mismatch of only 0.3%. This enables the defect-free growth of layers of several ten nanometres thickness without reaching the critical thickness where defects would be formed. Moreover, by carefully tuning the growth conditions, an intact GaP layer can be produced even on CMOS-compatible exact Si(001) substrates[8,9]. Nevertheless, as current device dimensions are decreased to end up in the range of interface widths, the exact interface morphology between Si and GaP plays an increasing role, and knowledge about the thermally stable, intrinsic configuration is needed to ensure optimal integration of the active III/V device. Therefore, quantitative understanding of the interface formation and structure has a direct impact on device performance. Furthermore, the exact interface structure between any two materials must be known to enable meaningful conclusions to be drawn regarding fundamental physical processes occurring across interfaces, such as charge or energy transfer.

Interfaces between III/V semiconductors, for example, accommodate small difference in lattice parameters by elastic deformation of one of the components. Especially for In- and Sb-containing materials it is also widely accepted that In or Sb, respectively, segregate towards the surface of the growing material and in consequence abrupt interfaces are rather difficult to achieve in semiconductor heteroepitaxy[10,11]. Interface formation might however be different if there is a significant difference in electronegativity of the single constituents, like for the GaP/Si material combination studied here.

In addition to the improvement of existing devices, knowledge of the underlying thermodynamic and kinetic factors for interface formation allows the design of materials with desired interface morphologies. In this sense, deriving the first principle rules to understand the formation of semiconductor heterojunctions has been a long-standing research interest of the surface and interface scientific communities[12].

## 2. Results and Discussion

### 2.1. Quantification of the interface structure

State-of-the-art aberration (probe)-corrected scanning transmission electron microscopy (TEM), where electrons scattered from the specimen into high angles are collected by an annular detector (HAADF: high angle annular dark field imaging), was applied to determine the atomic structure of the GaP/Si transition region. The scattering contrast, which is proportional to the atomic number of the scatterer and also depends on the microscope settings and sample parameters, was simulated using an absorptive potential method[13]. This approach yields a quantitative distribution of the elemental composition across the interface at atomic resolution. One can clearly resolve the individual atomic columns in the GaP layer and the Si substrate in the experimental HAADF images (**Figure 1**a & (b)), the Ga atom columns having the brightest contrast due to the largest atomic number, followed by the Si and P atoms. A thick (20 nm) TEM sample region is shown (Figure 1a) next to a thin (8 nm) TEM sample region (Figure 1b).This way of displaying the micrographs was chosen because structured interface morphologies on a nanometre scale are potentially imperceptible in thick TEM samples due to projection effects. However, the thick TEM samples contain identical information on the interface morphology, as will be shown by quantitative analysis. The chemical composition on each atomic column was derived by quantitative modelling of the electron scattering, as described in the *Experimental section* (see **Figure S1** for the contrast simulation details). The Si occupancy of each atomic column across the interface is presented for the thick and thin sample regions in Figure 1c and (d), respectively. The transition region between GaP and Si was found to exhibit a structure drastically different from the commonly assumed one: The interface is neither atomically abrupt, nor does it have a purely interdiffused profile. It stretches over a region significantly wider than two monolayers, which is the expected roughness resulting from a charge neutrality interface model[14]. Surprisingly, the interface region extends over several atomic layers. Moreover, this interface region constitutes a peculiar morphology that is exceedingly apparent in the thin TEM sample. The sample shows pyramidal structures recognized by triangular features on {111} lattice planes or slightly higher {112} index planes separating GaP and Si occupations. The intermixing of GaP and Si can also be observed in the thick sample's image. However, projection effects tend to overlay the distinct pyramids more than in the thin sample, as the morphology expands to only several nanometres. At this point, it should be noted that the Si surface was determined to be atomically flat prior to GaP deposition[9].

Lateral integration of image contrast yields the quantitative composition of elements across the interface, as depicted in **Figure 2** (blue data represent the experiment, red and green data represent simulation results, as discussed later). Again, data from thick (a) and thin (b) sample regions are presented. Both images were taken from the same TEM sample and result in identical intermixing. This extends over about seven atomic layers. As expected, average intensities for the thick as well as the thin sample yield the same intermixing, since we average over the structure of the interface. In order to assess a possible structured morphology across the interface, the quantitative composition profiles are provided next to the standard deviation of the composition along the integrated line scan. This standard deviation is called "clustering" and increases with the degree of structuring present at the interface. The clustering is larger for the thin TEM sample, which confirms a structured interface morphology that is more eminent in TEM samples with thicknesses approaching the characteristic length of the structuring. Nevertheless, thick TEM samples equivalently contain all the information on the interface intermixing.

The MOVPE growth conditions of the GaP/Si heterostructure were varied over a wide range, as summarized in the *Experimental Section*, in order to separate extrinsic from intrinsic influences on the interface formation. The growth parameters were chosen and monitored with extreme care. Low growth temperatures were applied in order to establish intrinsic interface morphologies as opposed to trivially interdiffused ones resulting from high temperatures. The striking, structured morphology at the transition region between Si and GaP layers was observed for all growth conditions investigated. Irrespective of the miscut of the substrate or the choice of the element first deposited in epitaxy, the highly unexpected structure features pyramidal shapes and intermixing over about seven monolayers at the GaP/Si interface. Integrated compositions (Si fraction) of GaP/Si interfaces grown under different conditions are compared in Figure 2c. The quantitative depth profiles of these samples are equivalent, proving the characteristic interface morphologies are identical. This intrinsic interface morphology can *only* be changed by significantly increasing the growth temperature (“High temperature”, blue data points in Figure 2c). As expected, a significantly wider, interdiffused interface is found for the high temperature growth conditions. Its morphology is unstructured and does not show any characteristic clustering profile (the corresponding atomically resolved HAADF STEM image and its quantitative simulation are shown in **Figure S2**).

We conclude that the intrinsic GaP/Si interface is significantly wider and reveals more structural features than previously suggested morphologies derived from a simple model[14]. The previous model considers charge neutrality at the interface and describes an extension of the interface of two monolayers. Moreover, no structured interfaces have been suggested so far. It is the aim of the theoretical modelling presented in the following to understand the physical origins of this interface geometry and whether there are thermodynamic or kinetic influences on the formation of this characteristic structure during the growth. The insights gained can be generalized towards the formation of other III/V-IV interfaces in semiconductor heteroepitaxy.

### 2.2. Computational Modelling

Computations of the electronic structure at the interface and kinetic modelling of the growth were performed to shed light on the experimental observations. At first, the question arises whether computations can also lead to the intermixing observed at the interface.

Growth processes are dominated by surface-diffusion of the atoms deposited. According to transition state theory, diffusion rates are determined by the activation energy required to move one atom to another minimum position on the surface. Thus, first principles density functional theory (DFT) computations were applied to determine the lateral diffusion barriers of Si, Ga and P atoms on the surfaces apparent during growth. It turns out that for the Si(001) surface used experimentally, the barriers for Si (0.47 eV) and Ga (0.11 eV) adatoms are much smaller compared to P (1.27 eV) adatoms. This is in line with previous experimental and theoretical studies: Diffusion barriers of 0.6 – 1.0 eV[15–18] were found for Si adatoms, while lower barriers were calculated for Ga adatoms (<0.5 eV[19]) and higher barriers for P adatoms (0.94 eV[20]) compared to Si[21]. A similar ratio of diffusion barriers for the adatoms Si, Ga and P was found for the Ga- and P-terminated GaP(001) surfaces. In **Figure 3**, the hopping pathways for the adatoms on the three possible surfaces are outlined. The pathways are thereby highlighted by red arrows with the origin being the starting point and the arrow head marking the end position of the hopping movement. One species (P atoms) is thus less mobile than the other species (Si and Ga atoms) in a microscopic analysis of diffusion on those surfaces.

The dynamic nature of the experimental deposition and interface formation can now be modelled by using this first principle result to make a rational choice of parameters for a large-scale kinetic Monte Carlo (KMC) simulation of the growth procedure using a Bortz-Kalos-Lebowitz (BKL) algorithm[22]. This method is applicable because elementary bonding processes and diffusion dominate the growth. The simulation, run on a diamond cubic lattice, consisted of adsorption and diffusion events mimicking the epitaxial growth with a comparable growth rate of 1 monolayer/s and a simulation temperature of 750 K. Energy barriers for adatom hopping were calculated in an Arrhenius-type approach from bond energies to nearest and next-nearest-neighbor atoms which determine the mobility of the species (see *Supporting Information* for details). If the KMC simulation is run with the premise derived from the DFT data above (one species being less mobile than the others, i.e. exhibiting a higher hopping barrier), then the experimental interface features are quantitatively reproduced. The depth indicates the same amount of intermixing, spanning approximately seven monolayers in the direction of growth (Figure 2a and (b), red data points). Moreover, if one starts growth modelling on a smooth Si surface (**Figure 4a)**, even the morphology of the GaP/Si interface region from KMC simulations is strikingly similar to the experimental observations of pyramid formation (Figure 4b, the GaP layer grown was removed to emphasize the Si interface structure). This is confirmed by the quantitative clustering analysis, which is in excellent agreement with the experimental observation for line scans across the interface of thin and thick TEM samples (Figure 2a and (b), red data points). This agreement is notably only found if one diffusing species (here P) is less mobile than the others. If the same parameters are chosen for all species, the resulting interface structure is always interdiffused and not structured (Figure 2a, green data points), whereby the width of the interdiffused region then depends on the simulated growth temperature. In short, the diffusion characteristics during growth mentioned above lead to an intermixing of atoms within an interface region of seven atomic layers.

However, the question remains, why do we find a structured, pyramidal interface morphology? Previous models suggested flat, one- or two-layer intermixed GaP/Si interfaces based on density functional theory (DFT) computations and rationalized by electron-counting models[14,23]. This puzzling finding can be understood from relative stabilities of intrinsic interfaces, which we calculated by DFT. Interface formation energies for GaP(001)/Si(001), GaP(111)/Si(111) and GaP(112)/Si(112) interfaces, also considering one-layer intermixing, were determined (**Figure 5**). We found randomly intermixed structures over several layers to be much less stable. The interface formation energies ($\Delta E_{if}$) are defined as

$$\Delta E_{if} = \left[ N/2\left(E_{Si} + E_{GaP}\right) - NE_{GaP/Si} \right] / A_{(001)} \qquad \text{Equation (1)}$$

where $E_{GaP/Si}$ is the energy of the interface supercell, $E_{Si}$ and $E_{GaP}$ are the total energies of supercells of the same size containing only Si or GaP bulk material, respectively, and *N* is a normalisation factor (1 for slab cells and 1/2 for bulk cells). $\Delta E_{if}$ is normalized to the unit cell area of the (001) interface $A_{(001)}$, which is orthogonal to the material's growth direction[24,25]. All $\Delta E_{if}$ values are positive, as expected for metastable materials that do not represent the global thermodynamic equilibrium structures[26]. The structures chosen for the DFT investigation of the GaP/Si interfaces represent the major growth directions and also consider intermixed structures leading to charge compensated interfaces[14,27]. Contrary to previous arguments predicting a diverging interface energy[25], a compensation of the interface dipole moment is not necessary and convergence is achieved with sufficiently large supercells. The supercells were constructed by elongating the silicon bulk cell by eight times the lattice constant in the respective direction and substituting half of the layers by GaP. This resulted in a $(Si)_{16}(GaP)_{16}$ supercell for all interfaces with two atoms in each layer (see **Figure 6**). A vacuum region of 16.6 Å was added for the slab cells and the resulting surfaces were passivated by hydrogen atoms on both sides of the slab. The $(001)_{im}$ and $(111)_{im}$ interfaces were modelled with bulk supercells of the composition $(Si)_{15}(\text{intermixed})_1(GaP)_{15}(\text{intermixed})_1$ and $(Si)_{23}(\text{intermixed})_1(GaP)_{23}(\text{intermixed})_1$, respectively. The "intermixed" layers thereby contain one Si and one Ga/P atom. For all interfaces, two possible terminations were investigated. Due to a beneficial construction of supercells (Figure 6) and the normalisation procedure used, the energies of different interfaces can be directly compared. Relaxation of the atomic positions in the interface structures resulted only in small effects as was found before for coherent interfaces[23,25] in contrast to larger local strain effects found in lattice-mismatched interfaces[28]. Also, considering configurational entropy only leads to minor corrections.

We find the Ga-terminated interface to be more stable compared to the P-terminated interface in all cases (for (001) and (111) there are exclusive Si-Ga or Si-P contacts at the interface; for a definition of termination for other interfaces, see Figure 6). For the (001) interface, which represents the growth direction, the one-layer intermixed structure $(001)_{\mathrm{im}}$ is more stable compared to the atomically flat interface, in accordance with previous findings[24,29]. The (111) interface, which lies at 35° to the growth direction, exhibits similar stabilities to $(001)_{\mathrm{im}}$. In this case, intermixing leads to an energy increase for $(111)_{\mathrm{im}}$. Regarding these orientations, the formation energies for both terminations are comparable, as was found previously for GaAs/ZnSe interfaces[25]. By contrast, the Ga-dominated termination $(112)_{\mathrm{Ga}}$ for the (112) interface is significantly more stable than the inverse P-dominated termination $(112)_{\mathrm{P}}$. This results in $(112)_{\mathrm{Ga}}$ being the most stable interface investigated. This can be understood by a close look at the chemical bonds at the interface between Si and non-silicon atoms, which are often termed “wrong bonds” (Figure 6). They dominate the electrostatic stabilization of the respective interface. For $(112)_{\mathrm{Ga}}$, one Si atom binds to two Ga atoms and two Si atoms have a bond to a P atom each. The inverse pattern is found for $(112)_{\mathrm{P}}$ (one Si binding to two P and two Si binding to one Ga each). These bonding patterns as the origin for the different stabilities of (112) interface terminations were postulated previously based on experimental and conceptual considerations[30], although with the inverse sign. The same pattern is also found for the (001), $(001)_{\mathrm{im}}$ and (111) interfaces: Si-Ga bonds destabilize less than Si-P bonds, and two bonds to non-silicon atoms have a higher energy penalty than one bond (Figure 6).This might lead to the conclusion that simple bond counting is enough to estimate the interface stabilities. This is, however, not the case, because no simple rule can be found to connect the stabilization energies for interfaces with Si binding to both Ga and P atoms (i.e. $(001)_{\mathrm{im}}$, $(111)_{\mathrm{im}}$, (112)) to the number of these bonds. Additionally, the relative energy ordering of the different interfaces cannot be explained by such a simple model. Only first principle calculations with good structural models are able to account for the chemical environment and deliver energies accurate enough for predictive analysis of these systems. The analysis of interface formation energies, thus, leads to the conclusion that $(112)_{\mathrm{Ga}}$ interfaces should preferentially be formed.

How does this help us understand the formation of the seven-layer intermixed trigonal structures observed experimentally? Considering the conclusions drawn from surface diffusion and KMC (intermixing occurs if one immobile species present) and DFT-based interface stabilities (high-index interfaces preferred), pyramids containing (112) or (111) facets are likely to be formed in the experimental procedure. Energetically close-lying facets are likely to be formed as well, thus leading to the pyramidal shape observed in experiments. Nevertheless, these structures are overgrown during the continued growth of GaP overlayers. Thus, the surface diffusion necessary to build the pyramids cannot continue and the resulting morphology is covered by bulk GaP. Pyramidal structures might form in the final lattice, with one facet composed of the most stable Ga-terminated (112) interface and the other facets by the second or third most stable interfaces.

## 3. Conclusion

Quantitative atomic resolution STEM of GaP/Si reveals an intrinsic pyramidal interface morphology. This morphology is stable under a wide range of growth conditions and can only be altered if growth temperatures are set to unreasonable high values so that interdiffusion dominates. Theoretical modelling by KMC and DFT has shown that this faceted interface structure is indeed the stable one for the examined material system. These findings allow general conclusions to be made concerning interface formation in semiconductor growth processes via heteroepitaxy. If two materials with different polarity or element combinations with highly different electronegativities are grown, there is a strong influence of the chemical environment on the structural morphology at the interface (thermodynamic drive). Hence, in heteroepitaxy, not only strain plays a key role in the formation of interfaces. In addition, the different mobility of relevant species on the surface results in diffusion (kinetic drive) and determines the width of the interface region assembled.

## 4. Experimental Section

*Growth procedure:* The GaP layers were grown on silicon substrates via metal organic vapor phase epitaxy (MOVPE) in an Aixtron AIX 200 GFR reactor. Prior to growth, a wet chemical etching procedure was applied to the exact Si(001) substrates. A homoepitaxial buffer was grown using silane as precursor. It has been verified by Scanning Tunneling Microscopy from samples transferred under vacuum that the Si surfaces after this treatment and prior to GaP growth were atomically flat. Triethylgallium and tertiarybutylphosphine were used as precursors for Ga and P, respectively. Optimized growth conditions were applied after the nucleation layer growth, which result in a minimum amount of anti-phase boundaries[8].To investigate the influence of the growth conditions on the interface structure, crucial parameters like temperature and pre-flow of the precursors and substrate off-cut were varied. All nucleation layers were grown in pulsed mode, where the P and Ga precursor are offered sequentially. For the samples shown in the paper, two temperature regimes were investigated: low-temperature nucleation at 450 °C (“Exact”, “2° off”, “Reversed Polarity”) and high temperature nucleation at 675 °C (“High temperature”). For the low temperature growth, the substrate off orientation was varied (“Exact” ⇔ “2° off”). The element bonding to the Si first was changed to achieve both GaP polarities on the same Si surface (“Exact” ⇔ “Reversed Polarity”).

*STEM (Scanning Transmission Electron Microscopy) characterization and modelling*

*TEM Sample preparation:* After the growth, electron transparent foils were prepared via conventional mechanical polishing followed by 5 KeV argon ion milling from both sides with an angle of incidence of 4° in a Gatan PIPS. Final polishing was carried out at 1.7 keV to reduce the amount of amorphous material on the samples. The viewing direction was chosen along a <110> axis of the Si substrate. Before starting the TEM (transmission electron microscopy) measurements, the samples were treated in a Fishione model 1020 plasma cleaner to remove residual hydrocarbon contaminations.

*STEM-Measurement:* The HAADF (high angle annular dark field)-Scanning TEM (STEM) measurements were carried out in a JEOL 2200 FS, operating at 200 kV, which is equipped with an aberration corrector for the probe forming lens system. The condensor aperture used results in a convergence semi-angle of 24 mrad and the annular detector collects electrons scattered in the range between 43 and 173 mrads. The parameters of the amplifier, namely brightness and contrast were chosen in a way that neither low intensities are lost nor the detector is saturated at high intensities. A linear feedback behavior of the detector with respect to the impinging electron current was verified by varying the probe current by using different probe size settings and different condenser apertures sizes.

*STEM image analysis:* For comparison of the experimental data with simulations, images were analyzed in a quantitative manner. In the following the procedure for their derivation is summarized. In a first step the background noise, i.e. the counts generated by the amplifier without electrons hitting the detector, is subtracted. The background noise can be determined by the acquisition of a STEM image with closed beam valve. Information on the chemical composition is essentially localized on the atomic columns while the region between the columns is also sensitive to effects of strain and disorder[31,32]. The commercially available Peak Pairs software[33] was used to determine the positions of the atomic columns with subpixel accuracy. To reduce the influence of experimental noise, e.g. fly back errors during the scan process or uncertainties in determination of the peak positions, the intensity was averaged in a circular region around each peak position. The radius of integration was chosen as 1/3 of the next neighbor distance which turned out to be the optimum value for reduction of noise without introducing influences due to the neighboring peaks or the background between the peak positions. The appropriate units to compare the experiments with simulations are fractions of the impinging beam and not the counts given by the detector. One way to derive these values is the normalization of the measured intensity to the intensity of the impinging beam via a detector scan[34]. Here we decided to use relative intensities instead, as it is not sensitive to the used settings of the amplifier as long as one sticks to the linear regime. Therefore the measured intensities in an image were normalized to the highest one, i.e. the intensity of a pure Ga column.

*Simulation of STEM images:* Complementary multislice simulations were performed using the HREM package in an absorptive potential approximation[13]. The decisive parameters (residual aberrations, convergence angle and detector range) were experimentally determined and taken into account in the simulation. The sample thickness as well as the chemical composition was varied to investigate their influence on the HAADF intensity individually.

The data obtained, i.e. the thickness-composition matrix (see Figure S1), served as a database for the comparison with experimental data.

*Density Functional Theory (DFT) computations:* Periodic density functional theory (DFT) based calculations were performed applying a GGA functional (PBE[35], found to be reliable for Si/GaP interfaces[36]) together with a semi-empirical dispersion correction scheme (D3(BJ))[37,38].The use of a projector-augmented wave (PAW)[39,40] formalism allowed the truncation of the plane-wave basis set at a kinetic energy cutoff of 350 eV (adatom hopping) and 400 eV (interfaces), respectively. The Brillouin zone was sampled by Γ-centered k-meshes with 8x8x1 (hopping), 4x4x2 ((001)-interfaces), 8x4x1 ((111) and (112)-interfaces) k-points via the Monkhorst-Pack method[41]. Spin polarization was considered in all calculations. The VASP code, version 5.3.5 was used[42,43]. The total energy of the system was converged to $10^{-6}$ eV in every electronic relaxation step. Construction of all supercells was based on a silicon bulk cell with diamond structure using the experimental lattice constant (a = 5.431 Å).

The supercell for the adatom hopping barriers consisted of eight layers of silicon atoms representing the (001) surface model with an unreconstructed top layer and bottom layer saturated by hydrogen atoms. A vacuum region of 12.2 Å was added. This setup represents the model chosen in the subsequent KMC simulations. P-terminated surfaces were generated by substituting the top four layers of Si by alternating Ga- and P-layers (resulting in a $(Si)_4$-Ga-P-Ga-P layer structure). Ga-terminated surfaces carried one more Ga-layer ($(Si)_4$-$(GaP)_2$-Ga). No structural relaxation of the supercells was allowed. Minima and transition states were found via structural relaxation of the adatom positions until residual forces were converged to <0.01 eV/Å using a quasi-Newton (variable metric) algorithm[44]. Vibrational frequency calculations at the Γ-point were carried out via density functional perturbation theory[45,46] to identify transition state structures (one imaginary mode). The transition states presented here connect two minima whereas a complete hopping step ends at the translationally equivalent minimum position in a neighboring cell. As the adatom positions were not restricted to ideal lattice sites, this required two elementary steps for the Si and P adatoms, but only one for Ga. However, the additional hopping barriers for Si and P were small compared to the rate-determining ones presented in Figure 3 and showed identical trends.

Details on the Kinetic Monte Carlo simulations are described in the *Supporting Information*.

## Supporting Information

Supporting Information is available from the Wiley Online Library or from the author.

## Acknowledgements

Support from the German Science foundation (DFG) in the framework of the Research Training Group "Functionalization of Semiconductors" (GRK 1782) and the CRC 1083 ("Structure and Dynamics of internal Interfaces") is gratefully acknowledged. A.S. thanks the Beilstein Foundation for funding. R.T. and A.S. thank the HLR Stuttgart and LOEWE-CSC Frankfurt for computational resources.

Received: ((will be filled in by the editorial staff))
Revised: ((will be filled in by the editorial staff))
Published online: ((will be filled in by the editorial staff))

[1] G. E. Moore, *Proc. IEEE* **1998**, *86*, 82.

[2] "International Technology Roadmap for Semiconductors," can be found under http://www.itrs.net/reports.html, accessed 05 2015.

[3] J. Robertson, *Reports Prog. Phys.* **2005**, *69*, 327.

[4] R. Chen, T.-T. D. Tran, K. W. Ng, W. S. Ko, L. C. Chuang, F. G. Sedgwick, C. Chang-Hasnain, *Nat. Photonics* **2011**, *5*, 170.

[5] S. Liebich, M. Zimprich, a. Beyer, C. Lange, D. J. Franzbach, S. Chatterjee, N. Hossain, S. J. Sweeney, K. Volz, B. Kunert, W. Stolz, *Appl. Phys. Lett.* **2011**, *99*, 071109.

[6] H. Kroemer, *J. Cryst. Growth* **1987**, *81*, 193.

[7] B. Kunert, S. Zinnkann, K. Volz, W. Stolz, *J. Cryst. Growth* **2008**, *310*, 4776.

[8] K. Volz, A. Beyer, W. Witte, J. Ohlmann, I. Nmeth, B. Kunert, W. Stolz, *J. Cryst. Growth* **2011**, *315*, 37.

[9] B. Kunert, I. Németh, S. Reinhard, K. Volz, W. Stolz, *Thin Solid Films* **2008**, *517*, 140.

[10] N. Grandjean, J. Massies, M. Leroux, *Phys. Rev. B* **1996**, *53*, 998.

[11] A. Rosenauer, D. Gerthsen, D. Dyck, M. Arzberger, G. Böhm, G. Abstreiter, *Phys. Rev. B* **2001**, *64*, DOI 10.1103/PhysRevB.64.245334.

[12] A. Franciosi, *Surf. Sci. Rep.* **1996**, *25*, 1.

[13] K. Ishizuka, *Ultramicroscopy* **2002**, *90*, 71.

[14] W. Harrison, E. Kraut, J. Waldrop, R. Grant, *Phys. Rev. B* **1978**, *18*, 4402.

[15] Y. Mo, J. Kleiner, M. Webb, M. Lagally, *Phys. Rev. Lett.* **1991**, *66*, 1998.

[16] G. Brocks, P. J. Kelly, R. Car, *Phys. Rev. Lett.* **1991**, *66*, 1729.

[17] A. P. Smith, J. K. Wiggs, H. Jónsson, H. Yan, L. R. Corrales, P. Nachtigall, K. D. Jordan, *J. Chem. Phys.* **1995**, *102*, 1044.

[18] Y.-W. Mo, J. Kleiner, M. B. Webb, M. G. Lagally, *Surf. Sci.* **1992**, *268*, 275.

[19] T. Hitosugi, Y. Suwa, S. Matsuura, S. Heike, T. Onogi, S. Watanabe, T. Hasegawa, K. Kitazawa, T. Hashizume, *Phys. Rev. Lett.* **1999**, *83*, 4116.

[20] J. M. Bennett, O. Warschkow, N. A. Marks, D. R. McKenzie, *Phys. Rev. B - Condens. Matter Mater. Phys.* **2009**, *79*, DOI 10.1103/PhysRevB.79.165311.

[21] G. Brocks, P. J. Kelly, R. Car, *Surf. Sci.* **1992**, *269-270*, 860.

[22] A. Bortz, M. Kalos, J. Lebowitz, *J. Comput. Phys.* **1975**, *17*, 10.

[23] O. Romanyuk, T. Hannappel, F. Grosse, *Phys. Rev. B - Condens. Matter Mater. Phys.* **2013**, *88*, DOI 10.1103/PhysRevB.88.115312.

[24] G. X. Qian, R. M. Martin, D. J. Chadi, *Phys. Rev. B* **1988**, *38*, 7649.

[25] A. Kley, J. Neugebauer, *Phys. Rev. B* **1994**, *50*, 8616.

[26] R. G. Dandrea, S. Froyen, A. Zunger, *Phys. Rev. B* **1990**, *42*, 3213.

[27] M. D. Pashley, *Phys. Rev. B* **1989**, *40*, 10481.

[28] R. G. Dandrea, C. B. Duke, *Phys. Rev. B* **1992**, *45*, 14065.

[29] O. Supplie, S. Brückner, O. Romanyuk, H. Döscher, C. Höhn, M. M. May, P. Kleinschmidt, F. Grosse, T. Hannappel, *Phys. Rev. B* **2014**, *90*, DOI 10.1103/PhysRevB.90.235301.

[30] S. L. Wright, *J. Vac. Sci. Technol.* **1982**, *21*, 534.

[31] V. Grillo, K. Mueller, K. Volz, F. Glas, T. Grieb, a Rosenauer, *J. Phys. Conf. Ser.* **2011**, *326*, 012006.

[32] M. Herrera, Q. M. Ramasse, D. G. Morgan, D. Gonzalez, J. Pizarro, A. Yáñez, P. Galindo, R. Garcia, M. H. Du, S. B. Zhang, M. Hopkinson, N. D. Browning, *Phys. Rev. B - Condens. Matter Mater. Phys.* **2009**, *80*, DOI 10.1103/PhysRevB.80.125211.

[33] P. L. Galindo, S. Kret, A. M. Sanchez, J. Y. Laval, A. Yáñez, J. Pizarro, E. Guerrero, T. Ben, S. I. Molina, *Ultramicroscopy* **2007**, *107*, 1186.

[34] J. M. Lebeau, S. Stemmer, *Ultramicroscopy* **2008**, *108*, 1653.

[35] J. P. Perdew, K. Burke, M. Ernzerhof, *Phys. Rev. Lett.* **1996**, *77*, 3865.

[36] K. Steiner, W. Chen, A. Pasquarello, *Phys. Rev. B - Condens. Matter Mater. Phys.* **2014**, *89*, DOI 10.1103/PhysRevB.89.205309.

[37] S. Grimme, J. Antony, S. Ehrlich, H. Krieg, *J. Chem. Phys.* **2010**, *132*, DOI 10.1063/1.3382344.

[38] S. Grimme, S. Ehrlich, L. Goerigk, *J. Comput. Chem.* **2011**, *32*, 1456.

[39] P. E. Blöchl, *Phys. Rev. B* **1994**, *50*, 17953.

[40] G. Kresse, *Phys. Rev. B* **1999**, *59*, 1758.

[41] H. J. Monkhorst, J. D. Pack, *Phys. Rev. B* **1976**, *13*, 5188.

[42] J. Hafner, *J. Comput. Chem.* **2008**, *29*, 2044.

[43] G. Kresse, *Phys. Rev. B* **1996**, *54*, 11169.

[44] P. Pulay, *Chem. Phys. Lett.* **1980**, *73*, 393.

[45] X. Wu, D. Vanderbilt, D. R. Hamann, *Phys. Rev. B - Condens. Matter Mater. Phys.* **2005**, *72*, DOI 10.1103/PhysRevB.72.035105.

[46] G. Kresse, J. Hafner, *Phys. Rev. B* **1993**, *47*, 558.

[47] A. Rosenauer, K. Gries, K. Müller, M. Schowalter, A. Pretorius, A. Avramescu, K. Engl, S. Lutgen, *J. Phys. Conf. Ser.* **2010**, *209*, 012009.

[48] T. Grieb, K. Müller, R. Fritz, M. Schowalter, N. Neugebohrn, N. Knaub, K. Volz, A. Rosenauer, *Ultramicroscopy* **2012**, *117*, 15.

[49] K. Reyes, P. Smereka, D. Nothern, J. M. Millunchick, S. Bietti, C. Somaschini, S. Sanguinetti, C. Frigeri, *Phys. Rev. B - Condens. Matter Mater. Phys.* **2013**, *87*, DOI 10.1103/PhysRevB.87.165406.

[50] P. Gaillard, J.-N. Aqua, T. Frisch, *Phys. Rev. B* **2013**, *87*, 125310.

[51] K. Werner, A. Beyer, J. O. Oelerich, S. D. Baranovskii, W. Stolz, K. Volz, *J. Cryst. Growth* **2014**, *405*, 102.

**Figure 1**. Atomically resolved STEM HAADF images of the GaP/Si interface region in [110] viewing direction for thick (a) and thin (b) regions of the same TEM sample. Corresponding 2D plots of the GaP/Si interface composition (distortion-corrected, simulated scanning TEM image) across the interfaces projected onto the Si-(011) plane for thick (c) and thin (d) TEM sample. The occupancy of each atomic column with Si is plotted in (c) and (d).

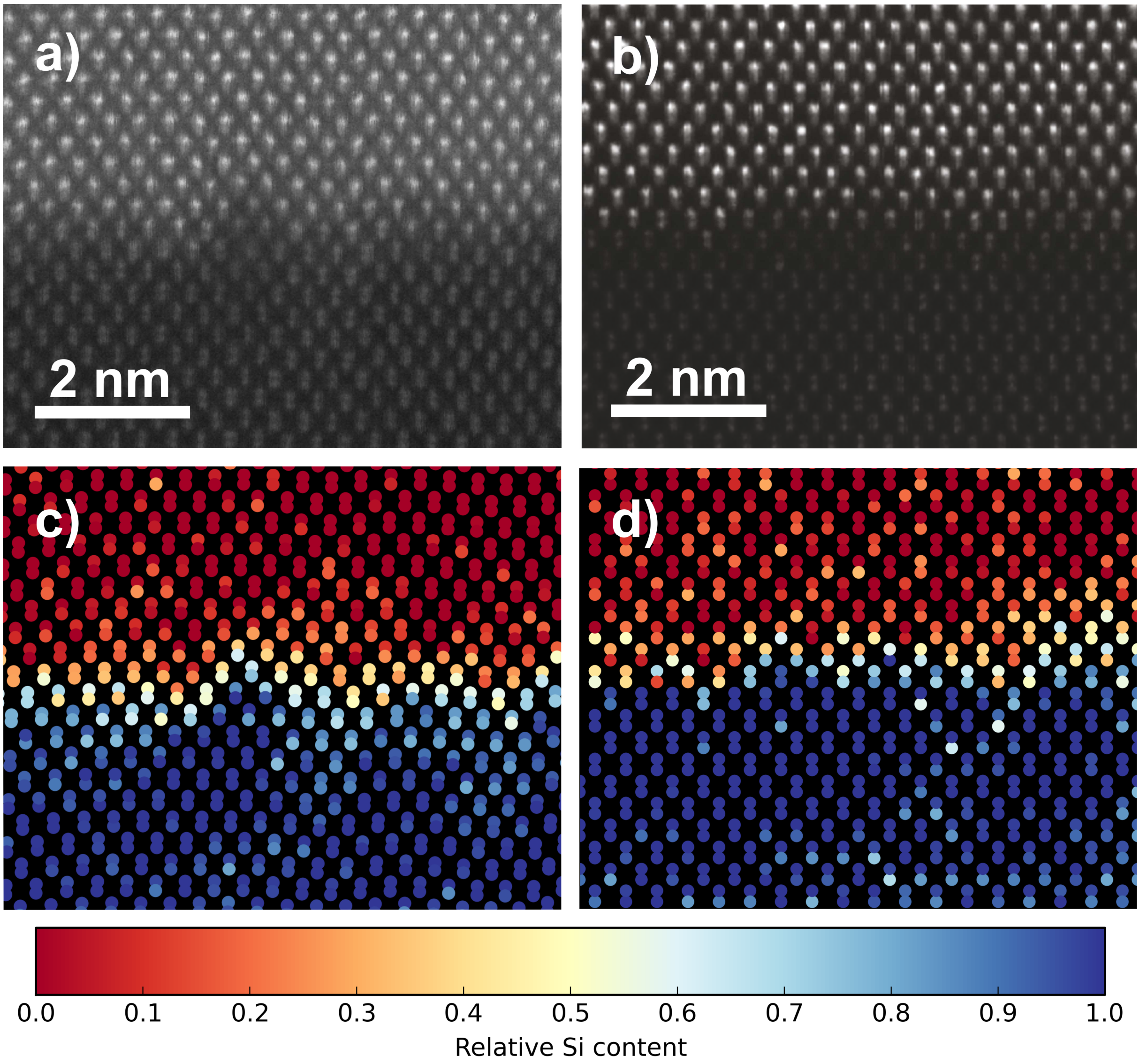

**Figure 2**. Silicon fraction on each atomic column and a measure of clustering (standard deviation of composition data in integration direction) vs. monolayers across the GaP/Si interface of the (a) thick (20 nm) and (b) thin (8 nm) TEM sample (blue) compared to the corresponding simulation results (red). The region of significant intermixing is indicated in the composition profiles in grey. The theoretical Si depth profile and clustering for the pure diffusion case is shown as green curve in (a). In (c) integrated Si depth profiles across the GaP/Si interfaces for several different samples grown under highly different conditions are shown. The growth conditions are explained in more detail in the *Experimental Section*.

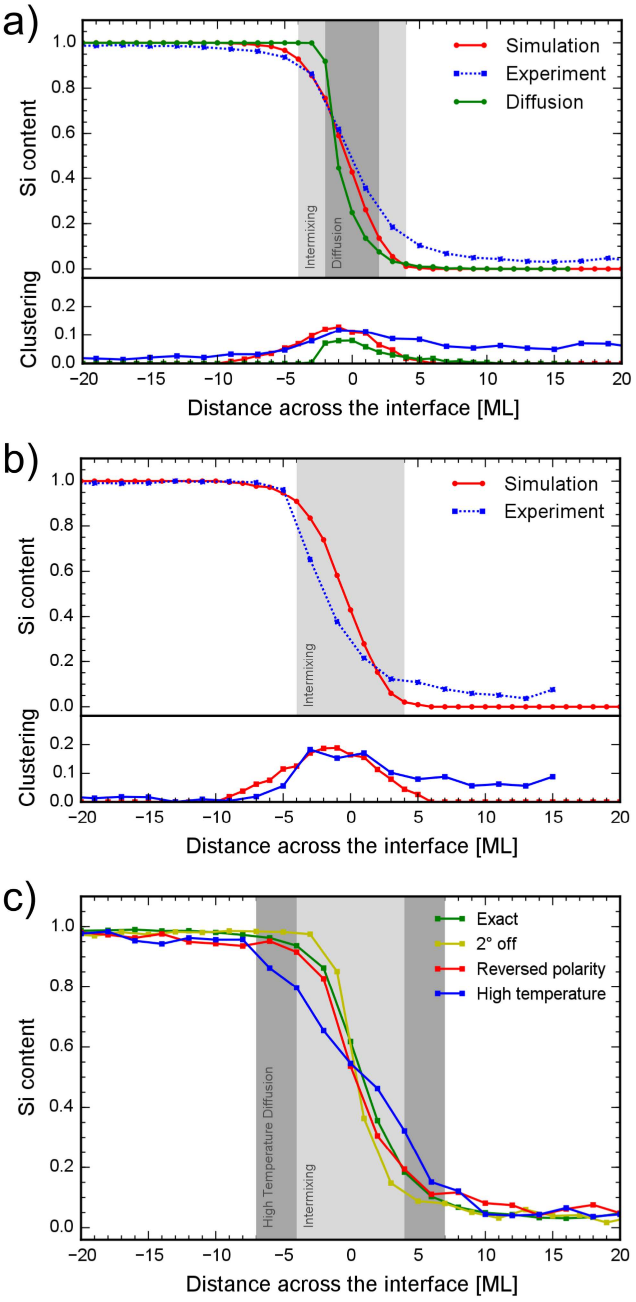

**Figure 3.** Minimum (Min) and transition state (TS) positions of Si (left), Ga (middle) and P (right) adatoms on (a) Si(001), (b) P-terminated and (c) Ga-terminated GaP/Si(001) substrate from atop. Adatom positions are indicated via arrow origin (Min) and arrow head (TS). The three top-most substrate layers can be distinguished from one another by decreasing atomic radii. Barrier heights for the hopping movement are given in eV below the respective scetch. Color code: Si – blue, P – green, Ga – orange.

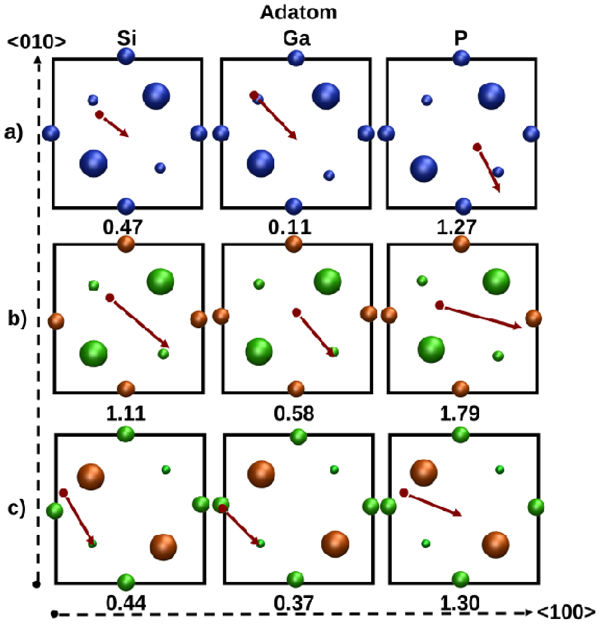

**Figure 4**. Silicon surfaces prior to and Si/GaP interface after GaP deposition from the KMC simulation. Similar to the experiment, the Si surface after Si deposition in the KMC simulation was atomically flat (a). After GaP deposition, a structured Si interface is obtained ((b): the Ga and P atoms were removed from the crystal after simulation for clarity), which is structured as experimentally observed.

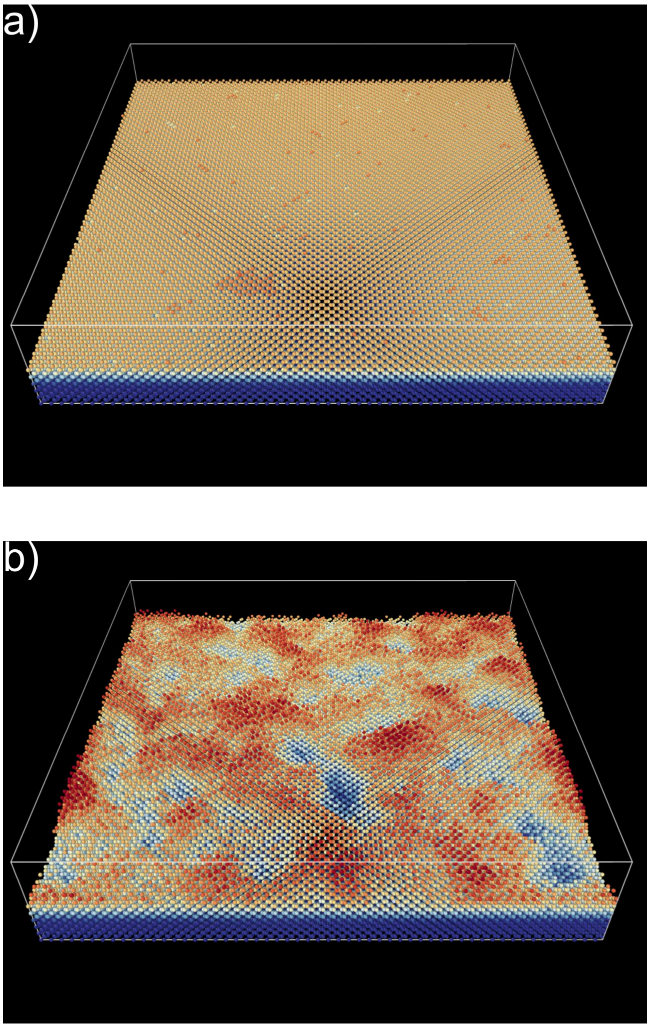

**Figure 5.** (a) Representation of the computed GaP/Si interface cell models at (111), (001) and (112) (Color code: Si – blue, P – green, Ga – orange). (b) interface formation energies $\Delta E_{if}$ for the abrupt and intermixed structures calculated by periodic DFT. Color code: orange – Ga-terminated interfaces, green – P-terminated interfaces.

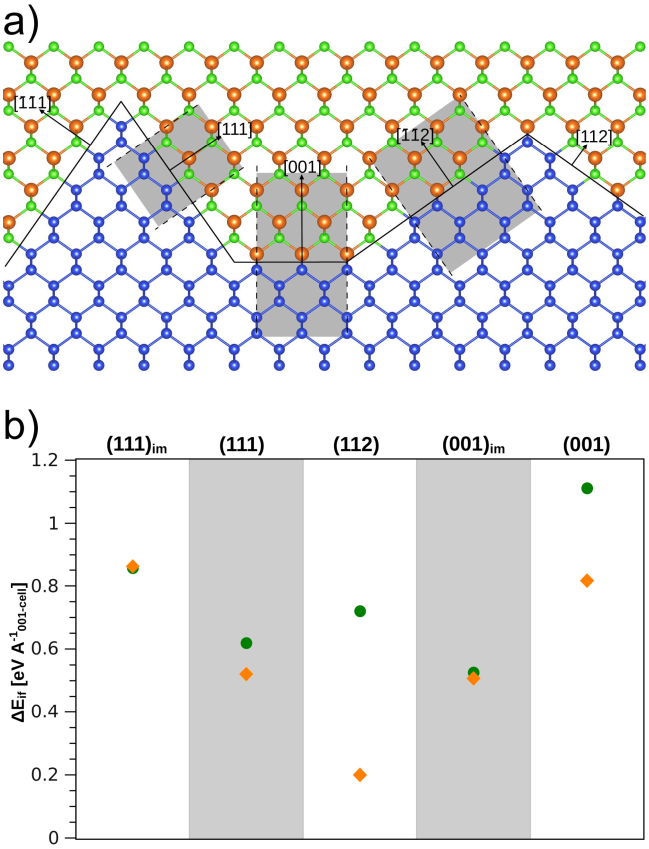

**Figure 6.** Structural models used for the DFT computation of $\Delta E_{if}$. Shown are the Ga-terminated interface models. Si(-P/-Ga)$_n$ (fourth column) indicates *n* P/Ga atoms binding to one Si atom at the interface for the given termination (third column). Color code: Si – blue, P – green, Ga – orange.

| Inter-face | Structural model | Termi-nation | Bonds at the interface |
|---|---|---|---|
| (001) | 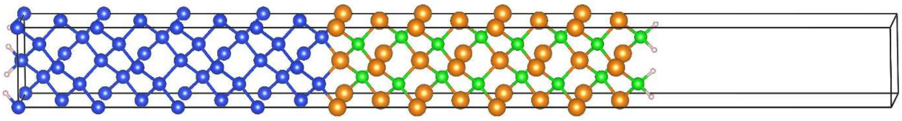 | Ga | Si(-Ga)$_2$ (2x) |
| | | P | Si(-P)$_2$ (2x) |
| (001)$_{im}$ | 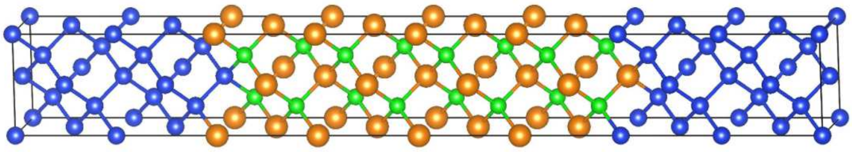 | Ga | Si-Ga (2x); Si(-P)$_2$ |
| | | P | Si-P (2x); Si(-Ga)$_2$ |
| (111) | 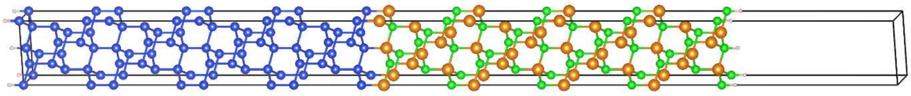 | Ga | Si-Ga (2x) |
| | | P | Si-P (2x) |
| (111)$_{im}$ | 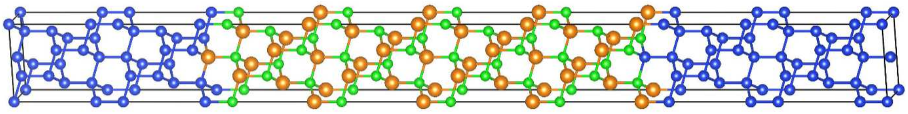 | Ga | Si-Ga, Si(-P)$_3$; Si-P, Si(-Ga)$_3$ |
| | | P | Si-Ga, Si(-P)$_3$; Si-P, Si(-Ga)$_3$ |
| (112) | 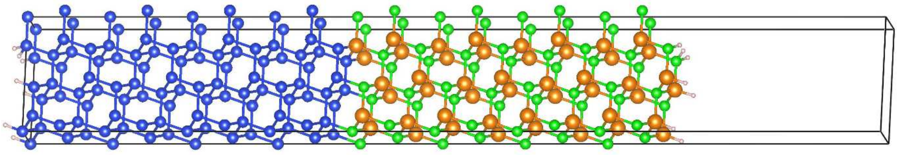 | Ga | Si-P (2x), Si(-Ga)$_2$ |
| | | P | Si-Ga (2x), Si(-P)$_2$ |

**ToC entry**

**Technologically relevant III/V semiconductors** epitaxially grown on silicon substrates are investigated in detail. Atomic resolution transmission electron microscopy as well as theoretical modelling reveal the intrinsic interface structure. A highly unexpected interface with pyramidal shape and about seven layers of intermixing is found and driving forces for its formation are explained.

ToC Figure

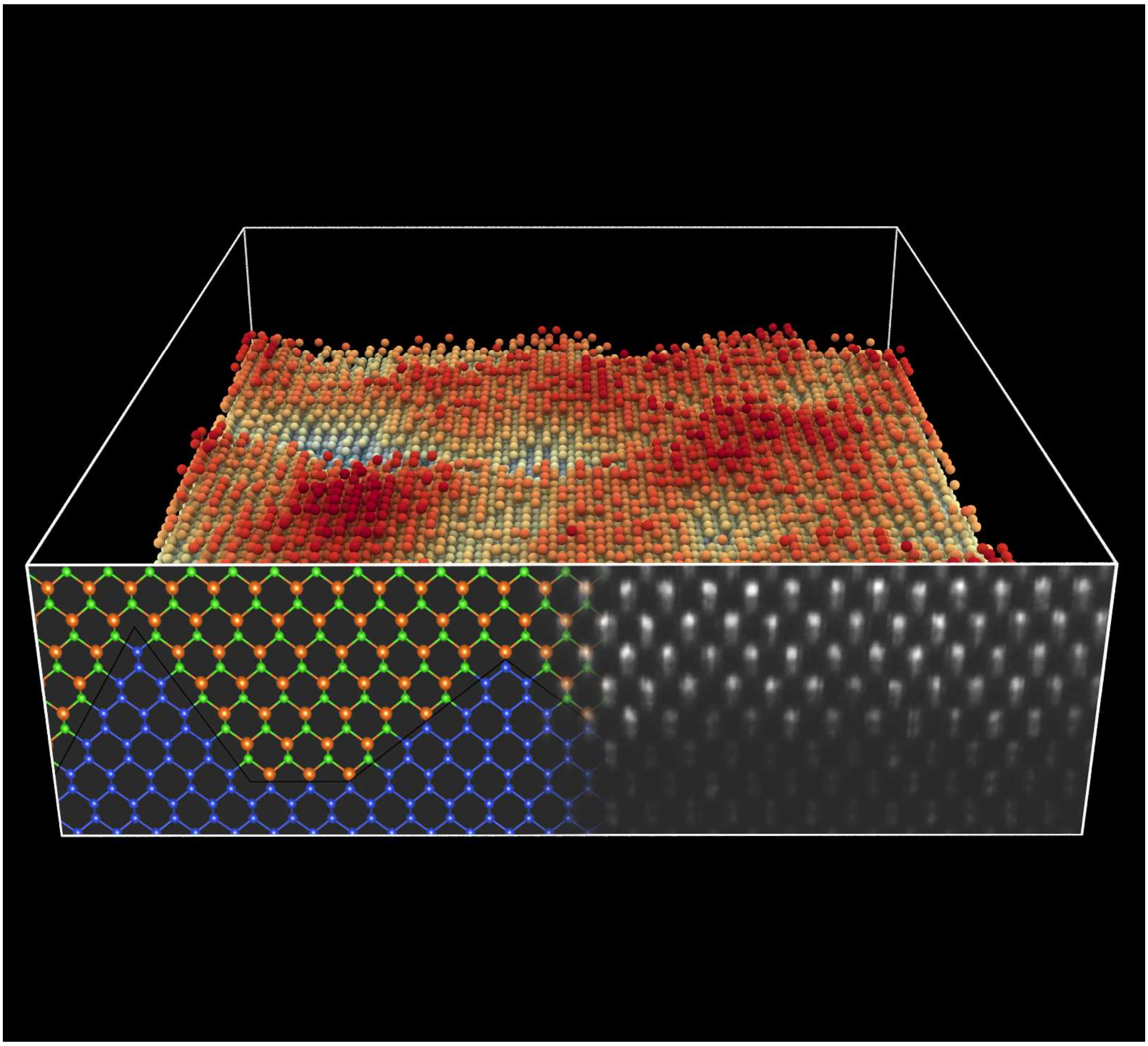

# Supporting Information

## Pyramidal Structure Formation at the Interface between III/V Semiconductors and Silicon

*Andreas Beyer, Andreas Stegmüller, Jan O. Oelerich, Kakhaber Jandieri, Katharina Werner, Wolfgang Stolz, Sergei D. Baranovskii, Ralf Tonner*, Kerstin Volz**

In Figure S1a the HAADF intensities simulated for pure GaP (blue squares) and Si (blue circles) are drawn against the thickness of a TEM sample. As relative intensities are used instead of absolute ones for the determination of the composition the Si intensity normalized to the GaP intensity is also drawn (red circles in Figure S1a, please read right scale). The latter graph exhibits a monotonous behavior meaning that a sample thickness results in a specific ratio of GaP to Si and vice versa. Therefore the actual sample thickness can be derived from Si/GaP intensity ratios measured in the regions of perfect crystal far away from the interface region.

At fixed thicknesses the influence of the amount of Si in an atomic column on the HAADF intensity was determined for both sublattices separately.  The dependence of the intensity on the Si content is summarized in Figure S1b. To allow for definite interpretation of the intensity it was assumed that the group III sublattice is occupied by Ga and Si only, while the group V sublattice is occupied by P and Si, i.e. no antisites are present. Therefore the intensity on each atomic column can be converted directly into the amount of Si present.

This procedure is similar to an approach used for ternary III/V materials[1,2] but additionally exploits the atomic resolution achievable with an aberration corrected microscope. As the atomic resolution measurements were limited to thin regions of the TEM sample absorptive potential is a good approximation and a more time consumable frozen phonon calculation is not necessary. Moreover the influence of beam broadening while travelling through the sample is reduced by choosing thin sample regions. In addition, nanoscale structures at interfaces can be detected for thin samples only, as projection effects are avoided.

**Figure S1**. Simulated HAADF STEM intensities versus the sample thickness for pure GaP (blue squares) and pure Si (blue circles) are depicted in (a). The corresponding y-axis on the left hand side is scaled in fractions of the impinging beam. The red circles show the dependence of the intensity ratio of Si and GaP on the thickness. The corresponding y-axis can be found on the right hand side. The dependence of the intensity on the chemical composition for different thicknesses is summarized in (b).

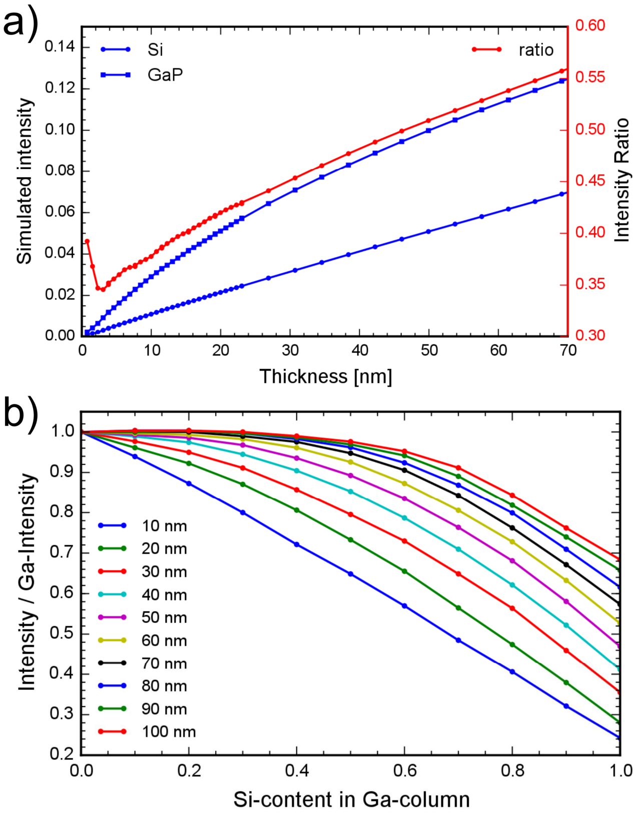

In Figure S2 the HAADF STEM image and the corresponding quantitative evaluation for the sample grown at “high temperature” is shown (blue depth profile in Figure 2c). The interdiffused instead of a structured interface can be seen very well.

**Figure S2.** Atomically resolved STEM HAADF images of the GaP/Si interface region in [110] viewing direction for a sample grown at high temperature (a). The corresponding 2D plot of the GaP/Si interface composition across the interface projected onto the Si-(011) is plotted in (b).

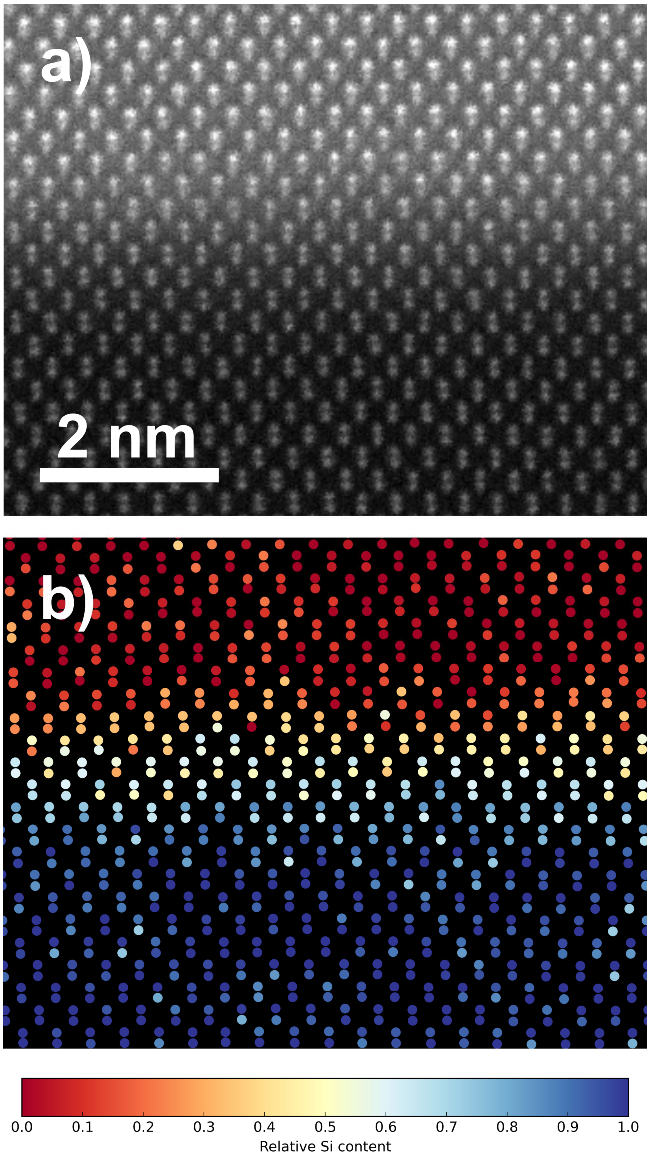

*Kinetic Monte Carlo simulations:* The Kinetic Monte Carlo (KMC) simulations were carried out using a Bortz-Kalos-Lebowitz (BKL) algorithm[3]. Atoms were constrained to a diamond cubic lattice at all times, and occupied lattice sites were assured to always be connected to the substrate (two layers of immobile Si) via chains of nearest-neighbor bonds. Periodic boundary conditions were applied in directions [100] and [010] perpendicular to the growth direction, [001]. The simulation consisted of sequences of two atomistic events: Atom diffusion, in which an adatom hops to an unoccupied adjacent lattice site within the second coordination sphere, and atom adsorption, where a new atom arrives at a random unoccupied lattice position on the sample surface. While the diffusion events were enabled at all times, adsorption was switched on and off according to the current growth or relaxation phase.

The rates of the adsorption events of all three atomic species (Si, Ga, P) were chosen to attain an overall growth rate of 1 ML/s, which was also set in the experiment. Diffusion event rates were calculated using the following Arrhenius equation:

$$\nu_i = \nu_0 * \exp(-E_i/k_B T) \qquad \text{Equation (S1)}$$

In this equation, $\nu_0$ is the frequency of atomic vibrations, $E_i$ is the energy barrier for leaving the atom's current position, T is temperature, and $k_B$ the Boltzmann constant. In the simulations, values of $\nu_0 = 2.5 \times 10^{13} s^{-1}$, which is within the typical order of the atomic vibration frequencies, and T = 750 K, being close to the experimental conditions (see Section *Growth Procedure*), were used. The energy barriers $E_i$ were calculated as a sum over neighboring atoms within the second coordination sphere, i.e., the nearest- and next-nearest-neighbors[4,5]. Each atomic bond to one of these neighbors was assigned a specific energy that depends on the atomic species and the distance of the two atoms. The chosen bond energies are: (0.30, 0.15) for Si-Si, Si-Ga, Ga-Ga, P-Ga, Ga-P, P-P and (0.60, 0.20) for P-Si, Si-P with the values in brackets being tuples of nearest- and next-nearest-neighbor bonds in eV, respectively. The values for the Si-Si, Si-Ga, and Ga-Ga bonds, 0.3 eV and 0.15 eV, have recently been proven suitable to reproduce etching effects of Ga deposition on Si(001) substrates[6].

The simulation was started with an initial substrate system of two completely filled layers of Si. These atoms were not allowed to perform any diffusion steps throughout the simulation. Then, 25 ML of (mobile) Si atoms were grown onto the substrate and were then relaxed for 10s without additional growth, resulting in a smooth surface with only some unstable 1 ML islands and single adatoms on the upmost surface layer. After the substrate growth, 10 ML each of Ga and P were grown layer by layer onto the Si surface, starting with P and including a relaxation pause of 1s after each completed layer.

References

[1] A. Rosenauer, K. Gries, K. Müller, M. Schowalter, A. Pretorius, A. Avramescu, K. Engl, S. Lutgen, *J. Phys. Conf. Ser.* **2010**, *209*, 012009.

[2] T. Grieb, K. Müller, R. Fritz, M. Schowalter, N. Neugebohrn, N. Knaub, K. Volz, A. Rosenauer, *Ultramicroscopy* **2012**, *117*, 15.

[3] A. Bortz, M. Kalos, J. Lebowitz, *J. Comput. Phys.* **1975**, *17*, 10.

[4] K. Reyes, P. Smereka, D. Nothern, J. M. Millunchick, S. Bietti, C. Somaschini, S. Sanguinetti, C. Frigeri, *Phys. Rev. B - Condens. Matter Mater. Phys.* **2013**, *87*, DOI 10.1103/PhysRevB.87.165406.

[5] P. Gaillard, J.-N. Aqua, T. Frisch, *Phys. Rev. B* **2013**, *87*, 125310.

[6] K. Werner, A. Beyer, J. O. Oelerich, S. D. Baranovskii, W. Stolz, K. Volz, *J. Cryst. Growth* **2014**, *405*, 102.

# Theoretical investigations on the stability of gallium phosphide - silicon interface structures

Andreas Stegmüller and Ralf Tonner*

*Department of Chemistry and Material Sciences Center, Philipps-University Marburg,*
*Hans-Meerwein-Str. 4, 35032 Marburg, Germany*

E-mail: tonner@chemie.uni-marburg.de

Phone: +49 (0)6421-2825418. Fax: +49 (0)6421-2821826

## Abstract

The morphology of the gallium phosphide - silicon interface is faceted and interdiffused about eight atomic layers which results from a combination of kinetic growth effects and thermodynamic stabilization of abrupt interfaces at (111) and intrinsically charge-compensated structures at (112) and (113). Different configurations of those are compared to (001) by computing absolute formation energies with periodic density functional theory applying both slab- and bulk-type supercells. As can be distinguished between specifically Ga- or P-terminated interfaces a detailed explanation on local interface properties is provided in an attempt to quantitatively explain the stabilities found. Simple counting of non-octet bonds is unable to severe divergence of formation energies of Ga- and P-dominated GaP-Si interfaces at (112) and (113). On the other hand, structural relaxation, averaged electrostatic potentials and partial charges based on natural bond orbitals (NPA) were used successfully support qualitative trends suggested by the Electron Counting Model for the stabilities of interfaces at (001) and

---

*To whom correspondence should be addressed

(111). It was concluded that only periodic calculations from first principles quantitatively account for the chemical environment necessary to predict interface properties.

# Introduction

Silicon-based logical devices have been the fundament of electronic applications since decades. For increasing their performances, device miniaturization and integration of novel materials are two major strategies.[1,2] Both rely on well-defined interface morphologies between stacked thin films as those determine the electronic band alignment and thus the conduction properties from one material to the other.[3,4]

Functional III/V compound semiconductors with different band gaps are being developed for the integration into Si-based quantum-well structures. Those are superstructures composed of stacked thin films with thicknesses in the nano-scale. By combining films of materials with narrow and wide band gaps, a laser can be realized.[2,5] However, to achieve adequate laser performances, defect-free crystalline films with atomically abrupt interfaces are required.[6] Both polarity and mechanical strain originate from the structural morphology of the interface and affect the electronic structure of the materials.[7–10] To some extent, material compositions (thus, strain) and interface structure (thus, polarity) are controlled by the growth conditions.[11,12]

One has to distinguish between local effects directly at the interface (excess charges, stress) and film-wide consequences of lattice-mismatch (strain), thermal expansion and the polarity of III/V materials. The first is determined by the atomic structure and local composition, and the latter affects phase stability and the extended electronic structure. Both properties relate mutually to growth.

Gallium phosphide films (GaP) on silicon substrates (Si) are important representatives of almost lattice-matched heterostructures that can be grown via epitaxial deposition techniques.[6] GaP is used as structural buffer layer to other materials lattice-mismatched to Si.

In this system, mechanical strain causes only small local distortions at the interface[13] so that the interface is usually assumed to be either atomically abrupt or interdiffused within one or two atomic layers.[14,15] The interdiffused atomic reconstruction was interpreted as a consequence of the formation of non-octet Si-Ga and Si-P bonds which lead to an accumulation of charge at the interface (local dipoles) and destabilize the interface.[16] By intermixing every second atom along the interface plane, acceptor (Si-Ga, positive) and donor (Si-P, negative) bonds are placed at ratio 1:1 and the charge is compensated.[14] The Electron Counting Model (ECM) proposed by Pashley[17] was aimed to predict the stabilities of $sp^3$-hybridized semiconductor surfaces and was also applied for GaP-Si interface formations.[18] It is based on a known surface periodicity and predicts stabilization if all dangling bonds (unsaturated atomic states) can be paired by reconstruction (i.e. formation of new bonds, e.g. surface dimers) so that unoccupied states are located in the conduction band (CB) or doubly occupied states in the valence band (VB).

A model proposed by Dandrea et al. is based on counting non-octet bond electrons and long-range electrostatic contributions to predict formation energies of GaP-Si interfaces.[19] It was derived from first principles calculations (DFT, LDA) with bulk-type supercells. These calculations showed, that the intermixing also affects the film-wide polarization field along stacking direction.[9,19]

In bulk-type GaP-Si supercells, two interfaces are present. For the abrupt, uncompensated interfaces along [001] and [111], the modeled interfaces typically consist of opposite compositions (Si-Ga and Si-P) and the polarization field is oscillating in between. This is unfavourable and raises the energy of the model. Intermixed interface configurations or other orientations (e.g. [110] and [113][18]) have been reported to be charge-compensated without further reconstruction resulting in smaller polarization fields[20] and lower formation energies.[21] As the polarization affects the valence band offset (VBO), this interface property is vital for application as electronic conduction barrier.

Kley and Neugebauer discussed the polarization field in polar semiconductors in conjunction with the average charge density along growth direction.[20] The polarization field appears along within the heterocompound film and extends over the entire thickness modeled. In contrast, local dipoles in the bonding region of the interface were described which were attributed to the formation of non-octet bonds in accordance to the simple model introduced above. For GaP-Si(110) interfaces, Lazzouni et al. relaxed atom positions and evaluated local electrostatic properties based on LDA calculations.[13] A VBO of 0.55 eV was estimated including corrections for spin-orbit splitting and the self-interaction error.

Recent DFT calculations by Romanyuk et al.[18] on the GGA level provided relative formation energies of GaP-Si interfaces in the orientations (110), (111) and (113). Bulk-type periodic supercells were applied to evaluate interface energies, local potentials and charge densities of abrupt and intermixed (one atomic layer) configurations. Under P-rich conditions, the P-terminated GaP-Si(111) interface is abrupt (uncompensated), however, the compensated interface with intermixed configuration is more stable under Ga-rich conditions. The Ga-terminated GaP-Si(111) is estimated as more stable in the intermixed configuration under all conditions considered. These findings were interpreted in accordance to the ECM introduced above. VBOs for GaP-Si(110) and GaP-Si(111) were estimated as 0.5 eV and 0.76 eV, respectively.[18] For formation energies and electrostatic potentials, the size of the supercells is critical.This was found to be especially important for the formation energies of GaP-Si(111).

In a further study, Supplie et al.[15] investigated GaP-Si(001) interfaces applying DFT and slab-type supercells including a vacuum. Under P-rich conditions the abrupt P-terminated GaP-Si(001) interface is more stable than Ga-terminated and vice verse. However, most stabilization was found for the abrupt P-terminated configuration and it was thus concluded that P-Si bonds are more favorable than Ga-Si under P-rich conditions. Still, under equilibrium conditions the intermixed configurations are the most stable confiurations of GaP-Si(001) for the given arguments of charge compensation.

For the growth of GaP on Si(001) substrates under P-rich conditions at a growth temperature of 450 °C it was found that Ga tends to be the first layer in direct contact to Si.[6] Only at higher temperatures, Si-P form stable bonds at the interface in line with the results summarized above. The growth of an atomic P layer on Si is likely kinetically limited by the decomposition of the precursor molecule.[21]

We have recently reported a study on the growth of GaP on Si(001) substrates including high-resolution transmission electron microscopy imaging (TEM), kinetic Monte Carlo (KMC) simulation and DFT-based dertermination of adatom surface diffusion barriers and absolute interface formation energies for abrupt and intermixed GaP-Si(001), GaP-Si(111) and GaP-Si(112).[22] Two arguments were provided that show that the GaP-Si interface along [001] is unlikely to form over representative areas. Firstly, the atom transport kinetics during growth lead to an intermixing of up to eight atomic layers, which is presumably limited by overgrowth in the metal-organic vapour phase epitaxy (MOVPE) procedure. Secondly, intrinsic interface stabilities prefer microscopic orientations different to [001] driving the system to form a faceted morphology including mainly interfaces at (111) and (112). While GaP-Si(001) is favourable in the configuration with one intermixed atomic layer, GaP-Si(111) and GaP-Si(112) are preferred as abrupt interfaces. A combination of interfaces in multiple stable configurations leads to a faceted interface morphology including all orientations as observed in TEM images and in quantitative agreement with intermixing found in KMC simulations. Moreover, it was shown that Ga- and P-terminated configurations can explicitely be distinguished by calculating absolute formation energies from slab-type supercells. The results were in good agreement with bulk-type supercells containing both configurations.

In this study we follow the above approach and compute absolute interface formation energies and further properties of abrupt and intermixed configurations of GaP-Si interfaces in (001), (111), (112) and (113). We apply DFT with the GGA and the D3[23] correction for dispersion interactions. As it can be distinguished between Ga- and P-terminated interfaces, we present a total of 25 configurations and their absolute formation energies that can now be directly compared based on a uniform methodology. The configurations were chosen as to encompass both intrinsically compensated interface orientations and those that need to reconstruct, i.e. intermix, for stabilization. Intermixing had to be constrained to one atomic layer as to ensure balanced stoichiometry in the interface model and reference cells, respectively. Already, for some configurations, it was not possible to construct slab-type supercells ensuring identical stoichiometry with the corresponding reference cells. The sampling over a large number of configurations is advantageous for two reasons. The risk of missing an important configuration is lowered and a stability-weighted assembly similar to a Wulff construction can provide an estimate of the interface morphology based on the ideal facets.

In contrast to most previous studies, the absolute formation energies are independent of chemical potentials. Its application is certainly necessary for complex superstructures where the formation energy cannot be explicitly calculated e.g. due to mismatching stoichiometry in the interface model or the reference cells. However, the quantitative correlation of Ga- or P-rich conditions to experiment is not trivial as the nucleation phase is sensitive towards several physical and chemical processes of which many are not yet fully understood. Furthermore, the identification of the most suitable reference state for an element can be ambiguous.[24] Here, stoichiometric conditions are assumed so that direct correlation between atomic and electronic structure[25,26] can be drawn that is purely based on results from first principles without the uncertainty of how to match the chemical potential to experimental conditions. In this approach, individual atoms in the material-pure Si or GaP reference cells are in the exact same environment as in the interface cell (except close to the interface). It is possible to distinguish between Ga- and P-terminated abrupt and Si/Ga- and Si/P-intermixed interfaces. Explicit energies are provided for major GaP-Si interface configurations.[22] The results are interpreted to learn about their intrinsic character in terms of stabilization, chemical bonding and electronic properties.

The PBE functional has proven to be reliable both for the determination of minimum structures as well as discontinuities of the electrostatic potentials although band gaps are severely underestimated.[27,28] We thus use this approach to analyze structural and electrostatic properties of all GaP-Si interface configurations introduced in order to provide a chemical reasoning for the different stabilities found.

Local strain and lattice-mismatch are analyzed by decoupled relaxations of local atomic coordinates and the cell axis along stacking direction, respectively. Atomic partial charges are derived from the chemically motivated Natural Population Analysis which is based on localized bond orbitals and provides reliable data on the charges at the interfaces. This helps to rationalize the simple models introduced above by providing an actual charge for the atoms the interface is composed of. Moreover, it also provides a quantification of the charge distribution further away from the interface.

Finally, local potentials and potential offsets are computed in both slab- and bulk-type supercells.[29] This allows direct correlation of atomic to electronic effects for specific interface configurations and the detection of artifacts that are due to the model character of either slab- or bulk-type cells (e.g. insufficient size).

# Model Structures and Methods

## Model Structures and Supercells

In Figure 1, excerpts of the supercells representing the GaP-Si interfaces studied here are sketched along with the number of different types of non-octet Si-Ga and Si-P bonds normalized to a common interface area $A_{(001)} = a^2$ with Si's experimental lattice constant $a = 5.431$.[30]**(001)**, **(111)**, **(112)** and **(113)** refer to abrupt, i.e. atomically flat, interfaces containing an inter-atomic plane separating the Si and GaP films. Therein, the interfaces **(001)**, **(111)** and **(111)-sb** (separated bilayer) are composed of exclusively Si-Ga (Si-P) direct contacts and are hence named Ga-terminated (P-terminated) and referred to as **Ga-** (**P-**). The same nomenclature is applied for the interfaces **(112)** and **(113)** although those are composed of Si-Ga *and* Si-P bonds and considered intrinsically charge-compensated.

Refer to Figure 1 to distinguish between Ga- and P-dominated configurations of those.

The notation **-im** refers to an intermixed interface with one atomic layer of Si/E composition at ratio 1:1 (E = Ga, P), specified as **Si/Ga-** or **Si/P-**, respectively. Originating from the prevalent bilayer character of cubic zinc blende crystals along [111], **(111)-im-1** and **(111)-im-2** represent two different configurations (see Figure 1).

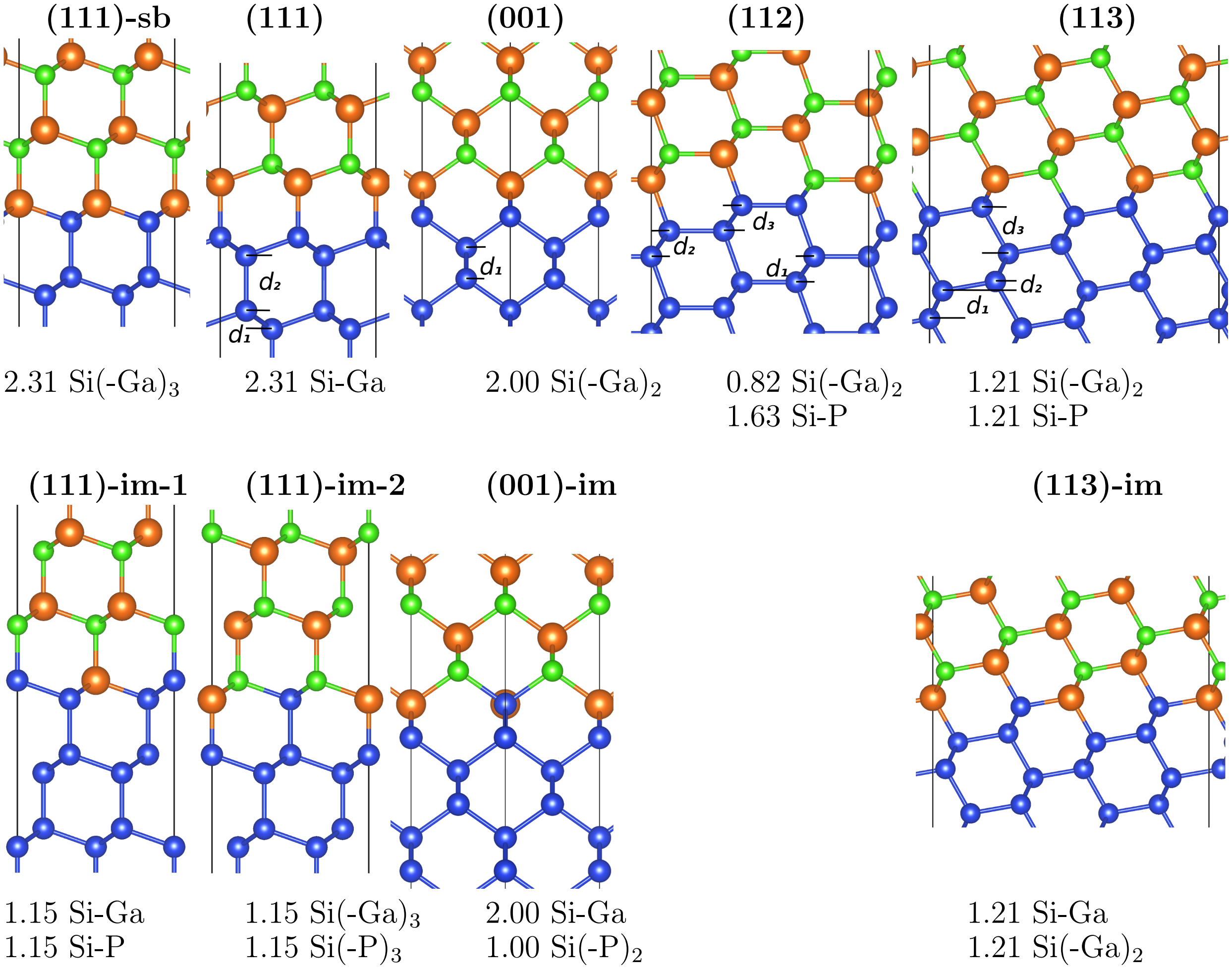

Figure 1: GaP-Si interface configurations investigated here (Ga-terminations shown). Below the structural models, the number of direct contacts (non-octet bonds) with Si are provided normalized to $A_{(001)}$. P-terminated configurations and bond counts can be derived by interchanging Ga and P element symbols.

Both bulk-type and slab-type model supercells were constructed from the *ideal* (unrelaxed) cubic Si unit cell. They are presented in Figure 8- Figure 12 and in the Supporting Information (Figure 13-Figure 15).

All abrupt interfaces were modeled as **Ga-** or **P-** slab-type supercells and as bulk cells containing both interfaces simultaneously. By converting the order of atoms in the GaP film (corresponding to its film polarity), one can specifically compute **Ga-** *or* **P-** interface formation energies applying the slab models. The supercells of **(001)** consist of 16 Si + 16 GaP atomic layers (**(111)**: 24 Si + 24 GaP, **(112)**: 24 Si + 24 GaP,**(113)**: 22 Si + 22 GaP). As all bulk cells contain an even number of GaP layers, they contain both **Ga-** and **P-** interfaces. Extended interface regions inside supercells are illustrated in Figure 1.

Intermixed interface structure were modeled only in bulk-type supercells due to stoichiometry constraints. **(001)-im** consists of 15 Si + 15 GaP + 2Si/E and **(111)-im** of 23 Si + 23 GaP + 2 Si/E atomic layers, while the two configurations **(111)-im-1** and **(111)-im-2** correspond to one E atom (E = Ga, P) intermixing into the interface $Si_2$ bilayer (two atomic layers in close contact) and a Si atom substituting E in a GaP bilayer. Configurations with Si substitutions at the second of the two atomic layers away from the interface plane were not considered here as they are expected to be less stable.[18] Intermixed configurations of **(112)** were neglected as they were expected to be less stable because charge compensation is lifted.

## Interface formation energy

We calculated absolute interface formation energies independent of any reference chemical potential[20,31] according to

$$\Delta E_{if} = \left( N E_{GaP-Si} - \frac{N}{2}(E_{GaP} + E_{Si}) \right) / A_{\mathbf{(001)}}, \tag{1}$$

where $N = 1$ for one interface in slab- and $N = 2$ for two interfaces in bulk-type cell models. $\Delta E_{if}$ is subsequently normalized to the unit cell area of GaP-Si(001) $A_{\mathbf{(001)}} = a^2$. $E_{GaP}$ and $E_{Si}$ are the respective absolute energies of Si and GaP reference cells which fulfill the following criteria: volume , number of atoms, the structure and the chemical environment of atoms outside the interface region must be identical in the (corresponding half of the) reference cells and the interface cell. Due to those restrictions, this approach is computationally demanding as reference cells need to be calculated for each interface configuration. The determination of $\Delta E_{if}$ is also restricted to *ideal* lattice sites and thus interfaces between materials with an (energertically) small lattice-mismatch. For those, however, the absolute $\Delta E_{if}$ can subsequently be corrected by the relative energy gain from relaxation, $\Delta E_{relax} = E_{relaxed} - E_{ideal}$, for each interface cell as

$$\Delta E_{if}^{opt} = \Delta E_{if} - \Delta E_{relax}. \tag{2}$$

For the individual GaP-Si configurations, $\Delta E_{if}$ was found to be large relative to the energetic consequence of the materials' lattice mismatch (see Results section Cell Elongation) justifying this approach.

## Electronic and atomic structure relaxation

Large structural models are necessary to reliably describe the GaP-Si interface structure by periodic density functional theory (DFT). We thus decided to apply the General Gradient Approximation (GGA) with the PBE functional,[32,33] the D3[23] dispersion correction and expand a set of plane wave basis functions. The projector-augmented wave formalism[34] was applied as implemented in VASP v5.3.5.[35,36] A kinetic energy of 400 eV truncated the basis set expansion and accurate convergence settings for the energies and structural relaxations (SCF energy: $< 10^{-6}$ eV, forces: $< 10^{-3}$ eV/Å), well-converged grid of $k$-points ($\Gamma$-centered Monkhorst-Pack, $8x4x1$ for all configurations) were used. The hydrogen-passivated surfaces in slab cells are separated by a well-converged vacuum of >16 Å.

Originating from the smaller lattice constant $a_{Si}$, the interface supercells were elongated stepwise along $c$. For all elongations, minima were detected proving that the energy gain from lattice relaxation is larger than the error introduced by increasing the size of the basis set with the cell volume. Subsequently, atomic positions were relaxed for each interface cell model at initial elongation state providing important information on the bonding situations at the interface and inside the films.

Lateral strain ($a$,$b$) was proven to be small in comparison to tetragonal strain along $c$, which is to be expected for the almost lattice-matched GaP-Si system.[37] The energies of the applied slab cells were converged within <17 meV $a^{-2}$ upon doubling the smallest cell axis $b$ proving the supercells are sufficiently sized.

For the slab model cells, a dipole correction was found have negligible effect with respect to total energy and averaged electrostatic potentials.

In this study, electronic energies are presented without thermodynamic corrections. For materials with small lattice-mismatch configurational entropy was found to be insignificant.[20]

For GaP-Si interfaces along [111], W = 6 different configurations are discussed here (abrupt and intermixed within one atomic layer) leading to an entropic energy gain of 123 meV/$(1/2\sqrt{2}a \times \sqrt{\frac{3}{2}}a)$ evaluated with[10]

$$T\Delta S_{config} = Tk_B ln(W) \tag{3}$$

at a typical growth temperature T = 763 K. Compared to the resulting absolute interface formation energies this is negligible.

There might be further interdiffused configurations of **(111)** with lower interface stability than the ones presented here.[18,38] However, those are likely configurations with two intermixed atomic layers which hampers direct comparison and enforces the application of much larger supercells.

## Partial charges and local potentials

The periodic basis functions (from VASP 4.6) of the *ideal* interface cells were projected onto a local Gaussian type basis (def2-SVP).[39] Subsequently, partial (atomic) charges were determined by a periodic version[40] of the Natural Population Analysis.[41]

Local electrostatic potentials were derived from the DFT wave function (VASP 5.3.5) and averaged over $a, b$ planes normal to $c$. Average curves determined by locally weighted linear regressions (smoothness parameter 0.2, 2 iterations) smooth the oscillations along the atomic planes in $c$. The materials' average potential levels $V_{av}$ were determined by these curves. They were also used to identify local polarizations at the interfaces and the polarization fields through the films.

All potential curves were shifted setting the average energy to 0 so that there was only a deviation of $10 meV$ to the average energy levels in Si and GaP reference cells with identical orientation.[42]

Potential offsets $\Delta V_{av}^{GaP-Si}$ were determined from the average potential curves across the interfaces. This property is important as it determines the valence band offset (VBO)[13] as

$$VBO = \Delta V_{av}^{GaP-Si} + \Delta E_{VBM}^{GaP-Si} + \Delta E_{SO}^{GaP-Si} \tag{4}$$

where $\Delta E_{VBM}^{GaP-Si}$ is the difference of the valence band maxima (VBM) of GaP and Si and $\Delta E_{SO}^{GaP-Si}$ is a correction for spin-orbit coupling (approx. 0.01 eV).[43]

## Results

In the series of abrupt, uncompensated GaP-Si interfaces **(111)**, **(001)** and **(111)-sb**, the interface Si atoms exhibit one (Si−E), two (Si(−E$_2$)) and three (Si(−E)$_3$) non-octet bonds, respectively (compare structures and bond counting in Figure 1). The latter configuration (**(111)-sb**) exhibits the interface plane intersecting a bilayer while the first (**(111)**) intersects in between two bilayers. In Table 1 the separations of *ideal* atomic layers normal to the crystal orientations investigated are collected.

Along [111], every second inter-layer separation corresponds to one Si-Si bond length ($d_1$). As a result, a characteristic bilayer structure is formed with two atomic layers in close

Table 1: Layer separations $d$ in Å of *ideal* diamond cubic Si lattice along orientations $c$ ($a$ = 5.431 Å). The atomic layers along [001] are equidistant.

| $c$ | [001] | [111] | [112] | [113] |
|---|---|---|---|---|
| $d_1$ | 1.358 | 0.784 | 1.109 | 1.228 |
| $d_2$ | 1.358 | 2.352 | 1.109 | 0.409 |
| $d_3$ | 1.358 | 0.784 | 1.109 | 2.047 |

contact ($d_1$) maximally separated from the next bilayer ($d_2$). This has consequences on the stabilities of interfaces formed within or outside of bilayers, and also on the structural relaxation inside a III/V zinc blende film away from the surface (see below).

Interfaces formed along [112] and [113] are intrinsically compensated as both Ga and P are in direct contact to Si interface atoms (Figure 1). However, the ratio of non-octet Si-Ga and Si-P bond counts is not necessarily 1:1 as in intermixed **(001)-im**. Abrupt **(112)** exhibits e.g. 0.82 Si−Ga and 1.63 Si−P bonds per normalized interface area and **(113)** has 1.21 Si(−Ga)$_2$ (i.e. two bonds to Ga per Si) and 1.21 Si−P. Opposite polarity is achieved by swapping Ga for P and vice verse, respectively.

Moreover, the chemical environments of interface atoms is affected by layer spacings and crystal orientation. We will quantify the effect of the individual chemical environments on interface stability by comparing formation energies of configurations with similar non-octet bond ratios.

For an illustration of the remaining intermixed configurations refer, to Figure 1.

## Interface formation energies for the ideal lattice

Absolute interface formation energies $\Delta E_{if}$ of GaP-Si interfaces based on DFT calculations applying models cells of slab- and bulk-type are presented in Table 2. Stoichiometry restrictions with the reference cells limited the usage to bulk-type cells for **(111)-sb**, **(001)-im** and **(111)-im**. However, comparing $\Delta E_{if}$ from slab cells containing a single, specific interface with data from bulk cells representing both configurations with complementary polarity (the average of **Ga-** and **P-** for a given configuration), deviations are less than 16 meV/$a^2$

(**(111)**). This proves (i) the model cells to be well-converged in size (separating one interface from either vacuum in slab or the second interface in bulk cells) and (ii) both approaches are suited for the calculation of absolute formation energies.

Table 2: Interface formation energies $\Delta E_{if}$ in $eVA^{-1}_{(001)}$ for GaP-Si configurations introduced in Figure 1. Results from different model cells are presented.

| | | **(111)-sb** | **(111)** | **(001)** | **(112)** | **(113)** |
|---|---|---|---|---|---|---|
| abrupt | **Ga-** | - | 0.521[a] | 0.817[a] | 0.196[a] | 0.811[a] |
| | **P-** | - | 0.619[a] | 1.111[a] | 0.733[a] | 0.304[a] |
| | aver.[d] | | 0.570[a] | 0.964[a] | 0.464[a] | 0.557[a] |
| | aver.[d] | 1.749[b] | 0.558[b] | 0.974[b] | 0.480[b] | 0.568[b] |
| **-im** (intermixed) | **Si/Ga-** | | 0.863[c] | 0.507[b] | | 0.783[a] |
| | **Si/P-** | | 0.863[c] | 0.527[b] | | 1.108[a] |
| | aver.[d] | | | | | 0.945[a] |
| | aver.[d] | | | | | 0.944[b] |

[a] from slab model cell

[b] from bulk model cell, average of **Ga-** and **P-** interface configurations

[c] average of **(111)-im-1** and **(111)-im-2** from bulk model cell

[d] average of **Ga-** and **P-** abrupt interfaces (i.e. **Si/Ga-** and **Si/P-** for **-im**) for the given configuration

Abrupt GaP-Si interfaces **(111)** were found to be more stable than **(001)** (0.570 vs. 0.964 eV/$a^2$). This holds for both **Ga-** and **P-** configurations and can be explained by two structural arguments. (Upon atom relaxation, **P-(111)** becomes more favourable than **Ga-(111)**, see results section below.) Fewer non-octet bonds as well as the formation of completed bilayers lead to an interface stabilization. A bilayer is charge neutral given it encloses a complete atomic layer of Ga and P, respectively. The ECM is fulfilled for a GaP bilayer and the separation to Si at the interface is maximal (comp. Table 1).

In **(001)**, the atomic layers are located at identical distances ($d_1$), leaving two non-octet bonds ($\mathrm{Si}(-\mathrm{E})_2$, E = Ga, P) per interface atom at smaller separation than in **(111)**. Both abrupt configurations are exclusively Ga- or P-terminated, the charge at the interface is thus uncompensated in **(001)** and, corresponding to more non-octet bonds, larger than in **(111)**.

Following the above arguments, **(111)-im** (bottom row in Table 2) is less stable than the abrupt configuration (0.863 vs. 0.570 eV/$a^2$). The intermixed atomic layer within the interface bilayer leads to an increase of one to three non-octet bonds per interface Si atom and the otherwise charge-neutral bilayer is disturbed. Remarkably, the average formation energies of configurations **(111)-im-1** and **(111)-im-2** are identical regardless of whether the intermixed layer is **Si/Ga-** or **Si/P-**. Romanyuk et al. showed that **Si/P-(111)-im-1** and **Si/P-(111)-im-2** deviate only by 19 meV/$a^2$.[18]

As the electronegativites of Ga and P cause different bond polarizations, the identical stabilization cannot be explained by the simple argument of charge compensation at the interface.

The least stable GaP-Si interface is **(111)-sb** where the terminating GaP bilayer is intersected by the interface. The average formation energy of **Ga-** and **P-** configurations is presented (0.863 eV/$a^2$). Interface atoms exhibit three non-octet bonds each (Figure 1) and the ECM leads to a deficit (excess) of $\frac{3}{4} \times 2.31$ electrons per interface Ga (P) atom (normalized to $a^2$). This is the maximum within the configurations presented in line with the highest $\Delta E_{if}$. Furthermore, the spatial separation of the interface atomic layers is small, i.e. within one bilayer ($d_2$), leading to a large concentration of excess charge at the interface according to ECM.[18]

In contrast to **(111)**, one layer of atomic intermixing at the interface is favorable for **(001)**. **Si/Ga-** as well as **Si/P-(001)** interfaces are regarded charge-compensated by ECM, although the situations are not exactly identical. **Si/Ga-(001)** (**Si/P-(001)**) exhibits 2.00 Si$-$Ga and 1.00 Si$(-\mathrm{P})_2$ bonds (2.00 Si$-$P, 1.00 Si$(-\mathrm{Ga})_2$). Due to eletronegativity, this represents different chemical environments for Ga and P atoms in the interface regions and is noticeable with different stabilities. Harrison et al.[14] proposed interface configurations with two atomic layers of intermixing containing both **Si/Ga-** and **Si/P-** layers. Within a symmetric unit cell, this model is expected to show even smaller differences in $\Delta E_{if}$ between **Si/Ga-** and **Si/P-**.[14]

The most stable interfaces are the abrupt **Ga-(112)** and **P-(113)**. Interface Si atoms are in contact to both Ga and P exhibiting various combinations of one and two non-octet bonds each. Although those configurations can be considered largely charge-compensated after the

ECM (comp. Figure 1), **Ga-(112)** and **P-(112)** as well as **Ga-(113)** and **P-(113)** show significantly different formation energies, respectively. The bonding pattern 0.82 $\mathrm{Si(-Ga)_2}$, 1.63 $\mathrm{Si-P}$ of **Ga-(112)** is most stabilized (0.196 $\mathrm{eV}/a^2$) followed by 1.21 $\mathrm{Si(-P)_2}$, 1.21 $\mathrm{Si-Ga}$ at **P-(112)** (0.304 $\mathrm{eV}/a^2$). Considering the formation energies of abrupt configurations with one $\mathrm{Si-E}$ and two $\mathrm{Si-(E)_2}$ non-octet bonds as reference it is not possible to simply add their contributions in order to evaluate the formation energies of compensated interfaces. While a quantitative trend can be recognized in $\Delta E_{if}((\mathbf{111})) \approx \frac{1}{2}\Delta E_{if}((\mathbf{001})) \approx \frac{1}{3}\Delta E_{if}((\mathbf{111})\text{-}\mathbf{sb})$, the abrupt, intrinsically compensated configurations **(112)** and **(113)** are dominated by the individual environment inside the interface region, i.e. first, second and third atomic coordination spheres.

Furthermore, in abrupt, non-compensated and intermixed, formally compensated interfaces, **Ga-** and **Si/Ga-** are more stable than the **P-** and **Si/P-** equivalents in the ideal lattice structure. One representative is the charged interface **(113)-im** that exhibits exclusively Si-E (E = Ga or P) contacts. **Ga-(113)-im** is stabilized by 0.783 $\mathrm{eV}/a^2$ while **P-** is less stable (1.108 $\mathrm{eV}/a^2$). The configurations **(001)**, **(111)** and **(001)-im** support this trend.

## Interface structure relaxation

Two aspects were studied by extensive geometry relaxation of GaP-Si interface formations next to justifying the assumption of lattice-matched GaP-Si material for the determination of $\Delta E_{if}$ in the *ideal* lattice.

Firstly, the energetic consequence of compressive strain caused by the chosen smaller lattice constant (experimental mismatch (Si, GaP): 5.431/5.451 = 0.37%)[44] was analyzed by a linear elongation of the supercells along $c$. The atomic lattice sites were kept constraint. Subsequently, the atom positions were relaxed within the elongated interface cells in order to quantify the effect of local strain both at the interface and within the bulk-like film. The cell dimensions were constrained in order to gain a clear separation from the extended effect related to lattice-mismatch.

Secondly, the consequences of local forces was investigated based on the displacement of atoms upon relaxation. In the following, the configurations **(001)**, **(111)**, **(001)-im**, **(111)-im**, **(112)** are discussed representing conceptual features of abrupt (non-compensated), abrupt (compensated) and intermixed (compensated) interfaces including the most stable known from literature.

### Cell elongation in c and atom relaxation

Interface formation energies upon cell elongation bulk and slab model cells are presented in Figure 2 and in Figure 3, respectively. The calculated elongation curves reveal shallow potentials indicating a negligible energetic consequence of the GaP-Si lattice mismatch (max. stabilization in bulk cells: 1.5% (**Si/Ga-(111)-im**), in slab cells: 3.8% (**Ga-(001)**)) relative to the *ideal* interface formation energies calculated.

Minima were found at elongations of max. 0.65 % (**(001)**) for bulk and 0.85 % (**Ga-(001)**) for slab models. The bulk mismatch is well represented by the average of all configurations. Bulk and slab models of relaxed **(112)** and **(111)** exhibit minimum energies very close to the experimental lattice mismatch (0.35 %). **(001)** models, especially abrupt **Ga-(001)** (1.00 %), show a tendency to stabilize at slightly larger elongations (Figure 3). Supercells with ideal configurations are slightly more strained (minima at larger elongations) than the respective cells with relaxed atom positions. However, all elongation energy curves are shallow indicating little effect of lattice-mismatch and strain.

As can be directly extracted from Figure 2, the order of stabilities (average of **Ga-** and **P-**) for the configurations presented is **(112)** < **(001)-im** < **(111)** < **(111)-im** < **(001)** and does not change upon atomic relaxation.

The abrupt bulk models presented have an almost constant energetic gain upon atom relaxation, i.e. relative to each other and upon cell elongation (Figure 2, left). While this is also approximately constant for **(001)-im**, **Si/Ga-(111)-im** is significantly more stabilized by atom relaxation than the equivalent **Si/P-(111)-im**. Note that the relative order is not

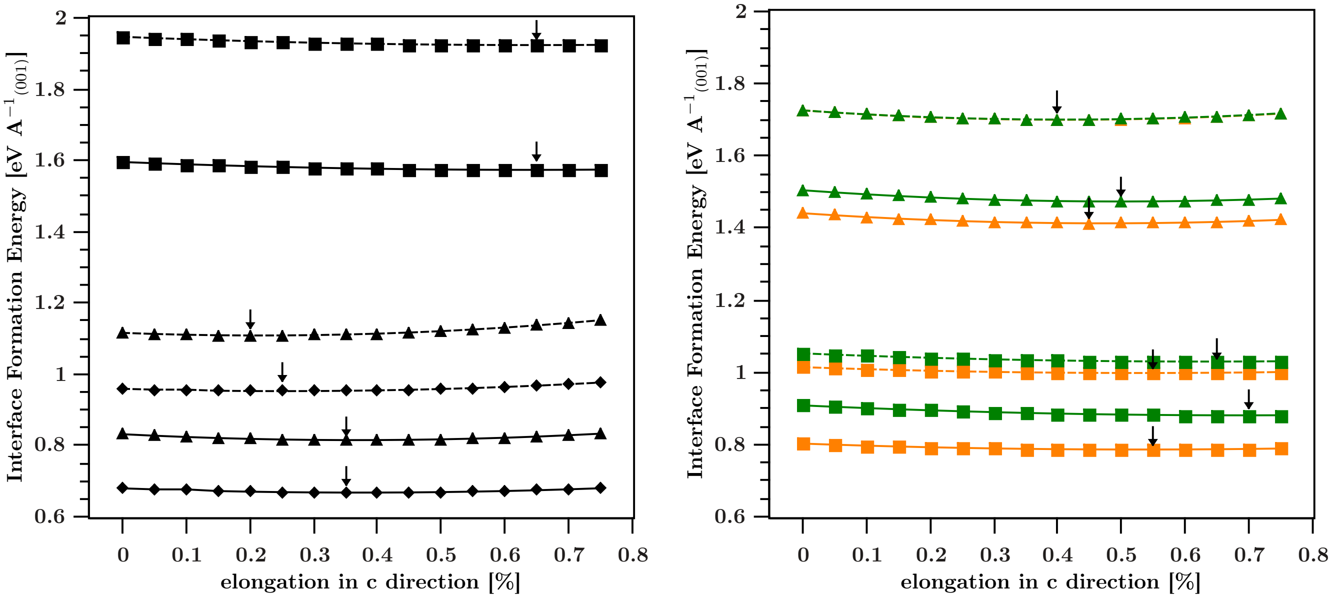

Figure 2: Bulk supercell elongation along $c$. Interface formation energies of **(001)** (squares), **(111)** (triangles) and **(112)** (diamonds) are provided for the elongated supercells at *ideal* (dashed lines) and relaxed (straight lines) atomic positions relative to the *ideal* Si lattice ($a$ = 5.431 Å), respectively. Intermixed interfaces were studied with **Si/Ga-** (orange) and **Si/P-** (green) intermixed atomic layers.

reversed as the *ideal* **(111)-im** configurations have identical $\Delta E_{if}$= $\frac{1}{2}$×1.7 eV/$a^2$ (Figure 2, right).

In Figure 3, slab models reveal that *ideal* abrupt Ga-terminated interfaces **Ga-(001)**, **Ga-(111)** and **Ga-(112)** are more stable than the P-terminated equivalents for all cell sizes considered. While **Ga-(001)**, **P-(001)** and **Ga-(111)** experience an approximately constant shift upon atom relaxation, **P-(111)** becomes more stable than **Ga-(111)** reversing the order of stability. **P-(111)** is stabilized by $\Delta E_{if}^{opt}$ = 0.35 eV/$a^2$ which is 57% of the *ideal* $\Delta E_{if}$. Cell elongation without atom relaxation brings 17.2 meV/$a^2$ corresponding to 2.8% and a shift of the minimum position with cell elongation from 0.05% to 0.35%. The order of stability for *relaxed* **(111)** models is in accordance with findings by Romanyuk et al..[18] **Si/Ga-** intermixed interfaces are more favourable than the **P/Si-** equivalents in accordance with the above trend for most Ga-terminated and Si/Ga-intermixed configurations.

On the other hand, **(112)** interfaces experience only minor energetic gain upon relaxation

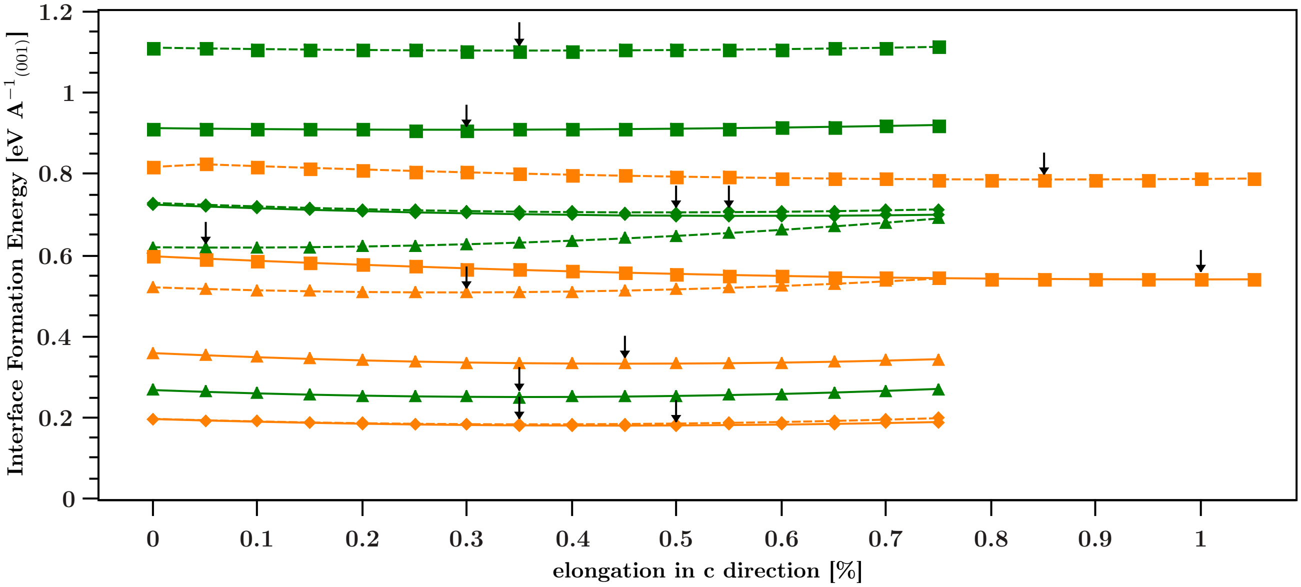

Figure 3: Slab supercell elongation along $c$. Interface formation energies of **(001)** (squares), **(111)** (triangles) and **(112)** (diamonds) are provided for the elongated supercells at *ideal* (dashed lines) and relaxed (straight lines) atomic positions relative to the *ideal* Si lattice ($a = 5.431$ Å), respectively. The bottom Si layers and all surface-passivating H atoms were constrained to their optimized positions in the reference lattice.

due to their (already) nearly charge-compensated character in the *ideal* lattice. Note the significant difference in stability between **Ga-(112)** and **P-(112)**.

### Average atomic layer displacements

The quantification of structural parameters is used as the first descriptor of the chemical bonding situation of the interfaces. Ideal lattices without elongation were used as initial structures. The average displacements of atomic layers upon atom relaxation are presented in Figure 4 (bulk models). Positive (negative) values indicate a local expansion (contraction) along *c*.

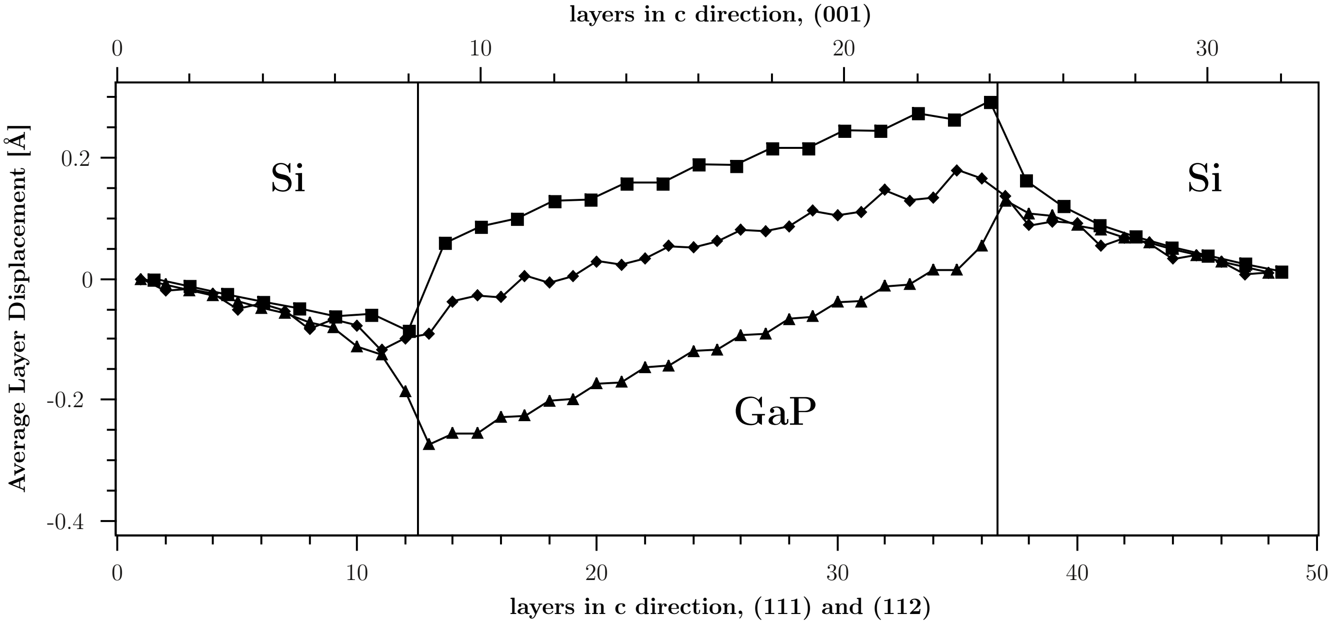

Figure 4: Average displacement of atomic layers normal to *c* (in Å) upon atom relaxation. Bulk interface cells are presented for abrupt GaP-Si interfaces at **(001)** (squares, top abscissa), **(111)** (triangles) and **(112)** (diamonds, bottom abscissa). The formal interface planes are indicated by vertical lines.

The bulk models of abrupt **(001)**, **(111)** and **(112)** commonly show contracting Si films indicated by negative slopes of the curve in the left and right parts of Figure 4 as the GaP layers in the center expand (positive slope). The displacements in conjunction with $\Delta E_{if}^{opt}$ is a good measure for the mechanical strain effect at the interfaces even though the calculated films are not as thick (16 and 24 Å) as in real, film-stacked III/V quantum-well superstructures.[12] The behaviour inside the films is linear, while the non-linear behaviour at the interfaces (vertical lines) offers insight into local effects.

For abrupt **(001)** and **(111)** interfaces, large displacements at the interface planes were calculated. This displacement is positive at **Ga-** termination indicating the Si-Ga separation to increase while the Si-P separation at **P-** decreases (large negative displacement, refer also to the slab model results in Figure 16).

Inside the GaP films in these orientations, every second layer is displaced by larger amplitudes representing atomic layers of Ga and P, to approach each other. Due to the natural bilayer structure this effect is largest along [111]. Ga and P layers close the ranks, compensating a local polarization along $c$ and increase the separation to neighbouring bilayers. Same trends were found by Zunger et al. suggesting local piezoelectric effects.[19] The displacements in the Si films are homogeneous.

For **(112)**, the structural reorganizations at the GaP-Si interfaces are much smoother. Moreover, the absolute displacements are significantly smaller than in **(001)** and **(111)** as each atomic layer contains both Ga and P elements and local polarization effects are thus smaller. However, the signs of maximum displacements at the **Ga-** and **P-** configurations support the classification of **(112)** interfaces as Ga- and P-dominated, respectively, in accordance to **(001)** and **(111)**. Inside the GaP film along [112] the layer averaging indicates the formation of tri- instead of bilayers in bulk model cells.

For intermixed **(001)-im** and **(111)-im** (Figure 5), contracting Si and expanding GaP films are concluded similar to the films with abrupt interfaces. The GaP film in **(111)-im** expands slightly more than in **(001)-im** indicated by a slightly increased positive slope between 14 and 36 Å. In contrast to the abrupt models, the curves do not show any steps which would indicate the formation of GaP bilayers. Note, that **(111)-im** was found to be significantly less favourable than abrupt **(111)** (0.863 vs. 0.558 eV/$a^2$). This trend is preserved upon relaxation (0.773 vs. 0.416 eV/$a^2$) as can be retraced by the formation

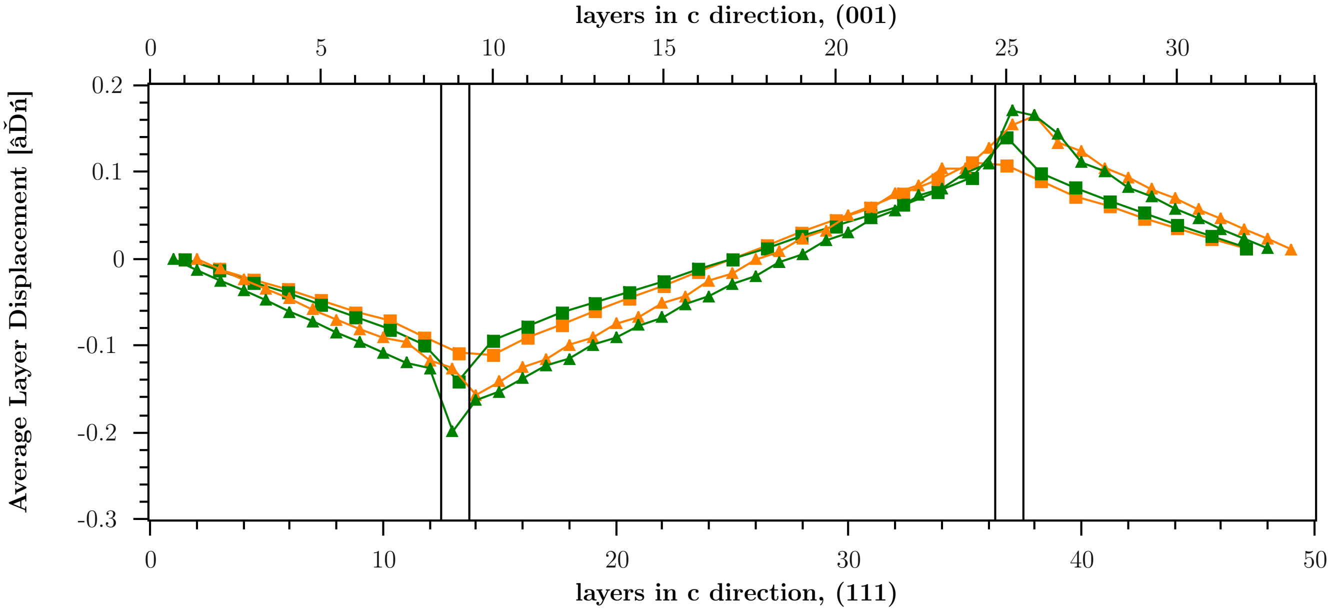

Figure 5: Average displacement of atomic layers normal to $c$ (in Å) upon atom relaxation. Bulk interface cells are presented for intermixed GaP-Si interfaces **(001)-im** (squares, top abscissa) and **(111)-im** (triangles, bottom abscissa). The formal interface planes are indicated by vertical lines.

energies of optimized interfaces presented in Table 3.

In both orientations, the **Si/P-** intermixed layers (inside vertical lines, green curves) exhibit larger local displacements at the interfaces than **Si/Ga-**, which are almost continuous (orange curves). In line with our results on abrupt interfaces presented above and previous calculations,[19] Si-P bond lengths are decreased and Si-Ga are increased. This is surprising for two reasons. (i) The difference of atomic radii is larger between Si and Ga than between Si and P and (ii) short bond lengths are often applied as an indicator for increased bond strength. Following the interface formation energies of abrupt configurations **(001)**, **(111)** and **(111)-sb**, this is not supported as **Ga-** is more stable than **P-**termination in all cases. This holds for *ideal* and relaxed interfaces (comp. Table 2 and Table 3).

The structural rearrangements of abrupt interfaces modeled in slab cells are in line with the results presented above for bulk models (see Supplementary Information, Figure 16). In all configurations, the average layer displacement is largest in an interface region of two atomic layers on either side of the formal interface plane. This is an important information

Table 3: Interface formation energies $\Delta E_{if}^{opt}$ after Equation 2 in eV$/a^2$ for abrupt and **im-** configurations of **(001)**, **(111)** and **(112)** GaP-Si with *relaxed* atomic positions (non-elongated supercells). Results from different model cells are presented.

| | | **(111)** | **(001)** | **(112)** |
|---|---|---|---|---|
| | **Ga-** | $0.359^a$ | $0.597^a$ | $0.196^a$ |
| abrupt | **P-** | $0.267^a$ | $0.913^a$ | $0.729^a$ |
| | aver.$^d$ | $0.313^a$ | $0.755^a$ | $0.462^a$ |
| | aver.$^d$ | $0.416^b$ | $0.798^b$ | $0.340^b$ |
| | | | | |
| | **Si/Ga-** | $0.721^c$ | $0.401^b$ | |
| **-im** (intermixed) | **Si/P-** | $0.753^c$ | $0.454^b$ | |

[a] from slab model cell

[b] from bulk model cell, average of **Ga-** and **P-** interface configurations

[c] average of **(111)-im-1** and **(111)-im-2** from bulk model cell

[d] average of **Ga-** and **P-** abrupt interfaces (i.e. **Si/Ga-** and **Si/P-** for **-im**) for the given configuration

as it shows that the relaxation at the interfaces are quantitatively important. Furthermore, it is also an indicator that these displacements are local and converge within two atomic layers on either side of the interface irrespective of crystal orientation.

Interface formation energies are decreased upon atom relaxation, however, the stability ranking of the configurations examined is preserved. **P-(111)** is the exception as it is stabilized from 0.619 to 0.267 eV$/a^2$ (Table 2 and Table 3). This is another indicator of the formation of a stable Si-P bond at this interface. In contrast, the Si$(-\mathrm{P})_2$ bonds at **P-(001)** gain less stabilization upon relaxation so that **Ga-(001)** remains more stable ($\Delta E_{if}^{opt}$ = 0.597 vs. 0.913 eV$/a^2$). For compensated interfaces, the stabilization through relaxation is much less significant. **(001)-im**, **(111)-im** and **(112)** gain, on average, 0.127, 0.089 and 0.124 eV$/a^2$, respectively, and the hierarchy is preserved.

## Atomic Partial Charges

Atomic partial charges of the interface model cells were obtained by NPA following a projection of the wave function onto a local basis. The results gained from abrupt slab cells and **im-** bulk cells show the polarization directly at and further from the interfaces. The interface regions are illustrated in Figure 6.

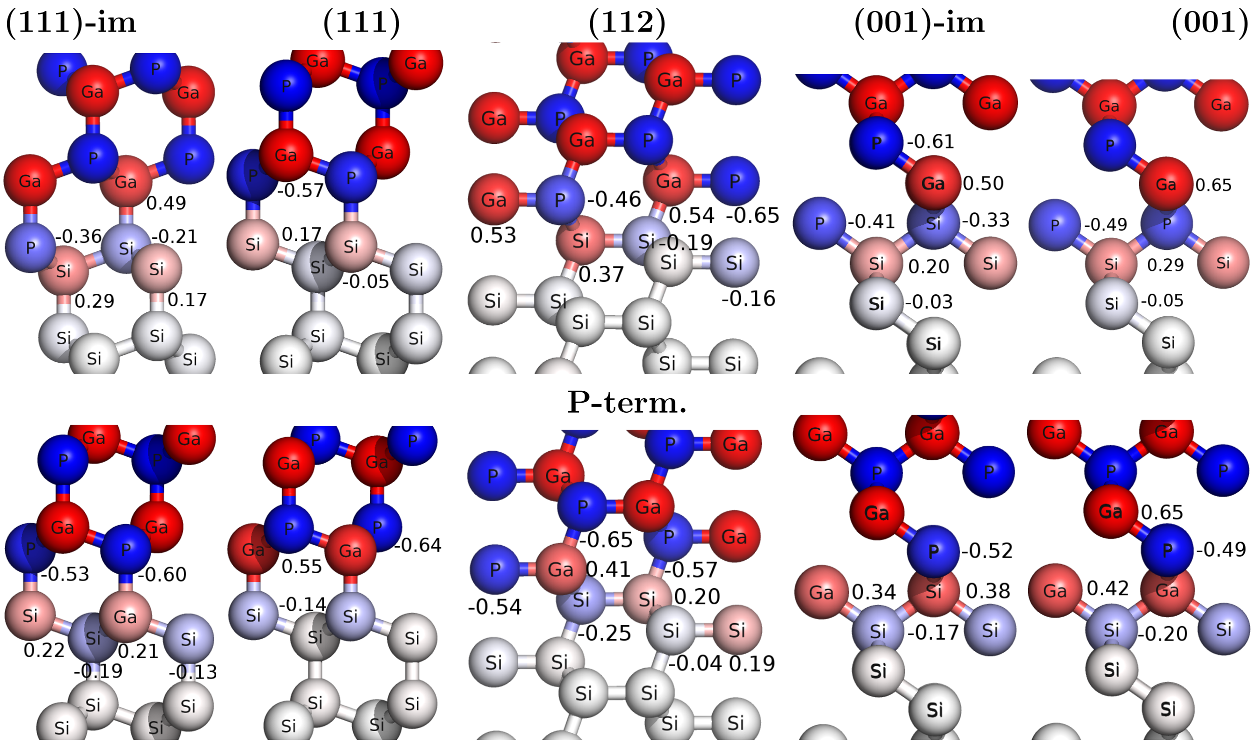

**(111)-im** **(111)** **(112)** **(001)-im** **(001)**

**P-term.**

**Ga-term.**

Figure 6: NPA charges projected as atom colors on interface structures. Element symbols are printed on, charges (in $|e|$) below or right hand to the atom spheres. Charges within $\leq \pm 0.02$ to the constant bulk polarization (Si: 0.00 (white), Ga: $+0.67$ (red), P: $-0.67$ (blue)) are not printed.

**(111)-im-2** is not shown as the charge distribution is in accordance to**(111)-im-1**.

A deviation from the bulk atomic partial charges is clearly present at the interfaces which, however, converges to constant partial charges within two atomic layers from the interface plane. Away from the interface, the charges converge to a constant ($q(Si)$=0.00; $q(Ga)$=+0.67, $q(P)$=-0.67) polarization where Si atoms are neutral and Ga (P) atoms are positive (negative) inside the GaP film. The sum of charges within this film is neutral.

This indicates, firstly, that the supercell models suitably represent charge distributions inside the material films. This polarization (by about 2/3 electrons per atom) can be rationalized by differences in electronegativity of the elements ($\chi(Si) = 1.90$, $\chi(Ga) = 1.81$, $\chi(P) = 2.19$).

Secondly, the deviation at the interface is indeed strongly localized to the interface region. Si atoms in direct contact with P become positively charged (**P-**, **Si/P-**) while Si atoms become negatively charged in contact with Ga (**Ga-**, **Si/Ga-**). The maximum deviations from the bulk polarization was found for interface atoms of least stable interfaces. For example, the following configurations are ordered by decreasing stability (in eV/$a^2$) and increasing absolute value of the partial charge (charge per interface Si atom, in $e$): **Ga-(111)** (0.521, 0.14) $<$ **P-(111)** (0.619, 0.17) $<$ **Ga-(001)** (0.817, 0.20) $<$ **P-(001)** (1.111, 0.29); **Si/Ga-(001)-im** (0.863 ,0.21) $\leq$ **Si/P-(001)-im** (0.863, 0.22); **Ga-(112)** (0.196, 0.05) $<$ **P-(112)** (0.733, 0.16) (average of two Si atoms considered for **(112)**). However, it is difficult to quantitatively correlate partial charges to the formation energies of more interdiffused configurations, e.g. **(111)-im** (Figure 6).

Within the intermixed atomic interface layers of **(001)-im** and **(111)-im**, the Si atoms adopt the polarization of its mixing partner element. It is thus negative in the **Si/P-** structures and positive in the **Si/Ga-** configurations. As an electrostatic response, the Si atoms second nearest to the interface are charged by small amounts of opposite sign, respectively, reflecting a damped, electrostatic oscillation originated in the GaP film.

The atomic partial charges of abrupt interfaces were summed into double layers representing $Si_2$ and GaP bilayer units. The results from bulk model cells of **(001)**, **(111)** and

**(112)** are presented in Figure 7.

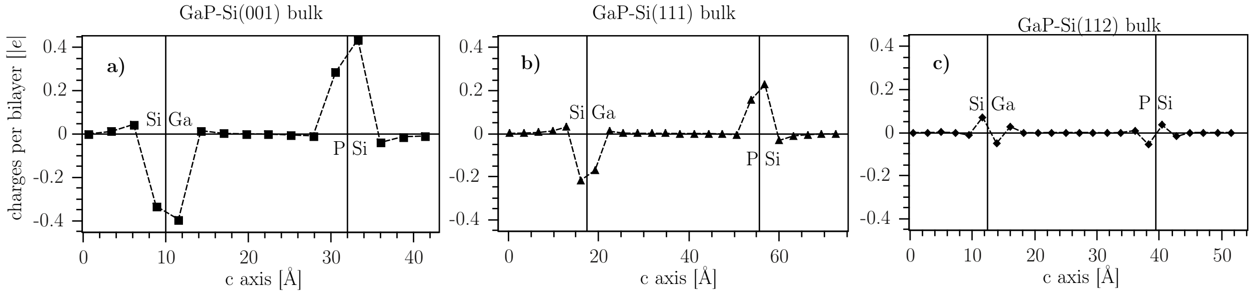

Figure 7: NPA charge per bilayers (two atomic layers normal to *c*) of bulk model cells a) **(001)**, b) **(111)** and c) **(112)**. **Ga-** and **P-** interfaces are indicated.

Indeed, inside the Si and GaP films away from the interfaces, the charge sums to neutrality. At the interfaces, however, local deviations are identified. Ga-terminated/-dominated interfaces are negatively and **P-** are positively charged. This charge is largest for **(001)** (ca. ±0.36 *e*), about half for **(111)** (ca. ±0.19 *e*) and significantly smaller in **(112)**. Note that the individual atomic charges usually exceed the bilayer sums (comp. Figure 6) which reflects compensation inside a bilayer.

Although the Ga-dominated **(112)** shows a slightly larger amplitude of charge summed over bilayers at the interface, the individual atomic layers are slightly more charged for **P-(112)** (0.17*e* vs. 0.15*e*), which is the less stable interface.

In **(001)** and **(111)**, the bilayers on each side of the abrupt interface ($Si_2$, GaP) are charged about similar amounts with identical sign. This is not the case for **(112)**, where the atomic layers are intrinsically compensated and the charge changes the sign across the interface plane (vertical line) from the $Si_2$ to the GaP bilayer, respectively.

Similar trends can be retrieved for the intermixed bulk and abrupt slab cell models (see Supplementary Information).

The general trend revealed for abrupt interfaces is: large bilayer charges destabilize the interface. The polarization of bilayers is more pronounced at the least stable interfaces of **(001)** than at **(001)-im** and **(111)**, which have moderate energies and charges.

## Layer-averaged local potentials along c

The electrostatic local potentials of interface supercells are presented as average over atomic layers normal to $c$.

The averaged potentials well resolve atomic layers and local polarization at the interface(s) as shown in the following. A detailed analysis of the manifold configurations modeled here is used to correlate atomic with electronic structure and the chemical bonding situation at the interfaces.

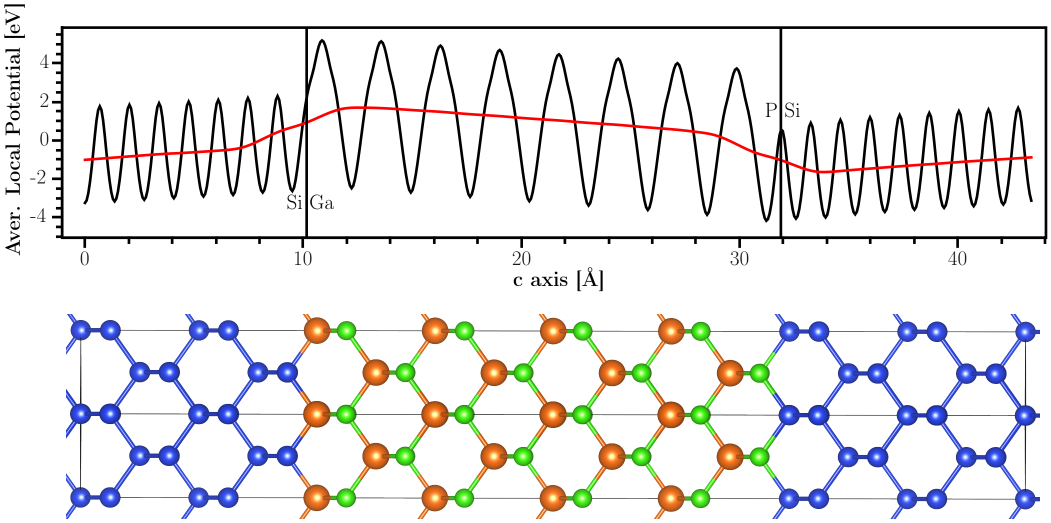

Figure 8: Plane-averaged local electrostatic potential along $c$ of the **(001)** bulk cell with the smoothed average (red). The interface planes are indicated by vertical lines.

Figure 8 presents the local potential of the bulk cell model of abrupt **(001)**. A polarization field[19] inside the GaP region indicates its polar character along $c$ which is also present in reference cells with pure GaP (not shown) and absent in pure Si films. The polarization field in the Si film regions is due to a direct electrostatic response within the supercell.

The potential offset $\Delta V_{av}$ across the interfaces was evaluated as 2.18 eV at the Ga-terminated (left in Figure 8) and 1.79 eV at the P-terminated interface (right). The potential energy levels were extracted from the average curve (red curve). Here, it converges to the

Si and GaP film values (here corresponding to the polarization field) within 2 atomic layers on each side of the interface. In other configurations the local dipoles extend more into the films as shown below.

The local potentials of the **(111)** and **(112)** bulk models are presented in Figure 9 and Figure 10, respectively.

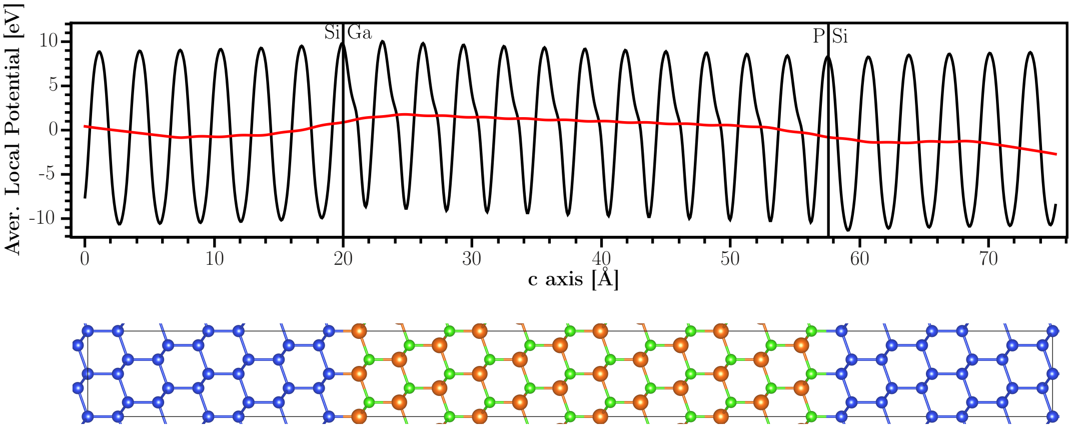

Figure 9: Plane-averaged local electrostatic potential along $c$ of the **(111)** bulk cell with the smoothed average curve (red). The interface planes are indicated by vertical lines.

**(111)** resolves the bilayer structure inside the GaP film. The potential calculated is sufficiently sensitive to resolve atomic Ga and P layers by the peak shoulders and minima, respectively, inside a bilayer's amplitude. The bilayer amplitudes exhibit negative values with respect to the smoothed average curve (red curve) within only 1.34 Å, which is less than the formal structural expansion of 1.57 Å separating the bilayers. Thus, the bilayers are considered almost charge-compensated units inside GaP. The potential offsets are 2.08 eV (**Ga-**) and 1.76 eV (**P-**) although it has to be noted that their determination is not distinct as the local polarization extends significantly into the films.

contrast to **(111)**

In **(112)**, the amplitudes of oscillating potential are much smaller in the GaP region than in the Si film. This is due to a compensation inside each *atomic* GaP layer almost to

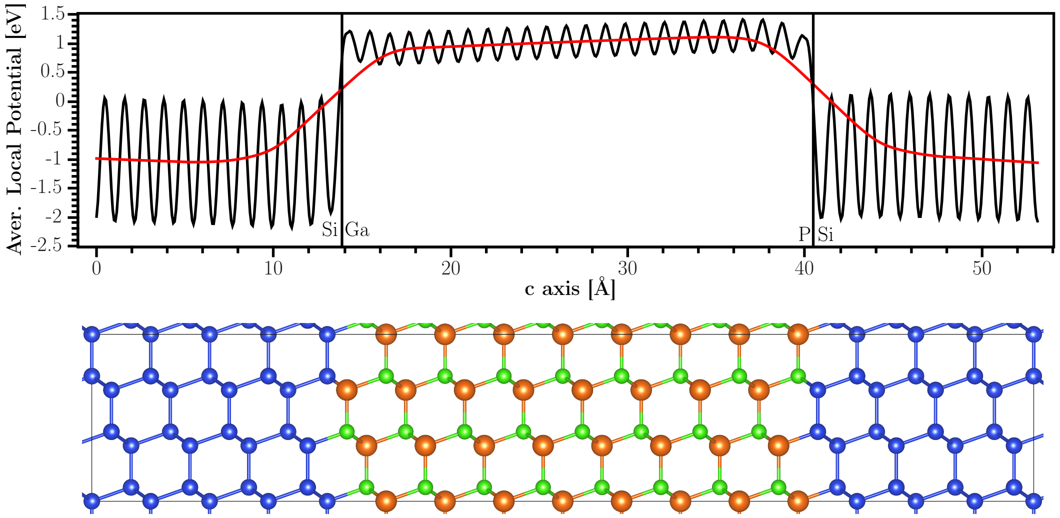

Figure 10: Plane-averaged local electrostatic potential along $c$ of the **(112)** bulk cell with the smoothed average (red). The interface planes are indicated by vertical lines.

neutrality. This average charge-compensation in GaP along [112] and is a valuable indicator for the stability of **(112)** interfaces. The film polarization, which has the negative pole situated at **P-(001)** and **P-(111)**,respectively, is almost non-polar in **(112)**. Only the first layers of GaP at the interfaces, as indicated in Figure 10, can be considered positive Ga- (left ) and negative P-dominated (right) interfaces, respectively. The potential offsets correspond to 1.88 and 1.87 eV, respectively. These values were evaluated at positions about 3-4 atomic layers away from the interface and thus reflect offsets between the films.

This is another indication that local polarizations strongly depend on the interfaces' atomic configuration.

The supercells with intermixed interface configurations show qualitatively different local potentials than abrupt equivalents and are presented in Figure 11 (**(001)-im**) and Figure 12 (**(111)-im**).

There is no film polarization along $c$ as the left and right interfaces in **(001)-im** bulk models are identical. **Si/Ga-** and **Si/P-** models have reverse film polarity as the order of Ga and P atomic layers was reversed during cell construction. Intermixed layers at both

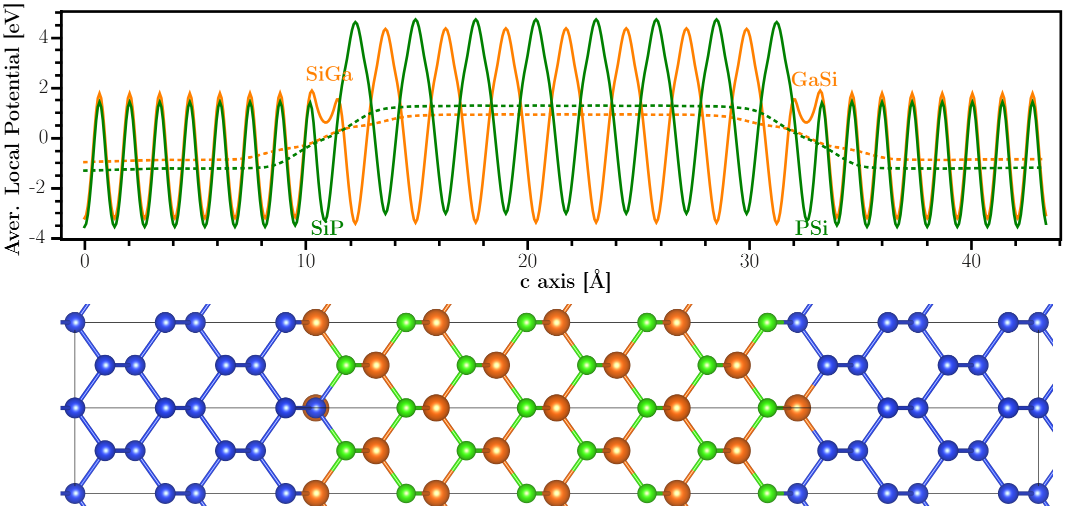

Figure 11: Plane-averaged local electrostatic potential along $c$ (straight lines, top) of the **(001)-im** bulk cell. **Si/Ga-** (center, orange curve) intermixed configuration is provided (bottom) while the **Si/P-** intermixed structure corresponds to swapping Ga and P atoms inside the GaP film. Smoothing functions introduced (dotted). The interface planes are indicated by vertical lines.

interface configurations lead to a smooth transition from Si to GaP film average levels within two atomic layers (comp. average curves) which is in agreement with abrupt **(001)**. The local polarization extends slightly more in **Si/Ga-** than in **Si/P-** intermixed configurations. The corresponding potential offsets 1.1 eV and 2.1 eV, respectively. We attributed this difference to the different polarization fields caused by the different interface configurations. Note that the total number of Si, Ga and P atoms is kept constant throughout the cell models.

Similar to abrupt **(111)**, the local potential of **(111)-im** resolves Ga and P atomic layers inside the characteristic bilayers (see Figure 12).

The polarization field allows to distinguish between the two intermixed configurations **(111)-im-1** and **(111)-im-2**. **Si/Ga-(111)-im-1** represents the positive pole (left, orange curve in Figure 12) and **Si/Ga-(111)-im-2** represents the negative pole (right). The field polarity is identical in **Si/P-(111)-im** (green curve). (Note that the interfaces appear in reverse order, **Si/P-(111)-im-1**: left, **Si/P-(111)-im-2**: right.)

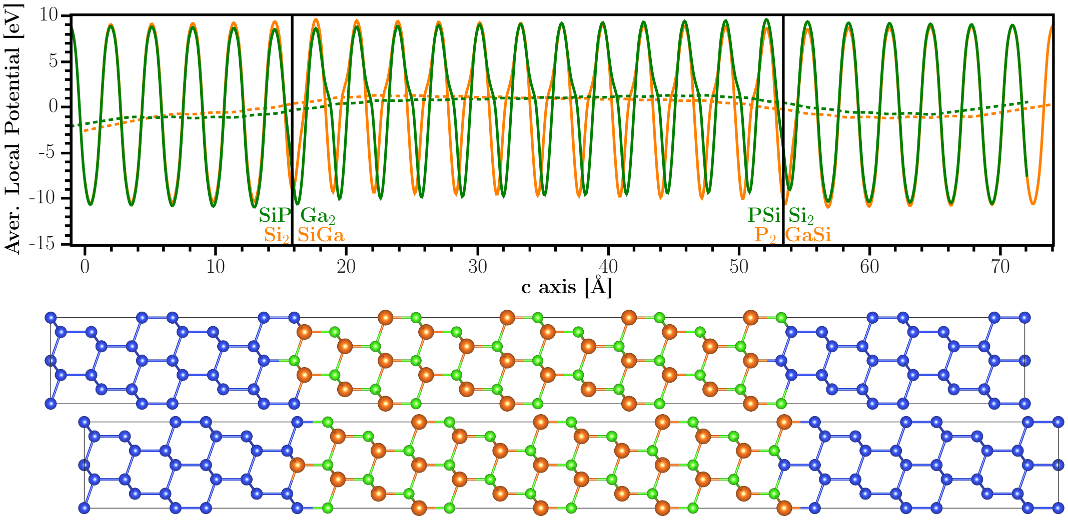

Figure 12: Plane-averaged local electrostatic potential along $c$ (straight lines, top) of the **(111)-im** bulk cell. **Si/Ga-** (orange curve, bottom structure model) and **Si/P-** (green curve[a], central structure) intermixed configurations are presented. Smoothing functions introduced (dashed). **Si/Ga-(111)-im-1** is found left hand and **Si/Ga-(111)-im-2** right hand in the potential plot. The **Si/P-** potential behaves inversely in accord to the cell models provided. The interface planes are indicated by vertical lines.

[a] **Si/P-**'s potential curve was shifted about -3.14 Å along $c$.

The curves were aligned so that the order of atomic layers inside the GaP film is identical for both **Si/Ga-** and **Si/P-** configurations (from left to right: PGa...PGa), so that the fine structure in the potential amplitudes well resolves the polarity within the GaP bilayers.

The local potential offset are 1.5 eV at **Si/Ga-** and 1.6 eV at **Si/P-** (average over both configurations **(111)-im-1** and **(111)-im-2**, respectively).

The local potentials from slab model cells are presented in Figure 13, Figure 14 and Figure 15 and specifically resolve (local and extended) features of **Ga-** and **P-**. The local potential in the vacuum region of the slab cells converges to the vacuum energy level (not shown).

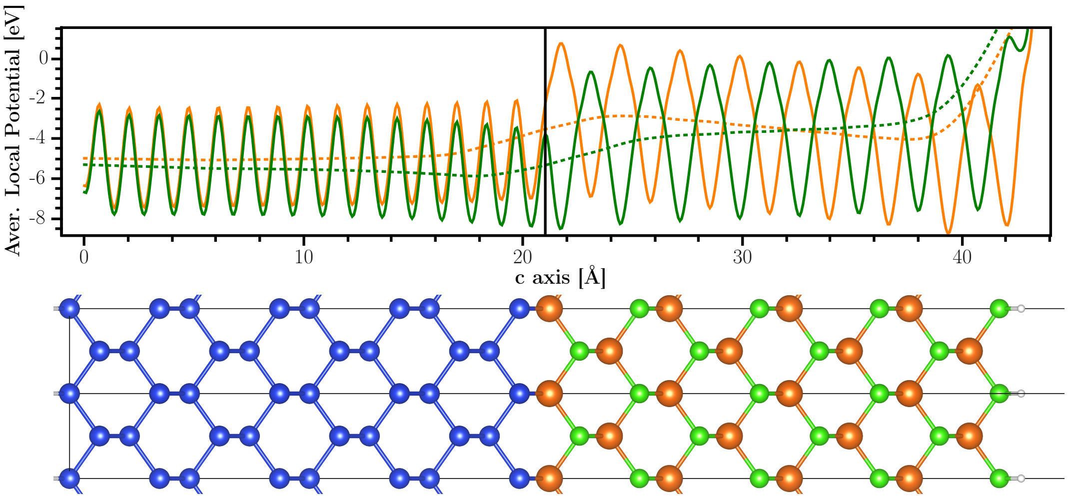

Figure 13: Plane-averaged local electrostatic potential along $c$ (straight lines, top) of **(001)** slabs neglecting any vacuum. The **Ga-(001)** model cell is shown (bottom, orange curves) while the **P-** configuration (green curves) is generated by transposing the Ga and P atoms inverting the GaP film polarity. Smoothed potentials were introduced as dashed lines. The interface planes are indicated by vertical lines.

The film polarization is clearly distinguishable in slab models with Ga- and P-specific terminations. **Ga-(001)** (**P-(001)**) has the positive (negative) pole at the interface, which is also found for **(111)** and even for **(112)** where each atomic layer is formally compensated and the polarization is less pronounced.

Furthermore, local behaviour at the interfaces can be extracted from the local potential curves. **P-(001)** is represented by the most negative amplitude directly at the interface P atomic layer while **Ga-(001)** has the most positive amplitude there (Ga layer charge deficiency by ECM).

Moreover, the transition region between the electrostatic film averages is shifted towards the GaP film (to the right) in **P-(001)** and towards the Si film (to the left) in **Ga-(001)**. The potential offsets were evaluated as 1.7 and 2.0 eV, respectively, at about three atomic layers on each side of the interfaces. The larger (smaller) offset corresponds to a negative (positive) charge at the interface region (sum over two bilayers) in **Ga-(001)** (**P-(001)**).

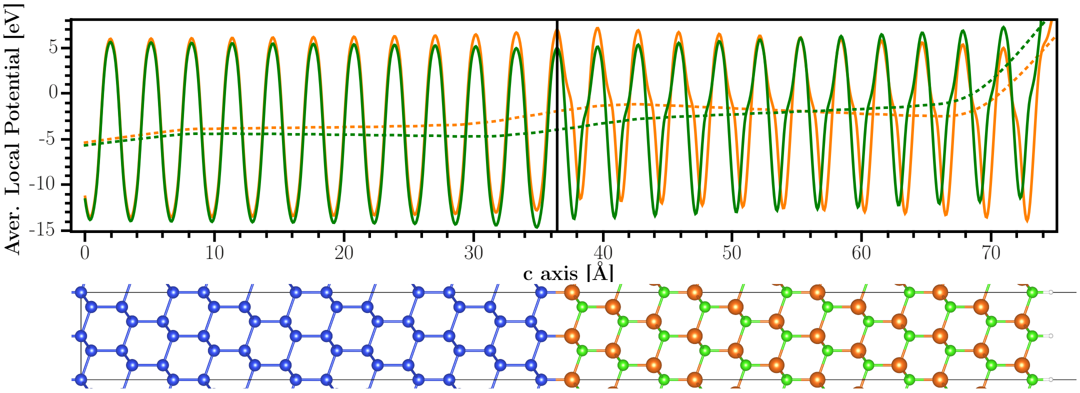

Figure 14: Plane-averaged local electrostatic potential along $c$ (straight lines, top) of **(111)** slabs neglecting any vacuum. The **Ga-(111)** model cell is shown (bottom, orange curves) while the **P-** configuration (green curves) is generated by transposing the Ga and P atoms inverting the GaP film polarity. Smoothed potentials were introduced as dashed lines. The interface planes are indicated by vertical lines.

For **(111)** slab models, a comparable local interface situation is found. The amplitudes for **Ga-(111)** are slightly more positive in the interface region than **P-(111)**'s. In contrast, the film polarization is less distinct corresponding to the intrinsically compensated bilayer units. Those units seem to make the whole film less polarizable. As in the bulk model cells, the polarity inside each GaP bilayer along $c$ is resolved in the electrostatic potential curves showing local minima in P atomic layers and (positive) shoulders at the Ga layers. The potential offsets are 2.2 eV (**Ga-**) and 2.0 eV (**P-**).

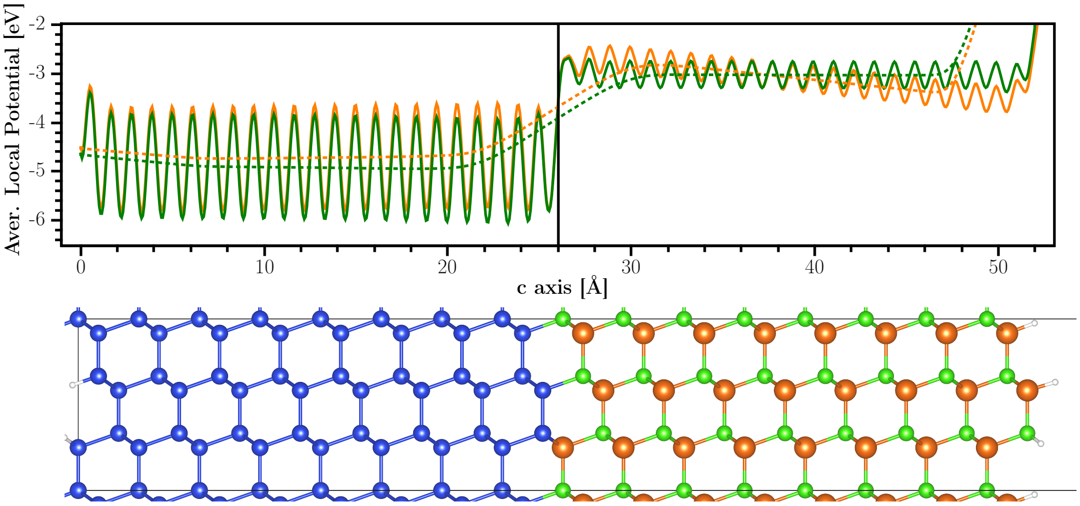

Figure 15: Plane-averaged local electrostatic potential along $c$ (straight lines, top) of **(112)** slabs neglecting any vacuum. The **Ga-(112)** model cell is shown (bottom, orange curves) while the **P-** configuration (green curves) is generated by transposing the Ga and P atoms inverting the GaP film polarity. Smoothed potentials were introduced as dashed lines. The interface planes are indicated by vertical lines.

Local potentials in **(112)** slab models are presented in Figure 15 and most valuable information is gained from the average curves (dashed lines).

Inside the GaP films, a polarization field is present carrying opposite signs in **Ga-(112)** and **P-(112)**. The local polarization at the interface is shifted in energy but *not* along the $c$-axis. The first is due to an alignment of the potential to the field. The potential offsets are 2.0 and 1.8 eV in **Ga-** and **P-**, respectively.

As in the **(112)** bulk models, every atomic GaP layer is intrinsically nearly compensated leading to small amplitudes fluctuating around the average.

# Summary and Conclusions

GaP-Si interfaces in (001), (111), (112) and (113) orientation with different local configurations were studied by periodic DFT (GGA) calculations applying bulk- and slab-type supercell models. Absolute interface formation energies were determined by material-pure Si and GaP reference cells of identical size and structure. It could be shown that both supercell model types converge to unequivocal stabilities for the configurations investigated. With the slab models it was possible to determine properties of specific interface structures such as Ga- and P-terminated or Si/Ga- and Si/P-intermixed configurations.

For interfaces at **(112)** and **(113)**, significantly different formation energies between **Ga-(112)** (0.196 eV) and **P-(112)** (0.733 eV) configurations were calculated which cannot be rationalized by any charge compensation model as both interface structures are considered intrinsically charge-compensated. In many other cases, Ga-terminated tend to be more stable than P-terminated interfaces with the exception of *relaxed* **P-(111)** and **(113)**.

The concept of charge-compensation at the interface was quantified by partial charges based on natural bond orbitals (NPA). The sum of charges across bilayers is negative at abrupt Ga-terminated interfaces and positive at P-terminated interfaces. Their absolute value is large for **(001)** (0.36 $e$), smaller for **(111)** (0.19 $e$) and vanishes to neutral for **(112)** (<0.1 $e$). For those configurations, the ECM or other charge-compensation models are qualitatively useful and correctly predict the order of formation energies for non-compensated, abrupt and formally compensated, intermixed interfaces **(001)**, **(001)-im** and **(111)** even distinguishing between **Ga-** (**Si/Ga-**) and **P-** (**Si/P-**) terminations. For average stabilities of **Ga-(112)**, **P-(112)**, **Si/Ga-(111)-im** and **Si/P-(111)-im** the models hold only qualitatively.

From the partial charge analysis more can be learned about the bonding situation of the GaP-Si system. While Ga (P) atoms inside the films are consistently positively (negatively) charged about 0.67$e$ in accordance to electronegativity, they take up negative (positive) charges at the interfaces which was calculated as the sum of charges within bilayers.

Local stress as well as strain effects over the extended films were investigated by structural relaxation. It was found that the almost lattice-matched GaP-Si system is well represented by supercells of silicon's ideal lattice. The simulated mismatch quantified by cell elongation well represented the bulk mismatch experimentally determined and the strain energy was found to be small ($<2$ % of the interface formation energy). On the other hand, local atomic relaxation at the interface lead to a change in relative stability in one case (preference for **P-(111)** over **Ga-(111)**). In all other configurations, the energies are decreased significantly upon atom relaxation but the ranking of stabilities is preserved with respect to the ideal lattice. Structure relaxation showed that local stress at the interfaces can clearly be distinguished from tetragonal strain due to the lattice mismatch. Local distortions are largest for uncompensated configurations and small for **(112)**. There is a tendency, especially along [111], to form GaP bilayers stabilizing the film as well as the interface. The formation of compensated bi- or trilayers along stacking direction is a new perspective on interface stabilization next to the reduction of non-octet bonds, charge and film polarization. At abrupt, Ga- or P-terminated interfaces, Si-P bond lengths is shortened upon relaxation in contrast to Si-Ga, which is elongated. This might be due to the much larger atomic radius of Ga compared to Si and P, however, Ga-terminated interfaces are in most cases found to be more stable than P-terminated.

Local, plane-average electrostatic potentials unveil film polarization inside GaP as well as local behaviour at the interface region, which allows to distinguish between intermixed and abrupt configurations. The model cells of intermixed configurations applied are (almost) non-polar over the films and allow a smooth transition between the electrostatic averages of Si and GaP. The transition regions of local potentials in abrupt interfaces is sensitive to Ga- and P-specific termination and in accordance to the concept of charge compensation inside atomic layers (as in **(112)**) or bilayers (**(111)**) as determined from slab models. It extents typically over two to three atomic layers on each side of an interface, which is in accordance to the results on interface partial charges and atomic relaxation. Potential offsets depend on this local polarization, which is sensitive to the atomic structure, and also on the polarization field across the supercell. **(112)** shows a significantly smaller polarization field than **(111)** and **(001)**.

In conclusion, (112) and (113) were identified as stable interfaces for GaP grown on Si. The electrostatic potential offset, partial charges and structural relaxation are local properties which extend about two atomic layers on each side of an GaP-Si interface for the 25 configurations investigated. Interface stability can qualitatively be estimated by the ECM and similar models, however, the formation energies of specific compensated configurations as well as the distinction between Ga- and P-terminated interfaces are determined by the individual chemical environments that can only be computed by self-consistent first principles methods.

## Acknowledgement

The authors thank HLRS, Loewe CSC and HRZ Marburg for computational capacities and support. The authors thank the research training group GRK 1782 (DFG) for funding. A.S. thanks the Beilstein Institut Frankfurt am Main for support.

## References

(1) Fang, S. F.; Adomi, K.; Iyer, S.; MorkocÌğ, H.; Zabel, H.; Choi, C.; Otsuka, N. *Journal of Applied Physics* **1990**, *68*, R31.

(2) Koukourakis, N.; Bückers, C.; Funke, D. A.; Gerhardt, N. C.; Liebich, S.; Chatterjee, S.; Lange, C.; Zimprich, M.; Volz, K.; Stolz, W.; Kunert, B.; Koch, S. W.; Hofmann, M. R. *Applied Physics Letters* **2012**, *100*, 092107.

(3) del Alamo, J. A. *Nature* **2011**, *479*, 317–323.

(4) Kunert, B.; Liebich, S.; Beyer, A.; Fritz, R.; Zinnkann, S.; Volz, K.; Stolz, W. *Journal of Crystal Growth* **2011**, *315*, 28–31.

(5) Hossain, N.; Jin, S. R.; Liebich, S.; Zimprich, M.; Volz, K.; Kunert, B.; Stolz, W.; Sweeney, S. J. *Applied Physics Letters* **2012**, *101*, 011107.

(6) Beyer, A.; Ohlmann, J.; Liebich, S.; Heim, H.; Witte, G.; Stolz, W.; Volz, K. *Journal of Applied Physics* **2012**, *111*, 0835341–6.

(7) Carrère, H.; Marie, X. In *Semiconductor Modeling Techniques*; Balkan, N., Xavier, M., Eds.; Springer Series in Materials Science; Springer Berlin Heidelberg: Berlin, Heidelberg, 2012; Vol. 159; Chapter 6, pp 153–195.

(8) Franciosi, A.; Van de Walle, C. G. *Surface Science Reports* **1996**, *25*, 1–140.

(9) Bylander, D. M.; Kleinman, L. *Physical Review B* **1990**, *41*, 3509–3512.

(10) Dandrea, R. G.; Duke, C. B. *Physical Review B* **1992**, *45*, 14065–14068.

(11) Kunert, B.; Volz, K.; Koch, J.; Stolz, W. *Journal of Crystal Growth* **2007**, *298*, 121–125.

(12) Nemeth, I.; Kunert, B.; Stolz, W.; Volz, K.; Németh, I. *Journal of Crystal Growth* **2008**, *310*, 1595–1601.

(13) Lazzouni, M. E.; Peressi, M.; Baldereschi, A. *Applied Physics Letters* **1996**, *68*, 75.

(14) Harrison, W. A.; Kraut, E. A.; Waldrop, J. R.; Grant, R. W. *Physical Review B* **1978**, *18*, 4402–4410.

(15) Supplie, O.; Brückner, S.; Romanyuk, O.; Döscher, H.; Höhn, C.; May, M. M.; Kleinschmidt, P.; Grosse, F.; Hannappel, T. *Physical Review B* **2014**, *90*, 235301.

(16) Davidovich, M. A.; Koiller, B.; Osório, R.; Robbins, M. O. *Physical Review B* **1988**, *38*, 10524–10532.

(17) Pashley, M. D. *Physical Review B* **1989**, *40*, 10481–10487.

(18) Romanyuk, O.; Hannappel, T.; Grosse, F. *Physical Review B* **2013**, *88*, 115312.

(19) Dandrea, R.; Froyen, S.; Zunger, A. *Physical Review B* **1990**, *42*, 3213–3216.

(20) Kley, A.; Neugebauer, J. *Physical Review B - Condensed Matter and Materials Physics* **1994**, *50*, 8616–8628.

(21) Narayanan, S. Mahajan, N. Sukidi, K, V. *Philosophical Magazine A* **2000**, *80*, 555–572.

(22) Beyer, A.; Stegmüller, A.; Oelerich, J. O.; Jandieri, K.; Werner, K.; Stolz, W.; Baranovskii, S. D.; Tonner, R.; Volz, K. *submitted* **2015**,

(23) Grimme, S.; Ehrlich, S.; Goerigk, L. *Journal of Computational Chemistry* **2011**, *32*, 1456–1465.

(24) Qian, G.-X.; Martin, R.; Chadi, D. *Physical Review B* **1988**, *38*, 7649–7663.

(25) Dunstan, P.; Wilks, S.; Burgess, S. *Applied Surface Science* **1998**, *123-124*, 533–537.

(26) Stekolnikov, A. A.; Furthmuller, J.; Bechstedt, F. *Physical Review B* **2002**, *65*.

(27) Steiner, K.; Chen, W.; Pasquarello, A. *Physical Review B* **2014**, *89*.

(28) Smith, P. V.; Radny, M. W.; Shah, G. A. *Journal of Computational Chemistry* **2014**, *35*, 1248–1254.

(29) Yin, W. J.; Tang, H.; Wei, S. H.; Al-Jassim, M. M.; Turner, J.; Yan, Y. *Physical Review B - Condensed Matter and Materials Physics* **2010**, *82*, 1–6.

(30) Okada, Y.; Tokumaru, Y. *Journal of Applied Physics* **1984**, *56*, 314–320.

(31) Schmidt, W. G.; Bernholc, J.; Bechstedt, F. *Applied Surface Science* **2000**, *166*, 179–184.

(32) Perdew, J. P. *Physical Review B* **1986**, *33*, 8822–8824.

(33) Perdew, J. P. *Physical Review B* **1986**, *34*, 7406.

(34) Blöchl, P. *Physical Review B* **1994**, *50*, 17953–17979.

(35) Hafner, J. *Journal of Computational Chemistry* **2008**, *29*, 2044–2078.

(36) Kresse, G.; Joubert, D. *Physical Review B* **1999**, *59*, 11–19.

(37) Grandjean, N.; Massies, J. *Journal of Crystal Growth* **1993**, *134*, 51–62.

(38) Romanyuk, O.; Grosse, F.; Proessdorf, a.; Braun, W.; Riechert, H. *Physical Review B* **2010**, *82*, 1–5.

(39) Schäfer, A.; Horn, H.; Ahlrichs, R. *Journal of Chemical Physics* **1992**, *97*, 2571–2577.

(40) Dunnington, B. D.; Schmidt, J. R. *Journal of Chemical Theory and Computation* **2012**, *8*, 1902–1911.

(41) Reed, A. E.; Weinstock, R. B.; Weinhold, F. *The Journal of Chemical Physics* **1985**, *83*, 735–746.

(42) Wu, Y.; Chan, M. K. Y.; Ceder, G. *Physical Review B - Condensed Matter and Materials Physics* **2011**, *83*, 1–7.

(43) Landolt-Bornstein, *Numerical Data and Functional Relationships in Science and Technology*; Springer: New York, 1982; pp Group III, Vol. 17 a–b.

(44) http://www.ioffe.ru/SVA/NSM/Semicond/. 2015.

# Supporting Information

Potentials of slab cells, illustrations, partial Charges from slab cells are provided.

# Slab cell relaxation

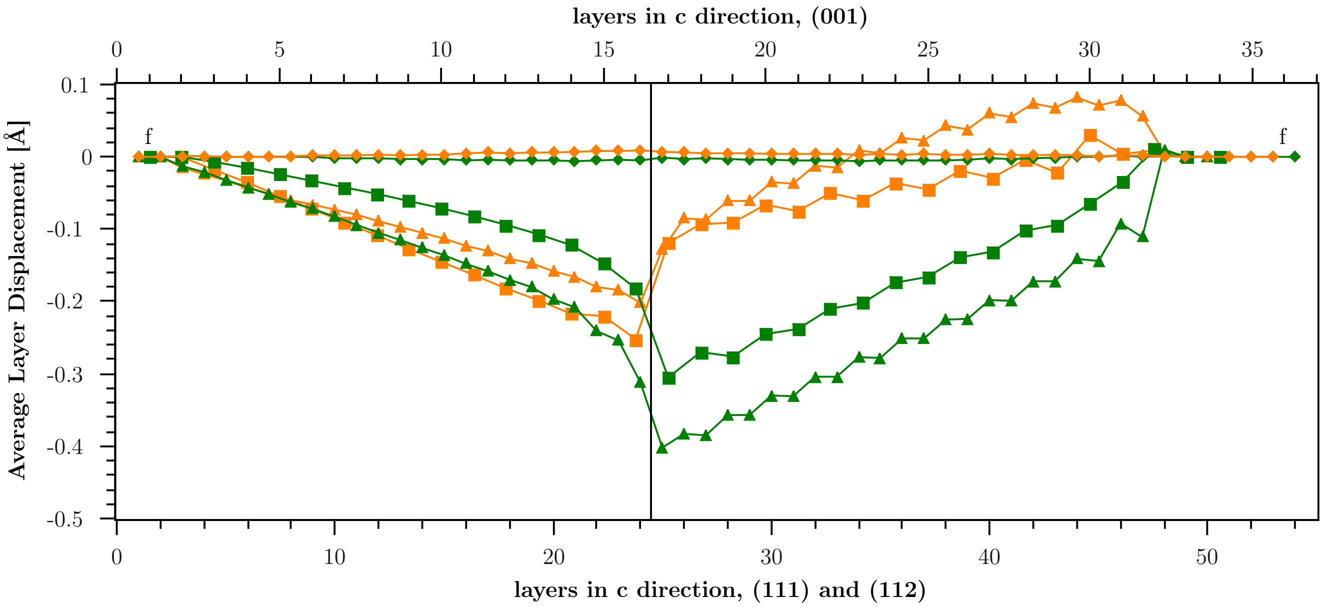

Figure 16: Average displacement of atomic layers normal to $c$ (in Å) upon atom relaxation. Slab interface cells are presented for GaP-Si interfaces **(001)** (squares, top abscissa), **(111)** (triangles) and **(112)** (diamonds, bottom abscissa). The lowest Si double layers and all passivating hydrogen atoms (top layers, partly truncated) were kept frozen (f). The formal interface planes are indicated by vertical lines.

The atom relaxation of slab cells was performed with the bottom Si double layer and all hydrogen atoms frozen, which is indicated with "f" in Figure 16 constraining the supercells to quantum-well heterostructure environment. GaP film expansion and agglomeration into bilayers inside the GaP films are in agreement with the results from bulk model cells for abrupt **(001)** (squares) and **(111)** (triangles).

Remarkably, **(112)** interfaces show almost no displacements as the structure is stable in the *ideal* lattice. An agglomeration into trilayers as observed in the bulk models, cannot be found in the slab cells.

# Bilayer charge sums

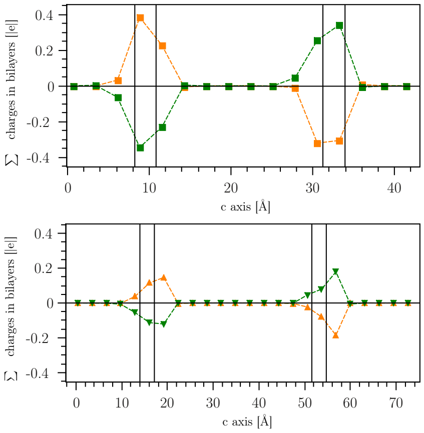

Figure 17: NPA charge sums per bilayers of bulk model cells **(001)-im** (top) and **(111)-im** (bottom). **Si/Ga-** (orange) and **Si/P-** (green) intermixed interface charges are represented as one data point per bilayer, respectively, i.e. two horizontal atomic layers, along the *c* direction of the supercells.

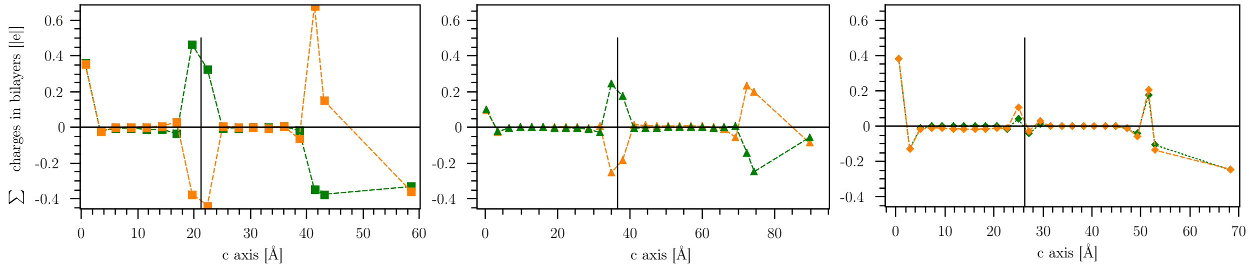

Figure 18: NPA charge sums per bilayers for slab model cells **(001)** (left), **(111)** slab (center) and **(112)** (right). Ga-terminated (orange) and P-term. (green) interface charges are represented as one data point per bilayer, respectively, i.e. two horizontal atomic layers, along the *c* direction of the supercells.

In slab cells, the H passivation layers were treated as one bilayer containing 4 **(001)**, 2 **(111)** and 4 **(112)** H atoms each.

Within bulk regions of the cells, Si as well as GaP, the bilayers generally add up to neutrality. At the interfaces (and H-passivated surfaces of slab cells), however, a polarization can be identified. Ga- and P-terminated interfaces in **(001)** and **(111)** are polarized by similar amounts and opposite signs (**Ga-** is negative, **P-** is positive) which also holds for intermixed structures. **(112)** is a special case as the polarization (i.e. the charge sum $\Delta q = \sum_n q_z$) at the interface is much smaller (0.1 $e$ as opposed to 0.4 $e$ for other systems) and **Ga-** and **P-**termination show the same sign.

(Although the Ga-dominated **(112)** shows the slightly larger amplitude of charge summed over bilayers, the individual atomic layers are more charged for the P-dominated termination (0.18$e$ vs. 0.15$e$, slab cells), which is the less stable interface.)